

2009

## A numerical modeling study on barotropic and baroclinic responses of the Chesapeake Bay to hurricane events

Kyoung-Ho Cho

*College of William and Mary - Virginia Institute of Marine Science*

Follow this and additional works at: <https://scholarworks.wm.edu/etd>



Part of the [Environmental Sciences Commons](#), [Marine Biology Commons](#), and the [Oceanography Commons](#)

---

### Recommended Citation

Cho, Kyoung-Ho, "A numerical modeling study on barotropic and baroclinic responses of the Chesapeake Bay to hurricane events" (2009). *Dissertations, Theses, and Masters Projects*. Paper 1539616608.

<https://dx.doi.org/doi:10.25773/v5-4s3d-sh30>

This Dissertation is brought to you for free and open access by the Theses, Dissertations, & Master Projects at W&M ScholarWorks. It has been accepted for inclusion in Dissertations, Theses, and Masters Projects by an authorized administrator of W&M ScholarWorks. For more information, please contact [scholarworks@wm.edu](mailto:scholarworks@wm.edu).

A NUMERICAL MODELING STUDY ON BAROTROPIC AND BAROCLINIC  
RESPONSES OF THE CHESAPEAKE BAY TO HURRICANE EVENTS

---

A Dissertation

Presented to

The Faculty of the School of Marine Science

The College of William and Mary in Virginia

In Partial Fulfillment

Of the Requirements for the Degree of

Doctor of Philosophy

---

by

Kyoung-Ho Cho

2009

## APPROVAL SHEET

This dissertation is submitted in partial fulfillment of

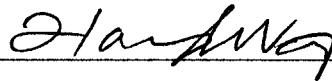
the requirements for the degree of

Doctor of Philosophy



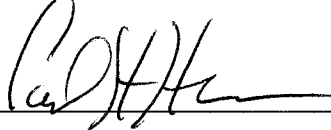
Kyoung-Ho Cho

Approved, February 2009



Harry V. Wang, Ph.D.

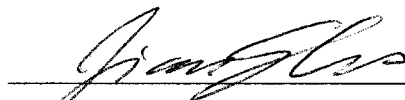
Committee Chairman/Advisor



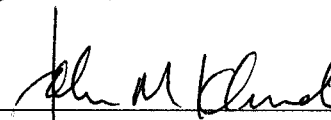
Carl H. Hershner, Ph.D.



John M. Brubaker, Ph.D.



Jian Shen, Ph.D.



John M. Klinck, Ph.D.

Old Dominion University

Norfolk, Virginia

# TABLE OF CONTENTS

	Page
ACKNOWLEDGEMENTS.....	vi
LIST OF TABLES.....	vii
LIST OF FIGURES .....	ix
ABSTRACT.....	xx
I. INTRODUCTION .....	2
1.1 Background.....	2
1.2 The barotropic and baroclinic responses of the Bay to the hurricane forcing ...	11
1.3 Objective and outline .....	18
II. DATA DESCRIPTION .....	20
2.1 Introduction.....	20
2.2 Hurricane Floyd in 1999 .....	22
2.3 Hurricane Isabel in 2003 .....	35
2.4 Summary .....	46
III. METHODOLOGY:	
HYDRODYNAMIC MODELS AND WIND MODEL .....	48
3.1 Introduction.....	48
3.2 ELCIRC model .....	50
3.2.1 Governing equations.....	50
3.2.2 Boundary and initial conditions.....	52
3.2.3 Methods for open boundary condition.....	53
3.2.4 Model configuration .....	62
3.3 SELFE model.....	67
3.3.1 Basic equations .....	67
3.3.2 Turbulence closure model .....	69
3.3.3 Boundary and initial conditions.....	70
3.3.4 Model configuration .....	72

3.4	Generation of meteorological forcing.....	78
3.4.1	Analytical wind model for hurricane events .....	78
3.4.2	Data interpolation .....	79
IV.	MODEL CALIBRATION .....	82
4.1	Introduction.....	82
4.2	Barotropic simulation.....	83
4.2.1	Astronomical tides.....	83
4.2.2	Subtidal surface elevation: storm surges .....	89
4.3	Baroclinic simulation.....	92
4.3.1	Water velocity .....	92
4.3.2	Salinity.....	95
4.4	Summary .....	95
V.	A BAROTROPIC RESPONSE OF THE CHESAPEAKE BAY TO HURRICANES FLOYD AND ISABEL .....	99
5.1	Introduction.....	99
5.2	Model analysis of storm surge dynamics.....	101
5.2.1	Hurricane Floyd.....	101
5.2.2	Hurricane Isabel.....	110
5.3	Analysis of barotropic flow motion .....	118
5.3.1	Horizontal distribution of depth-integrated flow.....	118
5.3.2	Calculation of volumetric transport.....	126
5.4	Effects of external forcing on sea surface elevation .....	136
5.4.1	Effect of local and remote winds.....	136
5.4.2	Effect of river inflows .....	138
5.5	Summary .....	140
VI.	A BAROCLINIC RESPONSE OF THE CHESAPEAKE BAY TO HURRICANES FLOYD AND ISABEL .....	142
6.1	Introduction.....	142
6.2	Meteorologically induced oceanic influx.....	145

6.2.1	Profiles of velocity and salinity during Hurricanes Floyd and Isabel .....	145
6.2.2	Calculation of volume fluxes along the cross-sections .....	152
6.2.3	Calculation of salt flux along the cross-sections .....	153
6.3	Hurricane-induced mixing process .....	168
6.3.1	Storm event experiments .....	168
6.3.2	Temporal variations of vertical structures .....	171
6.3.3	Dimensionless mixing parameters .....	183
6.4	Effects of local and remote winds on circulation and stratification.....	191
6.4.1	Vertical profiles of axial velocity .....	191
6.4.2	Time series of surface and bottom salinities .....	196
6.4.3	Vertical profiles of tidally averaged salinity .....	204
6.5	Effects of precipitation during hurricane event .....	210
6.5.1	Numerical scheme for representation of precipitation input .....	210
6.5.2	Effect of precipitation on salinity .....	212
6.6	Summary .....	215
VII.	ESTUARINE RECOVERY FROM HURRICANE FORCING AND INFLUENCE OF CONTINENTAL SHELF DYNAMICS .....	217
7.1	Introduction.....	217
7.2	Estuarine recovery from hurricane forcing and influence of river discharge ..	219
7.2.1	Method to estimate the estuarine recovery time scale.....	220
7.2.2	Estimation of recovery time from wind forcing .....	221
7.2.3	Effect of river discharge on salinity recovery time .....	229
7.3	Influence of continental shelf dynamics .....	236
7.3.1	Effect of Ekman transport.....	236
7.3.2	Effect of alongshore pressure gradient on the geostrophic balance .....	239
7.4	Summary .....	244
VIII.	DISCUSSION AND CONCLUSIONS .....	245
	APPENDIX.....	259
	LITERATURE CITED .....	262
	VITA .....	284

## ACKNOWLEDGMENTS

I would like to express my gratitude to all those who gave me the possibility to complete this thesis. The support and guidance provided by my advisor, Dr. Harry V. Wang, throughout the course of this research are gratefully acknowledged. Definition of the topic and selection of appropriate methodologies were greatly facilitated by his willingness to assist and instruct. I also wish to thank my other Advisory Committee members, Dr. Carl H. Hershner, Dr. John M. Brubaker, Dr. Jian Shen, and Dr. John M. Klinck for their valuable comments and constructive criticism to finalize this study. Furthermore I have to thank Dr. William C. Boicourt and Dr. Arnold Valle-Levinson for allowing me to share their observation data. My gratitude is extended to Mr. Mac Sisson for his great help on this manuscript.

Successful completion of this research would not have been possible without the scholarly knowledge and technical supports given by people in three-dimensional estuarine circulation modeling group. Notably, my god family donated their long hours to encourage me. Finally, I thoroughly thank my lovely wife, Eunji, and my family for their forbearance and invaluable supports to complete my degree.

## LIST OF TABLES

Table	Page
Table 1-1 Saffir-Simpson Hurricane Scale (SSHS).....	13
Table 1-2 Some comparative aspects of Hurricanes Floyd and Isabel. ....	13
Table 2-1 Station information and availability of observations during Hurricanes Floyd and Isabel in MD, DC, VA, and NC. ....	25
Table 2-2 Station Information of USGS daily streamflow data in eight tributaries of the Chesapeake Bay recording maximum values during Hurricanes Floyd (1999) and Isabel (2003). ....	45
Table 4-1 Comparison of observed and predicted mean tidal ranges at 21 tidal stations. ....	85
Table 4-2a Comparison of observed and predicted mean tidal amplitudes at 11 selected tide gauge stations.....	87
Table 4-2b Comparison of observed and predicted mean tidal phases at 11 selected tide gauge stations.....	87
Table 6-1 Comparison of observed stratification (ppt) between pre-storm and post-storm at four selected CBP stations during Hurricanes Floyd (1999) and Isabel (2003). ....	169
Table 6-2 Summary of numerical experiments performed. ....	169
Table 7-1 Estimated recovery time for sea surface elevation in the Chesapeake Bay from four-day wind forcing. Days are calculated from the wind termination day. ....	222
Table 7-2 Estimated recovery time for salinity in the Chesapeake Bay from four-day wind forcing. Days are calculated from the wind termination day.....	226
Table 7-3 Summary of additional experiments performed for river discharge event.....	232



Table 7-4 Estimated recovery time for salinity in the Chesapeake Bay for high river discharge experiments. Days are calculated from the wind termination day. ....235

## LIST OF FIGURES

Figure	Page
Figure 1-1 A map of the Chesapeake Bay and the Mid-Atlantic Bight along the East Coast of the United States.....	3
Figure 1-2 Tracks of Hurricanes Floyd (red) and Isabel (blue).....	15
Figure 2-1 A map of Chesapeake Bay observation station locations with bathymetric soundings (meters). Red circles represent water elevation data; green squares represent wind data; triangles represent current data (red: Year 1999; blue: Year 2003); cyan diamonds represent salinity data; and red stars represent riverflow. Red and green dashed lines represent the tracks of Hurricanes Floyd and Isabel, respectively. ....	21
Figure 2-2 Time series plots of wind data (left panels) and atmospheric pressure (right panels) at six selected stations (Thomas Point, MD; Lewisetta, VA; CBBT, VA; Chesapeake Light, VA; VA Beach, VA; Duck, NC from top to bottom) during Hurricane Floyd, 11-26 September, 1999, UTC.....	23
Figure 2-3 Time series plots of storm surges (in meters) at selected NWLON water level stations during Hurricane Floyd, 15-20 September, 1999, UTC. ....	27
Figure 2-4 Time series plots of observed longitudinal currents at three stations, Mid-Bay buoy, MD (upper panel), Newport News, VA (middle panel) and M5 (lower panel) near the Bay mouth, during Hurricane Floyd, 1999, UTC. Positive velocity represents flow directed out of the Bay. ....	28
Figure 2-5 Time series plots of low-pass filtered salinity data at two stations near the entrance of the Chesapeake Bay (top) and at two CBNERR stations in the York River estuary (bottom) during Hurricane Floyd, 1999, UTC. ....	33
Figure 2-6 Time series plots of daily riverflow data at three main rivers, Susquehanna, Potomac, and James, in 1999, UTC. The top panel shows the year-long record	

with the storm event period shaded and the bottom panel shows an expanded view of the discharge record within the storm event period.....	34
Figure 2-7 Time series plots of wind data (left) and atmospheric pressure (right) at six selected stations (Thomas Point, MD; Lewisetta, VA; CBBT, VA; Chesapeake Light, VA; VA Beach, VA; Duck, NC from top to bottom) during Hurricane Isabel, 11-26 September, 2003, UTC.....	36
Figure 2-8 Time series plots of storm surges (in meters) at selected NWLON water level stations during Hurricane Isabel, 17-22 September, 2003, UTC.....	40
Figure 2-9 Time series plots of observed longitudinal currents at two stations, Mid-Bay buoy, MD (upper panel), and Gloucester Point in the York River, VA (bottom panel) during Hurricane Isabel, 2003, UTC. Positive velocity represents flow directed out of the Bay.....	41
Figure 2-10 Time series plots of low-pass filtered salinity at four CBNERR stations in the York River during Hurricane Isabel 2003, UTC.....	43
Figure 2-11 Time series plots of daily riverflow data at three main rivers, Susquehanna, Potomac, and James, in 2003, UTC. The top panel shows the year-long record with the storm event period shaded and the bottom panel shows an expanded view of the discharge record within the storm event period.....	44
Figure 2-12 Relationship between wind speed and storm surge at CBBT, VA obtained from NOAA during Hurricane Floyd (a) and Hurricane Isabel (b). Red colors are the day of the surge peak, black colors are the day before the peak day, and blue colors are the day after the peak day. A black arrow denotes the maximum surge. ....	47
Figure 3-1 A coordinate system for the generation of subtidal sea surface elevation on open boundaries. The modified coordinate ( $x'$ , $y'$ , $z'$ ) are transformed from the original ( $x$ , $y$ , $z$ ) described in Janowitz and Pietrafesa (1996). All variables are non-dimensional except the variables that have a superscript (*). ....	60
Figure 3-2 A comparison of subtidal sea surface elevation between observed ( $x$ ) and calculated (lines) on the southern boundary (SB, red) and northern boundary (NB,	

blue) during (a) Hurricane Floyd and (b) Hurricane Isabel. The solid lines represent the values for the coastline and the dashed lines represent the values for the 200-m isobath.....	61
Figure 3-3 An unstructured orthogonal grid. The side shared by two adjacent elements (blue) and the segment joining their centers (red) should be orthogonal. ....	63
Figure 3-4 A horizontal grid of the Chesapeake Bay for the ELCIRC model. The grid has 66,802 elements, 40,591 nodes, and 107,419 side faces at the surface.....	64
Figure 3-5 A horizontal grid of the Chesapeake Bay for the SELFE model. The grid has 20,784 elements, 11,582 nodes, and 32,386 sides at the surface.....	74
Figure 3-6 A vertical grid of hybrid coordinate system used in the SELFE model: (a) a schematic view, (b) vertical view of the discretized model grid along the transect in Fig. 3-5, and (c) A unit of computational triangular prism with uneven bottom and top surfaces.....	75
Figure 4-1 Comparison of observed and predicted mean tidal ranges at 13 tidal stations on the West side (upper panel) and at 9 tidal stations on the East side (lower panel) of the Chesapeake Bay mainstem. Observations are denoted by 'x' and model predictions are denoted by the dashed line. ....	86
Figure 4-2 Correlations between observed and predicted tidal amplitudes (left panels) and between observed and predicted tidal phases (right panels) of four major tidal constituents, $M_2$ , $S_2$ , $N_2$ , and $K_1$ .....	88
Figure 4-3 Scatter plots of observed and predicted storm surge elevations at 6 selected observation stations for the 5-day period from September 15-19, 1999. Observations are on x-axis and predictions are on y-axis.....	90
Figure 4-4 Scatter plots of observed and predicted storm surge elevations at 6 selected observation stations for the 5-day period from September 17-21, 2003. Observations are on x-axis and predictions are on y-axis.....	91
Figure 4-5 Comparison of observed and predicted along-channel velocity: (a) surface and (b) mid-depth at the mid-Bay buoy station, (c) surface and (d) bottom at NN (Newport News) in James River, and (e) surface and (f) bottom at M5 near the	

Bay mouth, for the 20-day period in autumn 1999 including Hurricane Floyd, September 16 to 18. ....	93
Figure 4-6 Comparison of observed and predicted along-channel velocity: (a) surface and (b) mid-depth at the mid-Bay buoy station, and (c) surface and (d) bottom at GP (Gloucester Point) in York River, for the 12-day period in autumn 2003 including Hurricane Isabel, September 18 to 21.....	94
Figure 4-7 Comparison of observed and predicted salinity (surface and bottom) at ten selected stations: for spring 1999. Model results (red: bottom; blue: surface) and observed data (black circle: bottom; green circle: surface). ....	96
Figure 4-8 Comparison of observed and predicted salinity (surface and bottom) at ten selected stations: for spring 2003. Model results (red: bottom; blue: surface) and observed data (black circle: bottom; green circle: surface). ....	97
Figure 4-9 Comparison of observed and predicted salinity (surface and bottom) at five selected stations for autumn 1999 (left panels) and for autumn 2003 (right panels): Model results (red: bottom; blue: surface) and observed data (black circle: bottom; green circle: surface). ....	98
Figure 5-1 Surge height comparison between observed (crosses) and predicted (solid lines) at eight selected stations during Hurricane Floyd in September 1999.....	103
Figure 5-2 The locations of twenty stations (●) in the Chesapeake Bay model domain selected for storm surge analysis and fifteen transects (red lines) for transport analysis.....	105
Figure 5-3 Time series of surge height at 20 selected stations along the mainstem Bay from the Bay mouth (st01) to the upper Bay (st20) during Hurricane Floyd in September, 1999. ....	106
Figure 5-4 Spatial distributions of surge height for 20 selected stations from September 15 21:00 to September 18 01:00 (UTC) in 1999. ....	107
Figure 5-5 The time versus space plot of surge height for 20 selected stations during Hurricane Floyd in September 1999: 3D view (left) and top view with contour lines (right).....	109

Figure 5-6 Surge height comparison between observed (crosses) and predicted (solid lines) at eight selected stations during Hurricane Isabel in September, 2003. ....111

Figure 5-7 Time series of surge height at selected 20 stations along the mainstem Bay from the Bay mouth (st01) to the upper Bay (st20) during Hurricane Isabel in September, 2003. ....112

Figure 5-8 Spatial distributions of surge height for 20 selected stations from September 18 13:00 to September 20 01:00 (UTC) in 2003. ....116

Figure 5-9 The time versus space plot of surge height for 20 selected stations during Hurricane Isabel in September 2003: 3D view (left) and top view with contour lines (right). ....117

Figure 5-10 Horizontal distributions of depth-integrated flow (thin arrows) at the southern portion of the Chesapeake Bay during Hurricane Floyd with time sequence from (a) September 16 03:00 UTC to (f) September 17 12:00 UTC. Colored map represents storm height and the thick arrow specifies wind speed and direction recorded at CBBT, VA. ....120

Figure 5-11 Horizontal distributions of depth-integrated flow (thin arrows) at the northern portion of the Chesapeake Bay during Hurricane Floyd with time sequence from (a) September 16 03:00 UTC to (f) September 17 12:00 UTC. Colored map represents storm height and the thick arrow specifies wind speed and direction recorded at Lewisetta, VA. ....121

Figure 5-12 Horizontal distributions of depth-integrated flow (thin arrows) at the southern portion of the Chesapeake Bay during Hurricane Isabel with time sequence from (a) September 18 09:00 UTC to (f) September 19 18:00 UTC. Colored map represents storm height and thick arrow specifies wind speed and direction recorded at CBBT, VA. ....124

Figure 5-13 Horizontal distributions of depth-integrated flow (thin arrows) at the northern portion of the Chesapeake Bay during Hurricane Isabel with time sequence from (a) September 18 09:00 UTC to (f) September 19 18:00 UTC.

Colored map represents storm height and the thick arrow specifies wind speed and direction recorded at Lewisetta, VA. ....	125
Figure 5-14 One tidal-cycle mean volumetric transport at each transect (a) in the Chesapeake Bay mainstem and (b) its tributaries during Hurricane Floyd, 1999. ....	128
Figure 5-15 Time sequence of volumetric net transport ( $\text{m}^3 \text{s}^{-1}$ ) averaged over a tidal cycle at transects in the lower Chesapeake Bay during Hurricane Floyd, 1999. The positive value denotes seaward flux and red and blue colors represent the increase and decrease of water volume, respectively. ....	129
Figure 5-16 One tidal-cycle mean volumetric transport at each transect (a) in the Chesapeake Bay mainstem and (b) its tributaries during Hurricane Isabel, 2003. ....	133
Figure 5-17 Time sequence of volumetric net transport ( $\text{m}^3 \text{s}^{-1}$ ) averaged over a tidal cycle at transects in the lower Chesapeake Bay during Hurricane Isabel, 2003. The positive value denotes seaward flux and red and blue colors represent the increase and decrease of water volume, respectively. ....	134
Figure 5-18 Comparison of storm surge height among three cases, local (dash-dotted), remote (dashed), and combination (solid), at five selected stations during Hurricane Floyd, 1999 (left panels) and Hurricane Isabel, 2003 (right panels). .	137
Figure 5-19 Comparison of observed and predicted water surface elevations at Washington, DC, during Hurricane Isabel on September 2003.....	139
Figure 6-1 Longitudinal distributions of tidally averaged (25 hours) velocity and salinity in the along-channel section of the Chesapeake Bay for six selected days during Hurricane Floyd, 1999. ....	146
Figure 6-2 Longitudinal distributions of tidally averaged (25 hours) velocity and salinity in the along-channel section of the Chesapeake Bay for six selected days during Hurricane Isabel, 2003.....	147
Figure 6-3 Distributions of tidally averaged (25 hours) axial velocity (blue lines) and salinity (red lines) at the transect tr01 for six selected days during Hurricane	

Floyd, 1999. Velocity is represented by solid lines (seaward), dotted lines (landward), and thick lines (zero) in $\text{m s}^{-1}$ . .....	150
Figure 6-4 Distributions of tidally averaged (25 hours) axial velocity (blue lines) and salinity (red lines) at the transect tr01 for six selected days during Hurricane Isabel, 2003. Velocity is represented by solid lines (seaward), dotted lines (landward), and thick lines (zero) in $\text{m s}^{-1}$ . .....	151
Figure 6-5 Net volume flux across the entrance transect tr01: time series (a), and spatial distributions of net volume flux (b) and baroclinic volume flux (c) across tr01 averaged over one tidal-cycle on September 16, 1999. ....	154
Figure 6-6 Net volume flux across the entrance transect tr01: time series (a), and spatial distributions of net volume flux (b) and baroclinic volume flux (c) across tr01 averaged over two tidal cycles on September 18 to 19, 2003.....	155
Figure 6-7 Net salt flux across the entrance transect tr01: time series (a), and spatial distributions of net volume flux (b) and baroclinic volume flux (c) across tr01 averaged over one tidal-cycle on September 16, 1999. ....	157
Figure 6-8 One tidal-cycle averaged net salt flux at each transect (a) in the Chesapeake Bay mainstem and (b) its tributaries during Hurricane Floyd, 1999. ....	158
Figure 6-9 Time sequence of net salt flux ( $\times 10^5 \text{ ppt m}^3 \text{ s}^{-1}$ ) averaged over a tidal cycle at transects in the lower Chesapeake Bay during Hurricane Floyd, 1999. The positive value denotes seaward flux and red and blue colors represent the increase and decrease of salt, respectively.....	159
Figure 6-10 Time sequence of net salt flux ( $\times 10^5 \text{ ppt m}^3 \text{ s}^{-1}$ ) averaged over a tidal cycle at transects in the mid Chesapeake Bay during Hurricane Floyd, 1999. The positive value denotes seaward flux and red and blue colors represent the increase and decrease of salt, respectively.....	160
Figure 6-11 Net salt flux across the entrance transect: time series (a), and spatial distributions of net salt flux (b) and baroclinic salt flux (c) across tr01 averaged over two tidal cycles on September 18 to 19, 1999. ....	164



Figure 6-12 One tidal-cycle averaged salt flux at each transect (a) in the Chesapeake Bay mainstem and (b) its tributaries during Hurricane Isabel, 2003 (same legend as Figure 6-8). .....165

Figure 6-13 Time sequence of net salt flux ( $\times 10^5$  ppt  $m^3 s^{-1}$ ) averaged over a tidal cycle at transects in the lower Chesapeake Bay during Hurricane Isabel, 2003. The positive value denotes seaward flux and red and blue colors represent the increase and decrease of salt, respectively.....166

Figure 6-14 Time sequence of net salt flux ( $\times 10^5$  ppt  $m^3 s^{-1}$ ) averaged over a tidal cycle at transects in the mid Chesapeake Bay during Hurricane Isabel, 2003. The positive value denotes seaward flux and red and blue colors represent the increase and decrease of salt, respectively.....167

Figure 6-15 Selected period of four days for atmospheric forcing during Hurricane Floyd (a) and Hurricane Isabel (b). .....170

Figure 6-16 Time series plots of surface (blue) and bottom (red) along-channel velocities at five selected stations for the FL-C case (a to e) and for the IS-C case (f to j). Thin lines denote no wind case, vertical dashed lines denote the period of wind forcing, and positive value represents a seaward flow. ....173

Figure 6-17 Time series plots of surface (blue) and bottom (red) salinities at five selected stations for the FL-C case (a to e) and for the IS-C case (f to j). Thin lines denote the no wind case and vertical dashed lines denote the period of wind forcing....174

Figure 6-18 Vertical profiles of tidally averaged along-channel velocity at three stations with time sequence: (a) upper Bay; (b) mid Bay; (c) lower Bay for the FL-C case and (d) upper Bay; (e) mid Bay; (f) lower Bay for the IS-C case. The positive value represents a seaward flow. ....179

Figure 6-19 Vertical profiles of tidally averaged salinity at three stations with time sequence: (a) upper Bay; (b) mid Bay; (c) lower Bay for the FL-C case and (d) upper Bay; (e) mid Bay; (f) lower Bay for the IS-C case. ....182

Figure 6-20 Temporal variations of the gradient Richardson number (Ri) at three regimes for no wind case (a to c), the FL-C case (d to f), and the IS-C case (g to i). .....188

Figure 6-21 Temporal variations of the Wedderburn number ( $W$ ) at three regimes for no wind case (a to c), the FL-C case (d to f), and the IS-C case (g to i).....	189
Figure 6-22 Temporal variations of the horizontal Richardson number ( $Ri_x$ ) at three regimes for no wind case (a to c), the FL-C case (d to f), and the IS-C case (g to i). .....	190
Figure 6-23 Vertical profiles of tidally averaged along-channel velocity with time sequence for the FL-L case (left) and for the FL-R case (right) at three regimes (a,d: upper Bay; b,e: mid Bay; c,f: lower Bay). The positive value represents a seaward flow. ....	192
Figure 6-24 Vertical profiles of tidally averaged along-channel velocity with time sequence for the IS-L case (left) and for the IS-R case (right) at three regimes (a,d: upper Bay; b,e: mid Bay; c,f: lower Bay). The positive value represents a seaward flow. ....	195
Figure 6-25 Time series plots of surface (blue) and bottom (red) salinities at five selected stations for the FL-L case (a to e) and for the FL-R case (f to j). Thin lines denote the no wind case and vertical dashed lines denote the period of wind forcing....	197
Figure 6-26 Time series plots of surface (blue) and bottom (red) salinities at five selected stations for the IS-L case (a to e) and for the IS-R case (f to j). Thin lines denote the no wind case and vertical dashed lines denote the period of wind forcing....	201
Figure 6-27 Vertical profiles of tidally averaged salinity with time sequence for the FL-L case (left) and for the FL-R case (right) at three regimes (a,d: upper Bay; b,e: mid Bay; c,f: lower Bay).....	206
Figure 6-28 Vertical profiles of tidally averaged salinity with time sequence for the IS-L case (left) and for the IS-R case (right) at three regimes (a,d: upper Bay; b,e: mid Bay; c,f: lower Bay).....	209
Figure 6-29 Time series of observed precipitation (crosses) recorded at Norfolk International Airport, VA, during Hurricane Floyd and simplified precipitation as a model input (solid line). ....	213

Figure 6-30 Instantaneous salinity comparison between observation (red) and modeled results without precipitation (thin solid lines) and with precipitation (thick solid lines), at the observation stations near the Bay mouth: (a) mid-depth at M5, (b) near bottom at M5, and (c) near surface at M3, during Hurricane Floyd. ....214

Figure 7-1 Time series of salinity difference ( $\gamma$ ) at selected three stations for Experiment FL-C (a) and Experiment IS-C (b): Blue lines represent surface salinity and red lines represent bottom salinity. Black dashed lines denote 2% criterion of  $\gamma$  and green dashed lines denote wind turn-on day (A) and wind termination day (B). .....  
.....224

Figure 7-2 Time series of wind and salinity in the mid Bay during (a) Hurricanes Floyd and (b) Hurricane Isabel. Vertical dashed lines represent each characterized stage. ....227

Figure 7-3 Schematic maps of vertical salinity structure at each stage during Hurricanes Floyd (left) and Isabel (right). ....228

Figure 7-4 The records of winds at CBBT (upper panel) and river discharges in three rivers of the Chesapeake Bay (lower panel) on September, 2003. ....230

Figure 7-5 Idealized river discharge inputs for the experiments. ....231

Figure 7-6 Time series of salinity difference ( $\gamma$ ) at selected three stations for Experiments NW-MR (a), FL-CMR (b), and IS-CMR(c). Blue lines represent surface salinity and red lines represent bottom salinity. Dashed lines denote 2% criterion of  $\gamma$  and green dashed lines denote wind turn-on day (A), wind turn-off and 5Q river discharge turn-on day (B), and 5Q river discharge termination day (C). ....233

Figure 7-7 Time series of salinity difference ( $\gamma$ ) at three selected stations for Experiments NW-HR (a), FL-CHR (b), and IS-CHR(c). Blue lines represent surface salinity and red lines represent bottom salinity. Dashed lines denote 2% criterion of  $\gamma$  and green dashed lines denote wind turn-on day (A), wind turn-off and 10Q river discharge turn-on day (B), and 10Q river discharge turn-off day (C). ....234

Figure 7-8 Time series of simulated storm surge elevation (a) and salinity (b) at the entrance of the Chesapeake Bay during Hurricane Isabel with/without Coriolis force. ....238

Figure 7-9 The influence of subtidal alongshore pressure gradient (APG) during Hurricane Isabel on (a) surge elevation with observation (red cross) at CBBT, (b) surface salinity and (c) bottom salinity at CB7.4. Thin and thick lines denote the cases without and with APG, respectively.....242

Figure 7-10 Schematic maps of onshore current (GC) induced by geostrophic balance between barotropic pressure gradient force (PGF) and Coriolis force (CF) (left panel) and vertical salinity profile at cross-shore transect (right panel) on the continental shelf. ....243

Figure 8-1 Spatial distributions of surge ranges for six experiments during hurricane events, Floyd (a, b, and c) and Isabel (d, e, and f), respectively. ....251

Figure 8-2 Vertical profiles of alongshore velocity for wind forcings: (a) analytical solutions in the central regime (Hansen and Rattray, 1965) and (b) numerical simulations in the mid-Bay. Positive is seaward. ....252

Figure 8-3 Instantaneous salinity comparisons between observations, bottom (black circles) and surface (green circles), and predictions, bottom (red lines) and surface (blue lines), at Duck, NC, for two cases: (a) without an ambient flow and (b) with an ambient flow of  $10 \text{ cm s}^{-1}$  .....253

Figure 8-4 Subtidal sea surface distribution in time-distance frame: along-channel in the Chesapeake Bay (left panel) and cross-shore on the continental shelf (right panel). The interval of contour lines is 0.2 m. Red dashed lines denote the period of Hurricane Isabel. ....254

## ABSTRACT

The barotropic and baroclinic responses of the Chesapeake Bay to forcings from two hurricanes were investigated by using unstructured-grid three-dimensional hydrodynamic models. The model domain includes Chesapeake Bay proper, the tributaries, and its extended continental shelf in the mid-Atlantic Bight. Two hurricanes were studied: Hurricane Floyd of September, 1999 and Hurricane Isabel of September, 2003, both of which made landfall within 100 km of the Chesapeake Bay mouth. Hurricane Floyd in 1999 passed through the entrance of the Bay from southwest to northeast along the coastlines of Virginia as a Category 1 storm, whereas Hurricane Isabel in 2003 made landfall on the east coast of North Carolina and moved inland toward the northwest as a Category 2 storm.

For the barotropic simulation of the Bay responding to the hurricanes, the model results were compared with Bay-wide water level observations and the model showed reasonable prediction skill. It was found that the storm surge has two phases: a primary surge induced by the remote winds and a secondary surge induced by the local winds. For both hurricanes, the primary surge induced by remote winds propagated into the Bay initially, but the subsequent phase, influenced by the local wind, was notably different. Hurricane Floyd was followed by northerly (down-Bay) winds, that reduced the primary surge effect and caused a localized set-down; Hurricane Isabel was followed by southerly (up-Bay) winds, which superimposed on the primary surge effect and caused a localized set-up. The volume and salt fluxes were estimated at selected cross-sectional transects throughout the Bay, and it was found consistently for each transect that the net influx dominated during Hurricane Isabel while the net outflux dominated during Hurricane Floyd. For the Bay's tributaries, the large inland river discharge at the headwater can couple with the storm surge event to increase sea surface elevation on the second phase of sea surface elevation rise, which has a significant impact on inundation in the local low-lying areas.

For the baroclinic response of the Bay to the hurricanes, the model results agreed reasonably well with additional observed data: sea surface elevation, velocity, and salinity profiles. From the perspective of salt flux, oceanic saltwater influx was evidently pushed into the Bay from the continental shelf at the initial phase of Hurricanes Floyd and Isabel associated with storm surge and salt intrusion. In the second phase, follow up with, down-bay local winds of eastern-type storms tend to enhance the stratification whereas up-Bay local winds of western-type storms tend to reduce the stratification. The hurricane surface wind stress is the primary agent for destratifying water column by transferring generated turbulent kinetic energy to the lower layer. The wind-induced straining during Hurricane Floyd was verified using non-dimensional parameters that incorporated the wind direction and the horizontal salinity gradient. Direct precipitation of hurricane rainfall acted more like a point source onto the Bay surface water, which created a layer of low surface salinity on the sea surface. It has an implication

dynamically on generating a sea surface horizontal pressure gradient and re-distributing salinity field after the storm.

Extra efforts have been made to conduct idealized experiments for comparing long-term recovery of the Bay to the disturbance created by the two hurricanes. Realistic hurricane wind forcing was applied in a 4-day window with the same initial condition applied in the beginning, and the quasi-steady state condition achieved in the end. Through this exercise, it was found that it took Bay 5-7 days to return to normal condition from the sea surface elevation disturbances for both Hurricanes Floyd and Isabel. For the salinity fields, it took within a range of 20-30 days to recover to the pre-storm condition for the middle and southern portions of the Bay. For the northern portion of the Bay, however, due to the landward barotropic pressure gradient generated a strong salinity rebound and the associated oscillation subsequently after Hurricane Floyd passed, it required twice as long to recover. Sensitivity testing of the effect of river discharge (immediately after the storm) on the recovery time has also been performed.

Lastly, the influences of continental shelf dynamics on the Bay's response to the hurricane were examined. It was found that the along shelf wind contributed to the inflow and outflow at the Bay mouth in the form of Ekman transport, which complemented the contribution generated by the Bay's local wind. The onshore and offshore shelf wind also played a significant role. Because the cyclonic pattern of the hurricane wind field, when the hurricane made the landfall in the US East coast, an along-the-shelf pressure gradient from the north to the south was generated. This pressure gradient, coupled with the Coriolis and friction forces, can generate a quasi-geostrophic balance flow serving to prevent or enhance the inflow across the Bay mouth. The effect is particularly noticeable in the relaxation period during the hurricane passage.

A NUMERICAL MODELING STUDY ON BAROTROPIC AND BAROCLINIC  
RESPONSES OF THE CHESAPEAKE BAY TO HURRICANE EVENTS

# Chapter I

## INTRODUCTION

### 1.1 Backgrounds

#### Study area: Chesapeake Bay

The Chesapeake Bay (CB), located in the mid-Atlantic Bight along the U.S. East Coast, is a partially mixed estuary and the largest in the United States. The Bay is approximately 320 km long from its entrance at Capes Henry and Charles, Virginia to the mouth of the Susquehanna River at Havre de Grace, Maryland. Its widest point is just south of the Potomac River mouth, which is 50 km wide, and it has more than 7,000 km of shoreline (Figure 1-1). The entire CB system as a whole has a surface area of  $11.5 \times 10^3 \text{ km}^2$ , a mean low water volume of  $74 \text{ km}^3$ , and a mean depth of 6.46 m; for the bay proper only, the surface area is  $6.5 \times 10^3 \text{ km}^2$ , the mean low water volume is  $50 \text{ km}^3$  and the mean depth is 8.42 m (Schubel and Pritchard, 1986).

The CB is formed by complicated estuary and sub-estuaries that allow discharge from fifty major tributaries. The freshwater to the Bay is predominantly coming from the northern and western sides, and only a small portion is from the eastern side of the Bay. The total freshwater input to the CB system averages  $2,570 \text{ m}^3 \text{ s}^{-1}$ , derived from various tributaries. Approximately 45 % of the total is supplied by the Susquehanna River, which has a long-term average discharge of  $1,144 \text{ m}^3 \text{ s}^{-1}$  (Goodrich, 1988). The other four



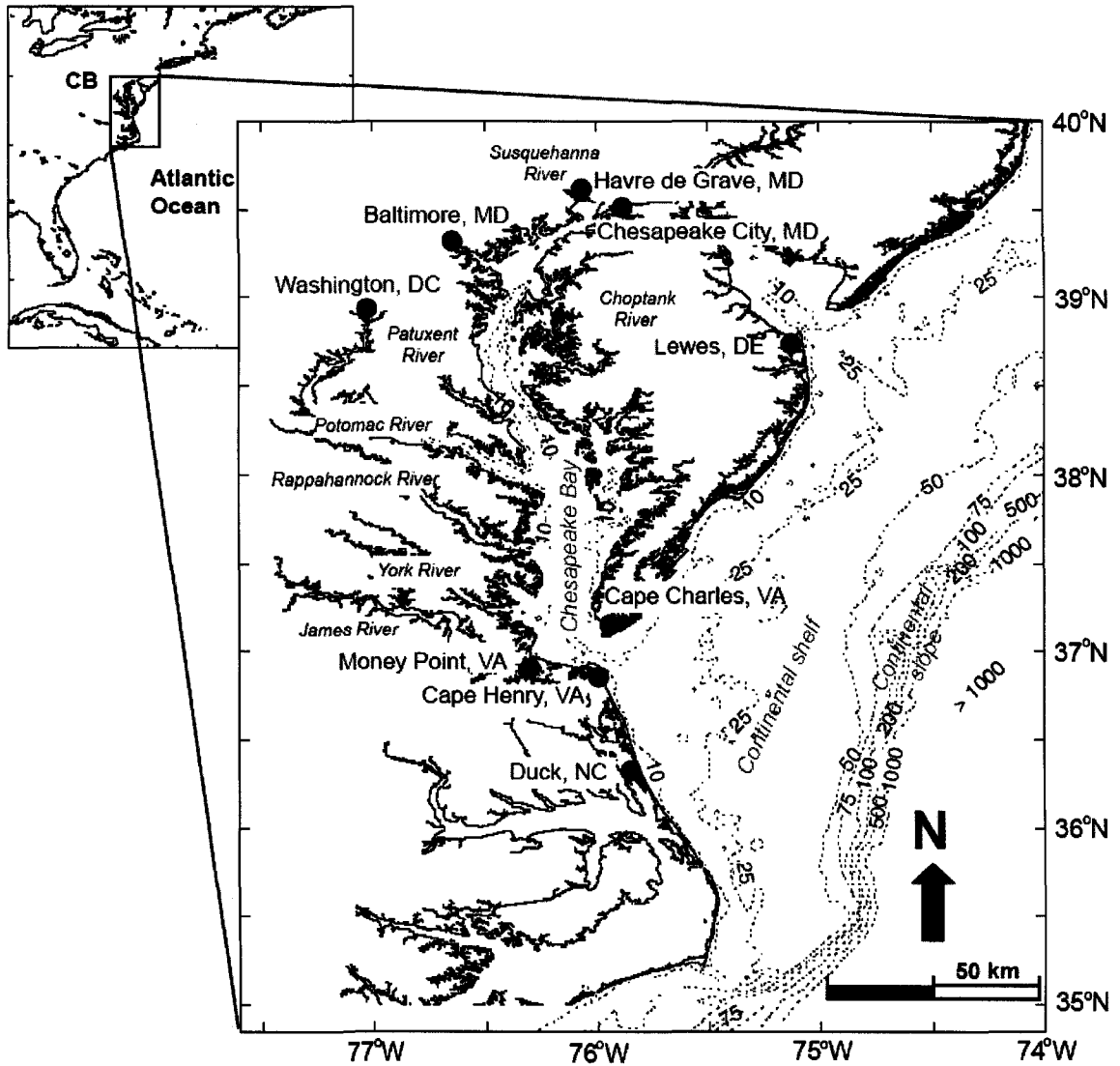


Fig. 1-1 A map of the Chesapeake Bay and the Mid-Atlantic Bight along the East Coast of the United States.

tributaries: Patuxent, Potomac, Rappahannock, and James combined contribute as much as the Susquehanna River. Nearly an equal amount of saltwater enters the Bay through the Bay entrance from the Mid Atlantic Bight shelf waters (Boicourt, 1973; Wang and Elliott, 1978; Beardsley and Boicourt, 1981; Valle-Levinson and Wilson, 1994; Valle-Levinson, 1995; Kourafalou *et al.*, 1996a; 1996b; Valle-Levinson *et al.*, 2001; Wong and Valle-Levinson, 2002; Valle-Levinson *et al.*, 2003). These exchange processes are complicated since the hydrodynamics at the entrance are influenced by a combination of tides, atmospheric forcing, buoyancy forcing, and geometric effects. Oceanic saltwater tends to enter the Bay in the northern portion of the entrance and through the bottom layer of the main channel, whereas estuarine water leaves through the southern portion (Valle-Levinson and Lwiza, 1997). The mean ocean-bay exchange rate is approximately  $8 \times 10^3 \text{ m}^3 \text{ s}^{-1}$ , corresponding to a time scale of 90 days (Austin, 2002).

### **Subtidal circulation in the CB**

The subtidal circulation pattern in the Chesapeake Bay shows a gravitational circulation driven by the longitudinal salinity gradient (Pritchard, 1952; 1956) and wind forcing (Weisberg, 1976; Wang, 1979b). Longitudinal salinity gradients are typically induced by freshwaters flowing from a river and salty waters entering from the Bay mouth. Most of the current variability in the region is in the subtidal or low-frequency band (2 to 10 days) that is directly forced by strong winds from synoptic storms (Beardsley and Boicourt, 1981). Wang and Elliott (1978) examined the subtidal variability in the Chesapeake Bay and Potomac River and its relationship to atmospheric wind forcing. They found that the dominant sea level fluctuation resulting from the up-Bay propagation of coastal sea level fluctuations was generated by the alongshore winds.

They concluded that water was driven out of the Bay by the northward wind and driven into the Bay by the southward wind, through the coastal Ekman flux. Their study suggested that the effects of interaction with the adjacent larger estuary should be included into an adequate model for the subtidal estuarine circulation. Klinck *et al.* (1981a) investigated and concluded that the free surface slope is responsible for the low-frequency, quasi-geostrophic coastal circulation induced by a moving wind stress. Additionally, Klinck *et al.* (1981b) examined the dynamical interaction of a narrow fjord with a wind-driven coastal regime using a linear, two-layer numerical model. For a variety of wind conditions, they showed that the wind-forced coastal circulation with its geostrophic alongshore currents has a strong effect on the circulation within the fjord. Olson (1984) revealed direct and indirect responses of the Bay to variations in wind stress, freshwater inflow, and coastal sea level by analyzing time series records related to circulation in the Chesapeake Bay. He found that the observed volume transport spectrum at the mouth of the Bay could be explained quantitatively as the combined response to independent wind stress and sea level fluctuations. According to his research, under normal weather conditions, a maximum in the volume transport spectrum (0.4 cycles per day (cpd)) in the upper Bay was caused by a local maximum in the wind spectrum, whereas 90 % of the volume transport variance (below 0.375 cpd) at the Bay mouth was induced by sea level fluctuations. However, the volume transport (as well as momentum flux) in the Bay under extreme wind conditions ( $> 10$  m/s) has not been well understood.

### **Water volume and salt transport exchanges**

The mechanism of wind-induced exchange at the entrance to Chesapeake Bay

was studied under relatively weak ( $< 10$  m/s) wind forcing conditions (Valle-Levinson *et al.*, 2001) and under hurricane events (Valle-Levinson *et al.*, 2002). They identified three scenarios of wind-induced exchange corresponding to different wind patterns: northeasterly (NE), southwesterly (SW), and northwesterly (NW) winds. The first drove water from the coast toward the lower Bay as well as from the upper Bay to the lower Bay, which was indicated by the surface elevation slopes across the Bay. SW winds caused opposite sea level gradients, which translated into near-surface outflows throughout the entrance and near-bottom inflows restricted to the channels. NW winds produced the same exchange pattern as northeasterly winds. In the tributaries, Sanford (1988) reported that intrusion of lower-layer water from the Bay into the Choptank River occurred as an episodic, wind-driven internal surge rather than as a slow, steady flow when strong wind was blowing from the northeast. Furthermore, Sanford and Boicourt (1990) noted that wind and tide forced internal oscillations of the pycnocline that advected saline/hypoxic water from below the pycnocline onto the flanks of the Chesapeake Bay and into the lower reaches of the Choptank River. They attributed the occurrence of saline/hypoxic water in their study to either internal waves or internal mixing. Kuo and Park (1992) contributed to the understanding of two mechanisms of wind-induced mass exchange at the Rappahannock River mouth, which result from 1) tilting of the pycnocline in the Bay and 2) shoreline and bathymetric configurations around the estuary – sub-estuary junction. They found that wind is the dominant factor influencing the properties of imported waters in the Chesapeake Bay – Rappahannock estuary system. They also suggested that mass exchange at the bottom of the river mouth could depend not only on the relationship between density-driven gravitational

circulation and wind-driven current, but also on the lateral variability of the pycnocline in the Bay in response to wind intensity and direction.

### **Wind-induced mixing and destratification**

Wind-induced vertical mixing tends to destratify the water column in a stratified estuary (Miller et al., 2005). Wind-induced destratification has been studied in the Chesapeake Bay. The destratification was frequently observed to occur from early autumn through mid-spring (Goodrich et al., 1987). It was verified numerically to result from storms in early autumn indicating that internal shear is a more effective mechanism for destratification than direct propagation of turbulence from the surface (Blumberg and Goodrich, 1990). However, hurricane-forced winds tend to cause intense turbulent mixing in the water column, temporarily transforming a partially mixed estuary to a vertically homogeneous estuary (Li et al., 2007). It was suggested that the combined remote and local wind forcing could have different effects on turbulent mixing.

Alternatively, wind stress increases estuarine stratification by reducing the longitudinal density gradient (Geyer, 1997; North et al., 2004; Scully et al., 2005; Chen and Sanford, 2009). Geyer (1997) showed that down-estuary winds enhanced surface outflow, significantly reducing the along-estuary salinity gradient. North et al. (2004) demonstrated that increased stratification was associated with down-estuary wind events, but did not address the role that the increased stratification may play in reducing vertical mixing and enhancing the baroclinically driven estuarine circulation. In the York River Estuary, VA, Scully et al. (2005) observed wind-induced straining, noting that down-estuary winds enhance vertical stratification whereas up-estuary winds tend to reduce vertical stratification. In an idealized, partially mixed estuary, Chen and Sanford (2009)

confirmed that wind straining of the along-channel salinity gradient exerts an important control on stratification, which promotes increases/decreases in stratification during down/up-estuary winds. When down-estuary wind stress increases, stratification shows an increase-then-decrease transition that indicates the competition between wind straining and direct wind mixing. In the Chesapeake Bay, a storm moving from south to north can generate different wind fields, which are dominated by northerly (down-estuary) winds or southerly (up-estuary) winds due to the Bay's orientation (Figure 1-1). It may cause a different destratification process during a storm.

### **Restratification and estuarine recovery following a storm**

Restratification in an idealized one-dimensional mixed layer can occur only by an increase in buoyancy (Niiler and Kraus, 1977; Price et al., 1987). In a fluid containing a horizontal density gradient, restratification is led by gravitational adjustment (Simpson and Linden, 1989). In a real partially mixed estuary, horizontal density gradients found in mixed layers generated by impulsive mixing by a storm can also lead to restratification (Tandon and Garrett, 1994). Subtidal adjustment of estuarine circulation is influenced by gravity. For density (or salinity), the gravitational adjustment of a two-layer system, initially separated by a vertical wall (Wang, 1984), can be applied to the estuaries. A strong wind stress during a hurricane disturbed the water column and made a well-mixed estuary but the horizontal salinity gradient still exists in the estuary. When the wind forcing terminates, the water column adjusts at the internal gravity wave phase speed to form a stably stratified (partially mixed) estuary. During and after the adjustment, sharp density fronts divide the two layers both horizontally and vertically. Density fronts of this type are often observed in estuaries (Geyer and Farmer, 1989). In the absence of

rotation, the adjustment process continues until the light water has spread evenly over the entire domain and the system has come to rest. However, when rotational effects are important, the geostrophic adjustment tends to lead to new stratification (Tandon and Garrett, 1995). Under the influence of the Coriolis force, the forward acceleration induced by the initial movement of the lighter water on the denser water creates a current that veers (to the right in the Northern Hemisphere) and can come into geostrophic equilibrium with the horizontal density gradient (Cushman-Roisin, 1994). Given the horizontal density gradient, Li et al. (2007) verified that both the gravitational and geostrophic adjustment theories provide predictions for the growth of stratification in the water column after a hurricane.

Estuarine recovery from a storm was initiated by the influence of the huge amount of freshwater on the estuarine circulation. A sudden, large injection of freshwater may involve several stages of the transient response of salinity distribution in lower Chesapeake Bay (Kuo et al., 1976). The rebound of salinity structure tends to start immediately after the passage of the flood water and manifests differently in the bottom and surface layers. Gong et al. (2007) reported that the timescale of estuarine recovery in the York River estuary from a hurricane is approximately in the range of 10 to 120 days, depending on the storm surge energy and the amount of river discharge. The freshwaters flowing out of the Bay generate a plume that could affect the interaction between the inner shelf and the Bay estuary. Barotropically, the lower Chesapeake Bay responds to local winds and coastal Ekman flux (Wang and Elliott, 1978; Wang 1979a; b) producing inflows/outflows larger than those produced by the estuarine circulation and river discharge. Wiseman (1986) posed the question of whether estuary plumes are modified

by momentum transfer from the wind or to large-scale forcing by the ambient coastal current. Valle-Levinson et al. (1996) examined the effects of seaward barotropic discharge at the estuary upstream boundary, suppressed coastal ambient flow, and salinity gradient variations on the volume inflows and outflows at the entrance to a wide estuary where rotational influences are important.

### **Seiche motion**

It also has been suggested that lateral variability plays an important role on controlling transport processes in other systems. Rotational effects on lateral variability were incorporated for the study of larger lakes like the Great Lakes of North America where Csanady (1968; 1972) observed a current regime and thermocline tilt associated with Ekman setup driven by steady, shore-parallel winds. Boicourt (1992) suggested that wind-driven circulation on the order of hours could aid and/or destroy vertical density stratification and be the cause of lateral variability in the system. Recently, wind-driven lateral variability in a partially mixed estuary was studied by Reynolds-Fleming and Luettich (2004). They concluded that the lateral response of the upper Neuse River Estuary (NRE) system was driven predominantly by across channel wind forcings and not by Ekman setup associated with along channel winds. This means that wind driven circulation is in the direction of the wind forcing (rather than at an angle to the right of the wind) when the water depth ( $< 4$  m in the upper NRE) is much less than the Ekman layer thickness (Csanady, 1967). They also suggested that additional variability at near diurnal periods might have been due to baroclinic seiches, and identified a lateral, barotropic seiche with a period of approximately 30 minutes. These variabilities have not yet been examined thoroughly in the Chesapeake Bay.



Seiche motion is one of the responses of an estuary to wind forcing. Elliott (1976) indicated that the local surface slopes induced by a winter storm provided evidence for the presence in the Patuxent River of a surface oscillation with a period of approximately 88 hours that may have arisen in response to internal seiching of the halocline. Chuang and Boicourt (1989) reported that seiche motions in the Chesapeake Bay are generally driven by the longitudinal (N-S) wind at 2- to 3-day time scales and are characterized by a node at the mouth and an antinode at the head of the Bay. They found that a 1.6-day period of seiche activity was related to the lateral (E-W) wind and concluded that both longitudinal and lateral winds are capable of causing seiche motion in the Bay and, hence, contribute to estuary-coastal ocean exchange.

## **1.2 The barotropic and baroclinic responses of the Bay to the hurricane forcing**

A hurricane, originally derived from the word *Huracan* from the Caribbean Taino Ameridian language, commonly denotes a tropical cyclone which occurs in the North Atlantic Ocean, the Northeast Pacific Ocean east of the dateline, or the South Pacific Ocean east of 160° E. It is characterized by low pressure at the eye center, a hurricane wall with extremely high wind around it, and a several-hundred-kilometer radius band of clouds associated with heavy rain. A hurricane is classified into five categories by its strength, which is characterized with maximum sustained winds of at least 33 m s<sup>-1</sup> (or 74 mi h<sup>-1</sup>) and storm surge of at least 1.0 m (or 3 ft) (Saffir-Simpson Hurricane Scale, Table 1-1). According to the glossary of National Hurricane Center (NHC) terms (<http://www.nhc.noaa.gov/aboutgloss.shtml>), storm surge is an abnormal rise in sea level accompanying a hurricane or other intense storm, and whose height is the difference

between the observed level of the sea surface and the level that would have occurred in the absence of the cyclone. Storm surge is usually estimated by subtracting the normal or astronomical tide from the observed storm tide which is the actual level of sea water resulting from the astronomic tide combined with the storm surge. While hurricanes can produce extremely strong winds and torrential precipitation, they are also able to generate high waves and damaging storm surge on the sea surface. Storm surges can produce coastal flooding, and heavy rains accompanying a hurricane can produce significant flooding inland. Typically, a hurricane moving from the open ocean to coastal seas brings salt water with storm surge into estuaries. Heavy rainfall also increases freshwater discharges from upstream portions of estuaries. These two aspects increase horizontal density and pressure gradients in estuaries and affect the estuarine circulation.

Hurricane-induced freshwater or saltwater influx in a partially mixed estuary have significant effects on not only physical properties, but also biogeochemical dynamics including submersed aquatic vegetation (SAV) (Valle-Levinson et al., 2002; Roman et al., 2005; Boicourt, 2005; Frazer et al., 2006; Miller et al., 2005; Reay and Moore, 2005; Tango et al., 2006; Trice et al., 2005). Saltwater flooding can also be caused by storm surges that significantly alter forest communities (Conner, 1993; Gresham, 1993; Williams, 1993; Conner and Inabinette, 2005).

Two distinct types of hurricanes were classified by their tracks through the Chesapeake Bay (Pore, 1960; 1965): eastern-type hurricanes that travel east of the Bay, and western-type hurricanes that pass west of the Bay. Eastern-type storms generated maximum surge in the southern portion of the Bay whereas western-type storms created highest surge in the northern part of the Bay. Recently, the Chesapeake Bay was hit by

Table 1-1 Saffir-Simpson Hurricane Scale (SSHS).

Categorization	Maximum Sustained Wind Speed mph (m s <sup>-1</sup> )	Minimum Surface Pressure (mb)	Storm Surge Height ft (m)
Category 1	74-95 (33-42)	> 980	3-5 (1.0-1.7)
Category 2	96-110 (43-49)	979-965	6-8 (1.8-2.6)
Category 3	111-130 (50-58)	964-945	9-12 (2.7-3.8)
Category 4	131-155 (59-69)	944-920	13-18 (3.9-5.6)
Category 5	> 155 (> 70)	< 920	> 19 (> 5.7)

Table 1-2 Some comparative aspects of Hurricanes Floyd and Isabel.

Name Aspects	Hurricane Floyd	Hurricane Isabel
Date	September 7-17, 1999	September 6-19, 2003
Landfalling location	North Carolina	North Carolina
Landfalling category (maximum)	Category 2 (4)	Category 2 (5)
Maximum wind speed and pressure	154 mph, 921 mb	161 mph, 920 mb
Pore's classification	Eastern	Western
Maximum storm surge in CB	1. 559 m (Money Point, VA)	2.487 m (Chesapeake City, MD)
Total rainfall onto CB (max)	10-15 inches	1-2 inches
Total river flows	291 billion gallons (September 16-22; USGS)	1,190 billion gallons (September 19-25; USGS)
Damage Estimates	\$ 4.5 billion (particularly NC)	\$ 3.6 billion (\$ 2.67 billion both VA and MD)

two tropical cyclones, Hurricane Floyd and Hurricane Isabel (Table 1-2). Both made landfall in North Carolina as a Category 2 hurricane and both occurred in mid-September (1999 and 2003, respectively). These two hurricanes had different tracks (Figure 1-2): Hurricane Floyd's track nearly paralleled with the coastal shoreline that corresponds to the eastern-type storm, whereas Hurricane Isabel's track was perpendicular to the coastal shoreline that corresponds to the western-type storm. The barotropic response of the Chesapeake Bay to the hurricanes was studied by Shen et al.(2005), Wang et al., (2005), Shen et al., (2006a), and Shen et al. (2006b), and the baroclinic response of the Bay to Hurricane Isabel in the York River tributary and Bay proper by Gong et al. (2007) and Li et al. (2007), respectively. However, in all the above studies, the continental shelf dynamics was not explicitly considered. As a result, the ocean influx and outflux estimated during the event was questionable because one does not know how much is contributed by the local wind versus the remote wind.

Hydrodynamics in a relatively shallow estuarine system is closely linked with fresh water input and the thermally induced stratified condition, which is then mixed by external forcings such as tides, winds (atmospheric pressure), and waves. The external forcings can incur motion themselves, but at the same time modify the mixing-stratification pattern, and, in turn, create a baroclinic water motion. In a partially mixed estuary such as Chesapeake Bay, tides and river inflows provide mixing and stratification to generate a gravitational (estuarine) circulation. It manifests as a basic state of two-layered circulation that represents a seaward flow at the surface and a landward flow at the bottom. Review papers on this subject can be found in Stommel and Farmer (1952); Pritchard (1952); Pritchard (1956); Hansen and Rattray (1965); Fischer (1972); Chatwin

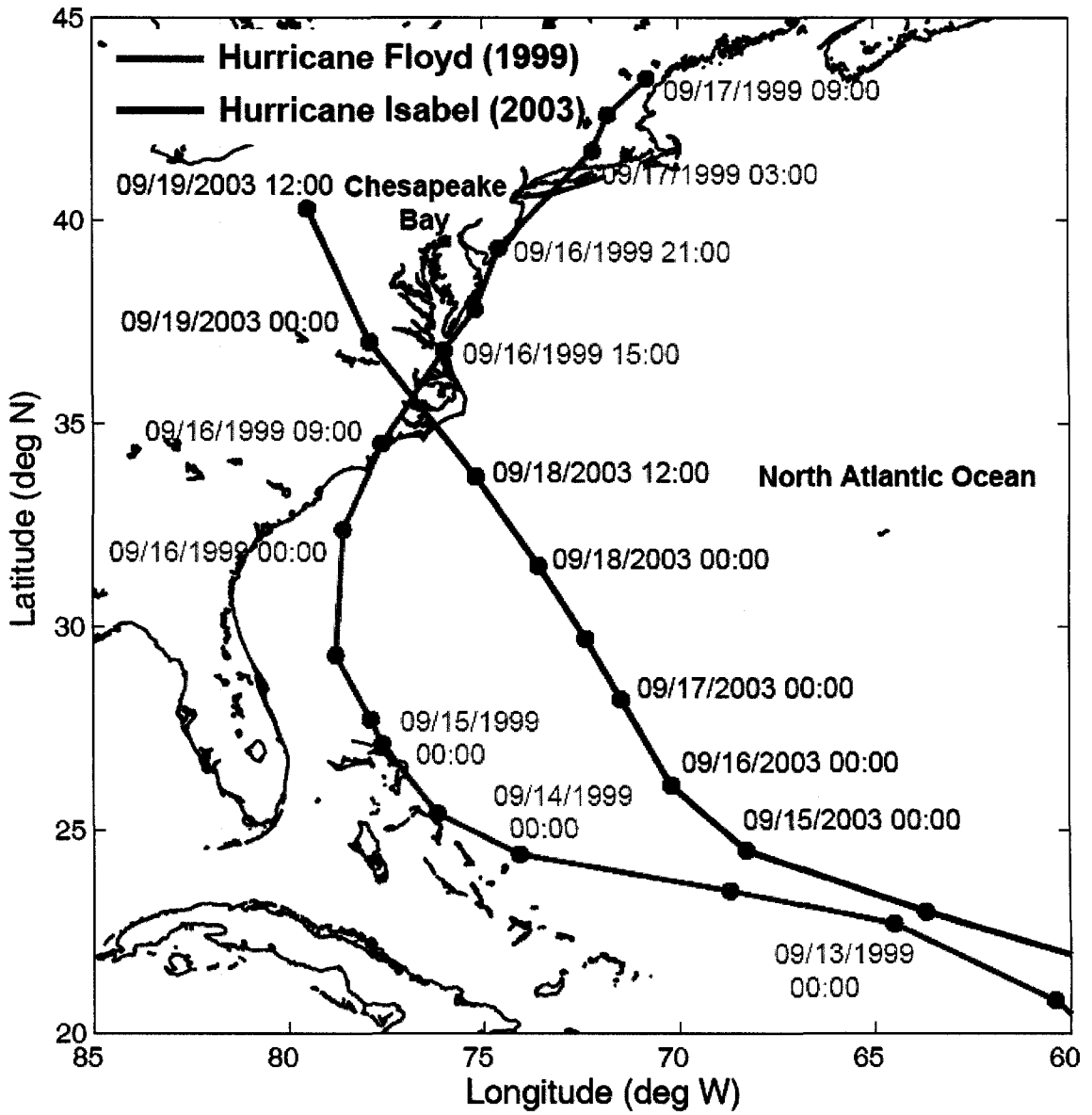


Fig. 1-2 Tracks of Hurricanes Floyd (red) and Isabel (blue).

(1976); Officer (1976); Csanady (1976); Dyer (1997); Geyer et al. (2000); Stacey et al. (2001); MacCready (2004). On top of the basic state flow pattern established by the river and tides as described, wind-driven motion can significantly modify this flow pattern either to intensify or weaken the gravitational circulation. How the hurricane wind condition creates a perturbation on the basic flow patterns and the subsequent restoration of these patterns is an issue at the core of this study.

The stratified water responds to wind forcing with many different modes superimposed upon one another. In the vertical, the response, in general, can be classified into many different modes each with its own eigenvalue (Kundu, 1990; Csanady, 1984). In this study, following responses of a partially mixed estuary to forcing from extreme wind events will be considered: 1) The barotropic response, that is, the response to the sea-surface slope induced by tides or atmospheric forcing. These forcing does not depend on the density of the water nor the depth of the water. 2) The baroclinic response, on the other hand, is the response that varies with the density of seawater and thus depends on the depth of the water. For example, the response induced by the buoyancy forcing such as freshwater discharge affects the weight of overlying seawater and, hence, the pressure, acting on a horizontal surface at depth. The horizontal variations in density cause the waters to follow the sea surface less and less with increasing depth and then stratify, that is, to develop baroclinic conditions (TOU, 2001).

During the past fifty years, many Chesapeake Bay researchers have studied the response to external forcing with various approaches. Observational investigations in this area include the analysis of long-term meteorological, tidal, and current velocity data in the upper Chesapeake Bay (Elliott *et al.*, 1978; Grano, 1982; Hamilton and Boicourt,

1983), in the middle part of the Bay (Vieira, 1983), in the Potomac River (Elliott, 1978; Wang and Elliott, 1978), and in the lower part of the Bay (Wang, 1979a; 1979b). All confirm that variable winds and water levels can induce large fluctuations. The analyses of short term period data in the mid-Chesapeake Bay (Pritchard and Vieira, 1984), in the Choptank River (Sanford and Boicourt, 1990), and in the mouth of the Rappahannock River (Kuo and Park, 1992) also have examined the vertical variations in residual current that respond to wind forcing. Additionally, the modeling studies have been accomplished using observations (Wang, 1980; Wang and Kravitz, 1980). Despite the progress made that is described above, two challenges remain. First, it is well-known that the wind can have local and remote effects. The question is what amount of the Bay's responses to the hurricane result from the local wind directly versus from the remote wind. A second question is how to specify a boundary condition to reflect the hurricane wind condition in a numerical modeling study.

Recent progress on better understanding of continental shelf dynamics as well as development of more sophisticated and efficient models helped to resolve the aforementioned issues. For example, a realistic boundary condition can be constructed and used successfully for storm surge simulation by incorporating the sea level observation measured at the coast during the storm. A considerable progress also has been made in developing two- and three-dimensional circulation models for a shallow water system. A hydrodynamic-numerical model for the estuarine circulation has been suggested to involve the external forcings (Grezechnik, 2000). Numerical hydrodynamic models are now able to simulate large-scale and small-scale circulations in the shallow water system with reasonable accuracy (Blumberg and Goodrich, 1990; Johnson et al.,

1993; Shen et al., 1999; Wang and Johnson, 2000). With the development of new, more sophisticated algorithms, the computational power of new processors allows us to run complex hydrodynamic models, providing us with a deeper insight into the physics governing motion and mixing in the shallow water systems. The models can therefore be used to increase understanding of the physical responses of the system to the external forcing.

As indicated above, very few studies so far have explicitly coupled estuarine response to the continental shelf dynamics and thus the ocean influx and outflux estimations during wind events were questionable. The aim of the present study is to contribute to a better understanding on the barotropic and baroclinic responses of the Bay to an extreme meteorological event, emphasizing a comparative study with a large domain extended into the continental shelf.

### **1.3 Objective and outline**

#### **Objective**

The overall objective of this study is to identify and quantify the barotropic and baroclinic responses of the Chesapeake Bay to two different types of hurricanes: Hurricane Isabel and Floyd. During the study, a start-of-the-art, unstructured grid semi-implicit, Eulerian-Lagrangian, finite element model (SELFIE) was used with well-calibrated observational variables, including water level, salinity, and velocities measured during the hurricane in the Bay. The specific objectives were:

1) to examine the temporal and spatial variation of the water level under the influence of hurricane wind fields



- 2) to quantify the volume transport induced by barotropic flows,
- 3) to identify the influence of river discharge on water level in the tributary,
- 4) to quantify the oceanic salt flux,
- 5) to characterize mixing induced destratification and restratification using non-dimensional parameters,
- 6) to identify the influence of local and remote wind forcings, and the effects of precipitation and continental shelf dynamics,
- 7) to identify the estuarine recovery process from hurricane forcing, and
- 8) to estimate the time scale of estuarine recovery.

## **Outline**

Chapter II summarizes the description and analysis of observations made during Hurricanes Floyd and Isabel. The next two chapters, Chapter III and Chapter IV, provide the descriptions of numerical methods and their calibrations, respectively. Chapter V reports on the barotropic response of Chesapeake Bay to two hurricanes, concentrating on the storm surge dynamics, and effects of different external forcing on sea surface elevation. Chapter VI focuses instead on the baroclinic responses of the Bay to two hurricanes. They included topics of oceanic salt influx, hurricane-induced mixing process, effects of local and remote winds and of precipitation. Chapter VII describes the estimation of the time scale for estuarine recovery from the forcing of hurricanes and the influence of continental shelf dynamics. In Chapter VIII the main results of the thesis are summarized with discussion. The implications of the work and potential future research are also presented.

## Chapter II

### DATA DESCRIPTION

#### 2.1 Introduction

In this study, five categories of data observed during two hurricane events (Floyd in 1999 and Isabel in 2003) are analyzed to verify mechanisms of physical phenomena and calibrate numerical model results: 1) historical water level data on the National Water Level Observation Network (NWLON) stations verified by the National Oceanic Atmospheric Administration (NOAA)'s National Ocean Service (NOS). 2) time series of water velocity from NOAA, the Chesapeake Bay Observing System (CBOS), and Virginia Institute of Marine Science (VIMS). 3) salinity data in the York River from the Centralized Data Management Office (CDMO) supported by the Chesapeake Bay National Estuarine Research Reserve (CBNERR) and VIMS. In addition to 2) and 3), Valle-Levinson *et al.* (2002) has collected water velocity and salinity data at the Bay mouth during Hurricane Floyd, and Boicourt (2005) has measured water velocity and salinity at the mid-Bay station during Hurricane Isabel. 4) wind and atmospheric pressure data from NOAA and the National Data Buoy Center (NDBC) for periods of both hurricanes. 5) river streamflow data in the tributaries of the Chesapeake Bay obtained from the U.S. Geological Survey (USGS) in both years.

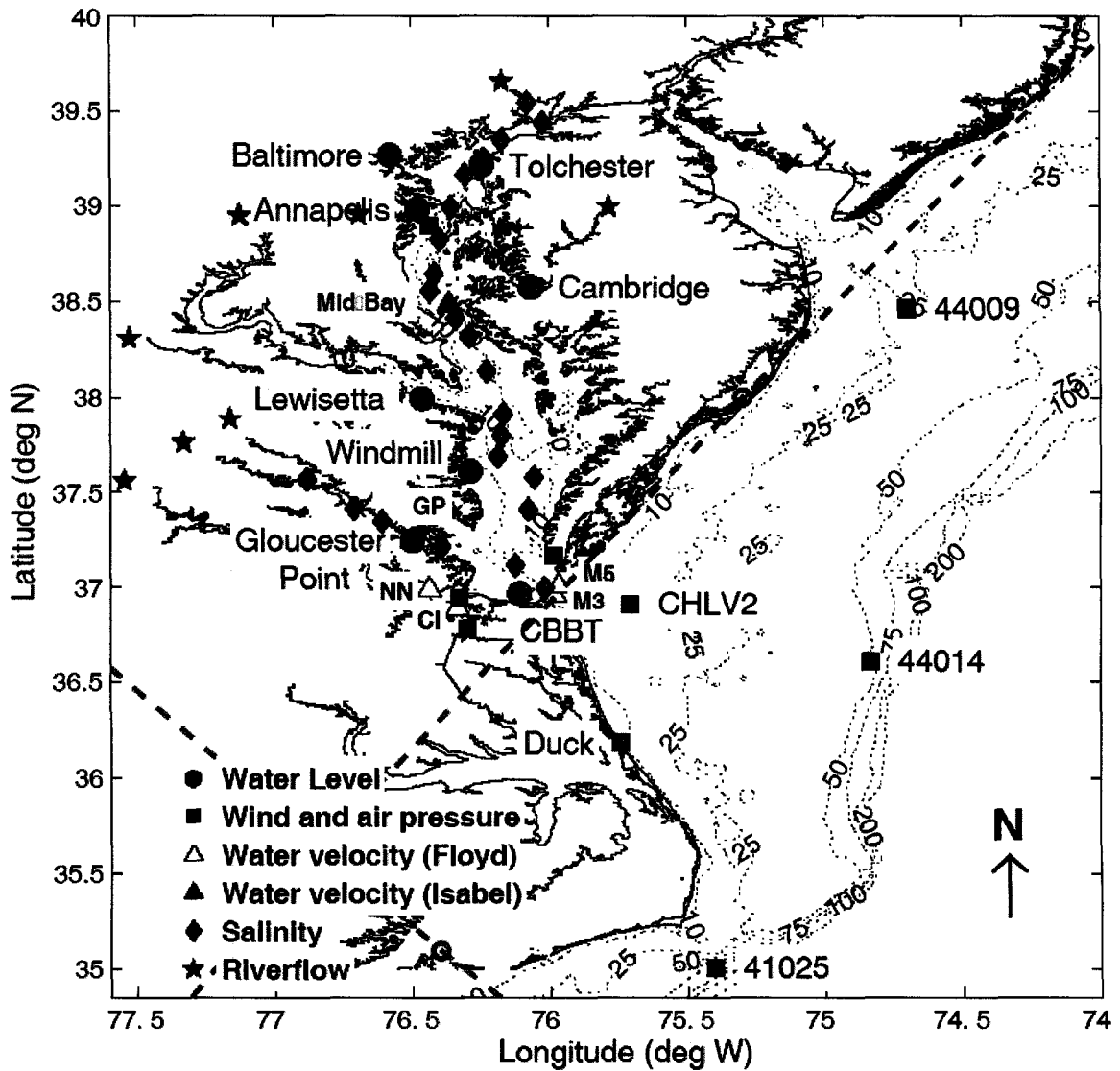


Fig. 2-1 A map of Chesapeake Bay observation station locations with bathymetric soundings (meters). Red circles represent water elevation data; green squares represent wind data; triangles represent current data (red: Year 1999; blue: Year 2003); cyan diamonds represent salinity data; and red stars represent riverflow. Red and green dashed lines represent the tracks of Hurricanes Floyd and Isabel, respectively.

## 2.2 Hurricane Floyd in 1999

### Meteorological data

During Hurricane Floyd, meteorological data were collected from a total of 13 stations operated by NOAA and NDBC (station locations shown as green squares in Figure 2-1). Typically, winds are measured at heights of 15-20 m above mean sea level (MSL) and atmospheric pressures are observed at heights of 10-15 m above MSL. Hourly wind data at six representative stations, Thomas Point, Lewisetta, CBBT, Chesapeake Light, VA Beach, and Duck, were plotted in Figure 2-2 (left panels). Winds are showing similar but different patterns throughout the stations. Initially, winds at all stations are blowing from the northeast. During the event, (15 to 18 September, 1999), at three stations (Chesapeake Light, VA Beach, and Duck), wind vectors were rotating clockwise and then blowing to the southeast, while wind vectors at the residual stations were showing counter-clockwise motion and then blowing to southeast. Wind speed diminished from lower latitude to higher latitude. These can be explained by the track of Hurricane Floyd, which is represented by the red dashed line in Figure 2-1. Floyd weakened over land after making landfall near Cape Fear, NC as a Category 2 hurricane that diminished to a Category 1 hurricane before passing into Virginia (Zervas et al., 2000). Thereafter, it followed the Atlantic coastline toward the northeast. Hurricane Floyd passed directly over the mouth of the Chesapeake Bay, with three stations located to the east of its track and another three stations to the west of its track. Therefore, wind patterns were determined and distinguished by this track of Hurricane Floyd.

Barometric pressure data were plotted on the right panels of Figure 2-2 as well. The lowest atmospheric pressures recorded were 970.2 millibars (mb) at the Chesapeake

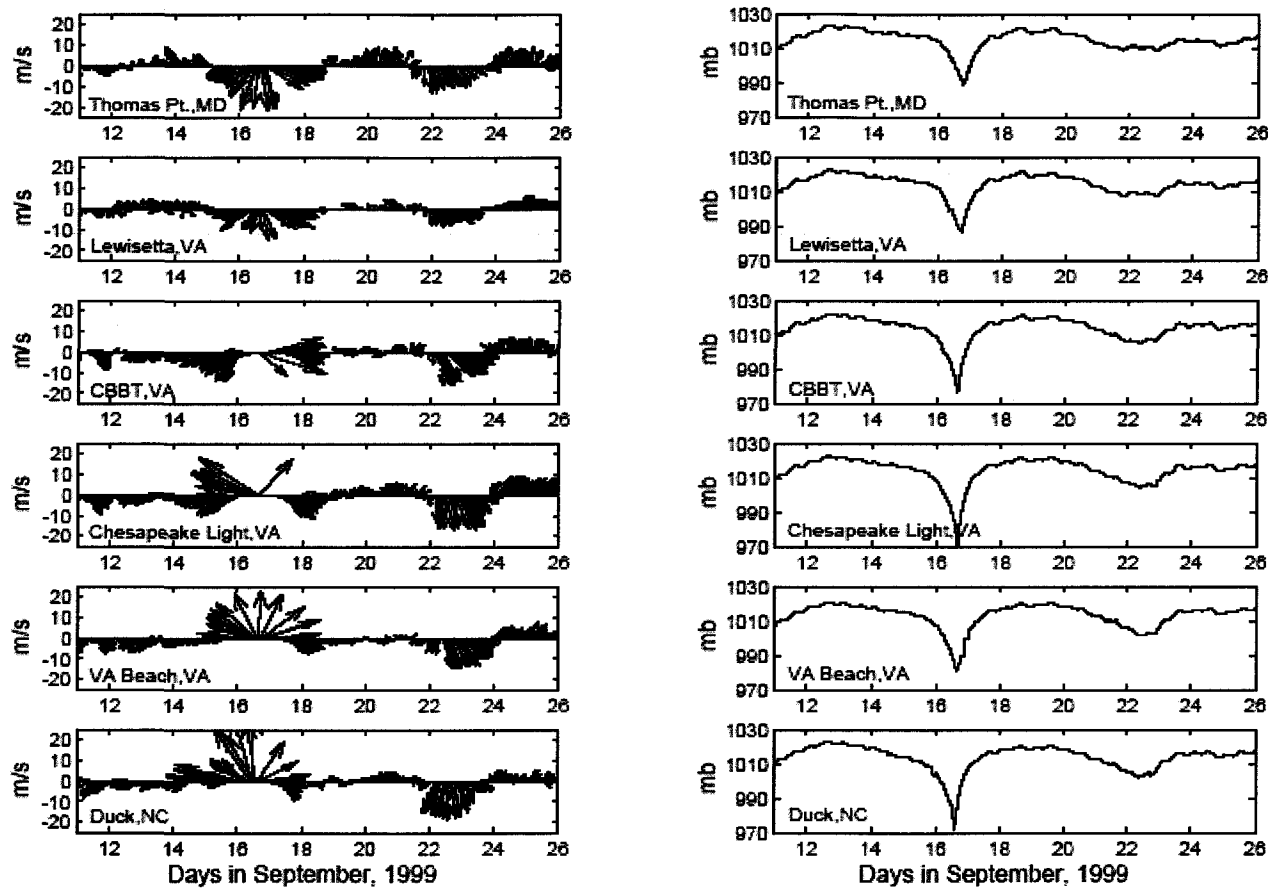


Fig. 2-2 Time series plots of wind data (left panels) and atmospheric pressure (right panels) at six selected stations (from top to bottom: Thomas Point, MD; Lewisetta, VA; CBBT, VA; Chesapeake Light, VA; VA Beach, VA; Duck, NC) during Hurricane Floyd, 11-26 September, 1999, UTC.

Light buoy station, 972.1 mb at Duck, and 976.4 mb at CBBT. A drop in atmospheric pressure over a body of water can raise water levels due to an inverse barometer effect. Simply, a 1-mb drop in atmospheric pressure corresponds to a 1-centimeter (cm) change in water level over open ocean (Harris, 1963). Roughly, the maximum effect could range from about 25 cm at Thomas Point, MD to about 45 cm at Chesapeake Light, VA.

In the coastal regions, the effect of the wind stress on water levels during a storm is often substantially greater than the inverse barometer effect (Zervas et al., 2000). There was an interesting feature at three NOAA/NWLON stations in the upper Chesapeake Bay, which showed negative storm surges in spite of high winds and low pressure. This means that the effect of the wind stress on water levels competes with that of the low pressure. There should then be a water level set-down induced by local wind stress (Shen et al., 2006a).

#### Water level data

The water level data were collected at the NOAA/NWLON stations in the Chesapeake Bay during Hurricane Floyd. These stations are shown in Fig. 2-1 and are represented by red circles. Information on the stations is detailed in Table 2-1. Each station provides two types of water level data: 1) observed water level (storm tide) and 2) predicted water level (astronomical tide). Basically, storm surge is calculated from the difference between the observed storm tide and the predicted astronomical tide (Bretschneider, 1966). Physically, storm surge consists of two primary components: 1) water level elevation due to wind stress produced by a storm and 2) water level elevation due to diminished atmospheric pressure within the storm.

Table 2-1 Station information and availability of observations during Hurricanes Floyd and Isabel in MD, DC, VA, and NC.

Station ID	Station Name	Coordinates		Observations*			
		Latitude (N)	Longitude (W)	WL	WD	WV	S
<b>NOAA</b>							
8570283	Ocean City Inlet, MD	38° 19.7'	75° 05.5'	X			
8571892	Cambridge, MD	38° 34.4'	76° 04.1'	X	X		
8573364	Tolchester Beach, MD	39° 12.8'	76° 14.7'	X	X		
8574680	Baltimore, MD	38° 16.0'	76° 34.7'	X			
8575512	Annapolis, MD	38° 59.0'	76° 28.8'	X			
8577330	Solomons Island, MD	38° 18.0'	76° 27.1'	X			
8594900	Washington, DC	38° 52.4'	77° 01.3'	X			
8632200	Kiptopeke Beach, VA	37° 10.0'	75° 59.3'	X	X		
8635150	Colonial Beach, VA	38° 15.1'	76° 57.6'	X			
8635750	Lewisetta, VA	37° 59.2'	76° 27.8'	X	X		
8636580	Windmill Point, VA	37° 36.9'	76° 17.4'	X			
8637624	Gloucester Point, VA	37° 14.8'	76° 30.0'	X			
8638610	Sewells Point, VA	36° 56.8'	76° 19.8'	X	X		
8638863	Chesapeake Bay BT, VA	36° 58.0'	76° 06.8'	X	X		
8639348	Money Point, VA	36° 46.7'	76° 18.1'	X	X		
8651370	Duck Pier, NC	36° 11.0'	75° 44.8'	X	X		
<b>NDBC</b>							
41025	Diamond Shoals, NC	35° 00.4'	75° 24.1'		X		
44009	Delaware Bay 26 NM, NJ	38° 27.8'	74° 42.1'		X		
44014	Virginia Beach 64 NM, VA	36° 36.7'	74° 50.2'		X		
TPLM2	Thomas Point, MD	38° 53.9'	76° 26.2'		X		
CHLV2	Chesapeake Light, VA	36° 54.6'	75° 42.6'		X		
<b>CBOS</b>							
mid-Bay	Mid-Bay station, MD	38° 18.0'	76° 12.0'			X(I)	X(I)
<b>VIMS</b>							
GP	Gloucester Point, VA	37° 14.8'	76° 30.0'			X(I)	
<b>ODU</b>							
M3	Chesapeake Bay mouth, VA	36° 57.7'	75° 59.1'			X(F)	X(F)
M5	Chesapeake Bay mouth, VA	37° 00.5'	75° 58.2'			X(F)	X(F)
<b>CBNERR</b>							
	Sweet Hall, VA	37° 34.0'	76° 50.0'				X
	Taskinas Creek, VA	37° 24.0'	76° 42.0'				X
	Claybank, VA	37° 18.0'	76° 33.0'				X
	Goodwin Islands, VA	37° 13.0'	76° 23.0'				X
<b>NOAA COP</b>							
	Newport News, VA	36° 59.3'	76° 26.4'			X(F)	
	Craney Island, VA	36° 53.3'	76° 20.3'			X(F)	

\* WL: water level; WD: wind; WV: water velocity; S: salinity; (I): only for Isabel; (F): only for Floyd

Time series of storm surges at eight selected stations in the Bay are shown in Fig. 2-3 (Zervas et al., 2000). Surge levels reached two peaks in the lower Bay from Chesapeake Bay Bridge Tunnel (CBBT) through Windmill Point, VA around 0700 and 1500 UTC 16 September, but then dropped rapidly after the storm passed. In contrast, the stations in the upper Bay from Annapolis through Tolchester Beach, MD showed negative values of storm surge throughout the storm period. The peak of storm surge seems to propagate from the lower Bay to the upper Bay, but settles down in the upper Bay.

#### Current data

During Hurricane Floyd, NOAA Current Observation Program (COP) was operating two Acoustic Doppler Current Profiler (ADCP) current meters in the lower James River estuary. The first station was located near the mouth of the Elizabeth River. The second station was located in the main shipping channel at Newport News near the mouth of the James River (Figure 2-1). The ADCPs were deployed on the bottom and sampled currents in 1-meter layers from a level close to the instrument head to a level near the surface (Zervas et al., 2000). The temporal plots of along-channel water velocity at two depths of the Newport News station are shown in Figure 2-4 (middle panel). Water velocities were observed at 1.7 m (blue) and 12.7 m (red) below MLLW. The sequence of local events can be divided into four periods of local wind speeds. During the first period between 22:00 UTC on September 15 and 06:00 UTC on September 16, current flowed into the James River and reached a maximum speed of about 0.75 m/s around 0500 UTC on September 16. This period is characterized by strong northeasterly



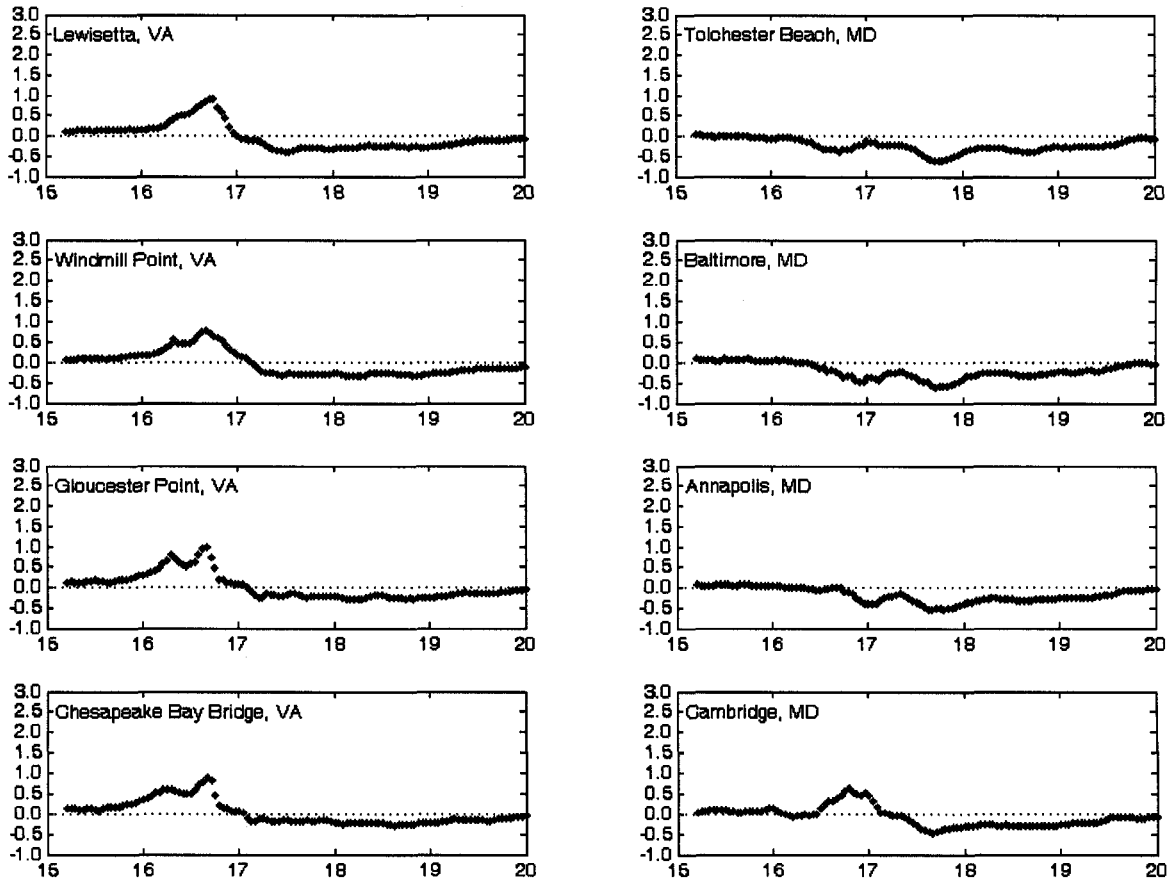


Fig. 2-3 Time series plots of storm surges (meters) at selected NWLON water level stations during Hurricane Floyd, 15-20 September, 1999, UTC.

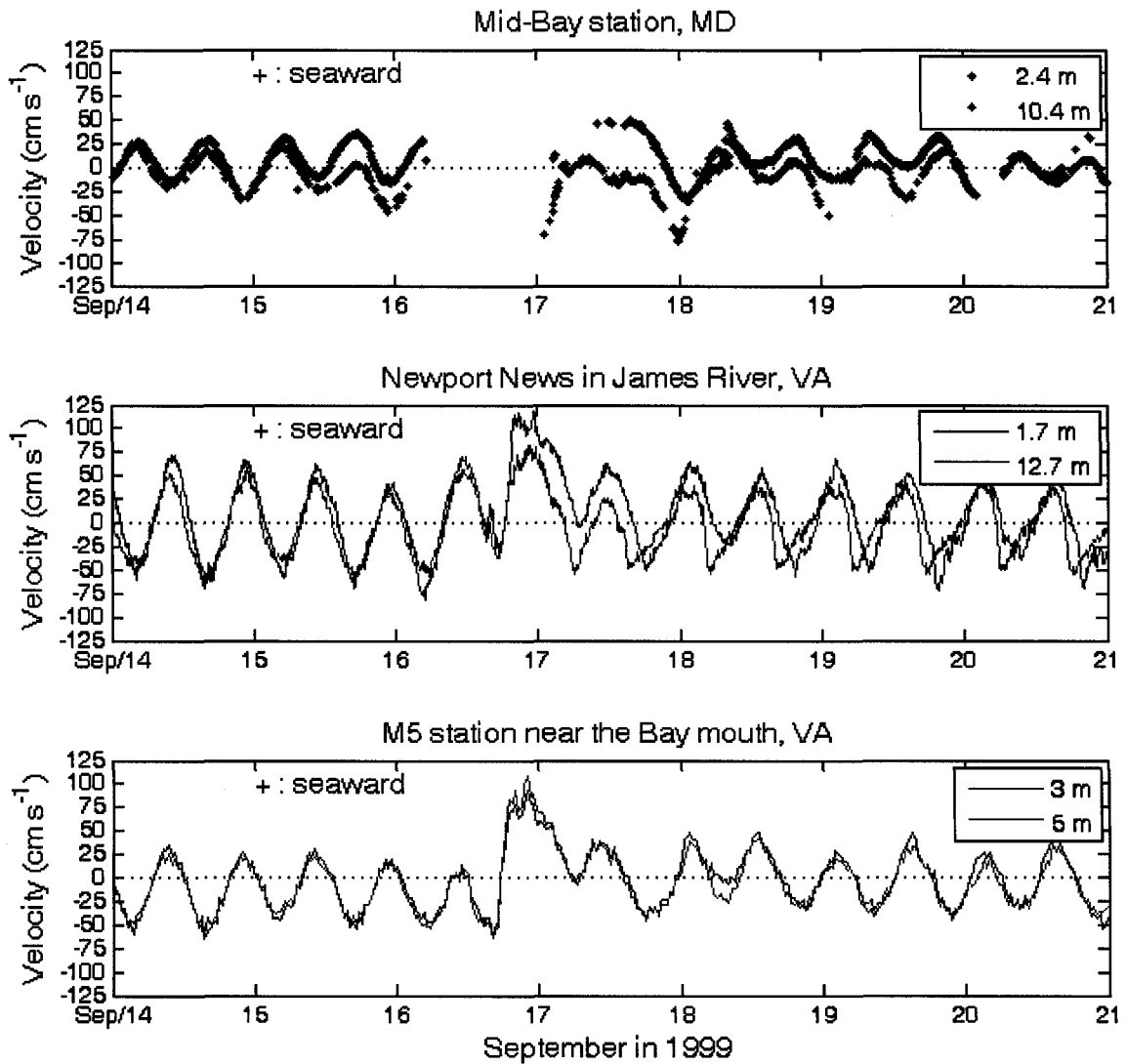


Fig. 2-4 Time series plots of observed longitudinal currents at three stations, Mid-Bay buoy, MD (upper panel), Newport News, VA (middle panel) and M5 (lower panel) near the Bay mouth, during Hurricane Floyd, 1999, UTC. Positive velocity represents flow directed out of the Bay.

winds of about 15.1 m/s recorded at Sewells Point on September 16, 04:00 UTC and it corresponds to the first peak of water level recorded at CBBT at 05:24 UTC on September 16. During the second period, between 05:00 and 16:00 UTC on September 16, relatively weak east-southeasterly winds of about 8~10 m/s occurred. There was no significant sub-tidal current in the James River. At the same time, water level decreased somewhat. During the third period, between 16:00 and 18:00 UTC on September 16, current direction changed abruptly to seaward, corresponding to a 90-degree rotation of local wind to a northerly direction showing its highest value of 20.7 m/s. The fact that seaward current rapidly developed in the James River suggests that it is directly caused by the wind stress on the James River pushing water toward the main Bay. Lastly, the period between 18:00 UTC on September 16 and 09:00 UTC on September 17 is marked by northwesterly winds gradually weakening from 20.7 m/s to 6.1 m/s and storm surge rapidly dropped due to the quantity of water driven out of the Bay. It is noteworthy that, from 03:00 to 09:00 UTC on September 17, surface and bottom currents had opposite directions. In other words, the bottom current was directed upstream while the surface current flowed downstream, even though they were in phase. It suggests that sustained northwesterly winds should affect the vertical structure of water velocity in the downstream region of the James River.

Another dataset was collected from CBOS. The CBOS station, mid-Bay buoy, water velocity was measured at 2.4-m and 10.4-m depths (top panel in Figure 2-4). Although a 1-day span of data was missed during the event, an interesting feature of current direction is shown. Bottom and surface currents had almost the same magnitude of velocity in the same direction until 06:00 UTC on September 15, during which time

southeasterly winds were dominant. The period between 06:00 UTC on September 15 and 10:00 UTC on September 16 was dominated by east-northeasterly winds with a maximum value of 18.3 m/s recorded at Cambridge, MD. Bottom and surface currents began to flow in different directions, i.e., landward at the bottom but seaward at the surface. Thereafter, northeasterly winds changed to northerly winds with the value of 16.7 m/s at 19:00 UTC on September 16. Unfortunately, no reasonable explanation of current pattern can be described at the mid-Bay buoy station because of current data missing in this period. Lastly, during the period between 19:00 UTC on September 16 and 21:00 UTC on September 17, winds changed to northwesterly counter-clockwise and wind speed gradually decreased from 16.7 m/s to 3.6 m/s recorded at Solomon Island, MD. Also for this period, bottom and surface currents still flowed in opposite directions. As described above, sustained northwesterly winds in the mid-Bay seem to affect the vertical profiles of water velocity.

Lastly, in autumn of 1999, water velocity was measured at the entrance of the Chesapeake Bay (Valle-Levinson et al., 2002). A 70-day deployment included the Hurricane Floyd event in mid-September 1999. ADCPs and three Inter-Ocean electromagnetic current meters (S4s) were deployed during September 7–9, 1999 at the entrance to the Bay. Bottom velocity (measured at 5 m depth) and mid-water velocity (measured at 3 m depth) at Station M5 were plotted in Figure 2-4 (bottom panel). Until 0500 UTC on September 16, northeasterly winds were dominant with a value of 17.5 m/s recorded at Chesapeake Light, VA. Those winds changed to east-southeasterly winds until 15:00 UTC on September 16 with the highest value of 26.6 m/s. During these two periods, bottom and surface currents flowed dominantly into the Bay. Water flows in

both depths rapidly changed from landward to seaward at 18:00 UTC on September 16, which corresponded to the wind rotating to a northwesterly direction. Both flows reached to a maximum value of about 110 cm/s at 22:00 UTC on September 16. Unlike what was observed at the previous two stations, currents had almost the same magnitude of velocity in phase. The apparent explanation is that the vertical stratification of currents was disrupted and water was well mixed due both to the strong wind stress and the shallow depth (6.4 m).

### Salinity data

Valle-Levinson et al. (2002) contributed salinity data measured from conductivity-temperature-depth (CTD) recorders. This measurement was conducted during the same period as ADCPs and S4 deployment and is described in Table 2-1. Bottom and mid-water depth salinity at Station M5 and surface salinity at Station M3 were plotted in Figure 2-5 (top panel). Data were filtered using the Lanczos filter and fluctuations with frequencies shorter than 34 hours were cut off. Salinity remained relatively high at Station M5 since northeasterly winds were blowing prior to Hurricane Floyd. No significant vertical stratification was shown during September 13 – 17. Bottom and surface salinities began to decrease from 23:00 UTC on September 17 and dropped by 5 parts per thousand (ppt) within a few hours. This is coincident with the period that northeasterly winds rotated counter-clockwise to become northwesterly at CBBT. Stratification began to increase immediately after salinity dropped. This suggests that Bay water flowed out and then slowly re-entered due to the barotropic pressure gradient force between the continental shelf and the Chesapeake Bay. It seems that

bottom salinity recovered faster than surface salinity. On September 22, there was further decrease of salinity levels at both the surface and the bottom. This decrease can be explained by the northwesterly wind event during September 22-24 (Figure 2-3). At Station M3, surface salinity slowly increased from 27 ppt prior to the passage of the center of Hurricane Floyd, and rapidly increased by 3 ppt during the occurrence of east-southeasterly winds. Sudden salinity drop by about 7 ppt seems to coincide with northwesterly winds. Thereafter, sub-tidal salinity fluctuated in the similar pattern of salinities at Station M5.

As other datasets, CBNERR measured surface salinity at two stations, Taskinas Creek and Claybank in the York River estuary, VA (Figure 2-1). Time series of low-pass filtered salinity data are plotted in Figure 2-5 (bottom panel). Salinity rapidly dropped and began to increase after passages of the storm and then slowly recovered to normal values over approximately one month. It is noteworthy that it takes the salinity a longer time than the returning time of either water levels or current fields to normal, which is within one week. Figure 2-6 shows the time history of daily river streamflow obtained from USGS at three main rivers, Susquehanna, Potomac, and James Rivers. Year 1999 had relatively low river discharge. For example, mean river discharge of the Susquehanna River in 1999 (value of  $760 \text{ m}^3 \text{ s}^{-1}$ ) is smaller than 37-year (from 1971 to 2007) mean value of  $1,185 \text{ m}^3 \text{ s}^{-1}$ . During September 17-18, daily streamflow in the Susquehanna River increased by  $1200 \text{ m}^3 \text{ s}^{-1}$ .

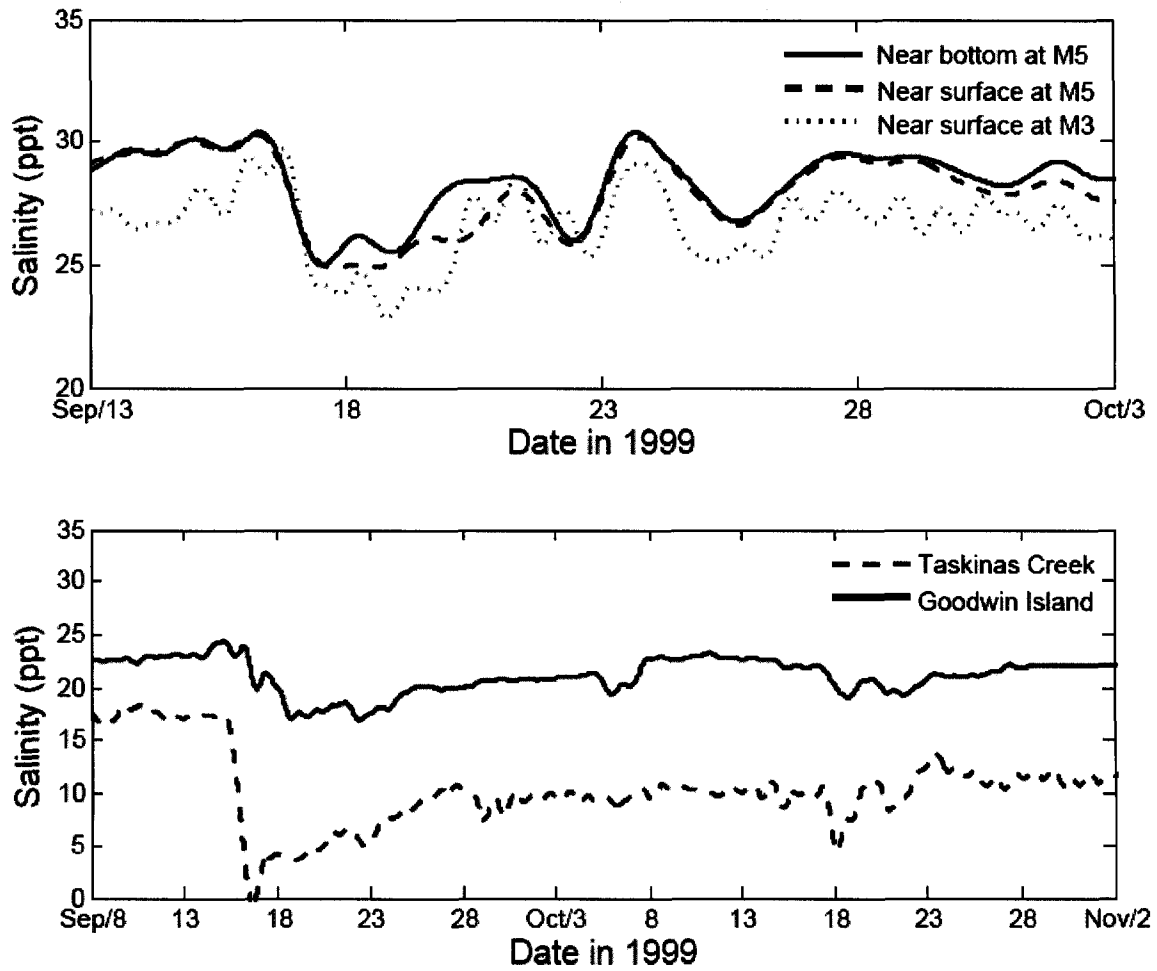


Fig. 2-5 Time series plots of low-pass filtered salinity data at two stations near the entrance of the Chesapeake Bay (top panel) and at two CBNERR stations in the York River estuary (bottom panel) during Hurricane Floyd, 1999, UTC.

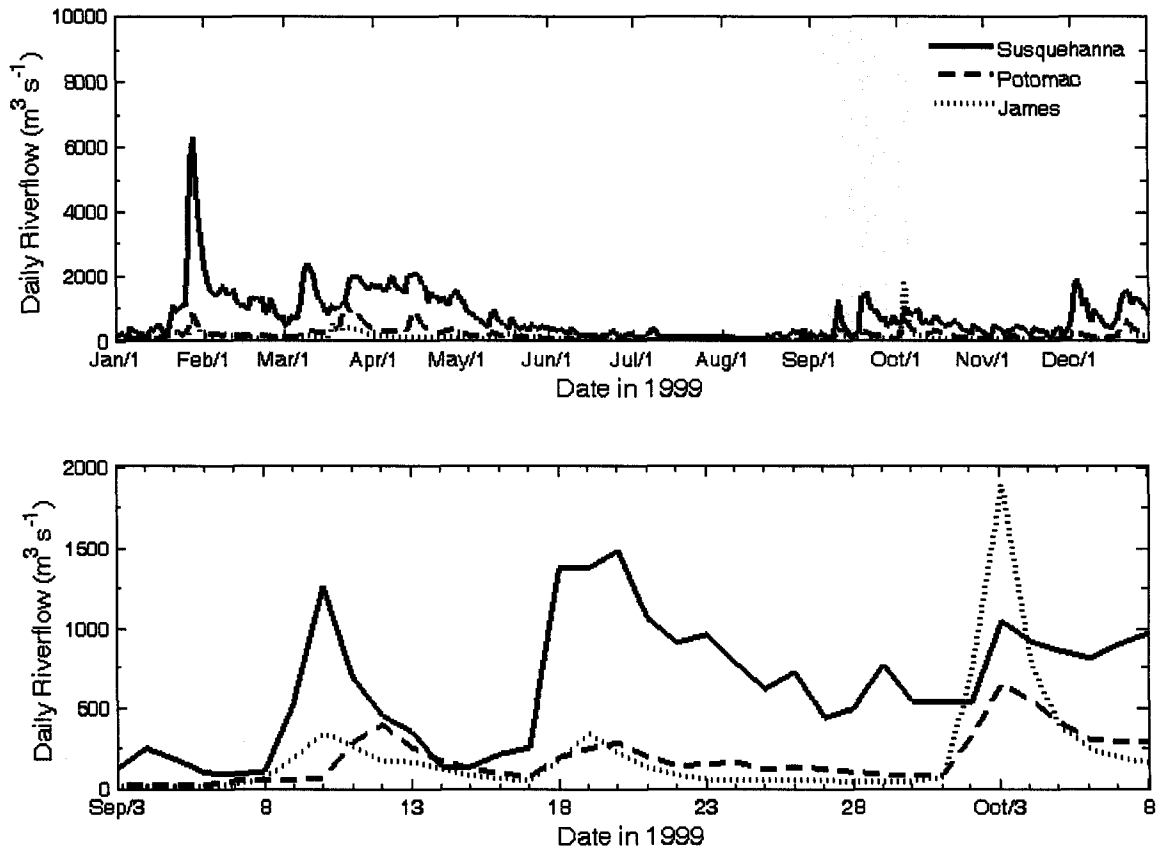


Fig. 2-6 Time series plots of daily riverflow data at three main rivers, Susquehanna, Potomac, and James, in 1999, UTC. The top panel shows the year-long record with the storm event period shaded and the bottom panel shows an expanded view of the discharge record within the storm event period.



## 2.3 Hurricane Isabel in 2003

### Meteorological data

Winds and atmospheric pressure levels were observed at 13 NOAA and NDBC stations around the Chesapeake Bay during Hurricane Isabel as described in the previous section (Figure 2-1). The time series of meteorological data at the 6 selected stations are displayed in Figure 2-7. After Isabel became a major hurricane in the central Atlantic Ocean, its trajectory moved northwestward along U.S. east coast areas. Strong northeasterly winds sustained for 2 days before Isabel made landfall along the North Carolina coast at 18:00 UTC on September 18. A two-day duration of northeasterly winds is sufficiently long to generate Ekman transport from offshore to U.S. east coast areas (Hovis et al., 2004). During the period between 18:00-19:00 UTC on September 18, northeasterly winds changed to easterly winds, with values of about 27.4 m/s at Duck, NC. Simultaneously, the lowest atmospheric pressure of 984.4 mb was recorded at the same station. Two hours later, winds initially rotated clockwise to southeasterly, with the highest value of 28.4 m/s, and then to southerly. Southerly winds blew until 12:00 UTC on September 19 and gradually decreased to about 10 m/s. At Chesapeake Light, VA, the wind pattern was very similar to that at Duck, NC. However, the lowest pressure of 990.6 mb and the highest southeasterly winds of 33.0 m/s were recorded during 21:00-22:00 on September 18. At this time, it could be expected that the maximum surge could be caused by highest east-southeasterly winds and lowest atmospheric pressure. At the three stations, CBBT, Lewisetta, and Thomas Point, wind intensity was relatively reduced due to the distance far from the trajectory of Hurricane Isabel. The time of the peak was retarded by 3-4 hours. Interestingly, according to the record at Thomas Point,

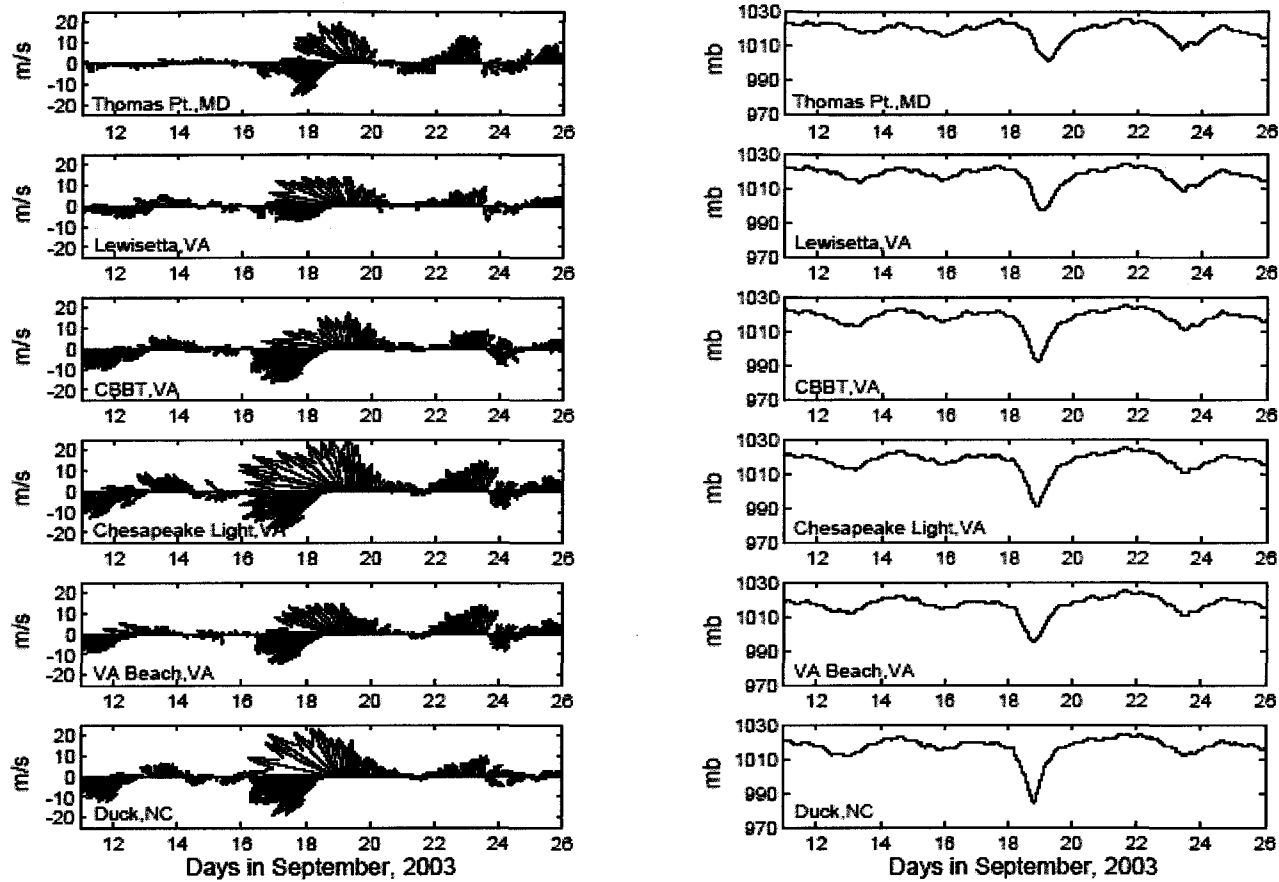


Fig. 2-7 Time series plots of wind data (left panels) and atmospheric pressure (right panels) at six selected stations (from top to bottom: Thomas Point, MD; Lewisetta, VA; CBBT, VA; Chesapeake Light, VA; VA Beach, VA; Duck, NC) during Hurricane Isabel, 11-26 September, 2003, UTC.

MD, southeast-southerly winds remained as strong as 20 m/s and there was a relatively high pressure of 1001.1 mb from 0300 to 12:00 UTC on September 19. This suggests that water level set-up could be induced by southeast-southerly winds in the northern half of the Chesapeake Bay until wind die-off at 15:00 UTC on September 20.

### Water level data

The water level data at the NOAA/ NWLON stations during Hurricane Isabel are available. Figure 2-8 shows the time series of storm surge at 8 selected stations from the mouth of the Bay through the upper Bay (station locations shown by red circles in Figure 2-1). This demonstrates that, at the CBBT station, storm surge was increasing until 22:00 UTC on September 18, reaching its maximum value of about 1.5 m, and rapidly dropping within a few hours through 05:00 UTC on September 19. The water level returned to normal following a 1.5-day fluctuation period at the station. Initially, a two-day duration of northeasterly winds could generate Ekman transport to the entrance of the Bay and make storm surge rise. On the heels of the initial surge, the easterly-northwesterly winds intensified the surge at the entrance of the Bay and it seemed to propagate to the upper Bay or its tributaries. The temporal pattern of storm surge at Sewells Point is very similar to that at CBBT. As propagating to the mid-Bay (see Windmill Pt. and Lewisetta), the surge decreased somewhat and yet it persisted for about 2 days. Estimated surge speed was 3.6 m/s from CBBT to Lewisetta. In the northern half of the Bay, the surge again increased moving north, showing peaks from 1.58 m at Cambridge (10:18 UTC on September 19) to 2.21 m at Tolchester Beach (12:48 UTC on September 19). The surge peak propagated with an approximate speed of 7.2 m/s. This speed is 2 times faster than

the surge peak speed in the southern half of the Bay. It can be expected that southerly winds set up the water level elevation and accelerated the surge speed in the northern half of the Bay (Wang et al., 2005; Shen et al., 2005; Shen et al., 2006b).

### Current data

There are two current datasets available during Hurricane Isabel. One was measured at CBOS mid-Bay buoy (blue triangle in Figure 2-1). The time plots of along-channel water velocity at two layers were demonstrated in Figure 2-9 (upper panel). Prior to the storm, north-northwesterly winds drove a typical two-layer wind-forced flow, with transport into the Bay at the lower layer and transport out of the Bay at the upper layer. On the late afternoon of September 18, southeast-southerly winds and an associated pressure deficit were sufficiently strong to drive the entire water column up the Bay at about 150 cm/s in speed. Boicourt (2005) and Roman et al. (2005) addressed the notion that this slab-like response was unusual - not only relatively weak winds driving two-layer flows but also because the typically strong stratification decouples the upper and lower layers. It is agreeable that the strong up-Bay winds created sufficient mixing energy to destroy vertical stratification. Remarkably, vertically mixed flows moved out of the Bay with 100 cm/s speeds on the afternoon of September 19, even though southerly winds still remained at about 10 m/s in speed. This implies that surface wind stress acting northward competes against horizontal barotropic pressure gradient force acting southward. At that time, the water level at Baltimore, MD was approximately 2 m higher than that at CBBT, VA. After the storm, relaxed flows in the

opposite direction subsequently reverted to a typical structure at midnight on September 19.

Regarding the other dataset, VIMS deployed a 600-kHz RDI ADCP at Gloucester Point, VA, from 16 to 25 on September 2003. It was providing high-quality data on waves, storm surge, currents, and acoustic backscatter throughout the water column before, during, and after the storm (Brasseur et al., 2005; Reay and Moore, 2005). Water velocity data were collected at 0.5-m depth intervals starting 1.8 m above the bed, while one-minute average velocity profiles were recorded every 5 minutes. Temporal variations of along-channel flows at two layers, near surface and near bottom, were plotted in Figure 2-9 (lower panel). Prior to the storm, northeasterly winds seemed to drive the water in the York River dominantly. On the afternoon of September 18, the high flow of the entire water column was recorded as being in the direction towards the York River, with values of 150 cm/s and 100 cm/s at the upper and lower layers, respectively. However, when wind velocities were maximal, the dominant direction compared favorably with the alignment of the York River just below Gloucester Point and, therefore, amplified the upper-layer water velocity in the along-channel direction during the peak (Brasseur et al., 2005). Six hours later, the river relaxed with reducing water velocity occurring 3-4 hours earlier than that observed at the mid-Bay buoy. The horizontal barotropic pressure gradient force appeared to be mainly balanced by wind stress and acceleration force.

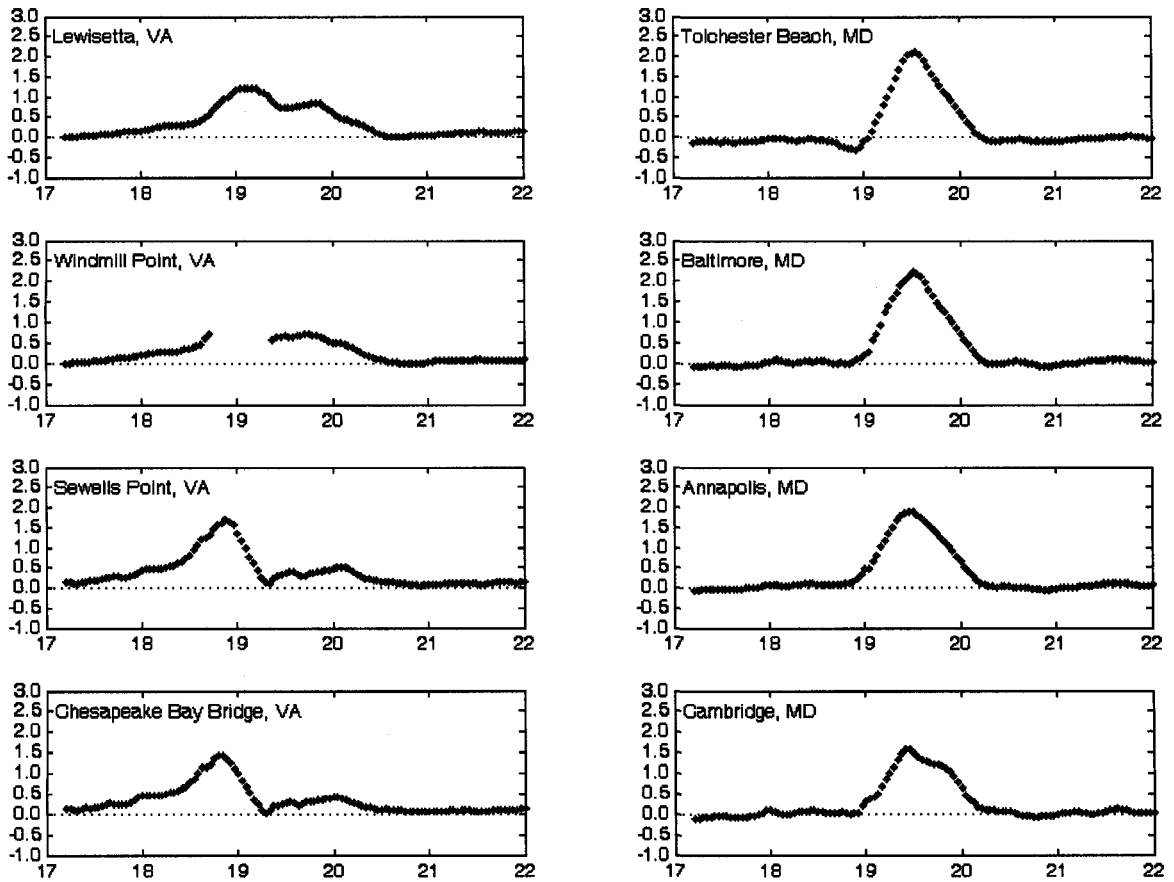


Fig. 2-8 Time series plots of storm surges (in meters) at selected NWLON water level stations during Hurricane Isabel, 17-22 September, 2003, UTC.

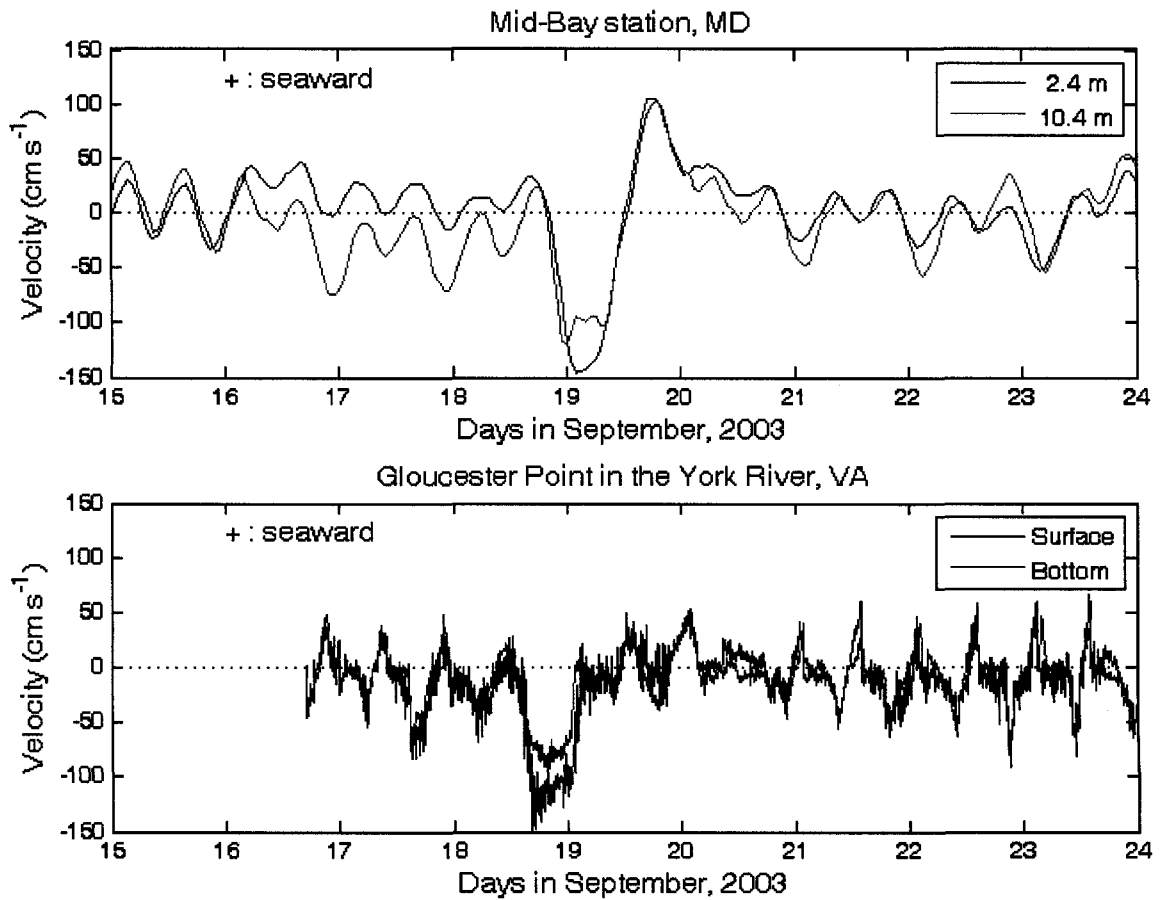


Fig. 2-9 Time series plots of observed longitudinal currents at two stations, Mid-Bay buoy, MD (upper panel), and Gloucester Point in the York River, VA (bottom panel), during Hurricane Isabel, 2003, UTC. Positive velocity represents flow directed out of the Bay.

### Salinity data

Salinity and other water quality parameters were measured from YSI-6600 sondes operated by CBNERR at fixed stations at Sweet Hall (SH), Taskinas Creek (TC), Clay Bank (CB), and Goodwin Island (GI) (Figure 2-1). The time series of low-pass filtered salinity are plotted in Figure 2-10. Additionally, a salinity sensor of VIMS's ADCP positioned at three additional sites (Whitehouse, Walkerton, and Mudpoint, VA) farther up the estuary provided information on salt-water excursion up the estuary before and after the storm (not shown). Sub-tidal salinities began to decrease from the afternoon of September 18 and continuously dropped by 8 ppt until October 5, although the record at GI was broken for about two weeks after the storm. It appears that dropped salinity gradually recovered from October 5 but still did not reach to normal value through the beginning of November. The time for salinity recovery is relatively long compared to that for the Hurricane Floyd event as described previously. This suggests that a river discharge, in the range of 2-10 times higher (Figure 2-11 and Table 2-2) during Hurricane Isabel than during Hurricane Floyd, appeared to retard salinity recovery. The huge amount of freshwater can sufficiently delay salinity in its recovery to normal conditions (Kuo et al., 1976). In the York River estuary, Gong et al. (2007) suggested that the recovery time of salinity decreased by storm surge is about 10 days while that of salinity decreased by freshwater is about 120 days. As described in the previous section, the estimated salinity gradient determined by salinity data appears to be balanced by the horizontal barotropic pressure gradient from the water surface slope and the friction to be balanced in the along-channel momentum equation.



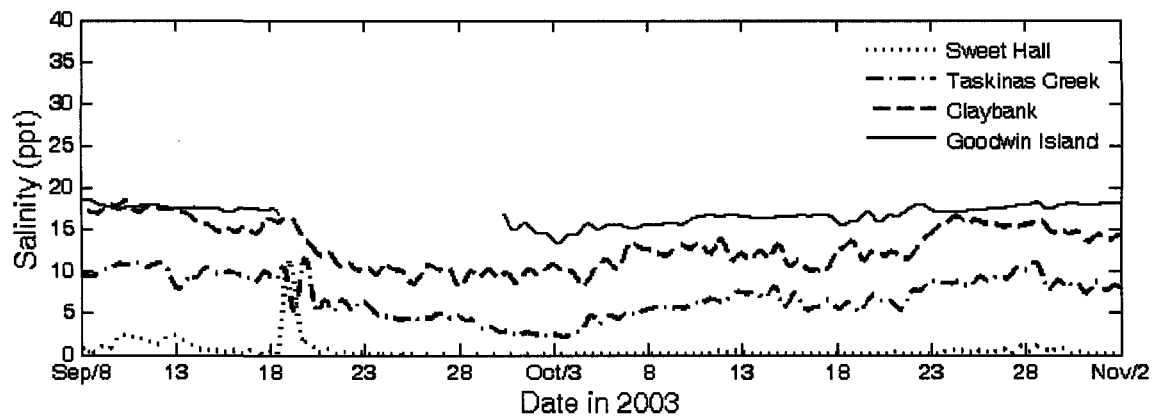


Fig. 2-10 Time series plots of low-pass filtered salinity at four CBNERR stations in the York River during Hurricane Isabel 2003, UTC.

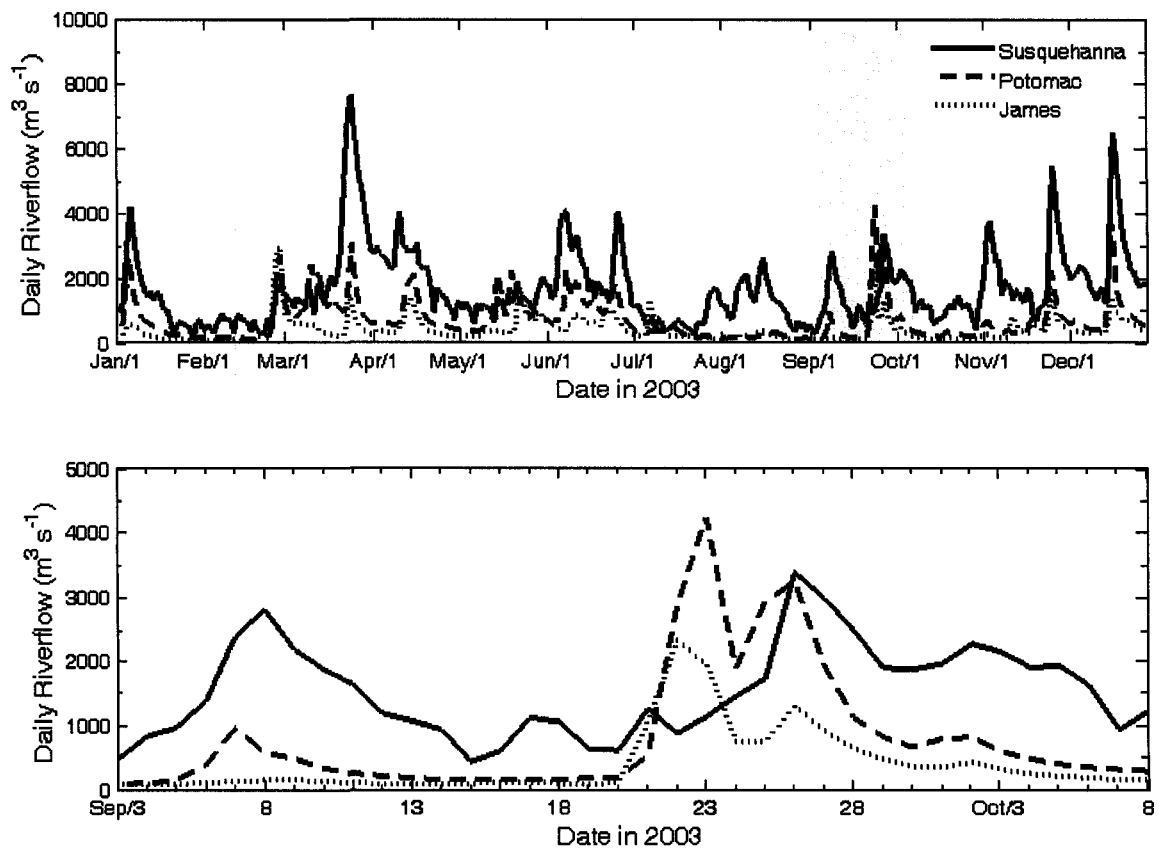


Fig. 2-11 Time series plots of daily riverflow data at three main rivers, Susquehanna, Potomac, and James, in 2003, UTC. The top panel shows the year-long record with the storm event period shaded and the bottom panel shows an expanded view of the discharge record within the storm event period.

Table 2-2 Station Information of USGS daily streamflow data in eight tributaries of the Chesapeake Bay recording maximum values during Hurricanes Floyd (1999) and Isabel (2003).

Station ID	River Name	Coordinates		Maximum (CMS)	
		Latitude(N)	Longitude(W)	Floyd	Isabel
01491000	Choptank River	38° 59' 50"	75° 47' 09"	158	36
01578310	Susquehanna River	39° 39' 28"	76° 10' 28"	1,476	3,380
01594440	Patuxent River	38° 57' 21"	76° 41' 37"	200	139
01646500	Potomac River	38° 56' 59"	77° 07' 40"	403	4,225
01668000	Rappahannock River	38° 18' 30"	77° 31' 46"	49	924
01673000	Pamunkey River	37° 46' 03"	77° 19' 57"	168	315
01674500	Mattaponi River	37° 53' 16"	77° 09' 48"	69	104
02037500	James River	37° 33' 47"	77° 32' 50"	352	2,324

## 2.4 Summary

Five types of dataset observed during two hurricane events have been described. Observed water elevation, water velocity, and salinity data will be used to verify the performance of a hydrodynamic model by comparing with model results in Chapter IV. Wind and atmospheric pressure data will be used for the interpolation method in Section 3.4 to generate the surface boundary forcing in the hydrodynamic models described in Sections 3.2 and 3.3. Daily river discharge data will be used for the river boundary condition in Section 3.3 to generate the buoyancy forcing in the hydrodynamic models. These data suggest that the relationship between winds and storm surges should explain 3 distinguishing stages of the coastal sea state generated by a hurricane (Ochi, 2003): growing (pre-storm) stage, transition (ongoing-storm) stage, and decaying (post-storm) stage. In the growing stage, Ekman transport is initialized by northeasterly winds driving water into the Chesapeake Bay. The maximum surges occurred by easterly winds were dropped quickly by northwesterly winds (Hurricane Floyd) or southerly winds (Hurricane Isabel) in the transition and decaying stages, respectively (Figure 2-12). The detailed mechanism will be discussed in Chapter V.

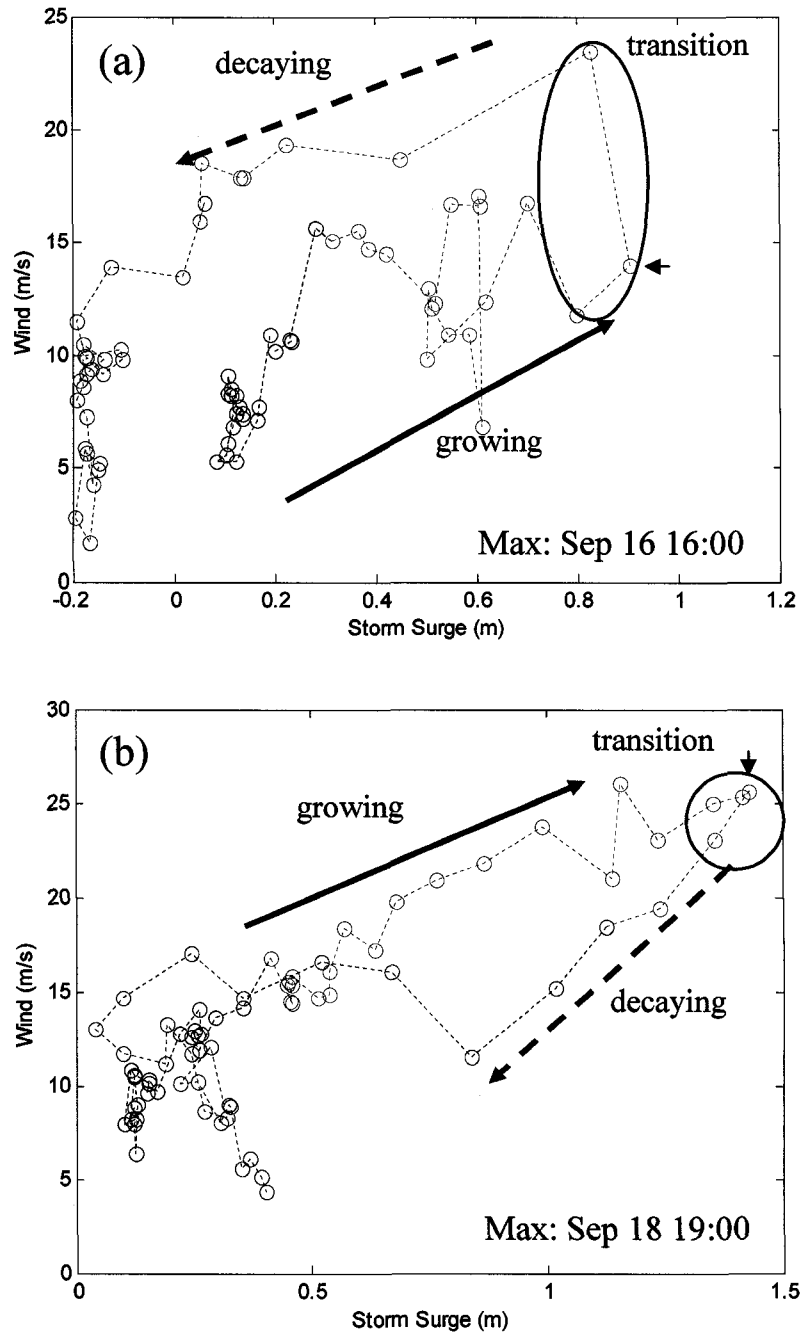


Fig. 2-12 Relationship between wind speed and storm surge at CBBT, VA obtained from NOAA during Hurricane Floyd (a) and Hurricane Isabel (b). Red colors are the day of the surge peak, black colors are the day before the peak day, and blue colors are the day after the peak day. A black arrow denotes the maximum surge.

## **Chapter III**

### **METHODOLOGY:**

### **HYDRODYNAMIC MODELS AND WIND MODEL**

#### **3.1 Introduction**

Two types of numerical models used for understanding hydrodynamics are described in this chapter. The Eulerian-Lagrangian CIRCulation (ELCIRC) model has been developed and released as an open source code. It was thoroughly validated with a number of benchmarks and selected field observations (Zhang et al., 2004; Baptista et al., 2005) and successfully applied to simulate tides and storm surges in the Chesapeake Bay (Wang et al., 2005; Gong et al., 2009). These applications verified that an algorithm of the model with unstructured grids is general and flexible for simulating tides and storm surges. Therefore, ELCIRC has been chosen for simulating barotropic response of the Chesapeake Bay to two hurricane events, Floyd in 1999 and Isabel in 2003. However, Zhang and Baptista (2008) indicated that, for baroclinic simulation, ELCIRC has three main limitations: 1) low-order accurate shape functions in continuity equation, 2) no guarantee of convergence for non-orthogonal grids, and 3) a staircase representation of the bottom in a vertical Z-coordinate system. The semi-implicit Eulerian-Lagrangian finite element (SELFE) overcomes the first two limitations by using a formal Galerkin finite-element framework and partially addresses the third limitation by using a hybrid

SZ-coordinate system vertically (Zhang and Baptista, 2008). They applied SELFE to the Columbia River estuary, and showed that it outperforms ELCIRC in simulating salinities at the observation stations as well as the extent of salinity intrusion. Recently, the baroclinic simulations of SELFE were performed and applied to the Danshuei River estuarine system and adjacent coastal sea in Taiwan (Liu et al., 2008a; Liu et al., 2008b). In addition, to increase the accuracy and stability of vertical turbulence mixing and stratification, SELFE adapted the General Ocean Turbulence Model (GOTM), which had been designed such that it can easily be coupled to three-dimensional circulation models and used as a module for the computation of vertical turbulent mixing (Umlauf and Burchard, 2005; Umlauf et al., 2007). Therefore, SELFE has been selected to simulate baroclinic response of the Chesapeake Bay to the hurricanes. In the following sessions, physical formation of the ELCIRC model (Section 3.2) and the SELFE model (Section 3.3) will be described. Further details of ELCIRC and SELFE beyond the description given above can be found in Zhang et al. (2004) and Zhang and Baptista (2008), respectively.

A parametric wind model is used for generating the meteorological forcing during hurricane events. This wind model has been adapted from the SLOSH (Sea, Lake and Overland Surges from Hurricanes) model developed by the US National Weather Service (Myers and Malkin, 1961; Jelesnianski et al., 1992), and recently successfully applied to hurricane events (Shen et al., 2005; Wang et al., 2005; Shen et al., 2006a; Shen et al., 2006b). The method of generating meteorological forcing will be briefly described in Section 3.4.

## 3.2 ELCIRC model

### 3.2.1 Governing equations

The ELCIRC (Eulerian-Lagrangian CIRCulation) model solves the primitive shallow-water equations using a semi-implicit Eulerian-Lagrangian finite-difference/finite-volume method on unstructured horizontal grids and unstretched vertical grids. The model is governed by a set of six hydrostatic equations based on the Boussinesq approximation with the depth-averaged Navier-Stokes equations, which represent conservations of mass and momentum, and conservations of salt and heat. For the purpose of barotropic simulation, the computations of salt and heat are neglected. The equations are solved for free surface elevation and water velocities in a Cartesian coordinate system with an eastward x-axis, a northward y-axis, and an upward z-axis, written as follows:

$$\frac{\partial u}{\partial x} + \frac{\partial v}{\partial y} + \frac{\partial w}{\partial z} = 0 \quad (3.2.1)$$

$$\frac{\partial \eta}{\partial t} + \frac{\partial}{\partial x} \int_{H_R-h}^{H_R+\eta} u dz + \frac{\partial}{\partial y} \int_{H_R-h}^{H_R+\eta} v dz = 0 \quad (3.2.2)$$

$$\frac{Du}{Dt} = fv - \frac{\partial}{\partial x} \left\{ g(\eta - \alpha\phi) + \frac{P_a}{\rho_0} \right\} + \frac{\partial}{\partial z} \left( K_{mv} \frac{\partial u}{\partial z} \right) + F_{mx} \quad (3.2.3)$$

$$\frac{Dv}{Dt} = -fu - \frac{\partial}{\partial y} \left\{ g(\eta - \alpha\phi) + \frac{P_a}{\rho_0} \right\} + \frac{\partial}{\partial z} \left( K_{mv} \frac{\partial v}{\partial z} \right) + F_{my} \quad (3.2.4)$$

where the symbols denote the following:

t : time [s];

x, y, z : Cartesian coordinates [m];



$\eta(x, y, t)$  : free surface elevation [m], measured relative to MSL in the positive z direction;

$u, v, w$  : Cartesian water velocity components at  $x, y$ , and  $z$ , respectively [m s<sup>-1</sup>];

$H_R$  : z-coordinate at reference level (Mean Sea Level, MSL) [m];

$h(x, y)$  : bathymetric depth [m];

$f$  : Coriolis parameter [s<sup>-1</sup>];

$g$  : acceleration of gravity [m s<sup>-2</sup>];

$\phi$  : tidal potential [m];

$\alpha$  : effective Earth elasticity factor (=0.69) (Schwiderski, 1980);

$P_a(x, y, t)$  : atmospheric pressure at the free surface [N m<sup>-2</sup>];

$K_{mv}$  : Z-component of the vertical eddy viscosity [m<sup>2</sup> s<sup>-1</sup>];

$F_{mx}, F_{my}$  : Horizontal diffusion term for momentum equations [m s<sup>-2</sup>];

These terms will be neglected because those are relatively small to the vertical viscosity terms (Oey et al., 1985).

The differential equation system for Equations (3.2.1) to (3.2.4) is closed with the hydrostatic approximation, appropriate initial and boundary conditions, and eddy viscosity. The water pressure is approximated by the hydrostatic equation:

$$\frac{\partial p}{\partial z} = -\rho_0 g \quad (3.2.5)$$

where  $\rho_0$  is the reference water density. Computed in bars, the pressure is determined by the integration over depth from the level  $z$  to the surface ( $H_R + \eta$ ), which gives:

$$p(z) = 10^{-5} [P_a + \rho_0 g (H_R + \eta - z)] \quad (3.2.6)$$

### 3.2.2 Boundary and initial conditions

#### Vertical boundary conditions

Vertical boundary conditions for horizontal momentum equations are described in this section. At the sea surface, the internal Reynolds stress is balanced by the applied shear stress. A bulk aerodynamic algorithm developed by Zeng et al. (1998) is used to account for ocean surface fluxes under various conditions of stability of the atmosphere. The balance between the internal Reynolds stress and the parameterized surface shear stress is enforced as follows:

$$\rho_0 K_{mv} \left( \frac{\partial u}{\partial z}, \frac{\partial v}{\partial z} \right) = (\tau_{wx}, \tau_{wy}) = \rho_a C_{Ds} |\overline{W}| (W_x, W_y) \quad \text{at } z = H_R + \eta, \quad (3.2.7)$$

where  $\rho_a$  is the air density [ $\text{kg m}^{-3}$ ],  $|\overline{W}| = (W_x^2 + W_y^2)^{1/2}$ ,  $W_x$  and  $W_y$  are the horizontal components of wind velocity at 10 m above the sea surface [ $\text{m s}^{-1}$ ], and  $C_{Ds}$  is the wind drag coefficient based on the following equation (Smith, 1980; Pond and Pickard, 1998):

$$C_{Ds} = 10^{-3} (0.61 + 0.063 |\overline{W}|) \quad \text{if } 6 \leq |\overline{W}| \leq 50 [\text{ms}^{-1}] \quad (3.2.8)$$

with constant  $C_{Ds}$  values outside the range.

At the bottom, the internal Reynolds stress is balanced with the bottom frictional stress varying along spatial and temporal scales with matching velocities at the bottom boundary layer, *i.e.*

$$\rho_0 K_{mv} \left( \frac{\partial u}{\partial z}, \frac{\partial v}{\partial z} \right)_b = (\tau_{bx}, \tau_{by}) = \rho_0 C_{Db} \sqrt{u_b^2 + v_b^2} (u_b, v_b) \quad \text{at } z = H_R - h \quad (3.2.9)$$

where  $C_{Db}$  is the bottom drag coefficient. Typically the coefficients are estimated by the logarithmic law given as follows:

$$C_{Db} = \left( \frac{1}{k} \ln \frac{\delta_b}{z_0} \right)^{-2} \quad (3.2.10)$$

where,  $k$  is the von Karman's constant (0.4),  $\delta_b$  is half the thickness of the bottom computational cell, and  $z_0$  is the local bottom roughness, on the order of 1 cm (Blumberg and Mellor, 1987).

### Coriolis parameter

In the momentum equations, the Coriolis acceleration represents the earth rotation, and the Coriolis parameter,  $f$ , is a sine function of latitude,  $\phi$ :

$$f(\phi) = 2\Omega \sin \phi \quad (3.2.11)$$

where  $\Omega = 7.29 \times 10^{-5} \text{ rad s}^{-1}$  is the angular velocity of the earth rotation. The  $\beta$ -plane approximation is used to minimize coordinate inconsistencies because the governing equations are written in Cartesian coordinates. Hence:

$$f = f_c + \beta(y - y_c) \quad (3.2.12)$$

where  $f_c$  is the Coriolis factor at the mid-latitude ( $y_c$ ) of the domain and  $\beta$  is the local derivative of the Coriolis factor at the same mid-latitude.

### 3.2.3 Method for open boundary conditions

The study area is extended to the 200-m isobath on the continental shelf as an alongshore boundary, and Ocean City Inlet, MD and Cape Hatteras, NC as northern and southern cross-shore boundaries, respectively. Blumberg and Kantha (1985) noticed that a principal difficulty in modeling continental shelf and estuarine circulations is that associated with the correct specification of open boundary conditions because the

observational data are usually insufficient to deduce water elevation, water flow, and baroclinicity along the open boundaries on a synoptic basis. Therefore, the most practical form of open boundary condition on a continental shelf region should be applied to permit the mean sub-tidal and tidal forcings to be prescribed and allow transients generated inside the region to be transmitted outwards.

Although methods used for determining the flow at the open boundary have been proposed for different situations (Palma and Matano, 1998; Palma and Matano, 2000; Blayo and Debreu, 2005), the key problem of open boundary conditions is the successful removal of interior waves without the internal reflection of waves from these boundaries (Grzechnik, 2000). Particularly, two types of barotropic boundary conditions for tidal and sub-tidal (induced by meteorological forcing) flows are considered in this study.

#### Dirichlet-type condition

In the tide simulation, it is sometimes adequate to use a Dirichlet-type (clamped) condition at the open boundary, where the elevation is set to the specific known value as follows:

$$\eta = \hat{\eta} \quad (3.2.13)$$

where  $\hat{\eta}$  is elevation specified at the open boundary. In case of a tide simulation in shallow waters, initial transients are damped by bottom friction and there are no internal flows driven by atmospheric or wind forcing (Bills, 1991). As an open boundary condition for tide elevation, the equilibrium tidal potential is expressed as follows (Reid, 1990):

$$\hat{\psi}(\phi, \lambda, t) = \sum_{n,j} C_{jn} f_{jn}(t_0) L_j(\phi) \cos \left[ \frac{2\pi(t-t_0)}{T_{jn}} + j\lambda + v_{jn}(t_0) \right] \quad (3.2.14)$$

where  $t$  is time relative to  $t_0$  (the reference time),  $C_{jn}$  is a constant characterizing the amplitude of a tidal constituent  $n$  of species  $j$ ,  $f_{jn}$  is the time-dependent nodal factor,  $v_{jn}$  is the time-dependent astronomical argument,  $j = 0, 1, 2$  are the tidal species ( $j=0$  declinational;  $j=1$  diurnal,  $j=2$  semidiurnal),  $L_0 = 3 \sin^2 \phi$ ,  $L_1 = \sin(2\phi)$ ,  $L_2 = \cos^2 \phi$ , and  $T_{jn}$  is the period of a constituent  $n$  for species  $j$ . At the open boundaries, the tidal elevation generated by nine constituents ( $M_2$ ,  $S_2$ ,  $N_2$ ,  $K_1$ ,  $O_1$ ,  $M_4$ ,  $M_6$ ,  $K_2$ , and  $Q_1$ ) are specified. The tidal harmonic constants, which were used to generate the elevation at the open boundary cells, are taken from the World Ocean Tide Model database FES95.2 (Le Provost *et al.*, 1994).

#### Flather-type radiation condition

In case of a storm tide simulation in shallow waters, the Dirichlet-type condition is inadequate as internally generated waves are reflected from the boundary and not allowed to exit from the model domain (Grzechnik, 2000). It is required that a boundary condition radiates outgoing waves to remove internal transients from the model. The extension of a Sommerfeld radiation boundary condition was originally proposed by Flather (1976). A passive radiation condition based on the propagation of a quantity  $\psi$  through a boundary:

$$\frac{\partial \psi}{\partial t} + c \frac{\partial \psi}{\partial n} = 0 \quad (3.2.15)$$

where  $n$  is the outward normal, and  $c$  is a velocity. The Flather-type condition is applied to the free surface elevation ( $\eta$ ), the long wave phase speed ( $c = \sqrt{gH}$ , where  $g$  is a gravitational acceleration and  $H$  is bottom depth), and a one-dimensional approximation of the continuity equations (Carter and Merrifield, 2007):

$$\frac{\partial \eta}{\partial t} + H \frac{\partial U_n}{\partial n} = 0 \quad (3.2.16)$$

which gives

$$\frac{\partial}{\partial n} \left[ U_n - \frac{c}{H} \eta \right] = 0 \quad (3.2.17)$$

Finally, integrating across the boundary gives:

$$U_n = \hat{U}_n \pm \frac{c}{H} (\eta - \hat{\eta}) \quad (3.2.18)$$

where  $\hat{U}_n$  and  $\hat{\eta}$  are normal velocity and surface elevation specified at the open boundary. This is applied at the cross-shore open boundary as generated waves mainly propagate perpendicular to the cross-shore transects. This form was successfully applied to a storm surge model during the Cyclone Disaster in April 1991 in the Northern Bay of Bengal (Flather, 1994) and extensively verified (Nycander and Döös, 2003). The Flather-type condition can be thought of as applying an adjustment to the externally prescribed normal velocity based on the difference between modeled and externally prescribed surface elevation, i.e., a volume error (Carter and Merrifield, 2007). The sign of the adjustment velocity depends on the boundary (positive for north and east boundaries and negative for south and west boundaries).

### Subtidal water elevation

In many coastal ocean models, the effect of the large-scale circulation is introduced by specifying the sub-tidal alongshore pressure gradient (Bishop, 1980; Csanady, 1976; Stommel and Leetmaa, 1972). This gradient represents external forcing from the continental shelf and is presumed to be independent of local forcing and dynamics. It has been proven that wind-induced variations dominate the sub-tidal frequency fluctuations of coastal sea level along the east coast of the United States (Wang, 1979a; Chao and Pietrafesa, 1980). Janowitz and Pietrafesa (1996) developed an analytical model to determine spatial and temporal variations in coastal sea levels for sub-tidal frequency motions. Their solution is based on the balance between the production of relative vorticity by bottom Ekman layer pumping and the topographically induced vertical velocity. They found that an upwelling/downwelling favorable wind stress causes a continual drop/rise in coastal sea level. Their model was successfully applied over the Mid Atlantic Bight from Woods Hole, MA to Cape Hatteras, NC and then to Charleston, SC. Their original steady-state solution for subtidal water elevation is as follows:

$$\begin{aligned} \eta(x, y) = & - T \left\{ \frac{2}{\sqrt{\pi}} y^{1/2} e^{-\zeta^2} - (1+x) \text{Erfc}(\zeta) + e^{(x,y)} \text{Erfc}(\zeta + \sqrt{y}) \right\} \\ & + \eta_{oc} e^{(x+y)} \text{Erfc}(\zeta + \sqrt{y}) \\ & + \int_0^\infty \eta_0(x') \left\{ e^{(x'+x+y)} \text{Erfc} \left( \frac{x+x'}{2\sqrt{y}} + \sqrt{y} \right) + \frac{1}{2\sqrt{\pi y}} \left( e^{-(x-x')^2/4y} - e^{-(x+x')^2/4y} \right) \right\} dx' \end{aligned} \quad (3.2.19)$$

where T is a non-dimensional number containing the wind stress response (= 1),

$$\zeta = x / 2\sqrt{y}, \quad \text{Erfc}(z) = \frac{2}{\sqrt{\pi}} \int_z^\infty e^{-t^2} dt, \quad \eta_0(x) \text{ is the elevations at } y=0, \text{ and } \eta_{oc} \text{ is the}$$

elevation at  $x=0, y=0$ . Physically, the first term on the right hand side results from the fact that the alongshore wind causes cross-shelf flow. The second term is associated with the production of coastal pressure gradients due to  $\eta_{oc}$ . The third term arises from the fact that any vorticity present at the upstream boundary requires a cross-shelf motion, and hence an alongshore change in water level, to balance the bottom friction-induced vertical velocity (Janowitz and Pietrafesa, 1996).

In this study, the coordinate in the alongshore direction needs to be transformed due to the consideration of surge propagation direction. The third term on the right hand side in Eq. (3.2.19) is also neglected by ignoring the vorticity balance. Therefore, since the solution for subtidal sea level has been modified by transforming from the southward positive coordinate system to the northward positive coordinate system (Figure 3-1), new steady-state solution can be derived as follows:

$$\eta(x, y') = -T \left\{ \frac{2}{\sqrt{\pi}} (L/L_y - y)^{1/2} e^{-\zeta^2} - (1+x) \text{Erfc}(\zeta) + e^{(x, L/L_y - y)} \text{Erfc}(\zeta + \sqrt{L/L_y - y}) \right\} + \eta_{oc} e^{(x+L/L_y - y)} \text{Erfc}(\zeta + \sqrt{L/L_y - y}) \quad (3.2.20)$$

where  $L_y$  is along-shelf scale. Then, the form of spatial and temporal variations becomes:

$$\eta^*(x, y', t^*) = \eta_{oc}^*(t^*) A(x, y') - \frac{\tau'^*}{\tau_{y0}} \eta_{ref} B(x, y') \quad (3.2.21)$$

$$A(x, y') = e^{(x+L/L_y - y)} \text{Erfc}(\zeta + \sqrt{L/L_y - y}), \text{ and} \quad (3.2.22)$$

$$B(x, y') = \frac{2}{\sqrt{\pi}} (L/L_y - y)^{1/2} e^{-\zeta^2} - (1+x) \text{Erfc}(\zeta) + e^{(x, L/L_y - y)} \text{Erfc}(\zeta + \sqrt{L/L_y - y}). \quad (3.2.23)$$



where,  $\tau^{*}$  is the alongshore component of observed wind stresses,  $\tau_{y0}$  and  $\eta_{ref}$  are the reference values for wind stress and water elevation at  $x=0$ , which will be used for the calibration. All variables are non-dimensional except the variables that have a superscript (\*), and defined well by Janowitz and Pietrafesa (1996). Figure 3-2 shows the comparison between observed water elevation and calculated water elevation at two stations, Duck, NC and Ocean City Inlet, MD, near the northern and southern open boundaries.

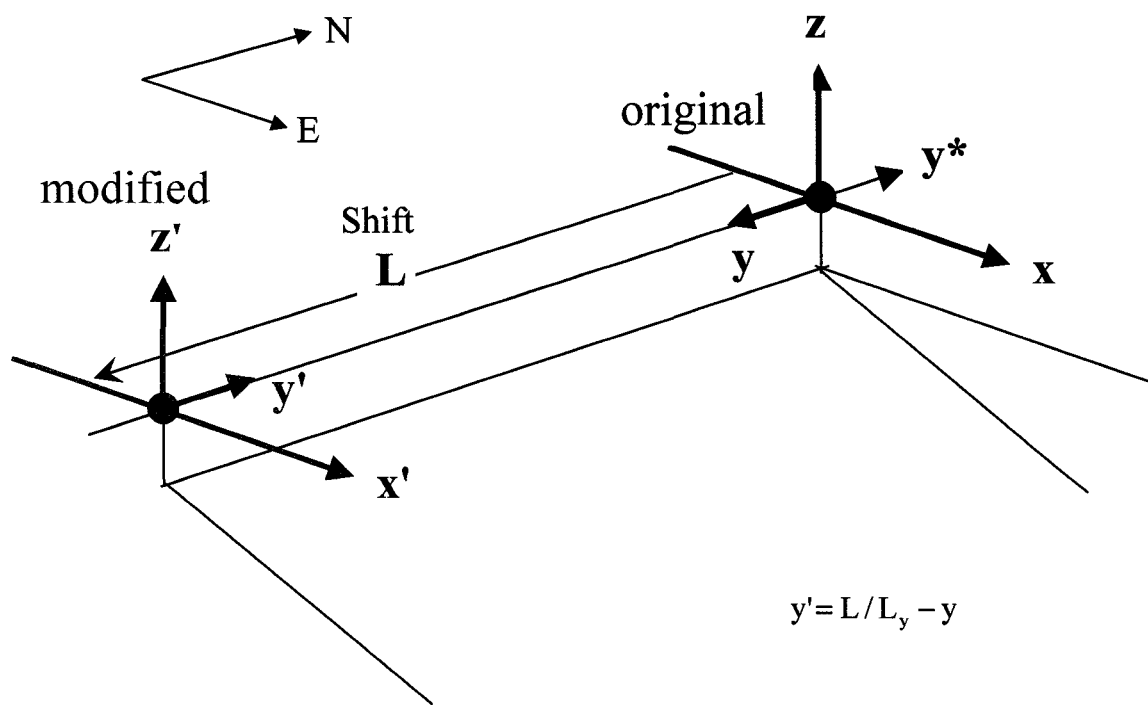


Fig. 3-1 A coordinate system for the generation of subtidal sea surface elevation on open boundaries. The modified coordinate  $(x', y', z')$  are transformed from the original  $(x, y, z)$  described in Janowitz and Pietrafesa (1996). All variables are non-dimensional except the variables that have a superscript (\*).

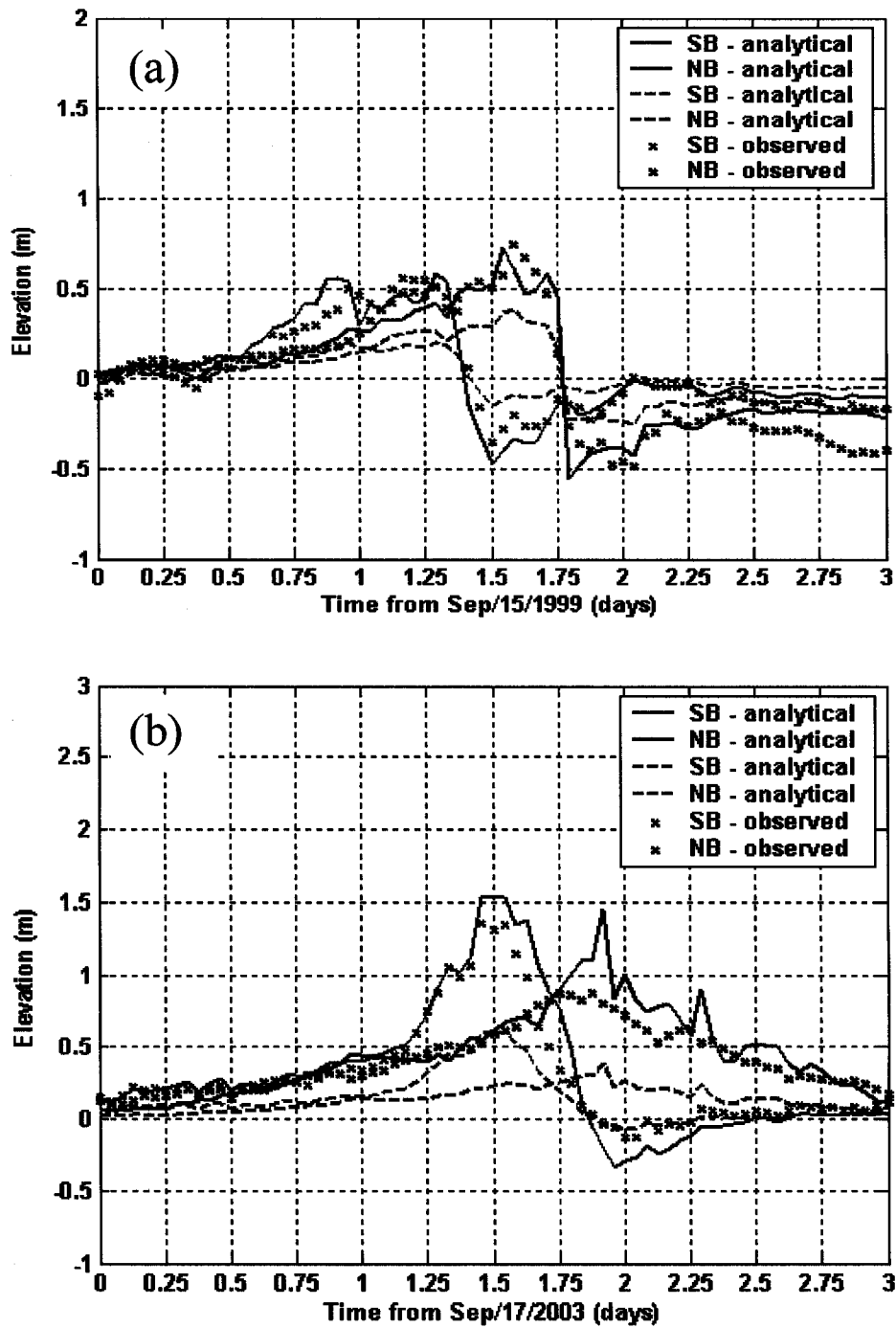


Fig. 3-2 A comparison of subtidal sea surface elevation between observed (x) and calculated (lines) on the southern boundary (SB, red) and northern boundary (NB, blue) during (a) Hurricane Floyd and (b) Hurricane Isabel. The solid lines represent the values for the coastline and the dashed lines represent the values for the 200-m isobath.

### 3.2.4 Model configuration

#### Horizontal grid and vertical grid

The ELCIRC model uses an orthogonal unstructured grid horizontally. The use of an unstructured grid provides flexibilities for coastal modeling such that the resolution of the grid can be increased in areas of interest and decreased over the remaining areas. This increases the accuracy and efficiency of the model. Another main advantage of using an unstructured grid is to resolve complicated geometries and shorelines so that the model calculates mass flux properly. An orthogonal unstructured grid is the most preferred application of unstructured grids. It can be shown, for unstructured grids, that the segment joining the centers of two adjacent elements (or polygons) and the side shared by the two elements (or polygons), have a non-empty intersection and are orthogonal to each other (Figure 3-3; Casulli and Walters, 2000). The element center coincides with the circum-circle center of the element, which is not necessarily the geometric center. Dirichlet triangulation with Voronoi tessellation forms a perfect unstructured orthogonal grid that the boundaries of elements are perpendicular bisectors of the lines joining the neighboring generating points (Weatherill, 1988). The horizontal grid of study area is shown in Figure 3-4, generated by JANET (Java net generator) with checking orthogonality. The grid has 66,802 elements, 40,591 nodes, and 107,419 side faces at the surface.

In the vertical, primitive equations are discretized over variable topography using a z-level grid. A simple finite difference discretization, not necessarily uniform, is adopted along the vertical direction. For the barotropic study, a single depth-integrated layer was used.

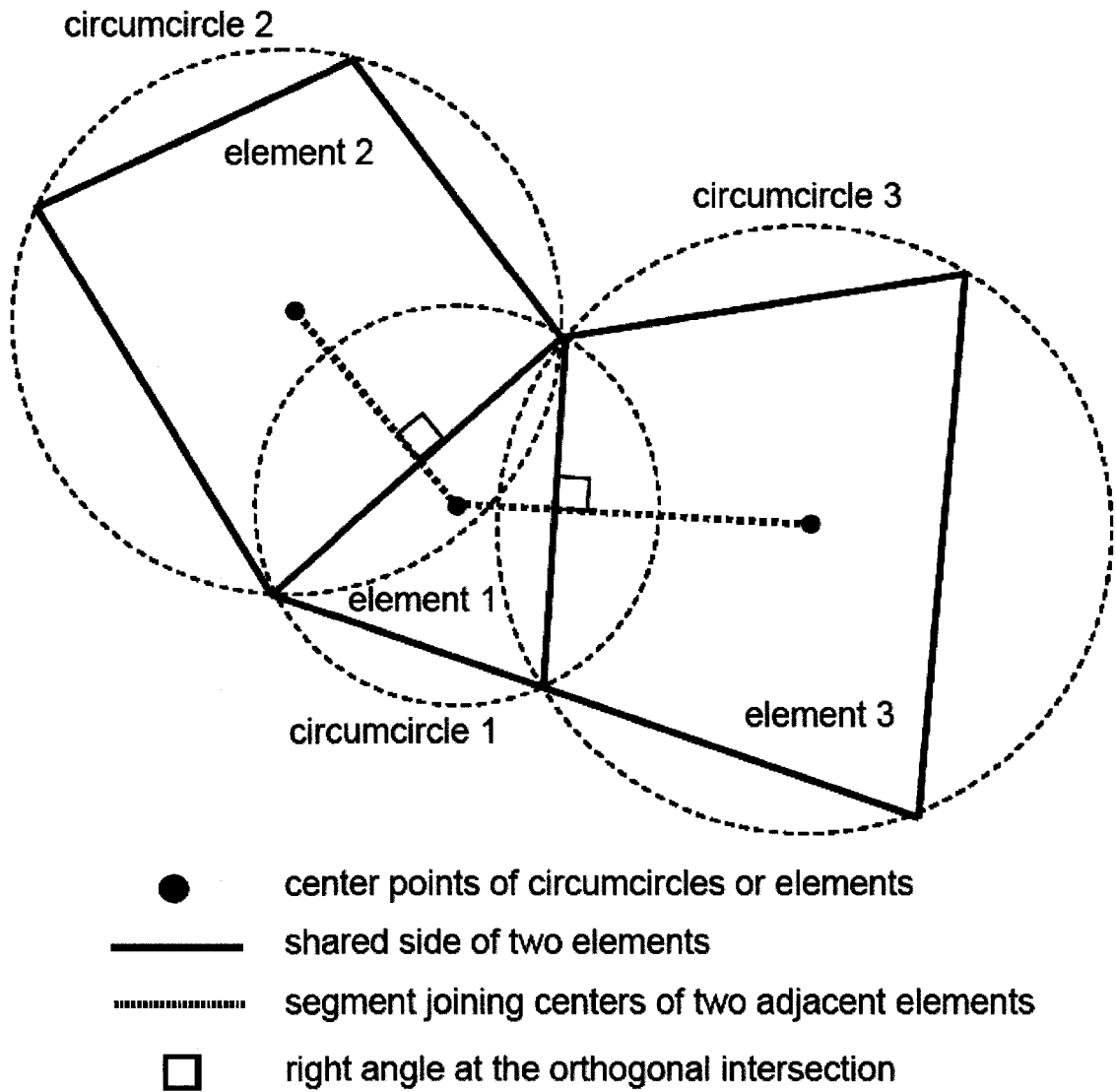


Fig. 3-3 An unstructured orthogonal grid. The side shared by two adjacent elements (blue) and the segment joining their centers (red) should be orthogonal.

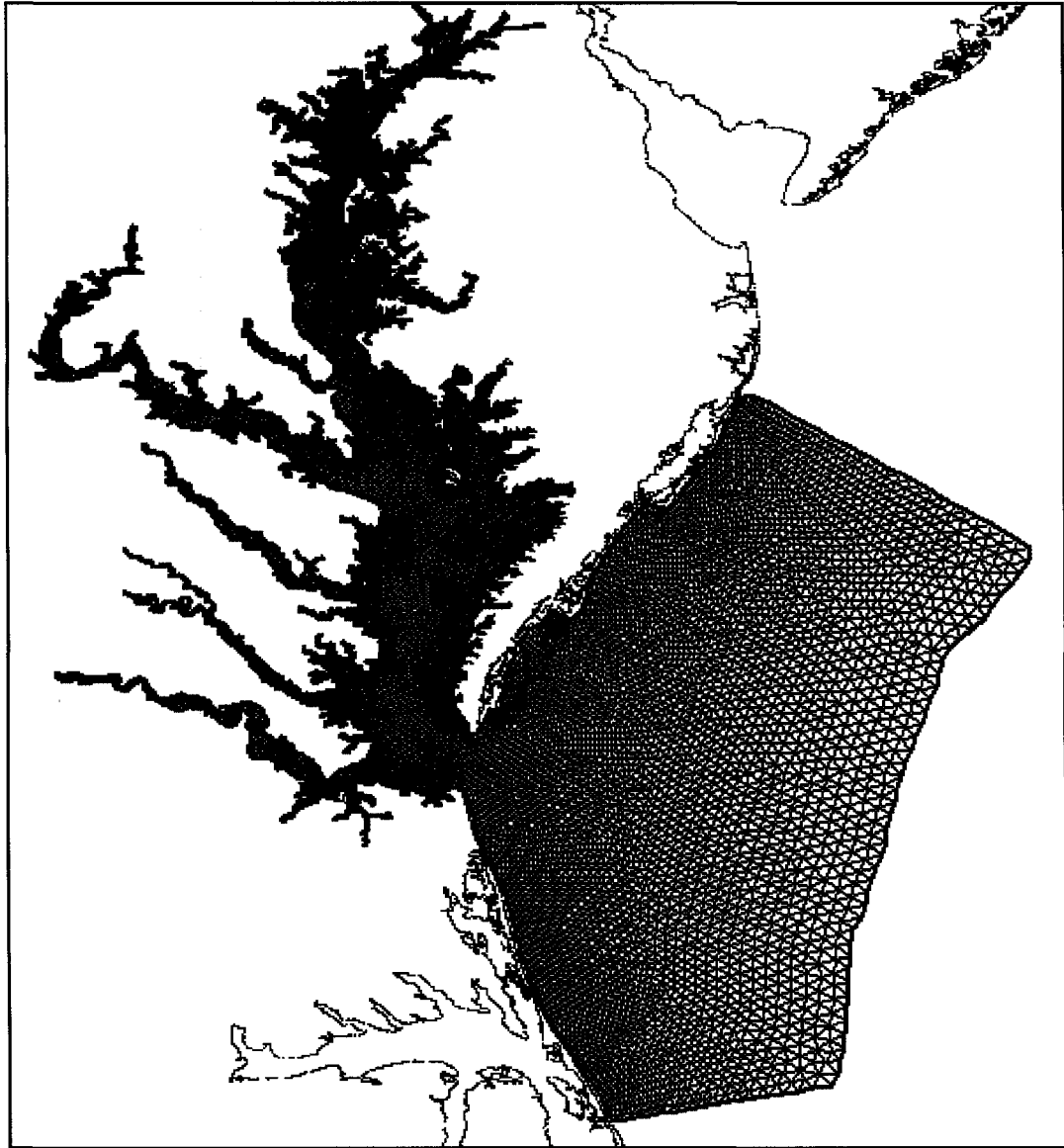


Fig. 3-4 A horizontal grid of the Chesapeake Bay for the ELCIRC model. The grid has 66,802 elements, 40,591 nodes, and 107,419 side faces at the surface.

## Numerical algorithm

The numerical formulation of ELCIRC is detailed in Zhang et al. (2004). The most important features of it are described as follows:

- 1) A semi-implicit scheme is used in all equations to ensure both stability and computational efficiency (Casulli and Cattani, 1994).
- 2) The normal component of horizontal velocity in the momentum equations is solved simultaneously with the depth-integrated continuity equation, while the tangential component is solved with finite differences.
- 3) The vertical velocity is solved from the three-dimensional continuity equation using a finite volume approach.
- 4) The solution for the total derivative in the momentum equations requires backtracking along characteristic lines, which is approximated by the Eulerian-Lagrangian Method.

These features follow those implemented by Casulli and Zanolli (1998) closely except for the computation of tangential velocity component, which improves the representation of Coriolis. The depth-integrated continuity equation and horizontal momentum equations are solved using a local coordinate system and these equations are invariant under a rotation in the (x, y) plane, and thus they retain their form under these local rotations. However, these equations now assure local conservation of normal and tangential momentum, respectively. Local and global volume conservations are imposed by using a semi-implicit finite-volume approach to integrate the continuity equation. A semi-implicit finite difference scheme is used to solve the normal momentum equation for a side of a grid element to increase stability. In the momentum equations, to avoid normal

Courant number constraints by incorporating advection in total derivatives, ELCIRC adapts the Eulerian-Lagrangian method as follows:

$$\frac{dx_i}{dt} = u_i^m(x_1, x_2, x_3, t) \quad \text{with } i = 1, 2, 3, \quad (3.2.25)$$

where  $m$  either represents time step ( $n$ ) or denotes a linear interpolant between the next time step ( $n+1$ ) and the present time step ( $n$ ). Hence, flow fields are always known beforehand. The integral to this method is capable of backtracking characteristic lines efficiently and accurately (e.g., see Oliveira and Baptista, 1998). Backtracking for momentum starts always at side centers. As a compromise between accuracy and computational efficiency, a simple Euler integration is used for backtracking but with a time step smaller than  $\Delta t$ . Also, linear interpolation is chosen at the feet of the characteristic lines for the momentum equations. The advantage of linear interpolation is to avoid numerical oscillations of the solutions but the disadvantage is to introduce numerical diffusion (Baptista, 1987). To reduce numerical diffusion before interpolating, the grid elements are sub-split into four and then used in the solution of the equations. The horizontal grid must thus be refined to reduce numerical diffusion.

ELCIRC follows a natural and robust handling of wetting and drying described in Casulli and Cheng (1992) and Casulli and Zanolli (1998). After all unknowns have been found for time step  $n+1$ , the free-surface indices are updated with the newly computed elevations. Elements become dry if  $h + \eta < h_0$  (a small positive number,  $h_0$ , typically having a value of 0.01 m). It is also noteworthy that the formulation for vertical discretization automatically reduces to the two-dimensional depth-integrated version (Zhang et al., 2004).



### 3.3 SELFE model

#### 3.3.1 Basic equations

The SELFE (Semi-implicit Eulerian-Lagrangian Finite Element) model developed by Zhang and Baptista (2008) is used to investigate the baroclinic response of the Chesapeake Bay to hurricane events. The model is governed by the three-dimensional shallow-water equations with the Boussinesq approximation, and transport equations for salt and heat. The equations are solved for free surface elevation, water velocities, salinity and temperature of the water in a Cartesian coordinate system that has an eastward x-axis, a northward y-axis, and an upward z-axis, written as follows (Zhang and Baptista, 2008):

$$\nabla \cdot \bar{\mathbf{u}} + \frac{\partial w}{\partial z} = 0 \quad (3.3.1)$$

$$\frac{\partial \eta}{\partial t} + \nabla \cdot \int_{-h}^{\eta} \bar{\mathbf{u}} dz = 0 \quad (3.3.2)$$

$$\begin{aligned} \frac{D\bar{\mathbf{u}}}{Dt} = & \bar{\mathbf{f}} - g\nabla\eta + \alpha g\nabla\phi - \frac{1}{\rho_0} \nabla p_A \\ & + \frac{\partial}{\partial z} \left( \nu \frac{\partial \bar{\mathbf{u}}}{\partial z} \right) - \frac{g}{\rho_0} \int_z^{\eta} \nabla \rho d\zeta + \nabla \cdot (\mu \nabla \bar{\mathbf{u}}) \end{aligned} \quad (3.3.3)$$

$$\frac{DS}{Dt} = \frac{\partial}{\partial z} \left( \kappa \frac{\partial S}{\partial z} \right) + F_s \quad (3.3.4)$$

$$\frac{DT}{Dt} = \frac{\partial}{\partial z} \left( \kappa \frac{\partial T}{\partial z} \right) + \frac{\dot{Q}}{\rho_0 C_p} + F_h \quad (3.3.5)$$

where

t : time [s];

x, y, z : Cartesian coordinates [m];

- $\eta(x, y, t)$ : free surface elevation [m];
- $\nabla$ : horizontal gradient  $\left( \frac{\partial}{\partial x}, \frac{\partial}{\partial y} \right)$  [ $\text{m}^{-1}$ ];
- $\bar{u}$ : Cartesian horizontal water velocity components (u, v) [ $\text{m s}^{-1}$ ];
- w: vertical velocity [ $\text{m s}^{-1}$ ];
- h(x, y): bathymetric depth [m];
- f: Coriolis parameter [ $\text{s}^{-1}$ ];
- g: acceleration of gravity [ $\text{m s}^{-2}$ ];
- $\phi$ : tidal potential [m];
- $\alpha$ : effective Earth elasticity factor (0.69) (Schwiderski, 1980);
- $\rho(x, y, t)$ : water density [ $\text{kg m}^{-3}$ ];
- $p_A(x, y, t)$ : atmospheric pressure at the free surface [ $\text{N m}^{-2}$ ];
- S, T: salinity and temperature of the water (psu,  $^{\circ}\text{C}$ )
- $\nu, \mu$ : vertical eddy viscosity and horizontal eddy viscosity [ $\text{m}^2 \text{s}^{-1}$ ];
- $\kappa$ : vertical eddy diffusivity, for salt and heat [ $\text{m}^2 \text{s}^{-1}$ ];
- $F_s, F_h$ : horizontal diffusion term for transport equations [ $\text{ppt s}^{-1}, ^{\circ}\text{C s}^{-1}$ ];  
These terms will be neglected because those are relatively small to the vertical diffusion terms (Oey et al., 1985).
- $\dot{Q}$ : rate of absorption of solar radiation [ $\text{W m}^{-1}$ ];
- $C_p$ : specific heat of water [ $\text{J kg}^{-1} \text{K}^{-1}$ ].

The differential equation system for Equations (3.3.1) to (3.3.5) is closed with the hydrostatic approximation [Eq. (3.2.5)], equation of state, parameterizations for horizontal and vertical mixing via turbulence closure equations, and appropriate initial and boundary conditions.

### 3.3.2 Turbulence closure model

SELFE adapts the Generic Length Scale (GLS) turbulence closure through the General Ocean Turbulence Model (GOTM) suggested by Umlauf and Burchard (2003; 2005), taking the advantages from most of the level 2.5 closure schemes [k-ε (Rodi, 1984); k-ω (Wilcox, 1998); Mellor and Yamada, 1982]. Basically, the equations of the turbulent kinetic energy (K) and of a generic length-scale variable (ψ) for transport, production, and dissipation are expressed by:

$$\frac{DK}{Dt} = \frac{\partial}{\partial z} \left( v_k^\psi \frac{\partial K}{\partial z} \right) + vM^2 + \mu N^2 - \varepsilon \quad (3.3.6)$$

$$\frac{D\psi}{Dt} = \frac{\partial}{\partial z} \left( v_\psi \frac{\partial \psi}{\partial z} \right) + \frac{\psi}{K} (c_{\psi 1} vM^2 + c_{\psi 3} \mu N^2 - c_{\psi 2} F_w \varepsilon) \quad (3.3.7)$$

where

$v_k^\psi, v_\psi$  : vertical turbulent diffusivities;

$c_{\psi 1}, c_{\psi 2}, c_{\psi 3}$  : model-specific constants (Umlauf and Burchard, 2003; Zhang et al., 2004);

$F_w$  : wall proximity function;

M, N: shear and buoyancy frequencies;

$\varepsilon$  : dissipation rate.

The generic length-scale is defined as

$$\psi = (c_\mu^0)^p K^m \ell^n \quad (3.3.8)$$

where  $c_\mu^0 = \sqrt{0.3}$ ,  $\ell$  is the turbulence mixing length, p, m, and n are constants to choose the different closure models. Therefore, vertical viscosities and diffusivities can be expressed by K,  $\ell$ , and stability functions are defined as follows:  $\nu = \sqrt{2} s_m K^{1/2} \ell$ ,

$\mu = \sqrt{2} s_h K^{1/2} \ell$ ,  $v_k^\psi = \frac{v}{\sigma_k^\psi}$ , and  $v_\psi = \frac{v}{\sigma_\psi}$ , where  $\sigma_k^\psi$  and  $\sigma_\psi$  are the Schmidt numbers,

and stability functions,  $s_m$  and  $s_h$ , are given by an Algebraic Stress Model (Kantha and Clayson, 1994; Canuto et al., 2001; Galperin et al., 1988). Dirichlet-type boundary conditions are used for specifying  $K$  and  $\ell$  at the free surface and the bottom as follows:

$$K = \frac{1}{2} B_1^{2/3} |\tau_b|^2, \ell = \kappa_0 d_b \text{ at } z = -h, \text{ and } \ell = \kappa_0 d_s \text{ at } z = \eta, \text{ where } \tau_b \text{ is a bottom}$$

frictional stress,  $\kappa_0$  is the von Karman's constant ( $= 0.4$ ),  $B_1$  is a constant, and  $d_b$  and  $d_s$  are the distances to the bottom and the free surface, respectively. The further description of the turbulence closure model in SELFE is detailed in Zhang and Baptista (2008).

### 3.3.3 Boundary and initial conditions

In SELFE, for vertical boundary conditions in horizontal momentum equations, Coriolis parameter, and barotropic boundary conditions, the same conditions are used as those described in Sections 3.2.2. However, the conditions for salinity and temperature must be specified.

#### Salinity

The Chesapeake Bay Program (CBP) has provided the vertical profiles of observed salinity in the Bay proper and its tributaries from 1984 to the present. In the Bay mainstem, salinity is monitored at 49 stations and sampled once each month during the late fall and winter months and twice each month in the warmer months at approximately 1-m to 2-m intervals (CBP, 1993). For outside the Bay, including the continental shelf region, salinity data are provided by the CORIOLIS Data Center (<http://www.coriolis.eu.org>). Salinity profiles from Argo profilers or oceanographic

vessels (XBT, CTD) are collected and controlled in real time by CORIOLIS. Using the salinity profiles from the CORIOLIS data base, real time weekly analysis is performed once a week. The fields are objectively analyzed on a grid with one-third-degree resolution in latitude and longitude at 57 levels in the vertical to 2000 m in the Atlantic Ocean. Salinity fields are performed by using the objective analysis method (Bretherton et al., 1976). Thus, using the vertical profiles of salinity at all available stations and grid points, initial conditions can be generated at each vertical layer and linearly interpolated in space. The Surface-water Modeling System (SMS) software is incorporated with this interpolation method. Spatially and temporally linearly-interpolated CORIOLIS salinities are imposed as open boundary conditions.

### Temperature

Temperature is kept constant because it can be shown that salinity in estuaries is a more dominant influence on water density than temperature, although vertical temperature stratification tends to reinforce density stratification by 9 % in severe conditions (Goodrich et al., 1987). As for initial and open boundary conditions, temperature is set to a constant value of 15 °C throughout space and time.

### Freshwater inflows

The Chesapeake Bay receives freshwater inflow from eight major rivers and from more than 150 creeks (Krome and Corlett, 1990). Since most of these creeks are ungaged and small, we can only account for freshwater measurements from the major rivers including the Susquehanna River (at the head of the Bay), the Patuxent, Potomac,

Rappahannock, Mattaponi, Pamunkey and James Rivers on the Western Shore, and the Choptank River on the Eastern Shore. Freshwater inflow records are provided by USGS (<http://waterdata.usgs.gov/nwis>). For the two years of interest, 1999 and 2003, daily mean freshwater inflows of the Susquehanna, Potomac and James Rivers are shown in Figures 2-6 and 2-11, respectively. River inflows are considered at 8 tributaries of the Chesapeake Bay as described in Table 2-2 with settings of 0 ppt of salinity and 15 °C of temperature as constants in time.

### 3.3.4 Model configuration

#### Horizontal and vertical grids

Horizontally, unstructured triangular grids are used in SELFE. Unlike what is described in ELCIRC, the orthogonality of the horizontal grid is not necessary since finite-element discretization is used. The generation of the horizontal grid is made by the SMS software. The connectivity of the grid is defined as follows: the three sides of an element  $I$  are enumerated as  $js(i,l)$  ( $l=1,2,3$ ). The surrounding elements of a particular node  $I$  are enumerated as  $ine(i,l)$  ( $l=1,2,\dots,nne(i)$ ), where  $nne(i)$  is the total number of elements inside the “ball” of the node. The horizontal grid used is shown in Figure 3-5, which has 20,784 elements, 11,582 nodes, and 32,386 sides on the surface. At least 3 horizontal grid cells resolve the channel of the main Bay. Although a more refined grid would sufficiently reduce numerical diffusion, computational efficiency should be considered as well because time step must be reduced as the grid becomes more refined.

In the vertical direction, SELFE uses hybrid-vertical coordinates, which means partly terrain-following S-coordinates and partly Z-coordinates (Figure 3-6a). The

terrain-following S layers are placed on top of a series of Z layers. The hybrid vertical coordinate system has the benefits of both S- and Z-coordinates: the S layers used in the shallow region resolve the bottom efficiently and the Z layers, which are only used in the deep region, fend off the hydrostatic inconsistency (Zhang and Baptista, 2008). The vertical grid used in the domain is shown in Figure 3-6b, which has 20 layers in S-coordinates and 10 layers in Z-coordinates. The 20 layers in S-coordinates cover the entire shallow region up to 43-m depth and the 10 layers in Z-coordinates cover from 43 m to 200 m in depth.

### Numerical algorithm

Numerical algorithm of SELFE is well described in Zhang and Baptista (2008).

The main features of SELFE are described as follows:

- 1) The model solves the differential equation system with finite-element and finite-volume schemes, with a semi-implicit method.
- 2) It uses the Eulerian-Lagrangian method (ELM) to treat the advection in the momentum equations.
- 3) It treats the advection terms in the transport equations with either the ELM, the finite-volume upwind method (FVUM), or the total variation diminishing (TVD) scheme.

SELFE solves the barotropic pressure gradient term in the momentum equation first with semi-implicit schemes and the baroclinic pressure gradient term explicitly. Due to the hydrostatic approximation, the vertical velocity is solved from Eq. (3.3.1) after the horizontal velocity is determined. The continuity equation discretized in finite-element

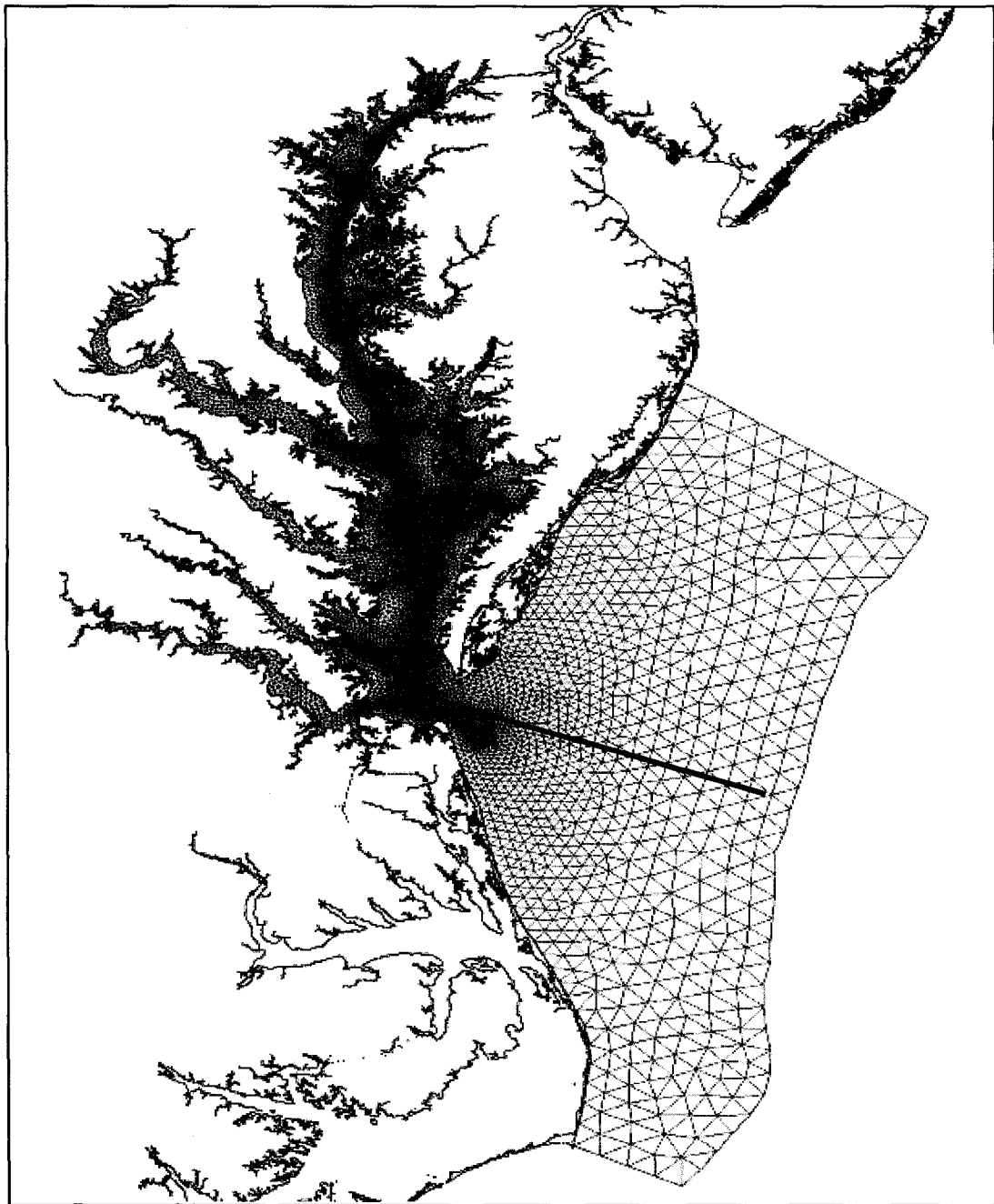


Fig. 3-5 A horizontal grid of the Chesapeake Bay for the SELFE model. The grid has 20,784 elements, 11,582 nodes, and 32,386 sides at the surface.



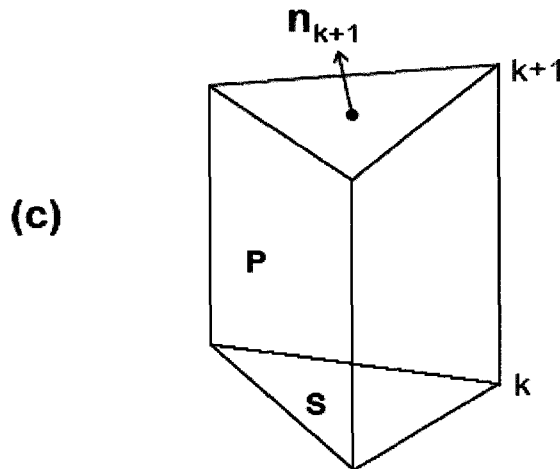
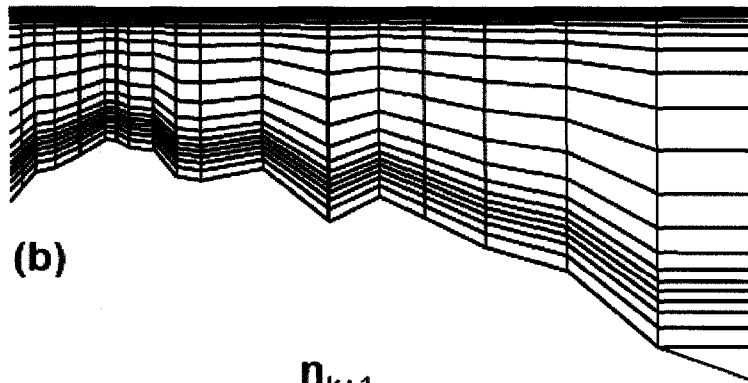
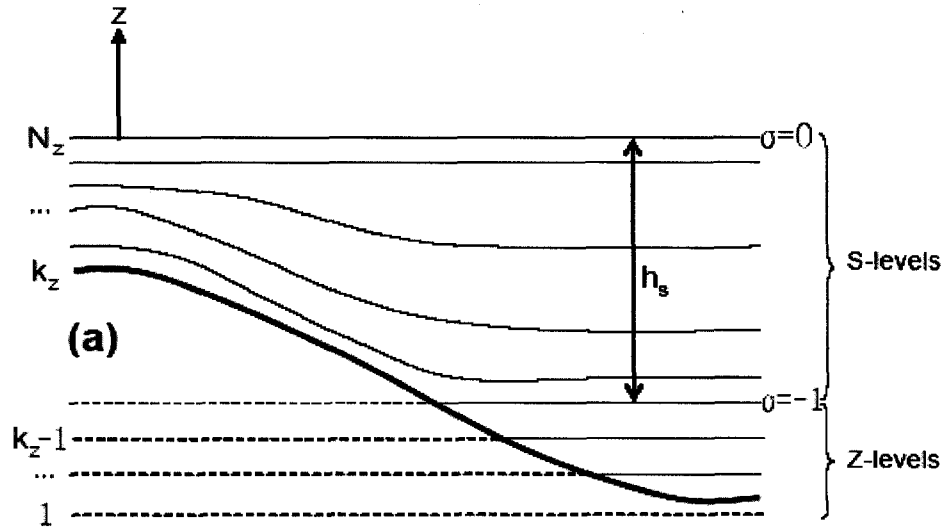


Fig. 3-6 A vertical grid of hybrid coordinate system used in the SELFE model: (a) a schematic view, (b) vertical view of the discretized model grid along the transect in Fig. 3-5, and (c) a unit of computational triangular prism with uneven bottom and top surfaces.

framework is solved in the weak form of a Galerkin weighted residual statement. In SELFE, linear shape functions are used as weighted functions. Since SELFE uses linear shape functions for the elevations, the two components of the horizontal velocity are solved from the momentum equation independently from each other after the elevations are found. This application is different from that used in ELCIRC. After the elevations are found at all nodes, SELFE solves the momentum Eq. (3.3.3) along each vertical column at side centers. A semi-implicit Galerkin finite-element method is used, with the pressure gradient and the vertical viscosity terms being treated implicitly, and other terms treated explicitly. After the velocities at all sides are determined, the velocity at a node is computed by a weighted average of all surrounding sides in its ball, evaluated by proper interpolation in the vertical. As an averaging procedure, the velocity at a node is computed within each element from the three sides using the linear shape function and is kept discontinuous between elements. Since this approach leads to parasitic oscillations, a Shapiro filter (Shapiro, 1970) can be used to suppress the noise. To solve the vertical velocity, finite-volume method is applied to a typical prism, as depicted in Figure 3-6c, because it serves as a diagnostic variable for local volume conservation when a steep slope is present (Zhang et al., 2004). The vertical velocity is then solved from the bottom to the surface, in conjunction with the bottom boundary condition  $(u,v,w) \cdot n = 0$ . The closure error between the calculated  $w$  at the free surface and the surface kinematic boundary condition is an indication of the local volume conservation error (Luettich et al., 2002). Because the primitive form of the continuity equation is solved in the model, this closure error is generally negligible.

SELFE treats the advection in the transport equations with three selectable methods as follows: 1) ELM, 2) FVUM, and 3) TVD. If the ELM is used, the transport equations are solved at nodes and side centers along each vertical column using a finite-element method, with the lumping of the mass matrix to minimize numerical dispersion. Since linear interpolation used in ELM leads excessive numerical diffusion, element-splitting or quadratic interpolation is used in ELM to reduce the numerical diffusion (Zhang et al., 2004; Zhang and Baptista, 2008). FVUM and the TVD scheme both guarantee mass conservation because the scalar variables (salinity or temperature) are defined at the center of a prism, which has five exterior faces (top and bottom, and three vertical faces). In FVUM, upwind scheme is used for horizontal advective fluxes. Thus the stability condition needs for the upwind scheme, the Courant number restriction, is given by:

$$\Delta t \leq \frac{V_{i,k}}{\sum |q_j|} \quad (3.3.9)$$

where  $V_{i,k}$  is the volume of the prism,  $q_j$  is all outflow horizontal advective fluxes,  $i$ ,  $j$ , and  $k$  are indices for elements, sides, and vertical layers, respectively. Despite the fact that the discretized transport equations do not conform to the depth-integrated continuity equation, the FVUM guarantees mass conservation. A higher-order finite-volume TVD scheme is a preferable option in SELFE. TVD is the technique of obtaining high resolution, second-order, oscillation free, explicit scalar difference schemes, by the addition of a limited anti-diffusive flux to a first-order scheme (Sweby, 1984). Osher (1984) defined the flux differences for a general three-point E-scheme, which is a class of

semi-discrete schemes approximating in the scalar conservation law. These flux differences are used to define a series of local Courant-Friedrichs-Levy (CFL) numbers.

### 3.4 Generation of meteorological forcing

#### 3.4.1 Analytical wind model for hurricane events

For the hurricane events, the wind and atmospheric pressure fields were generated by a parametric wind model used in SLOSH (Myers and Malkin, 1961; Jelesnianski et al., 1992). Based on the main hurricane parameters (i.e., hurricane path, atmospheric pressure drop, and radius of maximum wind speed), the model calculates wind speed, wind direction, and air pressure in the pattern of a circularly symmetric, stationary storm. Basically, tangential forces along a surface wind trajectory are balanced by normal forces to a surface wind trajectory. The governing equations in the polar coordinate system can be described as follows:

$$\frac{1}{\rho_a} \frac{\partial p}{\partial r} = \frac{k_s V^2}{\sin \theta} - V \frac{\partial V}{\partial r} \quad (3.4.1)$$

$$\frac{1}{\rho_a} \frac{\partial p}{\partial r} \cos \theta = fV + \frac{V^2}{r} \cos \theta - V^2 \frac{\partial \theta}{\partial r} \sin \theta + k_n V^2 \quad (3.4.2)$$

$$V(r) = V_M \frac{2(R_M)r}{R_M^2 + r^2} \quad (3.4.3)$$

where

$r$  : distance from the storm center (origin) [m];

$\theta$  : angle normal to isobars from the  $0^\circ$  ray toward the storm center  
[degree];

$p(r)$  : air pressure [ $\text{N m}^{-2}$ ];

- $\rho_a$ : air density [ $\text{kg m}^{-3}$ ];
- $V$ : wind speed [ $\text{m s}^{-1}$ ];
- $f$ : Coriolis parameter [ $\text{s}^{-1}$ ];
- $k_s, k_n$ : friction coefficient for tangential and normal directions,  
respectively [ $\text{m}^{-1}$ ];
- $V_M$ : maximum wind speed [ $\text{m s}^{-1}$ ];
- $R_M$ : radius of maximum wind speed [m].

The angle  $\theta$  represents the counterclockwise angle from the  $0^\circ$  ray of the polar axis (known as the positive x-axis in the Cartesian coordinate plane). The friction coefficients were determined based on historical hurricane simulations conducted by SLOSH. The profile of wind speed,  $V(r)$ , has a stationary, circularly symmetric pattern. Dynamically, the moving speed of storm is estimated by hourly hurricane track. Usually, the radius of maximum pressure gradient ( $R_p$ ) does not coincide with the radius of maximum wind speed (Holland, 1980). The ratio is defined as follows:

$$R_p / R_M = [B / (B + 1)]^{1/B} \quad (3.4.4)$$

where  $B$  is the scaling parameter determining the shape of the wind profile. Holland (1980) suggested that  $B$  lies between 1 and 2.5 reasonably for hurricanes. The detailed applications of this method can be found in Shen et al. (2006b) and Wang et al. (2005).

### 3.4.2 Data interpolation

The analytical wind model described above requires three parameters such as hurricane path, atmospheric pressure drop, and radius of maximum wind speed. This model is useful during the hurricane events but not applicable to normal weather

conditions. To generate atmospheric forcing with normal weather conditions, an interpolation method is applied by using the data measured at 13 stations as described in Chapter II (see Figure 2-1). The following section will describe the interpolation method used in this study.

### Inverse distance weighted interpolation

One of the most commonly used techniques for interpolation of scatter points is the inverse distance weighted (IDW) interpolation method. The IDW interpolation is based on the assumption that the interpolating surface should be influenced more by nearby points and less by more distant points. The interpolating surface is a weighted average of the scatter points and the weight assigned to each scatter point diminishes as the distance from the interpolation point to the scatter point increases. The Shepard's Method is the simplest form of IDW interpolation (Shepard, 1968). The equation used is as follows:

$$F(x, y) = \sum_{i=1}^n w_i f_i \quad (3.4.4)$$

where  $n$  is the number of scatter points in the dataset,  $f_i$  are the prescribed function values at the scatter points (e.g., the dataset values), and  $w_i$  are the weight functions assigned to each scatter point. The weight function used in the method is described as follows (Franke and Nielson, 1980):

$$w_i = \frac{\left[ \frac{R - h_i}{Rh_i} \right]^2}{\sum_{j=1}^n \left[ \frac{R - h_j}{Rh_j} \right]^2} \quad (3.4.5)$$

where

$$h_i = \sqrt{(x - x_i)^2 + (y - y_i)^2} \quad (3.4.6)$$

is the distance from the interpolation point  $(x, y)$  to scatter point  $(x_i, y_i)$ ,  $R$  is the distance from the interpolation point to the most distant scatter point, and  $n$  is the total number of scatter points.

## Chapter IV

### MODEL CALBRATIONS

#### 4.1 Introduction

Simulations using two hydrodynamic models and an analytical wind model described in Chapter III were conducted to examine the responses of the Chesapeake Bay to hurricane events. Prior to investigating the Bay's responses, one should address how well the models reproduce the observed circulation in the Bay during these events. The comparison will involve surface elevation, current, and salinity observations at the locations shown in Figure 2-1. The first level of model/data comparison is with the use of visual techniques. Plots of the time series of the comparison between the predicted values versus the observed values will be provided in support of that purpose (Krome and Corlett, 1990). The procedure used to quantitatively evaluate the performance of the models is based upon computing the mean absolute root mean square error (RMSE) as defined:

$$\text{RMSE} = \sqrt{\frac{1}{N} \sum_{i=1}^N (P_i - O_i)^2} \quad (4.1)$$

and the mean absolute relative error (ARE) defined as follows:

$$\text{ARE} = \frac{1}{N} \sum_{i=1}^N \left( \left| \frac{P_i - O_i}{O_i} \right| \right) \times 100(\%) \quad (4.2)$$



where  $0 \leq ARE \leq 100(\%)$ ,  $P_i$  is the model prediction at location (or time)  $i$  while  $O_i$  is the corresponding observed value at  $i$ . Krome and Corlett (1990) and Park et al. (2005) have shown that the use of Eqs. (4-1) and (4-2) provide an objective and meaningful description of a model's ability to reproduce reliable observations, respectively. Tidal and subtidal values will also be subjected to these analysis procedures. The barotropic and baroclinic calibrations for two hydrodynamic models, ELCIRC and SELFE, will be described in Sections 4.2 and 4.3, respectively.

## **4.2 Barotropic simulation**

Using a two-dimensional (2D) barotropic model, ELCIRC, tidal surface elevation was calibrated with the bottom drag coefficient described in Section 3.2. Although Spitz and Klink (1998) found that the drag coefficient varies between  $2.5 \times 10^{-4}$  and  $3.1 \times 10^{-3}$  with time, the drag coefficient for ELCIRC varies not with time but with space since the Bay's responses are more focused on subtidal characteristics. Subtidal surface elevation was verified with subtidal forcing (e.g., atmospheric forcing, river discharge, and the Earth's rotation) during two hurricane events, Hurricane Floyd in 1999 and Hurricane Isabel in 2003.

### **4.2.1 Astronomical tides**

The ELCIRC model was calibrated with respect to the bottom frictional coefficient by simulating mean tide characteristics. The open boundary conditions in ELCIRC were specified using the harmonic constants of nine constituents ( $M_2$ ,  $S_2$ ,  $N_2$ ,  $K_1$ ,  $O_1$ ,  $M_4$ ,  $M_6$ ,  $K_2$ , and  $Q_1$ ) as described in Section 3.2.3. In order to calibrate the

astronomical tides, model results were selected for the last 30 days of the 60-day model run. Table 4-1 lists the comparison of observed and predicted mean tidal ranges at the tidal stations along the west and east sides of the Chesapeake Bay mainstem. Modeled mean tidal ranges at 21 stations reproduced the tidal ranges from the NOAA Tide Tables with great accuracy (Figure 4-1). The Chesapeake Bay has the tidal characteristics of a reflected, damped Kelvin wave, with a larger tidal range on the Eastern Shore (Hicks, 1964; Carter and Pritchard, 1988; Zhong and Li, 2006). The mean tidal range decreases from 0.9 m at the Bay's entrance to a minimum of 0.27 m from Plum Point to Annapolis, MD, and then increases to 0.55 m at Havre de Grace, MD, located near the head of the Bay. The model reproduced these characteristics properly. For four major constituents ( $M_2$ ,  $S_2$ ,  $N_2$ , and  $K_1$ ), harmonic analysis was conducted using long-term tidal records at eleven NOAA tidal gauge stations described Tables 4-2a and 4-2b, and the correlation plots of mean tidal amplitudes and phases are shown in Figure 4-2. The model results have a high correlation with observed values and show low errors. Especially, the most dominant constituent  $M_2$  has an ARE value of 4.1 % and an RMSE value of 1.6 cm. A round-off error of a small amplitude (e.g.,  $S_2$ ,  $N_2$ , or  $K_1$ ) may cause a relatively high value of the ARE. The results show that the ELCIRC model is capable of reproducing tidal dynamics not only for the amplitude, but also for the propagation (phase), of tidal waves throughout the Chesapeake Bay.

Table 4-1 Comparison of observed and predicted mean tidal ranges at 21 tidal stations.

West Side			East Side		
STATION	OBS (m)	PRE (m)	STATION	OBS (m)	PRE (m)
Havre de Grace	0.550	0.620	Havre de Grace	0.550	0.620
Battery Pt.	0.370	0.440	Queenstown	0.400	0.440
Baltimore	0.340	0.413	Woolford	0.430	0.394
Annapolis	0.270	0.320	Chance, MD	0.670	0.652
Galesville	0.270	0.307	Crisfield, MD	0.610	0.607
Plum Point	0.270	0.280	Pungoteague	0.520	0.560
Solomon's Is.	0.370	0.355	Nassawadox	0.550	0.549
St. Mary's C	0.460	0.450	Old Plantation	0.730	0.695
Smith Pt. Lt.	0.370	0.390	Fisherman's Is.	0.910	0.931
Windmill Pt.	0.370	0.332			
Yorktown	0.730	0.620			
Newport News	0.790	0.721			
Cape Henry	0.850	0.833			
ARE (%)		10.5			5.5
RMSE (m)		0.054			0.036

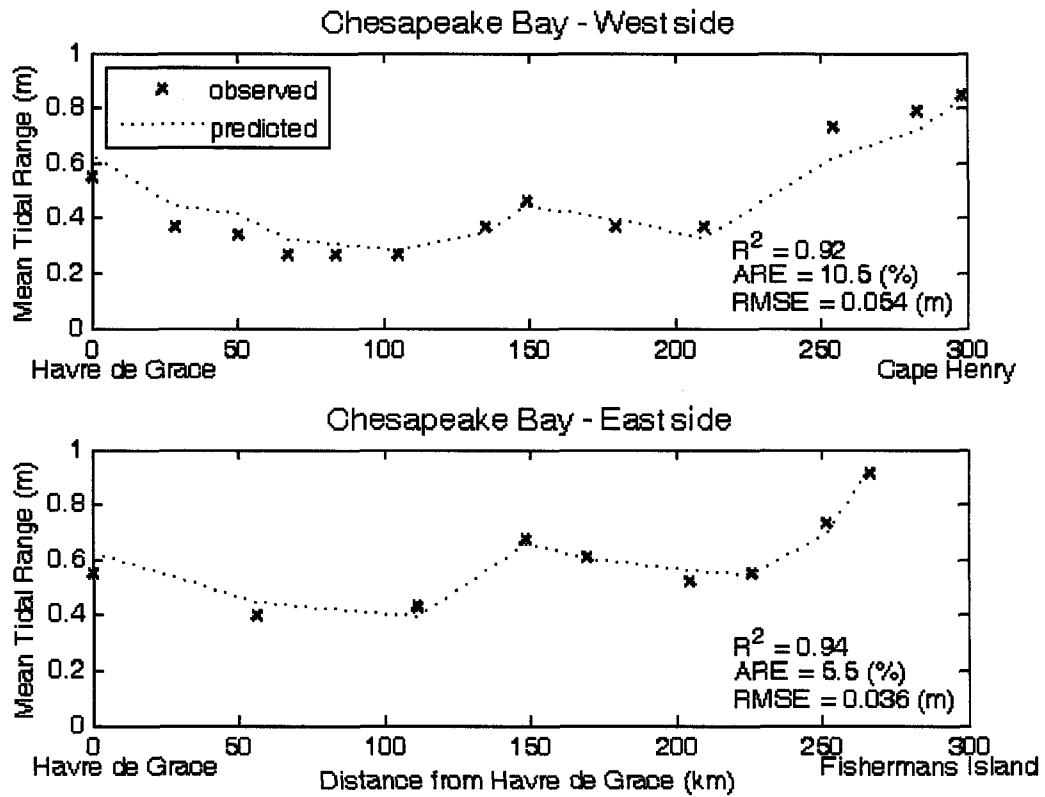


Fig. 4-1 Comparison of observed and predicted mean tidal ranges at 13 tidal stations on the West side (upper panel) and at 9 tidal stations on the East side (lower panel) of the Chesapeake Bay mainstem. Observations are denoted by 'x' and model predictions are denoted by the dashed line.

Table 4-2a Comparison of observed and predicted mean tidal amplitudes at 11 selected tide gauge stations. (unit: m)

STATIONS	M2		S2		N2		K1	
	OBS	PRE	OBS	PRE	OBS	PRE	OBS	PRE
CBBT	0.38	0.37	0.07	0.09	0.09	0.09	0.06	0.07
Kiptopeke	0.38	0.37	0.07	0.08	0.08	0.08	0.06	0.07
Gloucester Point	0.35	0.31	0.07	0.07	0.07	0.07	0.05	0.05
Windmill Point	0.17	0.16	0.03	0.04	0.04	0.04	0.03	0.03
Lewisetta	0.18	0.18	0.03	0.04	0.04	0.04	0.02	0.03
Solomon's Island	0.16	0.17	0.02	0.03	0.03	0.04	0.03	0.04
Cambridge	0.23	0.22	0.03	0.04	0.04	0.05	0.05	0.05
Annapolis	0.13	0.12	0.02	0.02	0.03	0.03	0.06	0.06
Baltimore	0.16	0.17	0.02	0.02	0.04	0.04	0.07	0.07
Tolchester Beach	0.17	0.19	0.03	0.04	0.04	0.04	0.07	0.07
ARE (%)		4.1		22.6		5.8		11.7
RMSE (m)		0.016		0.010		0.005		0.006

Table 4-2b Comparison of observed and predicted mean tidal phases at 11 selected tide gauge stations. (unit: deg)

STATIONS	M2		S2		N2		K1	
	OBS	PRE	OBS	PRE	OBS	PRE	OBS	PRE
CBBT	235.3	235.3	255.9	255.9	218.1	218.1	109.1	109.1
Kiptopeke	247.9	251.7	270.8	271.7	229.2	234.6	119.3	120.5
Gloucester Point	268.3	267.0	288.7	287.8	250.9	249.2	125.6	125.7
Windmill Point	317.3	326.6	334.0	344.7	297.2	309.8	148.7	159.4
Lewisetta	33.8	30.6	54.7	54.3	7.6	11.1	205.0	210.8
Solomon's Island	54.2	47.9	70.5	74.3	32.4	27.8	243.7	238.4
Cambridge	114.7	91.6	139.0	120.2	94.0	72.1	269.4	252.2
Annapolis	147.2	133.1	175.0	157.7	126.0	115.0	283.3	272.2
Baltimore	193.9	191.2	213.4	216.8	173.4	170.5	296.6	281.5
Tolchester Beach	202.7	194.4	227.4	222.0	176.0	173.0	287.9	277.5
ARE (%)		6.1		3.7		10.3		3.2
RMSE (deg)		9.8		9.1		9.2		9.7

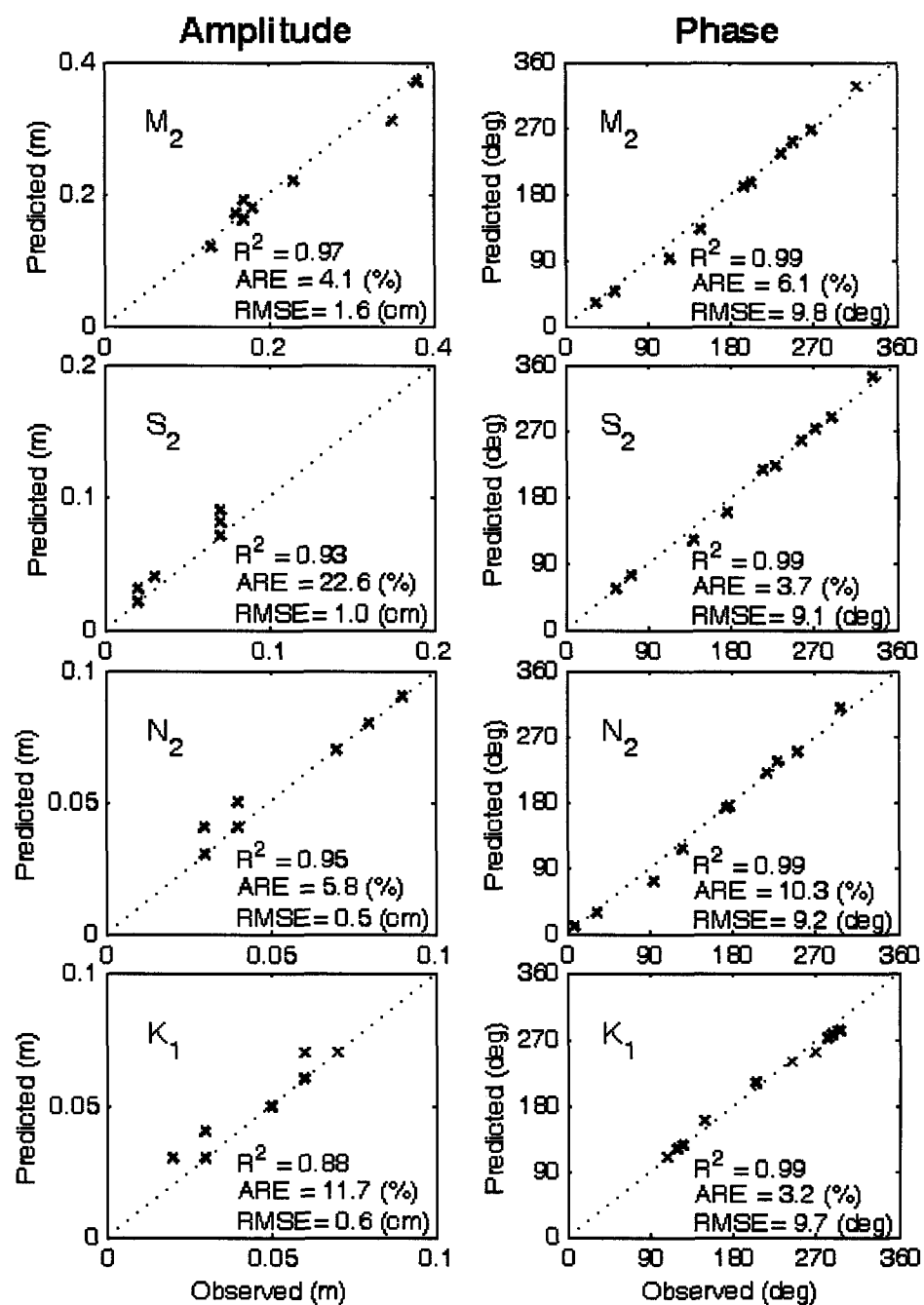


Fig. 4-2 Correlations between observed and predicted tidal amplitudes (left panels) and between observed and predicted tidal phases (right panels) of four major tidal constituents,  $M_2$ ,  $S_2$ ,  $N_2$ , and  $K_1$ .

#### 4.2.2 Subtidal surface elevation: storm surges

To verify the ELCIRC model under hurricane conditions, model runs were conducted for two 15-day periods, from September 10 to 24 in 1999 and from September 12 to 26 in 2003. The periods include Hurricane Floyd and Hurricane Isabel, respectively. Open boundary conditions for surface elevation and boundary conditions for surface forcing are described in Section 3.2.3 and Section 3.4, respectively. The scatter plots of storm surges at six selected stations during Hurricane Floyd in 1999 are shown in Figure 4-3. A 5-day period was used to verify the model. The model results have high values of  $R^2$  ( $> 0.90$ ) for all the observation stations, except the upper Bay station. The RMSE of predicted surges is on the order of 10 cm. Figure 4-4 depicts the scatter plots of storm surges during Hurricane Isabel in 2003. ELCIRC has a high correlation ( $R^2 > 0.90$ ) throughout the entire Bay and relatively low ARE. The predicted surges have the same order ( $\sim 10$  cm) of RMSE as those during Hurricane Floyd. Subsequently, the two-dimensional ELCIRC model has an approximately 2-cm error in tidal surface elevations and a 10-cm error in sub-tidal surface elevations during hurricane events.

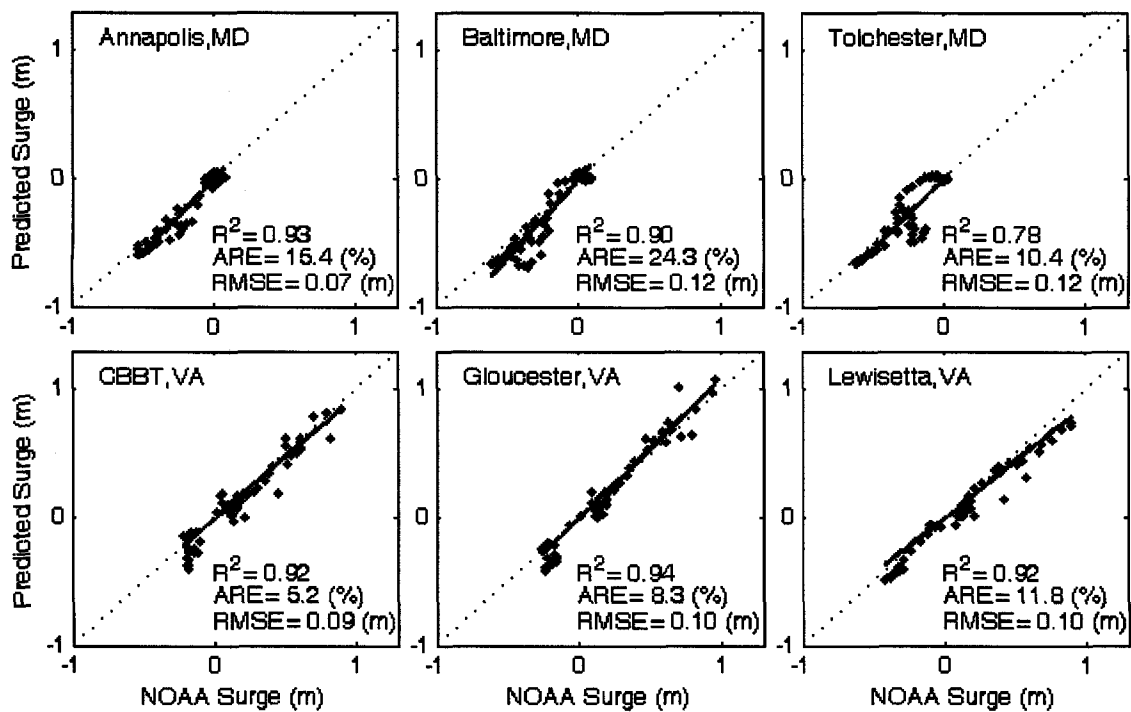


Fig. 4-3 Scatter plots of observed and predicted storm surge elevations at 6 selected observation stations for the 5-day period from September 15-19, 1999. Observations are on x-axis and predictions are on y-axis.



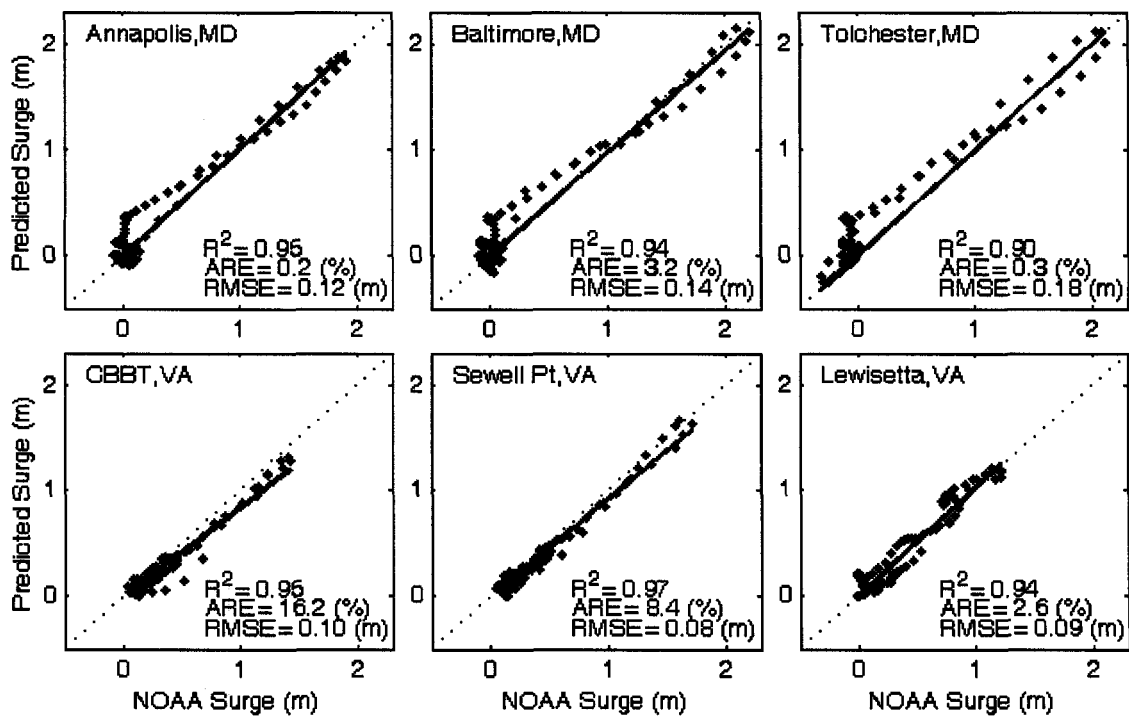


Fig. 4-4 Scatter plots of observed and predicted storm surge elevations at 6 selected observation stations for the 5-day period from September 17-21, 2003. Observations are on x-axis and predictions are on y-axis.

### **4.3 Baroclinic simulation**

Using a three-dimensional (3D) baroclinic model, SELFE, water surface elevation, water velocity, and salinity were calibrated with external forcings described above.

Zhong and Li (2006) found that the baroclinic model produces a more accurate prediction for water surface elevation and tidal currents than the tidal models which do not consider the effects of stratification. First, the model was executed for six months to stabilize the flow field and long-term calibrations from January to July were conducted in both years (1999 and 2003). For the hurricane events, another two runs were performed from August to December in both years.

#### **4.3.1 Water velocity**

For autumn 1999, predicted along-channel velocities were verified with observed velocities at three observation stations: mid-Bay buoy, Newport News (NN), and M5 (see Figure 2-1). Figure 4-5 shows that the modeled velocity reproduced the observed velocity at surface and bottom of three stations. The model run included Hurricane Floyd, which occurred during the shaded period. For autumn 2003, the modeled along-channel velocities were verified with the observed velocities at two stations: mid-Bay buoy and GP (see Figure 2-1). Similar to Figure 4-5, Figure 4-6 shows that the modeled velocity reproduced the observed velocity at both the surface and bottom of two stations. The model results indicate that the SELFE model is capable of reproducing time series of along-channel velocity during both hurricane events and vertical velocity profiles not only in the Chesapeake Bay main-channel but in its tributaries, the York and James Rivers.

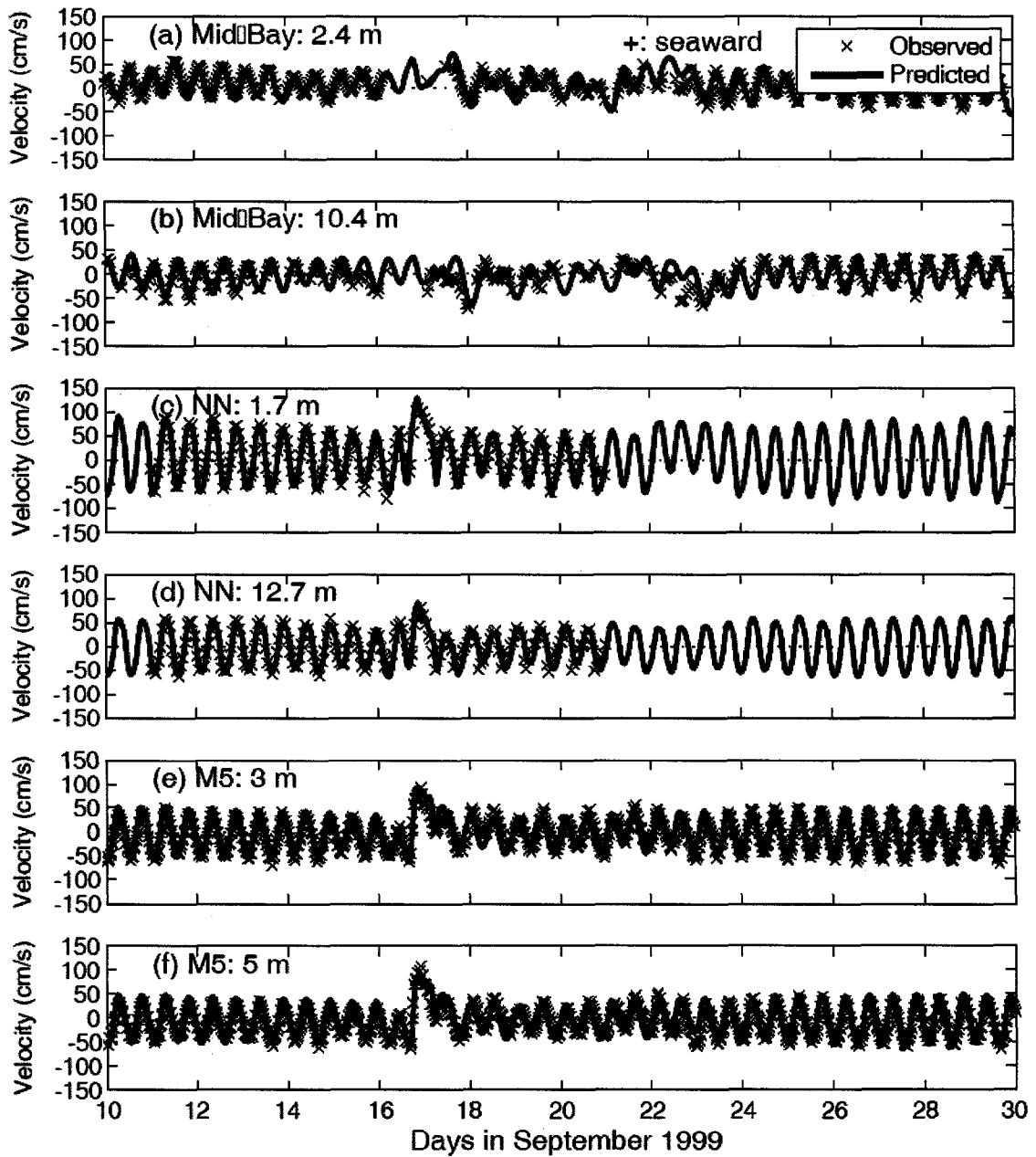


Fig. 4-5 Comparison of observed and predicted along-channel velocity: (a) surface and (b) mid-depth at the mid-Bay buoy station, (c) surface and (d) bottom at NN (Newport News) in James River, and (e) surface and (f) bottom at M5 near the Bay mouth, for the 20-day period in autumn 1999 including Hurricane Floyd, September 16 to 18.

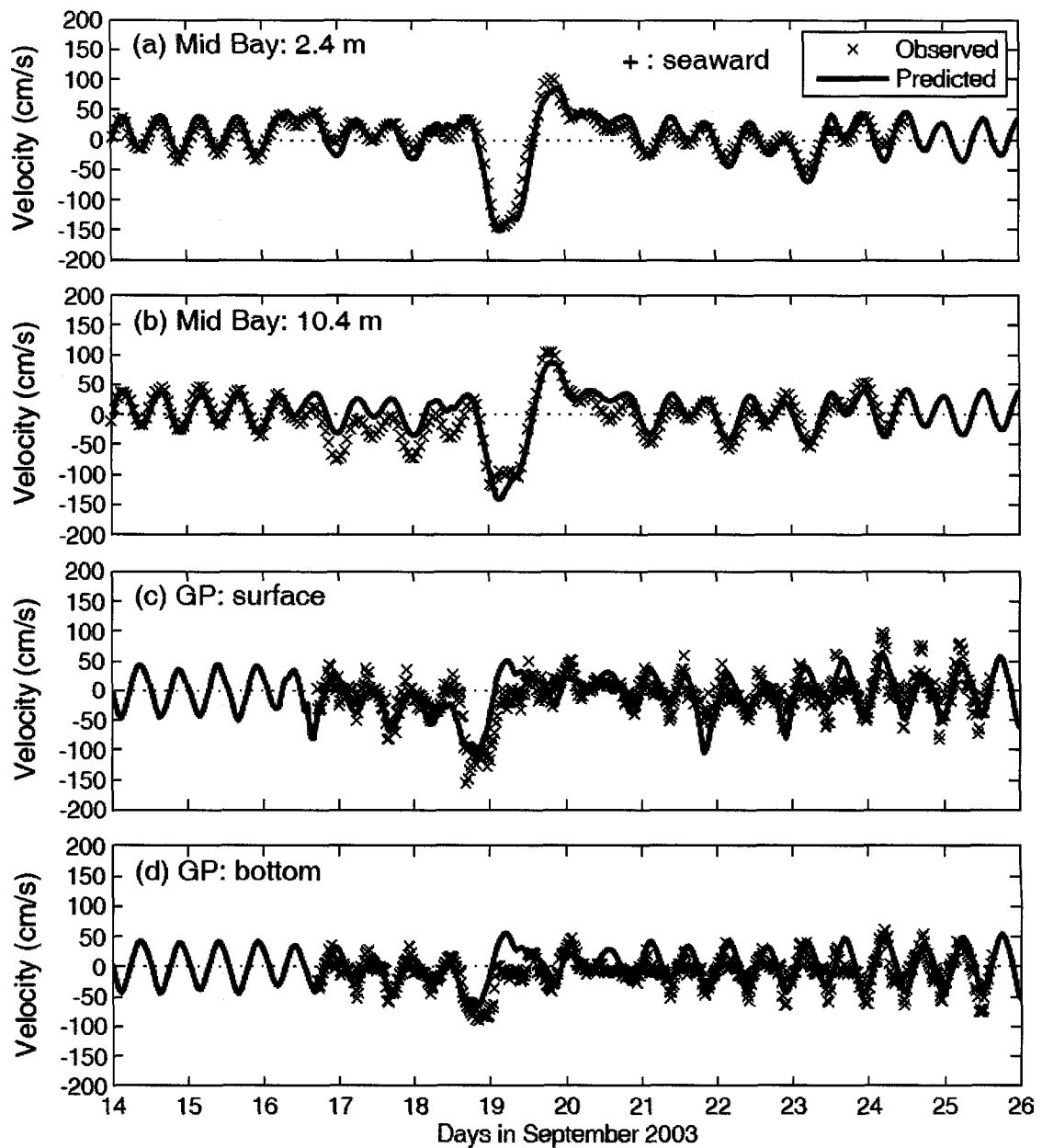


Fig. 4-6 Comparison of observed and predicted along-channel velocity: (a) surface and (b) mid-depth at the mid-Bay buoy station, and (c) surface and (d) bottom at GP (Gloucester Point) in York River, for the 12-day period in autumn 2003 including Hurricane Isabel, September 18 to 21.

### 4.3.2 Salinity

To verify the long-term salinity in SELFE, the modeled salinity was compared with monthly salinity data from CBP. River discharges and open boundary conditions for salinity were specified with the USGS daily streamflow data and the CORIOLIS salinity data, respectively, as described in Section 3.3.3. Since temperature was set to a constant value of 15 °C throughout space and time, temporal and spatial density variations induced by surface heating/cooling were not included. The comparisons of surface and bottom salinities at ten selected stations were plotted in Figures 4-7 and 4-8 for two 150-day periods in 1999 and 2003, respectively. SELFE reproduced the temporal salinity variation with a good agreement in vertical stratification. The model represented the surface salinity decreases induced by high freshwater inflow at the end of January in 1999 and at the end of March in 2003. Figures 4-9 depicts the comparisons of surface and bottom salinities at ten selected stations for two 60-day periods in 1999 and 2003, respectively. Overall, the model results indicate that the SELFE model has a capability of simulating the baroclinic response of the Chesapeake Bay to a hurricane event.

## 4.4 Summary

The hydrodynamic models have been verified with comparisons of sea surface elevation, water velocity, and salinity between the model results and the observed data for four periods. Model calibrations show that the models have a sufficient accuracy to simulate a hurricane event to examine the barotropic and baroclinic responses of the Chesapeake Bay to hurricane events. The Bay's barotropic response and baroclinic response to two hurricane events will be detailed in Chapters V and VI, respectively.

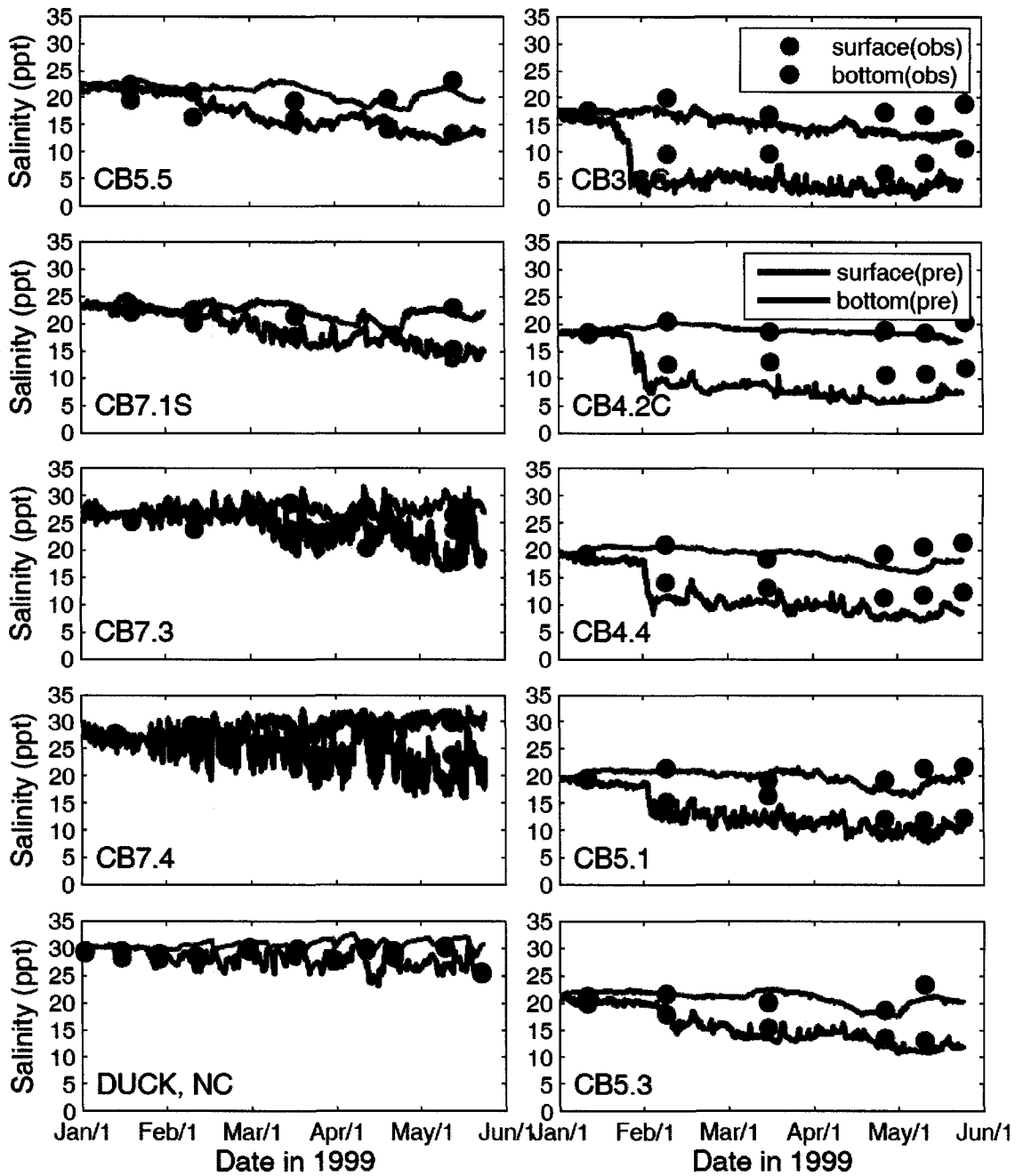


Fig. 4-7 Comparison of observed and predicted salinity (surface and bottom) at ten selected stations for spring 1999. Model results (red: bottom; blue: surface) and observed data (black circle: bottom; green circle: surface).

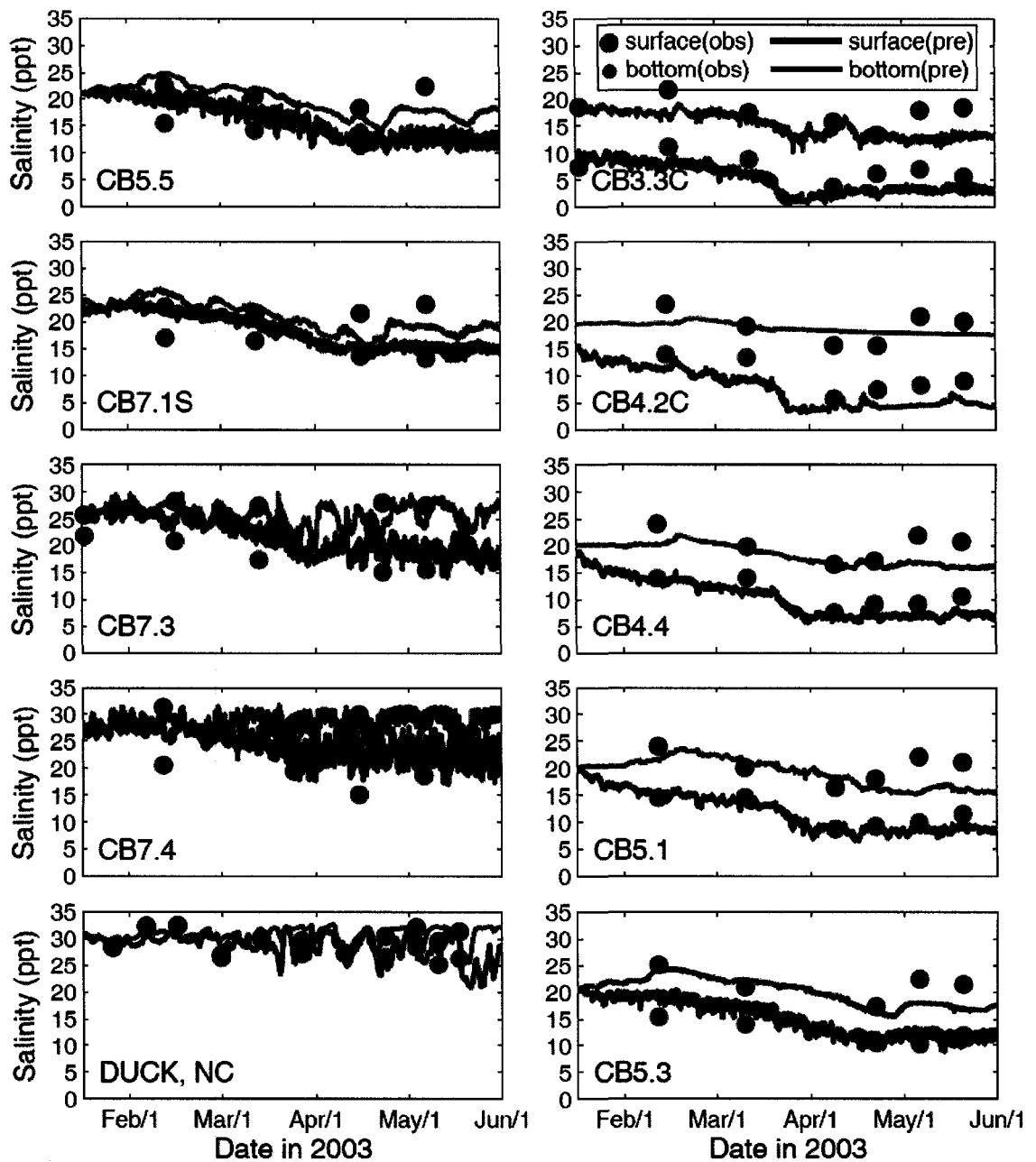


Fig. 4-8 Comparison of observed and predicted salinity (surface and bottom) at ten selected stations for spring 2003. Model results (red: bottom; blue: surface) and observed data (black circle: bottom; green circle: surface).

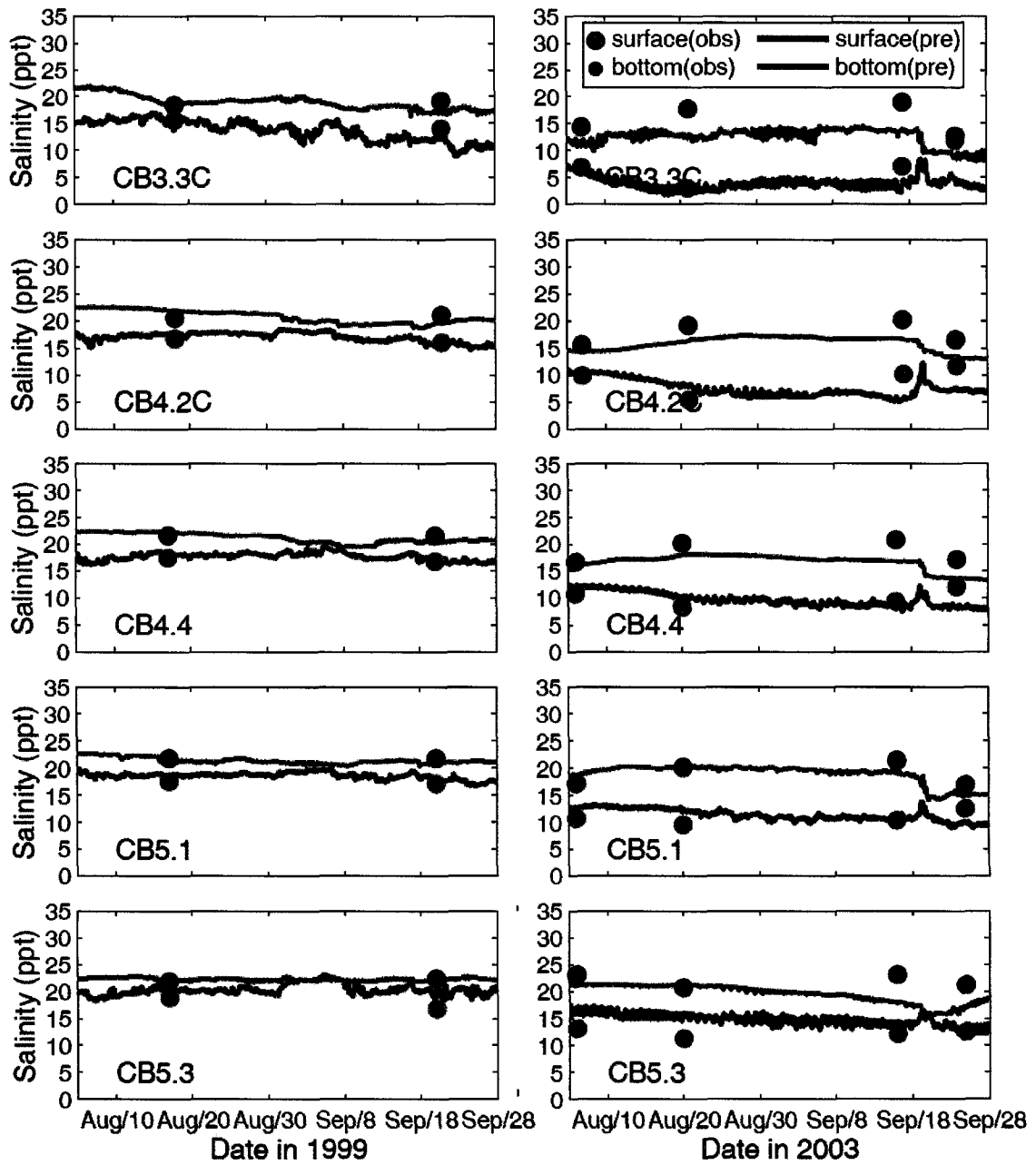


Fig. 4-9 Comparison of observed and predicted salinity (surface and bottom) at five selected stations for autumn 1999 (left panels) and for autumn 2003 (right panels): Model results (red: bottom; blue: surface) and observed data (black circle: bottom; green circle: surface).



## **Chapter V**

# **A BAROTROPIC RESPONSE OF THE CHESAPEAKE BAY TO HURRICANES FLOYD AND ISABEL**

### **5.1 Introduction**

A moving storm is known to generate both barotropic and baroclinic motions in the stratified ocean. It generates the barotropic wave motion of the coastal ocean and an oscillation of the sea surface elevation in a coastal or inland water body during a period ranging from a few minutes to a few days that result from the atmospheric forcing (Murty, 1984). Hurricane-generated storm surge has been studied continuously through the twentieth century. Harris (1956) summarized the status of research on hurricane-generated storm surge up to the early 1950's in the United States. He emphasized the systematic studies on the storm surge due to hurricanes along the East Coast of the United States. In the Chesapeake Bay, one of the largest partially mixed estuary in the world, hurricane-generated storm surge was initially studied by Bretschneider (1959) because, until then, only four hurricanes were sufficiently well documented: no name (1933), Connie (1955), Diane (1955), and Hazel (1957) (Murty, 1984). Pore (1960) addressed that six factors for storm surge generation and modification are considered significant in the Chesapeake Bay: wind set-up, transport of water by the short period wind waves, the atmospheric pressure effect (the inverted barometer effect), storm speed,

the variable depth of the water, and convergence or divergence of the storm surge in estuaries of varying width. Pore (1965) made a distinction between eastern-type storms (i.e., hurricanes traveling east of the Bay) and western-type storms (i.e., hurricanes passing west of the Bay). He indicated that eastern-type storms generate the maximum surge in the southern portion of the Bay whereas western-type storms create the highest surge in the northern part of the Bay. For storms of the past decade, Hurricane Floyd (1999) and Hurricane Isabel (2003) are representatives of eastern-type and western-type storms, respectively. Recently, numerical modeling studies have been conducted to examine the storm surge dynamics in the Chesapeake Bay during these two hurricanes (Shen et al., 2005; Wang et al., 2005; Shen et al., 2006a; Shen et al., 2006b).

Presently, the barotropic flow motion has been defined as a depth-averaged flow and the baroclinic motions are what remain after subtraction of the depth-averaged currents and are associated with the ocean stratification (Ginis and Sutyrin, 1995). Ginis and Sutyrin (1995) concluded that the sea surface elevation can be decomposed into four physically different components caused by geostrophic adjustment to the depth-averaged currents, wind stress divergence, inverted barometer effect, and baroclinic effects. They found that the maximum depth-averaged current is proportional to the maximum wind stress torque and the distance from the maximum current to the storm track is proportional to the maximum wind stress radius. Using a two-layer model, they demonstrated that nonlinear coupling between the baroclinic and barotropic modes is rather weak, and therefore these two modes may be calculated separately. In the deep ocean, the barotropic flow is affected by variability of the Coriolis parameter (Geisler, 1970), and the barotropic current response to hurricane forcing occurs within the near-

inertial wave band (Shay et al., 1990). On the other hand, storm-induced barotropic flow in shallow water is greatly influenced by bottom friction. Accordingly, a couple of numerical models were developed with different types of bottom friction parameterizations (e.g., Jelesnianski, 1965; Forristall, 1974; Hearn and Holloway, 1990). Therefore, the barotropic numerical model that has a capability to simulate the storm-induced barotropic flow with the appropriate bottom friction scheme should be applied to the shallow water systems to study the response of a partially-mixed estuary to a hurricane event.

The purpose of this chapter is to investigate the barotropic response of the Chesapeake Bay to hurricane events and it is outlined as follows: Storm surge dynamics, including analysis of the barotropic model results, are discussed in Section 5.2. The barotropic flow motion, with analysis of depth-integrated water velocity, is described in Section 5.3. Subsequently, the effects of local/remote winds and river inflows will be described in Section 5.4 as the external forcing effect. Lastly, the conclusions and summary are presented in Section 5.5.

## **5.2 Model analysis of storm surge dynamics**

### **5.2.1 Hurricane Floyd**

The ELCIRC model was spun up initially for 5 days from a cold start and then run for 10 days under real-time conditions during Hurricane Floyd. The forcing functions used include pressure and wind forcing obtained from the parametric wind model and interpolation method using observed wind data, and 9 astronomical tidal constituents at the open boundary as described in Chapter III. To obtain the predicted storm surges, two

numerical experiments were conducted: one is exerted by only tidal forcing and the other is forced by tidal and atmospheric forcings. Assuming that tides and surges are independent, storm surges can be obtained by subtracting the former from the latter. Figure 5-1 presents the comparison of surge height above mean sea level (MSL) between estimated values based on the observed data and simulated values at eight selected tidal stations in the Chesapeake Bay. The left panel starts with the southernmost station at CBBT and extends north through Gloucester Point, Windmill Point, and Lewisetta in Virginia. The right panel continues the sequence through the Maryland portion of the Bay, including Cambridge, Annapolis, Baltimore, and Tolchester Beach. At all stations the existing model has sufficient accuracy to analyze the fundamental property of storm surge dynamics.

#### Temporal variation of the surge

The simplest way to start the storm surge analysis is to simultaneously examine the time series for stations (Wang et al., 2005). Twenty stations, separated by approximately equal distance, were selected along the mainstem Bay (Figure 5-2). Time series of hourly surge heights at each station from 22:00 UTC on September 15 through 12:00 UTC on September 18 are shown in Figure 5-3. This figure shows that the first peak appeared at the mouth of the Bay (st01) around September 16 04:00 UTC and slightly increased at st02 a couple of hours later. The first peak corresponds to the northeasterly winds that generate not only local convergence but the Ekman transport from the continental shelf to the Bay. This peak seems to propagate to the north over time. The second peak around 0.8 m above mean sea level (MSL) was generated around

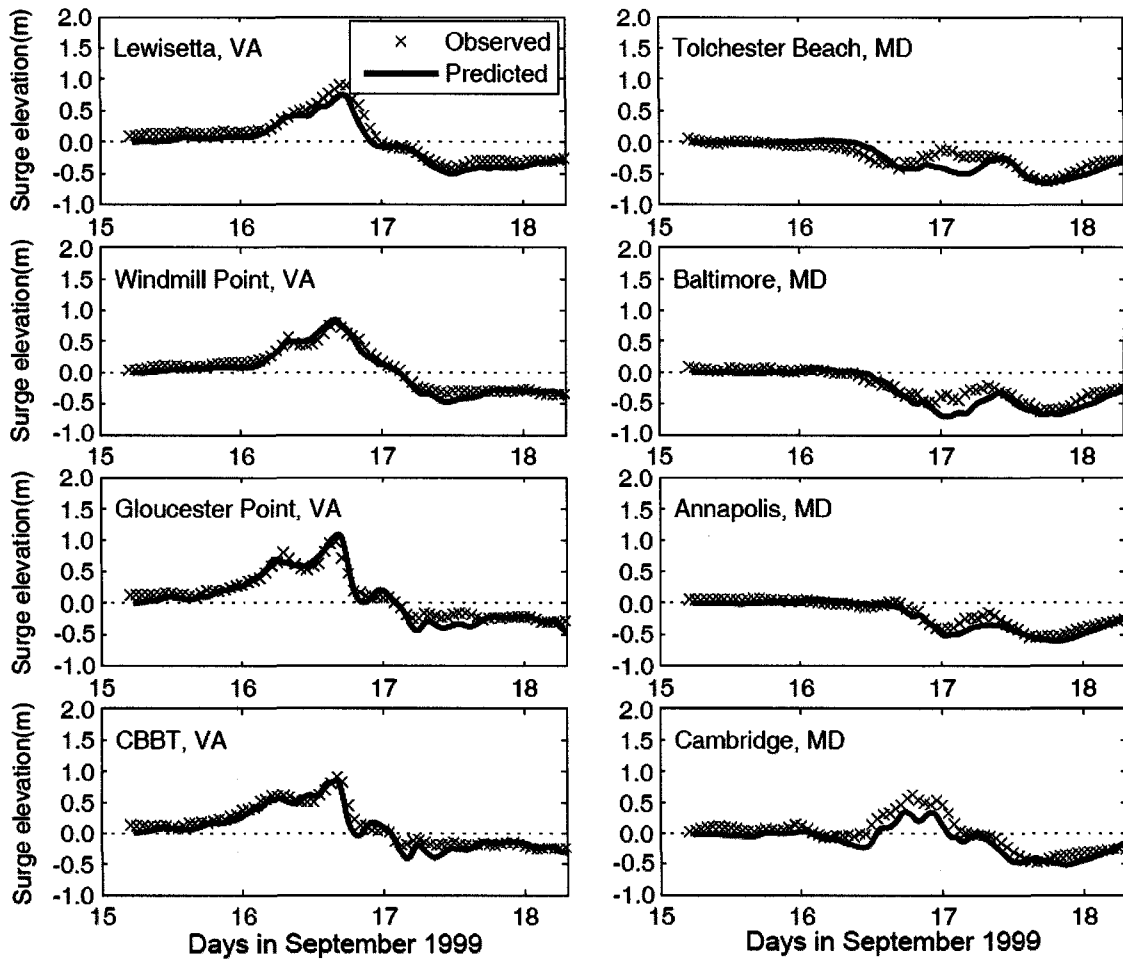


Fig. 5-1 Surge height comparison between observed (red crosses) and predicted (blue solid lines) at eight selected stations during Hurricane Floyd in September 1999.

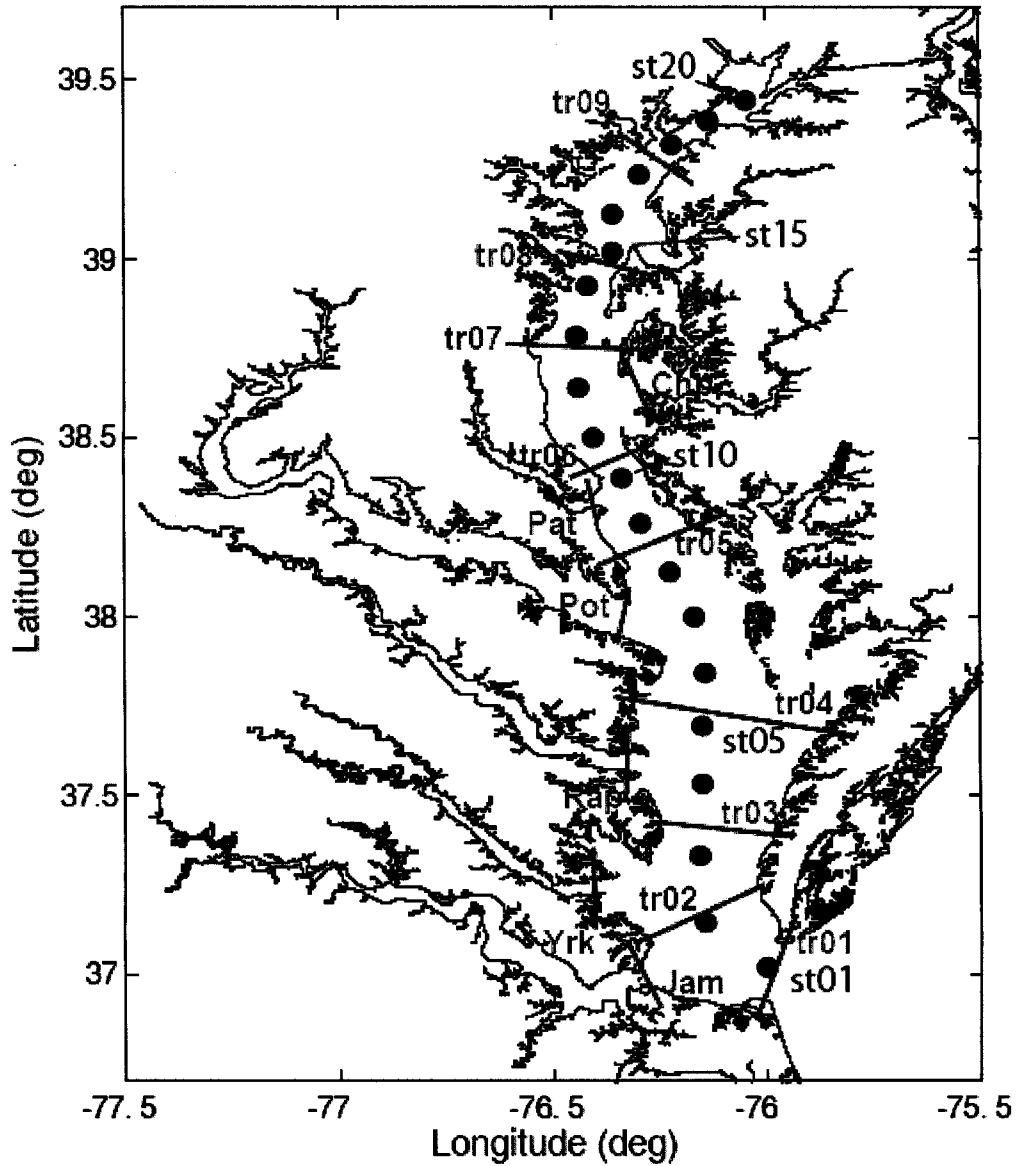


Fig. 5-2 The locations of twenty stations (●) in the Chesapeake Bay model domain selected for storm surge analysis and fifteen transects (red lines) for transport analysis.

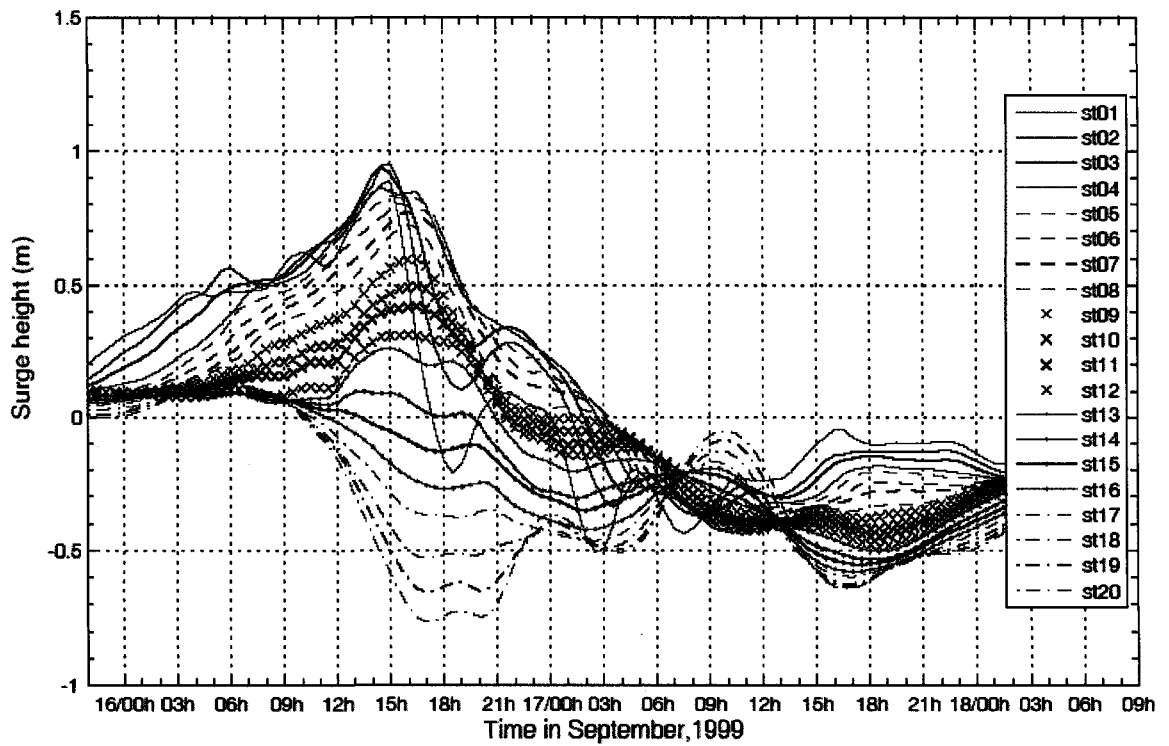


Fig. 5-3 Time series of surge height at 20 selected stations along the mainstem Bay from the Bay mouth (st01) to the upper Bay (st20) during Hurricane Floyd in September, 1999.

September 16 16:00 UTC in the lower Bay and the peaks from st01 to st04 occurred nearly simultaneously. At this moment, surge height decreased to around 0.5 m below MSL in the upper portion of the Bay. This indicates that the second peak in the lower Bay was initialized by northeasterly winds and superposed with the set-up induced by northerly winds, whereas the surge elevation in the upper Bay was set-down induced by local northerly winds.

#### Spatial distribution of the surge

The spatial curves of storm surges were plotted with time intervals of 4 hours starting at 20:00 UTC on September 15 (Figure 5-4). The surge height in the lower Bay increased until September 16 12:00 UTC, decreased until September 17 08:00 UTC, and increased again afterwards. On the other hand, the surge height in the upper Bay decreased to below zero until September 16 20:00 UTC, increased until September 17 08:00 UTC, and increased again afterwards. A distinguishing feature from the spatial curves of surge height during Hurricane Floyd is that the nodal point of the oscillation for the second surge was generated near Annapolis, MD, 220 km from the Bay mouth. The oscillation of surge heights south of the nodal point was opposite that north of the point.

#### The combined effect of the primary surge and wind-induced set-up/set-down

A three-dimensional view and top view of time-distance (t-x) graph with the contour of isolines for the surge height were plotted in Figure 5-5. In this t-x diagram, a time history of the elevation can be plotted by recording the contour along  $x_i = \text{constant}$  line at any specific location  $x_i$ . For two simultaneous records, a characteristic curve (also



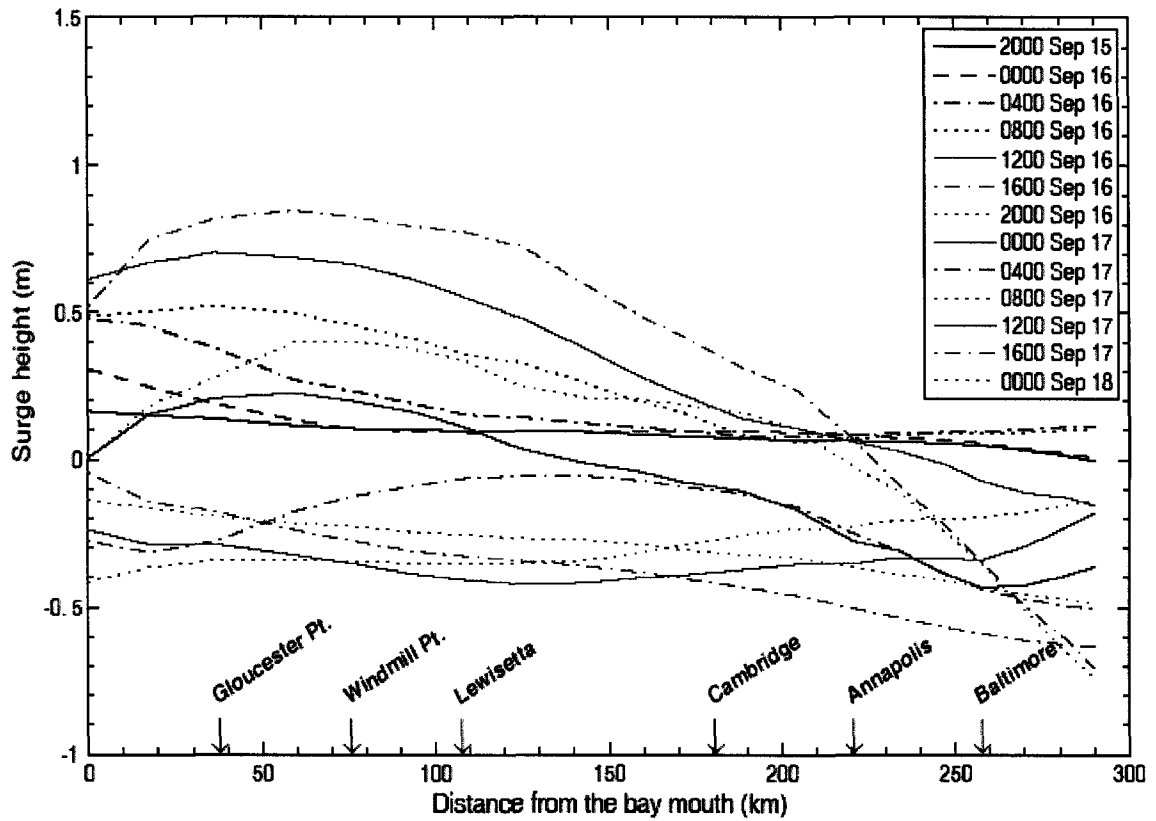


Fig. 5-4 Spatial distributions of surge height for 20 selected stations from September 15 21:00 to September 18 01:00 (UTC) in 1999.

called a wave ray—the path along which the wave propagates) can be obtained by connecting the similar phases (e.g., crest to crest or trough to trough) between the two records. The underlying purpose is to determine the path of the wave ray and the associated phase speed by using the relationship  $dx/dt = c(t, x)$  in the t-x plane, where  $c$  is the wave speed. As described previously, three ray curves can be identified: the first wave starting from September 16 06:00 UTC with approximately  $62 \text{ km h}^{-1}$  in speed propagated up to the mid-Bay (0.5-m contour line reached to 150 km at September 16 14:00 UTC). The second ray beginning around September 16 14:00 UTC occurred simultaneously in the lower Bay and the upper Bay generating set-up and set-down, respectively. Wind-induced set-up in the lower Bay superposed on the second surge but wind-induced set-down in the lower Bay cancelled out or overcame the surge. However, from September 16 15:00 UTC to 18:00 UTC, surge height quickly dropped in the lower Bay. During this 3-hour period, since storm eye passed over the Bay mouth, wind direction in the lower Bay suddenly changed from easterly wind to northwesterly wind and then northwesterly wind drove water out of the Bay. The third ray of negative surge started at the mouth around September 17 02:00 UTC and propagated to the upper Bay with approximately  $62 \text{ km h}^{-1}$  in speed propagated. The ray of negative surge appears to be generated from the continental shelf, since sea surface elevation on the shelf could be reduced by offshore winds after the storm moved northeastward.

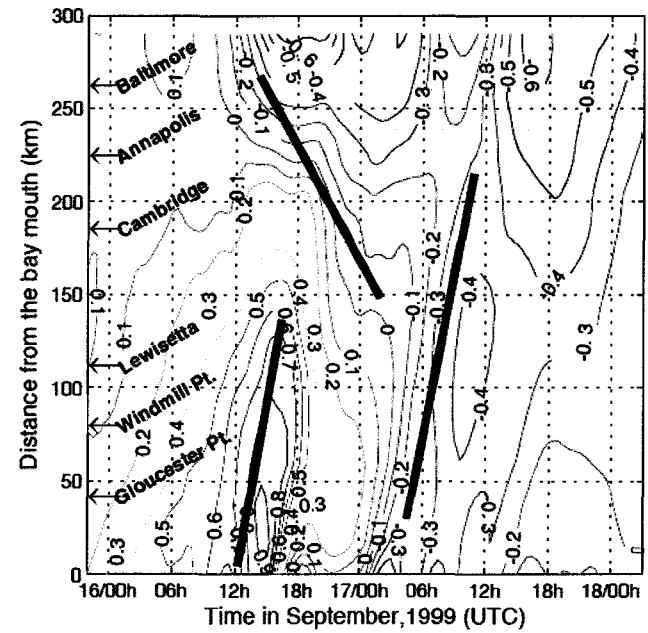
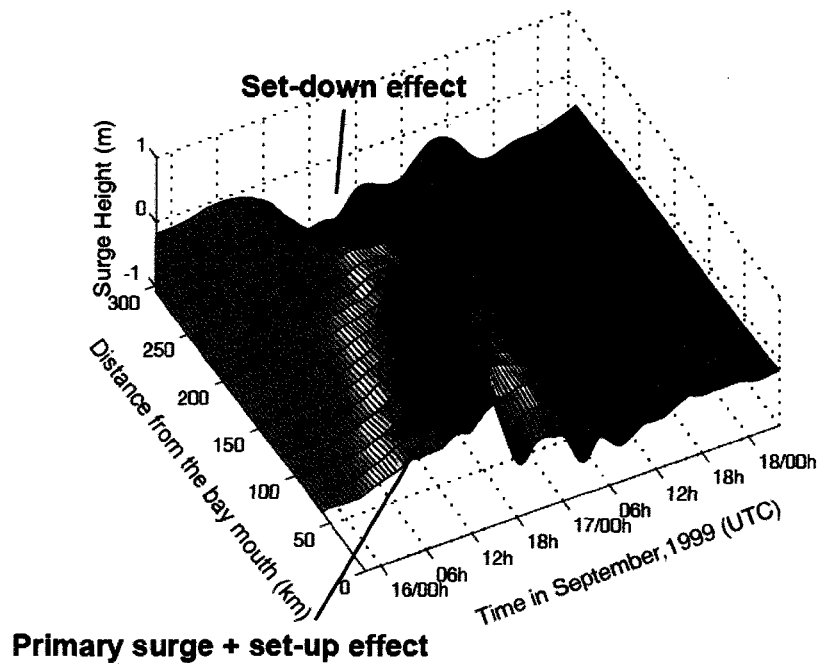


Fig. 5-5 The time versus space plot of surge height for 20 selected stations during Hurricane Floyd in September 1999: 3D view (left) and top view with contour lines (right).

## 5.2.2 Hurricane Isabel

The model for Hurricane Isabel was executed in the same manner as that for Hurricane Floyd. The simulated storm surges (solid lines) were plotted in Figure 5-6 compared with estimated storm surges (crosses). The comparison of model results with the observations was quite good for most of the stations. The model results are analyzed for storm surge dynamics as described in Section 5.2.1.

### Temporal variation of the surge

The time series of the surge height at each station were plotted together (Figure 5-7). The figure indicates that the primary surge appeared from the mouth at about September 18 18:00 UTC at CBBT with a predicted height of approximately 1.5 m. The amplitude of the primary surge decreased as it propagated northward until it reached the fourth station near the mouth of the Rappahannock River. Its amplitude then increased monotonically toward the northern Bay until reaching 2.5 m (modeled) near Tolchester Beach. In terms of temporal variation, the first three stations in the lower Bay responded differently from the remainder of the 17 stations in that the surge for the former stations dropped rapidly and fell below MSL. Their high-water duration, using the 75th percentile as a measure, lasted only for 12 hours. In contrast, the fourth to twelfth stations in the middle portion of the Bay displayed a much longer high-water duration, exceeding one full day.

### Spatial distribution of the surge

A snapshot of the spatial distribution of water elevation spanning the entire Bay can also be obtained using the selected 20 stations. Figure 5-8 shows the spatial curves plotted with time intervals of 4 hours starting on September 18 12:00 UTC and ending on

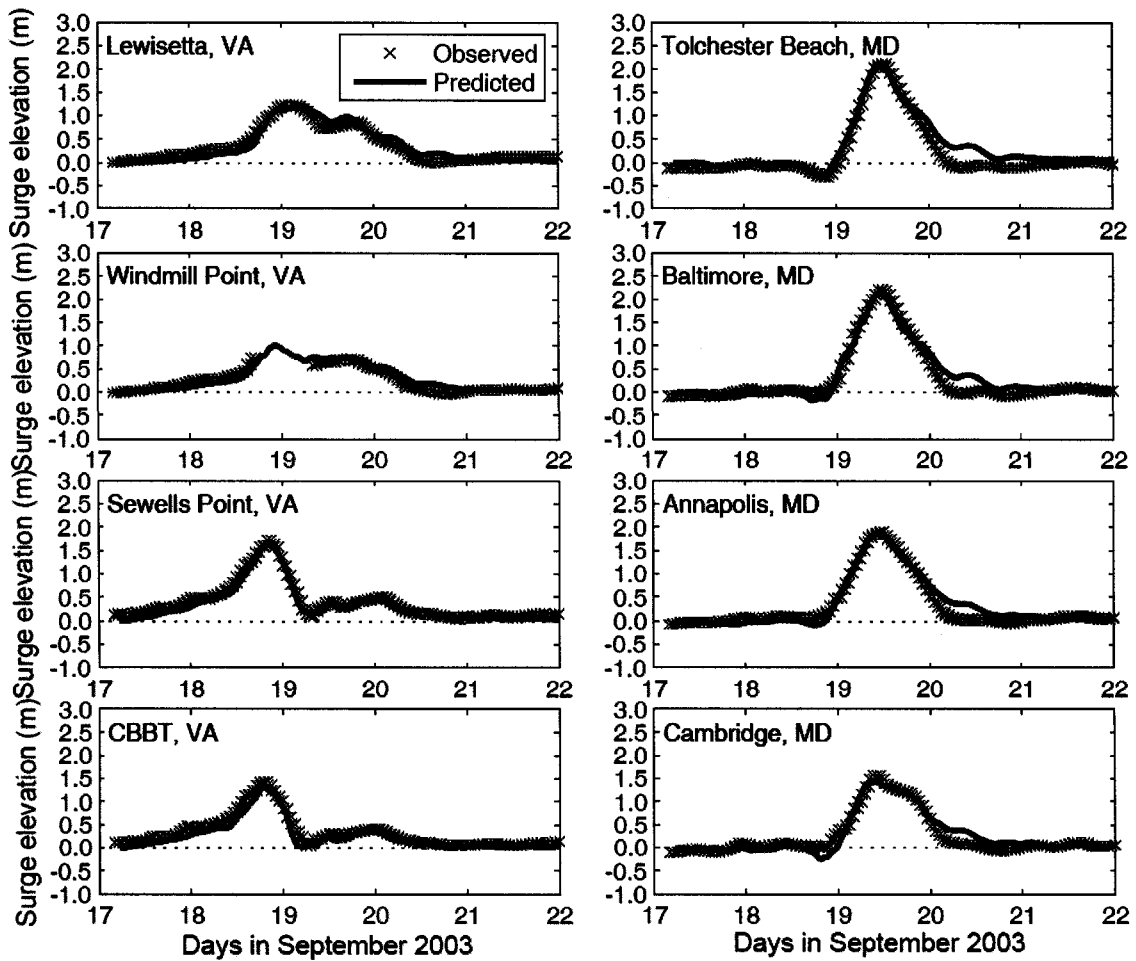


Fig. 5-6 Surge height comparison between observed (crosses) and predicted (solid lines) at eight selected stations during Hurricane Isabel in September, 2003.

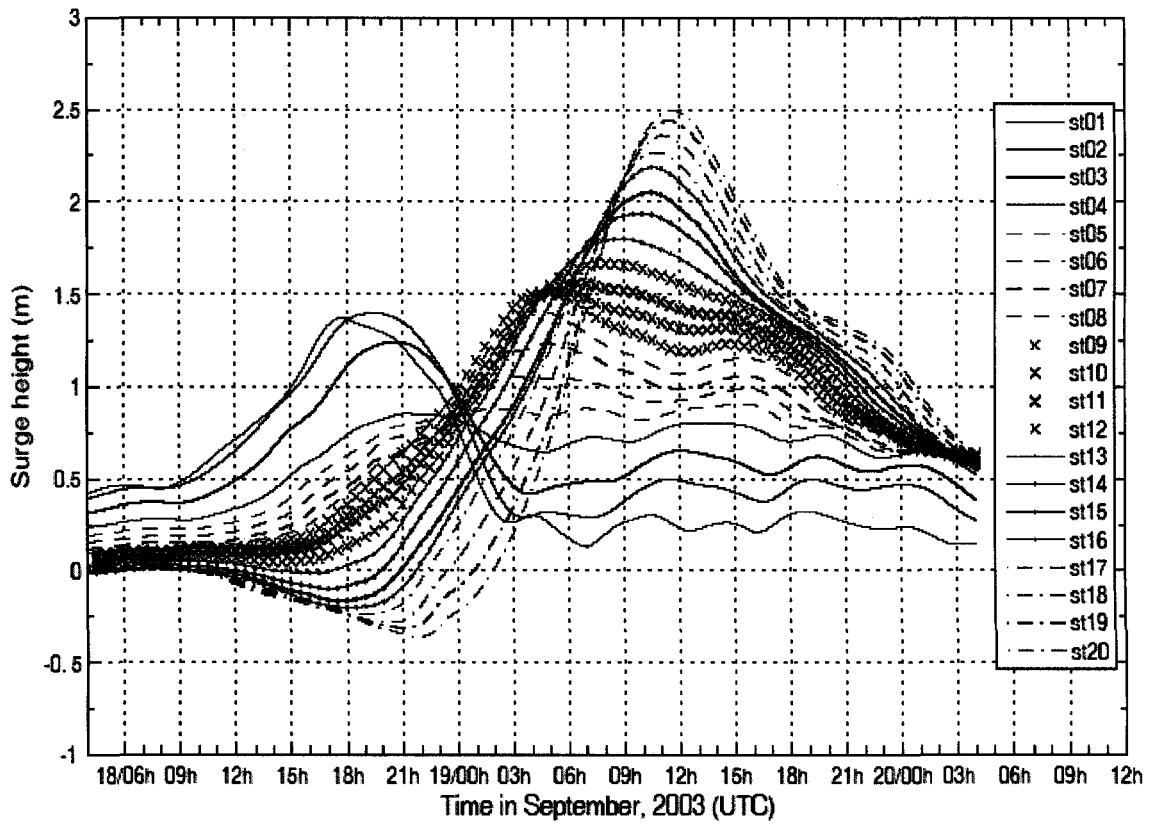


Fig. 5-7 Time series of surge height at selected 20 stations along the mainstem Bay from the Bay mouth (st01) to the upper Bay (st20) during Hurricane Isabel in September, 2003.

September 20 00:00 UTC. From spatial curves of the 16:00 and 20:00 UTC on September 18, the first-stage surge (primary surge) can be clearly identified in the lower Bay. The next three profiles, namely September 19 00:00 UTC, September 19 04:00 UTC, and September 19 08:00 UTC, revealed that a linear trend of set-up in the upper Bay and set-down in the lower Bay was evident with use of a 0.5-m water level as the benchmark mean sea level (see *The combined effects* section below for further explanation). The slope of the elevation on September 19 12:00 UTC—a fully developed set-up—was verified by a steady-state, analytical formula balanced between the hydrostatic pressure gradient and the wind stress (less than the bottom stress). A linear slope for a 2.1-m increase over a 250 km horizontal distance was estimated using a wind speed of  $15 \text{ m}\cdot\text{sec}^{-1}$  and a water depth of 6 m, which was comparable to the actual observation of 2.4 m at Tolchester Beach. Careful examinations of the spatial curves for September 19 00:00 UTC, September 19 04:00 UTC, and September 19 12:00 UTC revealed a pair of wave crests separated by 50 km moving northward. The advancing front in the upstream side toward the upper Bay is the primary wave, which was followed by the second-stage surge generated by southerly wind-induced setup. Eight of nine spatial elevation curves intersect through the Windmill Point station, where the set-up and set-down are separated; the elevation there maintains a small variation at approximately 0.5 m above MSL. On September 19 12:00 UTC, approximately 16 hours after the first-stage surge appeared at the Bay mouth, the elevation in the upper Bay finally reached the highest level at 2.5 m and retreated afterwards.

### The combined effects of the primary surge and wind-induced set-up/set-down

Based on the description in the previous section, at least two processes were involved in the evolution of the storm surge; namely, the primary surge and the second-stage surge by the southerly wind-induced set-up/set-down. Figure 5-9 shows a three-dimensional view and top view of a time-distance (t-x) plot with isoline contours of the surge height. Starting at  $x = 0$ ,  $t = 18$  hours on September 18 in the lower Bay, the first wave ray curve was determined by tracing through the crests of the primary surge; the phase speed was determined by its slope to be  $5.2 \text{ m}\cdot\text{sec}^{-1}$ . Similarly, at  $x = 285 \text{ km}$ ,  $t = 12$  hours on September 19 in the upper Bay, the second wave ray curve was determined by the crests to have a speed of  $6.4 \text{ m}\cdot\text{sec}^{-1}$ . In the Hurricane Isabel's case, both primary surge and secondary surge are forced by the same major wind system and originated from the Bay mouth, it is reasonable to assume that the temporal variation are in synchronized with the forcing wind frequency and are periodic stationary everywhere. With this assumption, the governing equation of vertical barotropic subtidal current and water elevations of Garvine (1985):

$$\begin{aligned} \frac{\partial u}{\partial t} + \frac{\partial \eta}{\partial x} + \lambda u &= W \cos \theta e^{it} \\ \frac{\partial \eta}{\partial t} + \frac{\partial u}{\partial x} &= 0 \end{aligned} \quad (5.1)$$

where  $x \equiv (\omega/c)x^*$ ,  $L \equiv (\omega/c)L^*$ ,  $t \equiv \omega t^*$ ,  $\eta \equiv \eta^*/a$ ,  $u \equiv hu^*/(ac)$ ,  $c = (gh)^{1/2}$ , and dimensionless wind parameter,  $W = \tau / (\rho \omega c a)$ , dimensionless bottom friction parameter,  $\lambda = Cd u_t / (h\omega)$ , and  $\theta$  is the angle of wind stress measured counterclockwise from  $x^*$ . Eq. (5.1) can be solved by assuming that

$$\eta(x, t) = A(x) e^{it}, \quad u(x, t) = U(x) e^{it} \quad (5.2)$$



subjected to boundary conditions:

$$\eta(0, t) = A(0)e^{it}, \quad u(L, t) = 0$$

The solution is

$$\begin{aligned} U(x) &= \frac{i}{K^2 \cosh KL} [A(0)K \sinh \{K(L-x)\} + W \cos \theta (\cosh KL - \cosh Kx)] \\ A(x) &= \frac{1}{K \cosh KL} [A(0)K \cosh \{K(L-x)\} + W \cos \theta \sinh Kx] \end{aligned} \quad (5.3)$$

where  $K$  is a complex wave number of order unity given by

$$K \equiv (-1 + i\lambda)^{1/2} = [(r-1)/2]^{1/2} + i[(r+1)/2]^{1/2}$$

where  $r \equiv (1 + \lambda^2)^{1/2}$ , a real number. It is noted that the both vertical averaged velocity and water level solutions are linear combination of two terms. The first term is a free wave solution corresponding to the wave generated by the remote wind and propagated into the Bay, whereas the second term is a forced wave corresponding to solution forced by the local wind  $W$ . The spatial distribution of water level for the free wave and forced wave are very different: the water level distribution induced by remote wind is a cosh function which nearly approaches to 1 if the argument is close to 0, whereas the water level distribution induced by local wind is a sinh function which is linearly proportional to the distance from the origin at the Bay mouth. This is qualitatively consistent with the water level simulated from the storm surge model. Further discussion can be found in Chapter VIII.

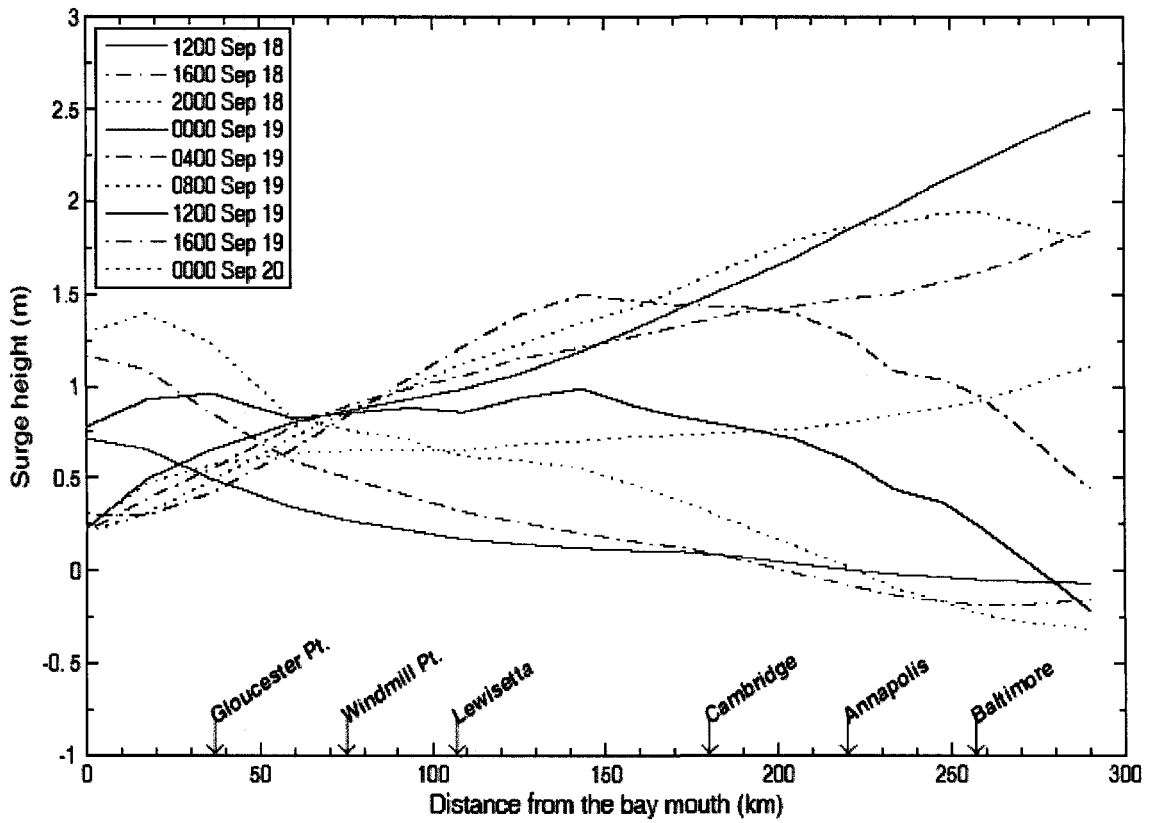


Fig. 5-8 Spatial distributions of surge height for 20 selected stations from September 18 13:00 to September 20 01:00 (UTC) in 2003.

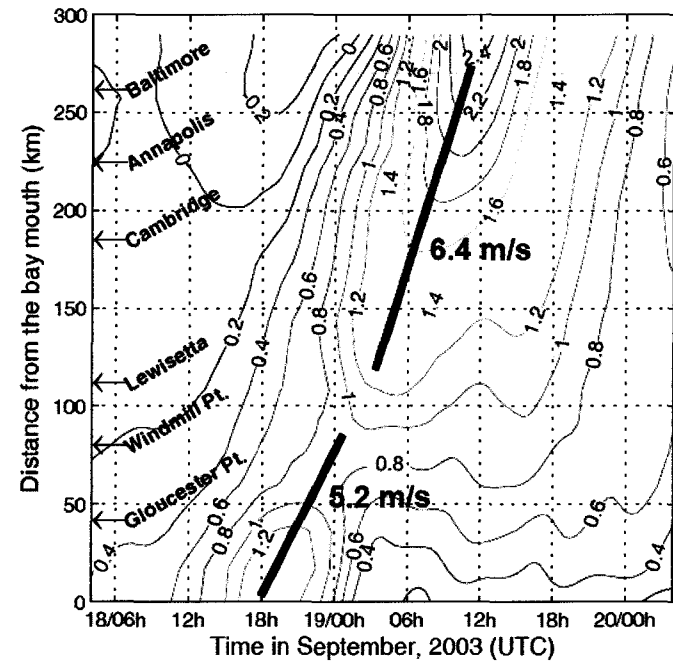
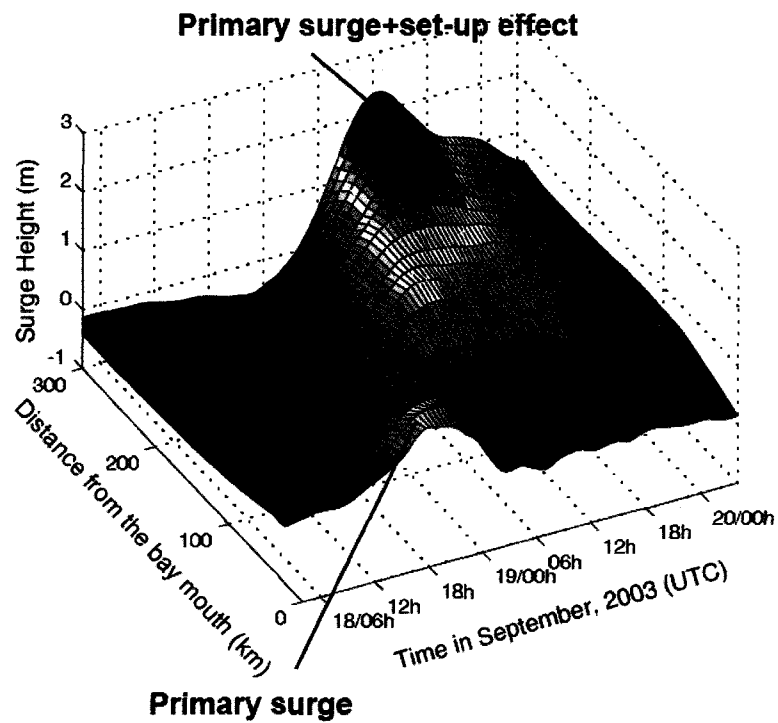


Fig. 5-9 The time versus space plot of surge height for 20 selected stations during Hurricane Isabel in September 2003: 3D view (left) and top view with contour lines (right).

### 5.3 Analysis of barotropic flow motion

Based on the model accuracy of velocity calibration as described in Chapter IV, the barotropic flow motion was analyzed. The best way to examine the barotropic flow motion in the Bay during hurricanes is to plot horizontal distributions of depth-integrated flow and to calculate the laterally-integrated volumetric transport that is summarized for each cell interface along transects dividing adjacent regions (Figure 5-2) (Cerco and Cole, 1994).

#### 5.3.1 Horizontal distribution of depth-integrated flow

##### Hurricane Floyd

Time-sequential depth-integrated flows were demonstrated in the Bay's southern portion (Figure 5-10) and northern portion (Figure 5-11). The intratidal variability in the flows was eliminated by a low-pass Lanczos filter. On September 16 03:00 UTC, a northeasterly wind of 12.3 m/s began to drive the water from the continental shelf into the Bay (Figure 5-10a) and from the mid-Bay to the lower Bay (Figure 5-11a), and consequently generated the first peak of storm surge in the lower Bay. As northeasterly/easterly winds in the southern Bay continued to blow with the same magnitude until September 16 16:00 UTC (Figure 5-10b,c) and northeasterly/northerly winds in the northern Bay drove the water from the upper Bay to the lower Bay (Figure 5-11b,c), barotropic flow increased and elevated the surge height to generate the primary surge (Valle-Levinson et al., 2002). As described in the previous section, this surge was combined with wind-induced set-up in the southern Bay whereas strong seaward flow driven by northeasterly/northerly winds created a set-down in the northern Bay. This set-

down restricted the landward flow from the Bay mouth. It appears to generate the convergence in the mid-Bay and make the swollen-up surge elevation in the mid-portion of the Bay (see September 16 16:00 UTC in Figure 5-4). On September 16 17:00 UTC, as the eye of the hurricane swept over the Bay mouth, the winds changed to northwesterly winds with a maximum speed of 23.4 m/s (not shown). From September 16 18:00 UTC, the surge height started to decrease (Figure 5-10d). The negative surge appears to propagate from the Bay mouth to the mid-Bay and the seaward flow was intensified (Figure 5-10e). At the same time, in the northern portion, the negative surge induced by northerly/northwesterly winds propagated to the lower Bay (Figures 5-11d, e and Figure 5-5). As a result, the surge heights inside the Bay had negative values and the intensified seaward flow became weakened over time (Figures 5-10f and 5-11f).

There are some distinct barotropic phenomena that occurred during Hurricane Floyd: 1) the inflow induced by northeasterly winds corresponded to the first peak of storm surge, 2) strong local northeasterly/easterly winds generated the second peak of storm surge at the mouth, 3) the intensified seaward flows from the northern Bay converged to the second surges in the mid-Bay and restricted the landward flows, and 4) northwesterly winds drove the water out of the Bay. The outgoing flows were stronger than incoming flows due to the following reasons: 1) water in the lower Bay was driven by local northwesterly winds out of the Bay; 2) the negative surge wave propagated from the southern continental shelf to the mouth (effect of remote offshore winds); 3) the barotropic flow out of the Bay was induced by a seaward horizontal pressure gradient force between the Bay and the shelf; and 4) the river discharge augmented the landward flows. The combination of these effects appears to cause the seaward current to become

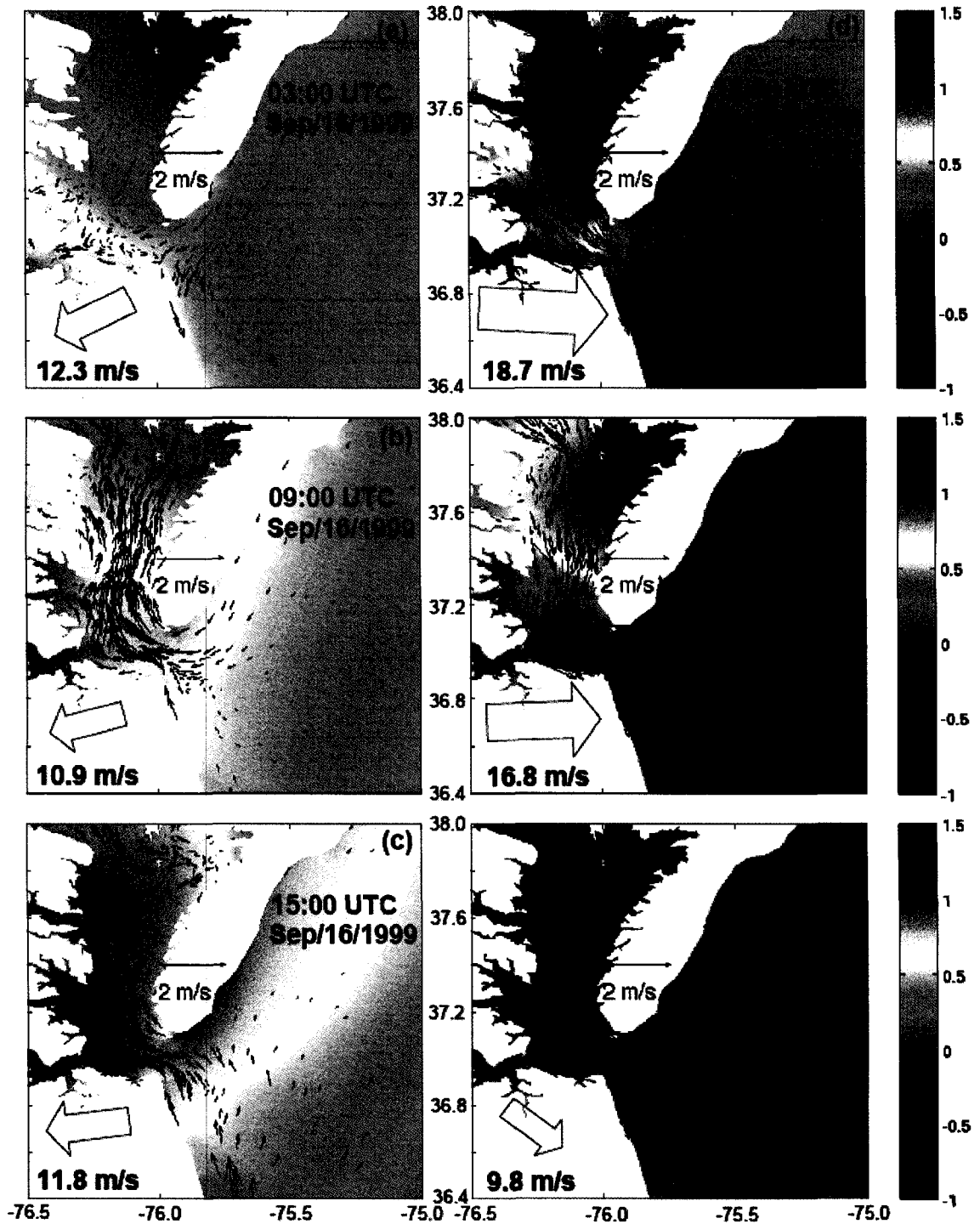


Fig. 5-10 Horizontal distributions of depth-integrated flow (thin arrows) at the southern portion of the Chesapeake Bay during Hurricane Floyd with time sequence from (a) September 16 03:00 UTC to (f) September 17 12:00 UTC. Colored map represents storm height and the thick arrow specifies wind speed and direction recorded at CBBT, VA.

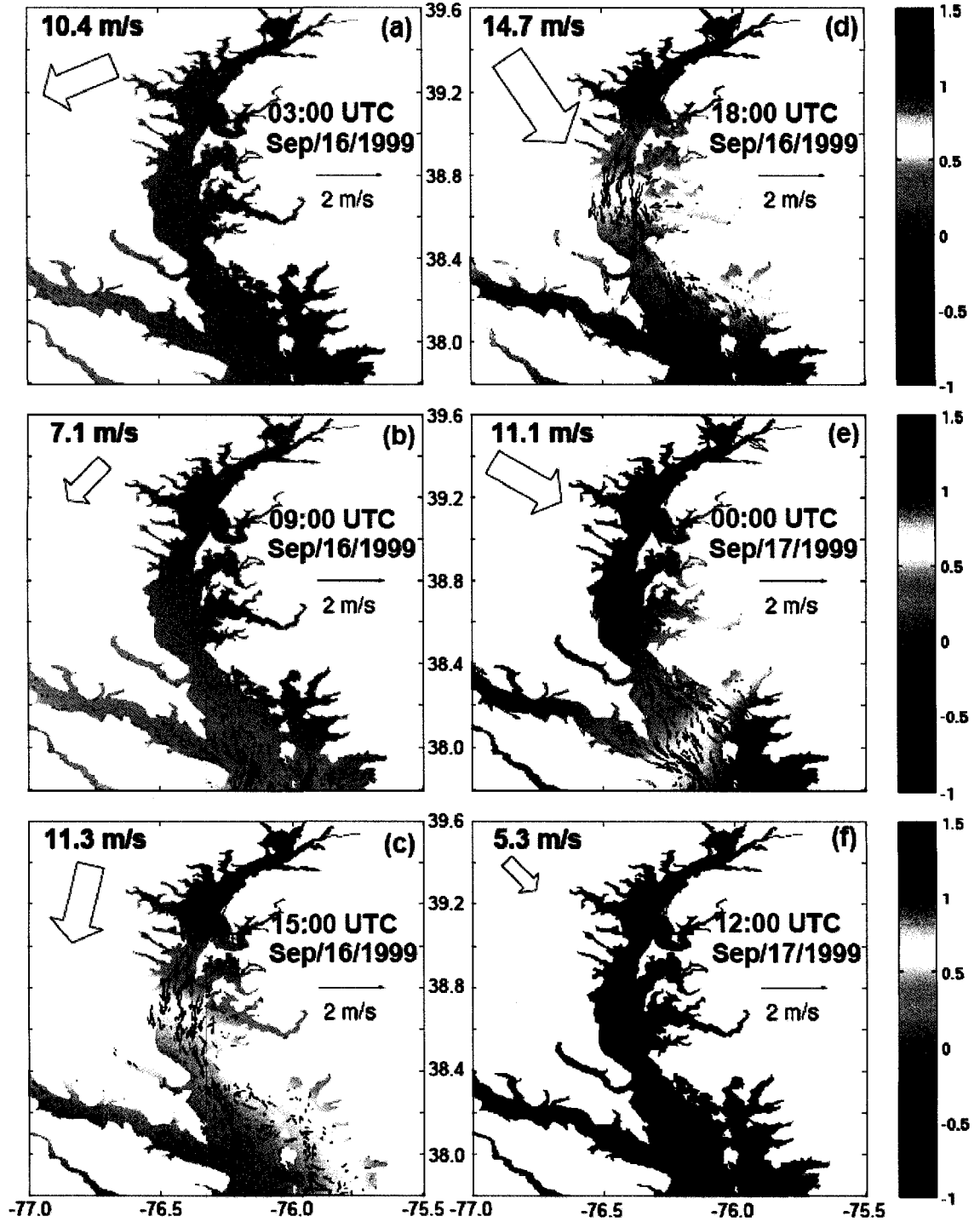


Fig. 5-11 Horizontal distributions of depth-integrated flow (thin arrows) at the northern portion of the Chesapeake Bay during Hurricane Floyd with time sequence from (a) September 16 03:00 UTC to (f) September 17 12:00 UTC. Colored map represents storm height and the thick arrow specifies wind speed and direction recorded at Lewisetta, VA.

stronger than the landward current that was generated during the storm.

### Hurricane Isabel

The barotropic flow during Hurricane Isabel was analyzed in the same way as that described during Hurricane Floyd. Time sequences of the sub-tidal depth-integrated flows were plotted in the Bay's southern portion (Figure 5-12) and northern portion (Figure 5-13). Initially, the seaward flows were driven by northeasterly winds (Figures 5-12a and 5-13a). According to the surge height recorded at CBBT (Figure 5-6), the surge increased gradually, even though the barotropic flow was seaward. This surge increase appears to be caused by the convergence (or set-up) that the southward flow from the mid-Bay to the mouth induced by northeasterly winds (effect of local winds) is stronger than the seaward flow at the mouth. This seaward flow may be weakened by the landward Ekman transport induced by northeasterly winds on the continental shelf (the effect of remote winds). From September 18 0900 UTC, the seaward flow in the lower Bay started to decrease and changed into a landward flow as the winds strengthened (Figure 5-12b). This period coincides with the time when surge increased fast in the lower Bay (see the first three stations in Figure 5-7). During the three-hour period of 1800 to 2100 UTC on September 18, the maximum easterly winds up to 23.0 m/s generated the strong landward flows corresponding to the primary storm surge in the lower Bay (Figure 5-12c). Over the same period, the seaward flows induced by local northeasterly winds in the upper Bay began to change into northward flows due to northward horizontal pressure gradient (Figure 5-13b,c). The southeasterly and southerly winds became dominant when Hurricane Isabel was passing west of the Bay. These



winds intensified the northward flows and generated wind-induced set-down in the lower Bay (Figure 5-12d,f) and wind-induced set-up in the upper Bay (Figure 5-13d,f). During this period, the peak of the surge height occurred in the upper Bay. On September 19 0900 UTC, the landward flows at the mouth began to change to seaward. Although the winds blew toward north or northeast, the barotropic flows were directed out of the Bay (Figures 5-12f and 5-13f). One of the reasons for this is that the seaward horizontal pressure gradient force competing against the northward wind stress began to predominate. Another reason is that the flow toward the northeast on the continental shelf drove the water out of the Bay (see Figure 5-12e,f). Additionally, freshwater discharge added to the landward flows.

During Hurricane Isabel, the barotropic flow motion can be summarized as follows: 1) the southward flow induced by local northeasterly winds and the Ekman transport from the shelf corresponded to the gradually increased surge height, 2) strong easterly winds at the mouth intensified the storm surge initialized by offshore northeasterly winds, 3) the northward flows intensified by the southerly winds gave rise to the maximum peak of the surge in the upper Bay, and 4) the seaward horizontal pressure gradient force drove the water out of the Bay to recover to a normal status. The volumetric transport will be discussed in the next section.

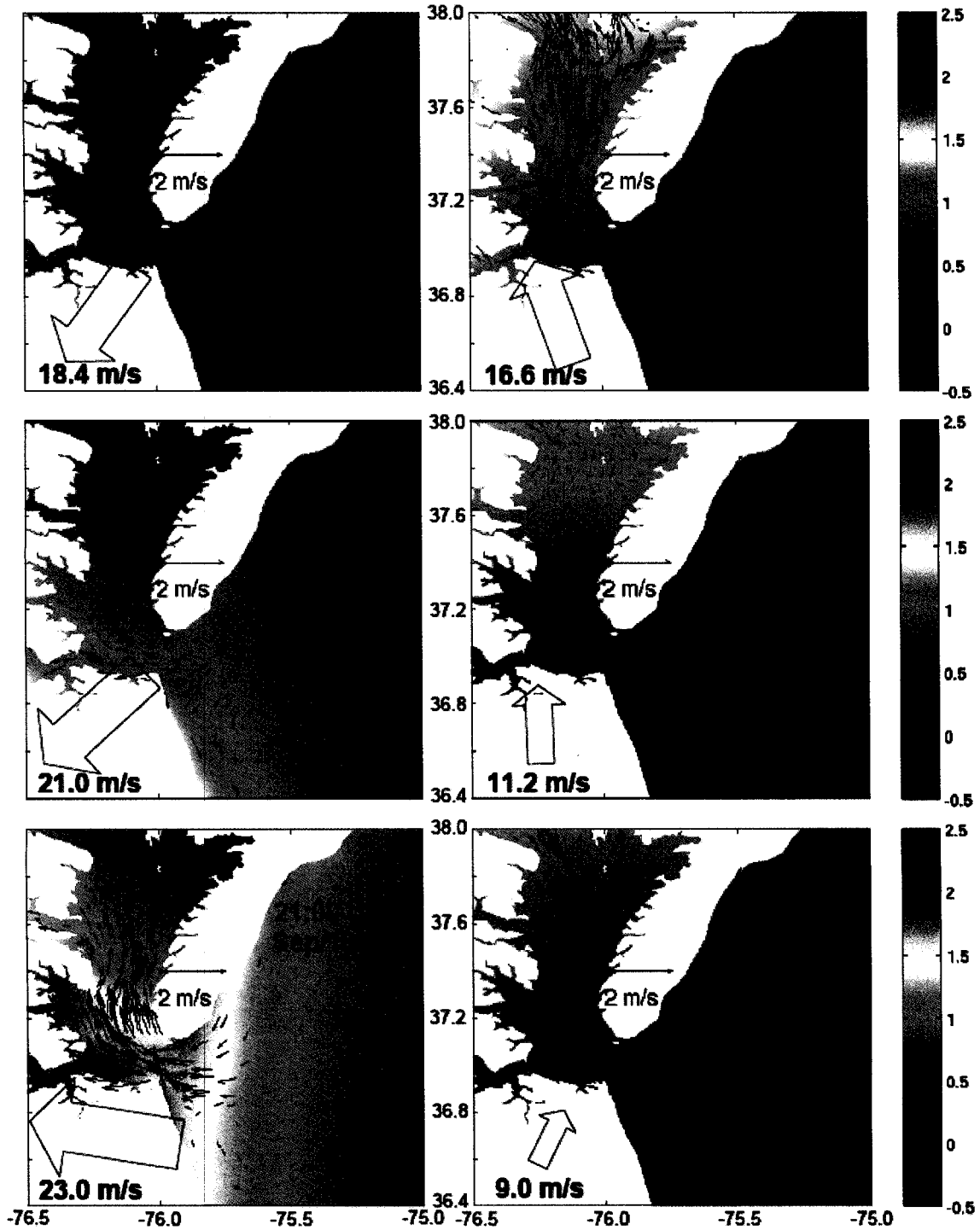


Fig. 5-12 Horizontal distributions of depth-integrated flow (thin arrows) at the southern portion of the Chesapeake Bay during Hurricane Isabel with time sequence from (a) September 18 09:00 UTC to (f) September 19 18:00 UTC. Colored map represents storm height and thick arrow specifies wind speed and direction recorded at CBBT, VA.

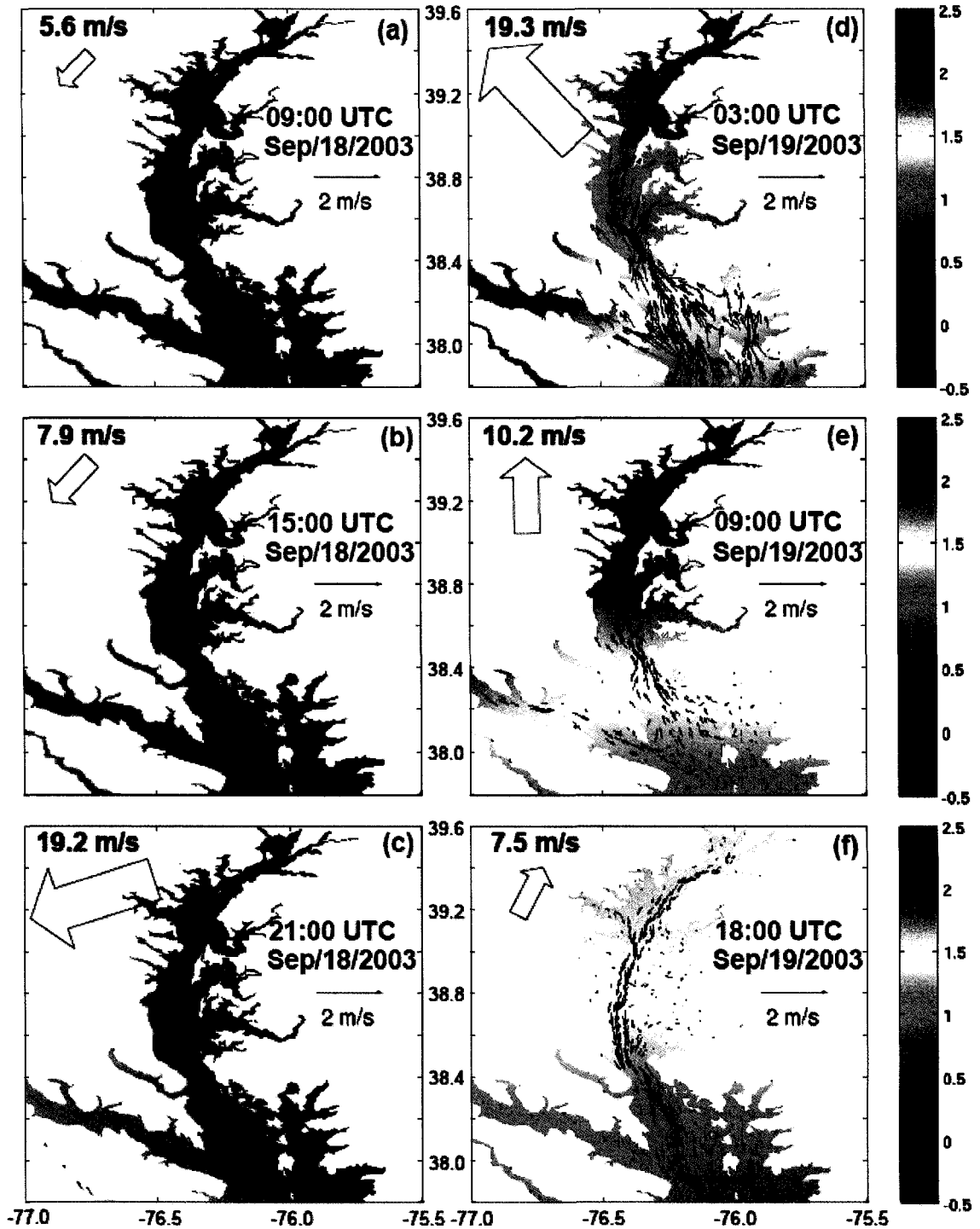


Fig. 5-13 Horizontal distributions of depth-integrated flow (thin arrows) at the northern portion of the Chesapeake Bay during Hurricane Isabel with time sequence from (a) September 18 09:00 UTC to (f) September 19 18:00 UTC. Colored map represents storm height and the thick arrow specifies wind speed and direction recorded at Lewisetta, VA.

### 5.3.2 Calculation of volumetric transport

Based on the continuity equation, the volumetric flux across a transect can be computed as follows (Gong et al., 2009):

$$F = \frac{dV}{dt} \quad (5.1)$$

where  $F$  is the flux ( $\text{m}^3 \text{s}^{-1}$ ),  $V$  is the instantaneous volume in the interior area delineated by the transect and the surrounding coastline for either the entire Bay or sub-estuaries. The instantaneous volume in a delineated area was calculated as the integration of cell volumes, which was defined as the cell area multiplied by the cell's total water depth (Vieira, 1985; Gong et al., 2009). Another way to calculate the transport is as follows (Kuo and Park, 1992):

$$F = \int_A u \, dA \quad (5.2)$$

where  $u$  is the velocity normal to each cell area ( $A$ ) of a transect. This method can be sufficient to estimate not only longitudinal flows along the mainstem, but also lateral volumetric exchanges between the Bay mainstem and its tributaries (Cercio and Cole, 1994). The time series of the volumetric flux across a transect represents only the temporal variation of the flux. Thus, in order to examine the spatial distribution of the flux, the flux was calculated at nine transects along the Chesapeake Bay mainstem and six transects in its tributaries (Figure 5-2) using Eq. (5.2).

#### Hurricane Floyd

The volumetric flux was averaged every half day over one tidal cycle to remove the intratidal variability. Half-daily net fluxes are shown in Figure 5-14. During

Hurricane Floyd, the net flux in the main Bay is characterized by the following three general patterns: 1) the landward fluxes at all transects were dominant through September 14, 2) the seaward flux became dominant from September 15 to 17, and 3) the landward flux again occurred after September 18 (Figure 5-14a). Normally, the flux shows the maximum value at the transect of the Bay mouth (tr01) and decreases as transects to the north (tr02 to tr09). Interestingly, during the second half of September 15, the net flux at tr01 was smaller than that at tr02. This indicates that influx in the region surrounded by tr01, tr02, and Jam, is larger than the outflux. This caused the convergence and increased the water volume in the region, and consequently the landward net flux occurred at the transect of the James River (Figure 5-15a). During the first half of September 16, the net fluxes across tr01 and tr02 were landward but those across tr03 to tr09 were seaward. Heading north to transect tr06, the net flux across each downstream transect was smaller than that across the upstream transect. Additionally, all net fluxes across five tributary transects (Jam to Pat) showed negative (landward) fluxes. This indicates that the landward flux across tr01 due to northeasterly winds was inhibited by the seaward flux from the upstream and, consequently, the convergence not only caused the landward net flux into the tributaries but also increased water volume (Figure 5-15b). During the second half of September 16 and the first half of September 17, a huge seaward net flux occurred due to strong northwesterly winds. As the net flux across the downstream transect was larger than that at the upstream transect, the divergence occurred in the lower Bay. It decreased water volume and caused the seaward net flux across transects of the tributaries (Figure 5-15c,d). During the second half of September 17, the seaward flux decreased noticeably and it was considerably similar to the first half of September 16

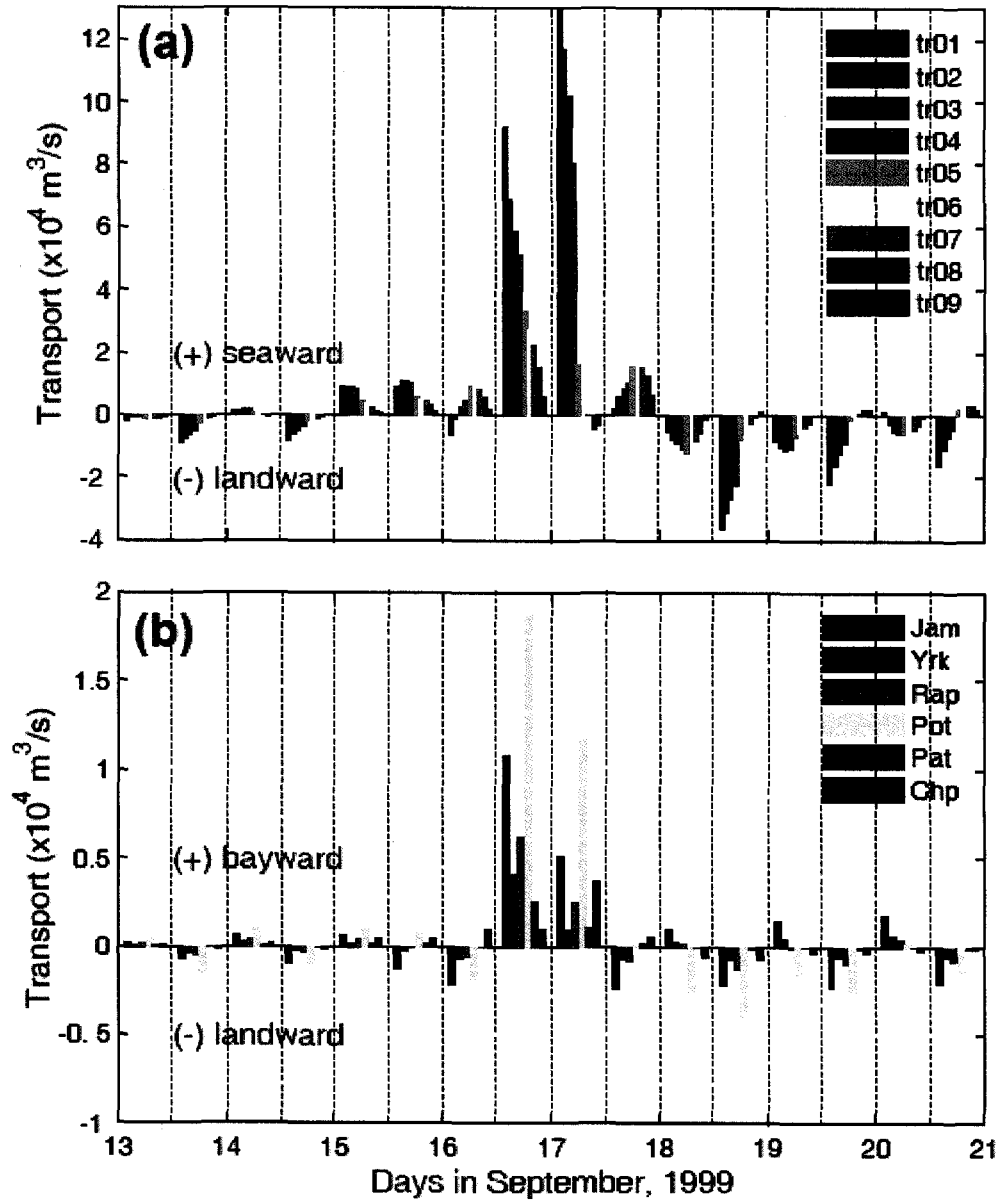


Fig. 5-14 One tidal-cycle mean volumetric transport at each transect (a) in the Chesapeake Bay mainstem and (b) its tributaries during Hurricane Floyd, 1999.

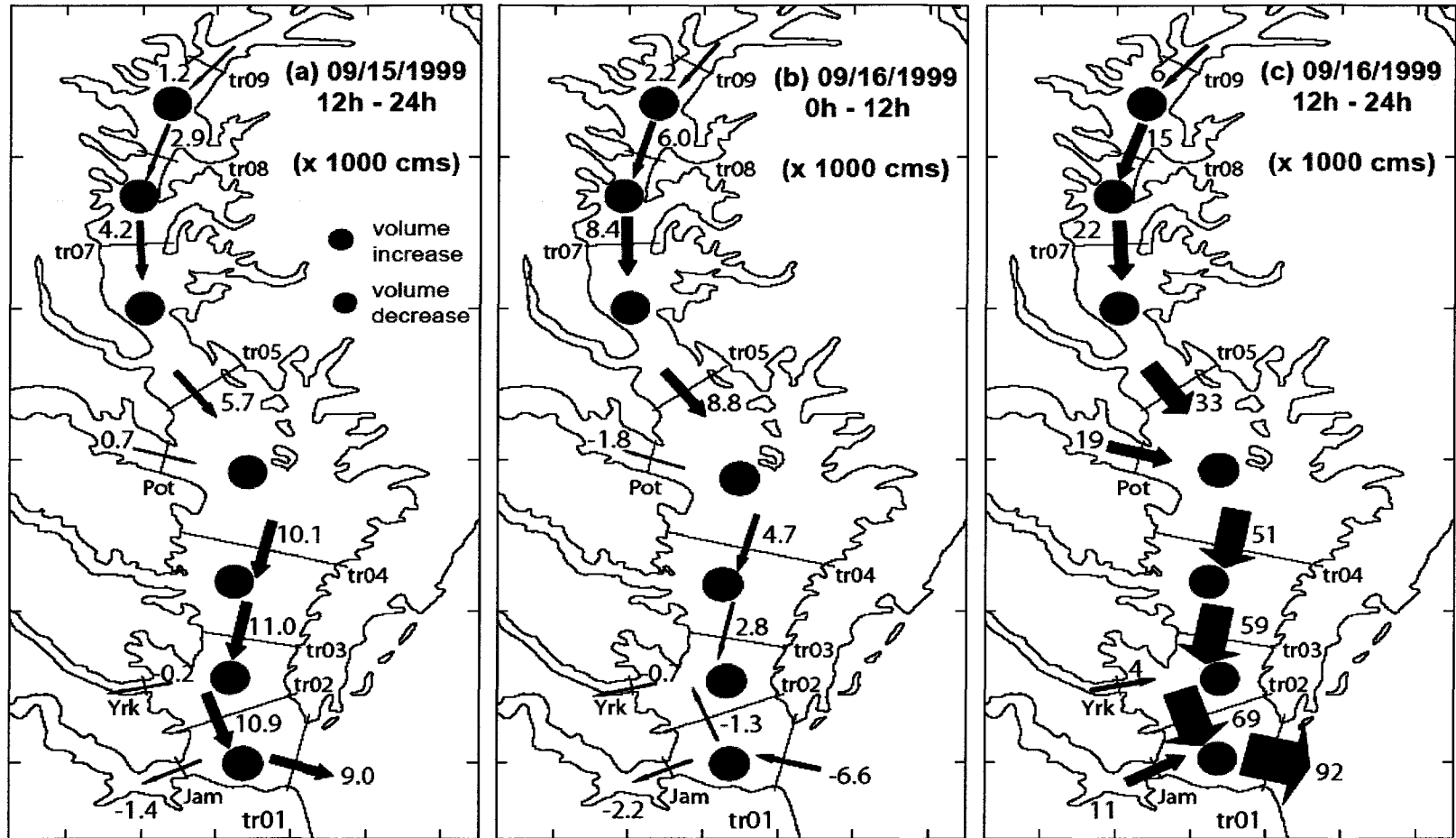


Fig. 5-15 Time sequence of volumetric net transport ( $\text{m}^3 \text{s}^{-1}$ ) averaged over a tidal cycle at transects in the lower Chesapeake Bay during Hurricane Floyd, 1999. The positive value denotes seaward flux and red and blue colors represent the increase and decrease of water volume, respectively.

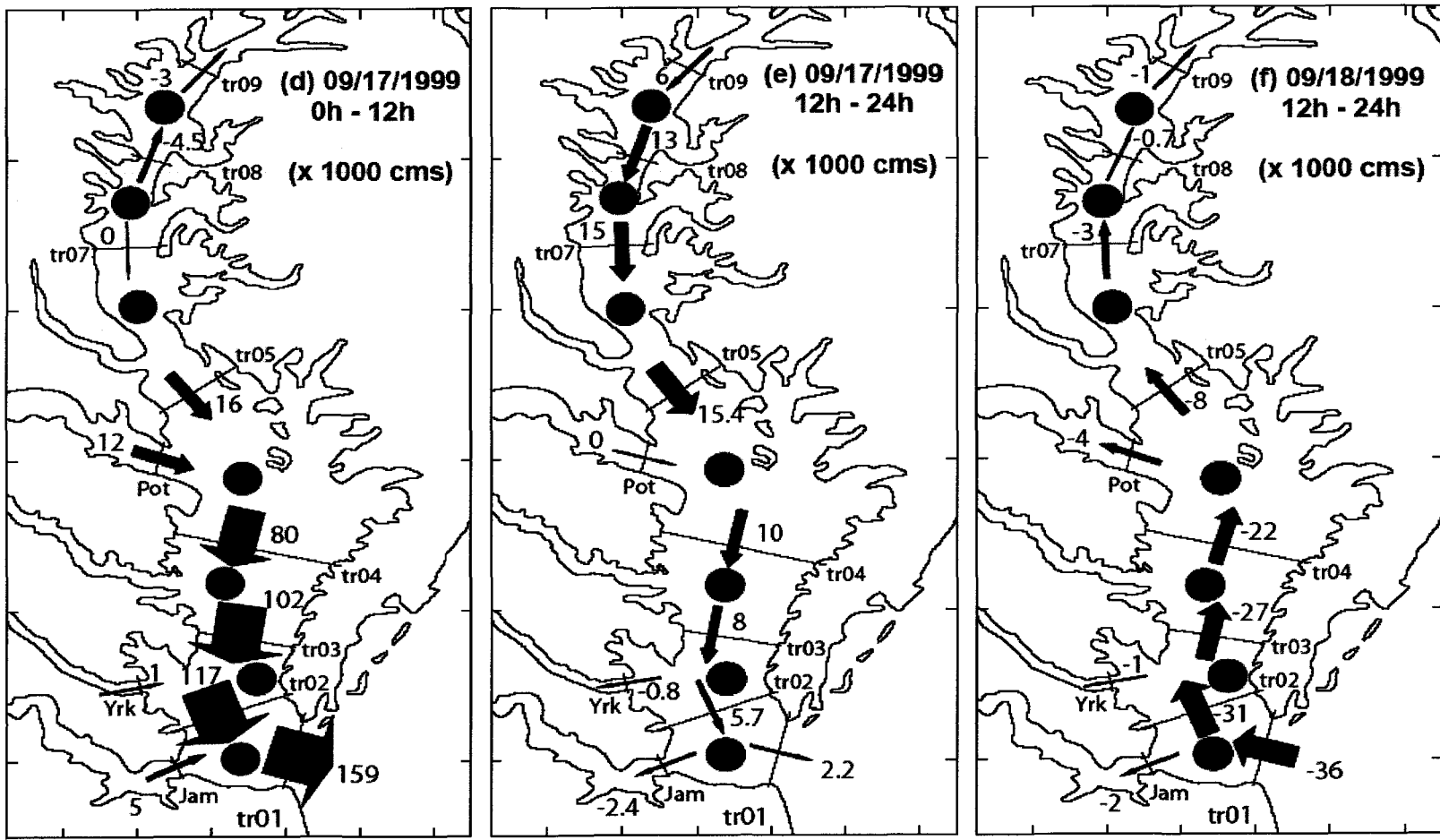


Fig. 5-15 Continued.



indicating water volume increased again (Figure 5-15e). After September 18, the landward flux was dominant across each transect and water volume gradually increased to recover (Figure 5-15f).

### Hurricane Isabel

The volumetric transport during Hurricane Isabel was analyzed in the same way as that performed during Hurricane Floyd. During Hurricane Isabel, the net flux in the Bay mainstem is characterized by three general patterns as follows: 1) the landward fluxes across all transects were dominant through September 17, 2) the huge landward flux occurred from the second half on September 18 through the first half on September 19, and 3) the huge return flux again headed seaward from the second half on September 19 to the first half on September 20 and then decreased (Figure 5-16a). From the second half of September 17 to the second half of September 18, the landward flux induced by northeasterly and easterly winds across downstream transects was larger than that across upstream transects. This caused the generation of a convergence to increase water volume in the lower Bay (Figure 5-17a,b). During the first half of September 19, when the winds changed to southeasterly and southerly winds, the landward flux across downstream transects became smaller than that across upstream transects. As a result, divergence occurred and decreased water volume in that region (Figure 5-17c). The net fluxes across transects became seaward during the second half of September 19. Although southerly winds blew, the seaward flux dominated. Since downstream flux exceeded upstream flux in the lower Bay, it increased water volume slightly (Figure 5-17d). During the first half of September 20, the seaward flux increased but the flux

across downstream transects was smaller than that across upstream transects, so that the water volume decreased (Figure 5-17e). One day later, the seaward flux again decreased but, still, water volume decreased as well (Figure 5-17f).

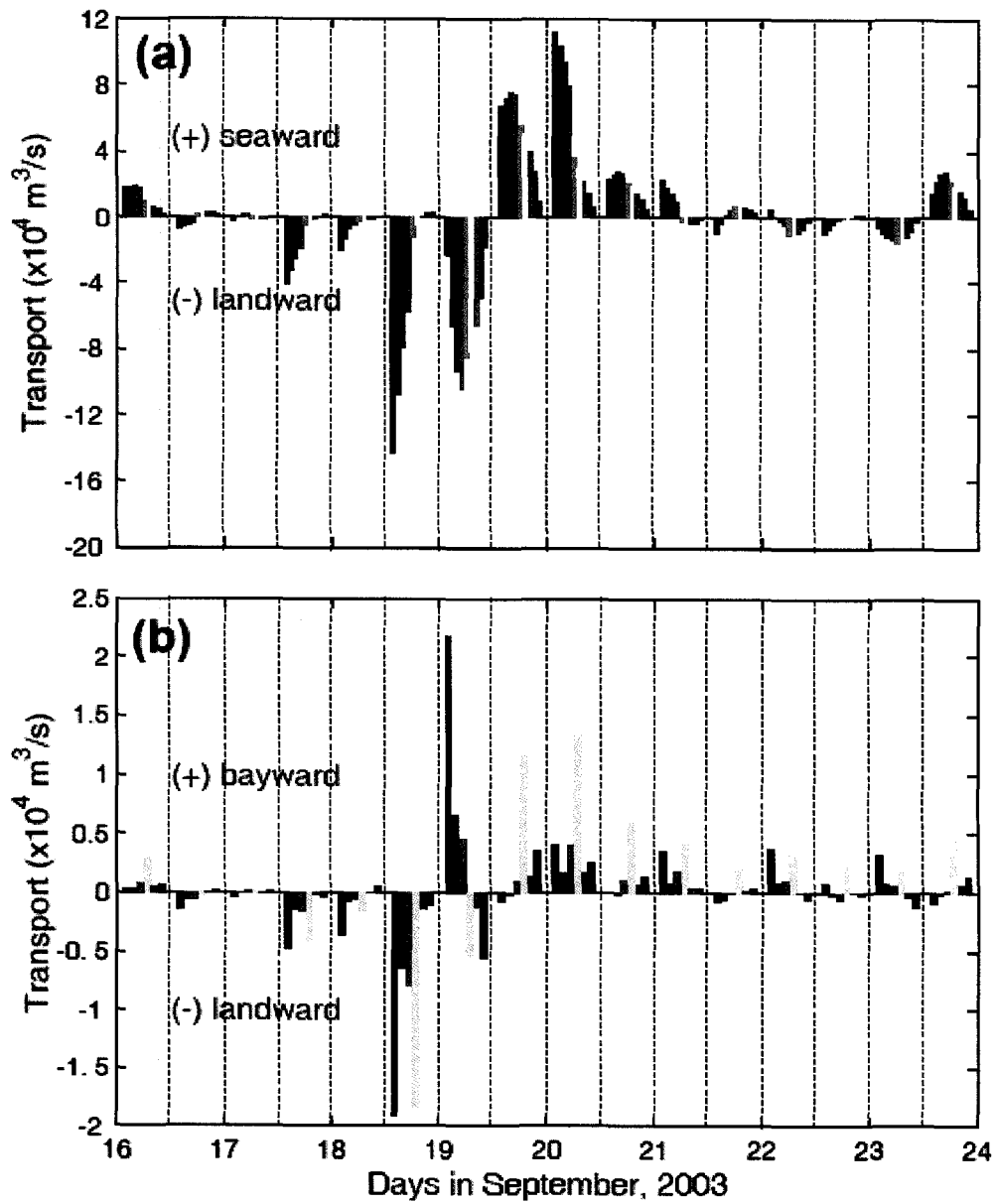


Fig. 5-16 One tidal-cycle mean volumetric transport at each transect (a) in the Chesapeake Bay mainstem and (b) its tributaries during Hurricane Isabel, 2003.

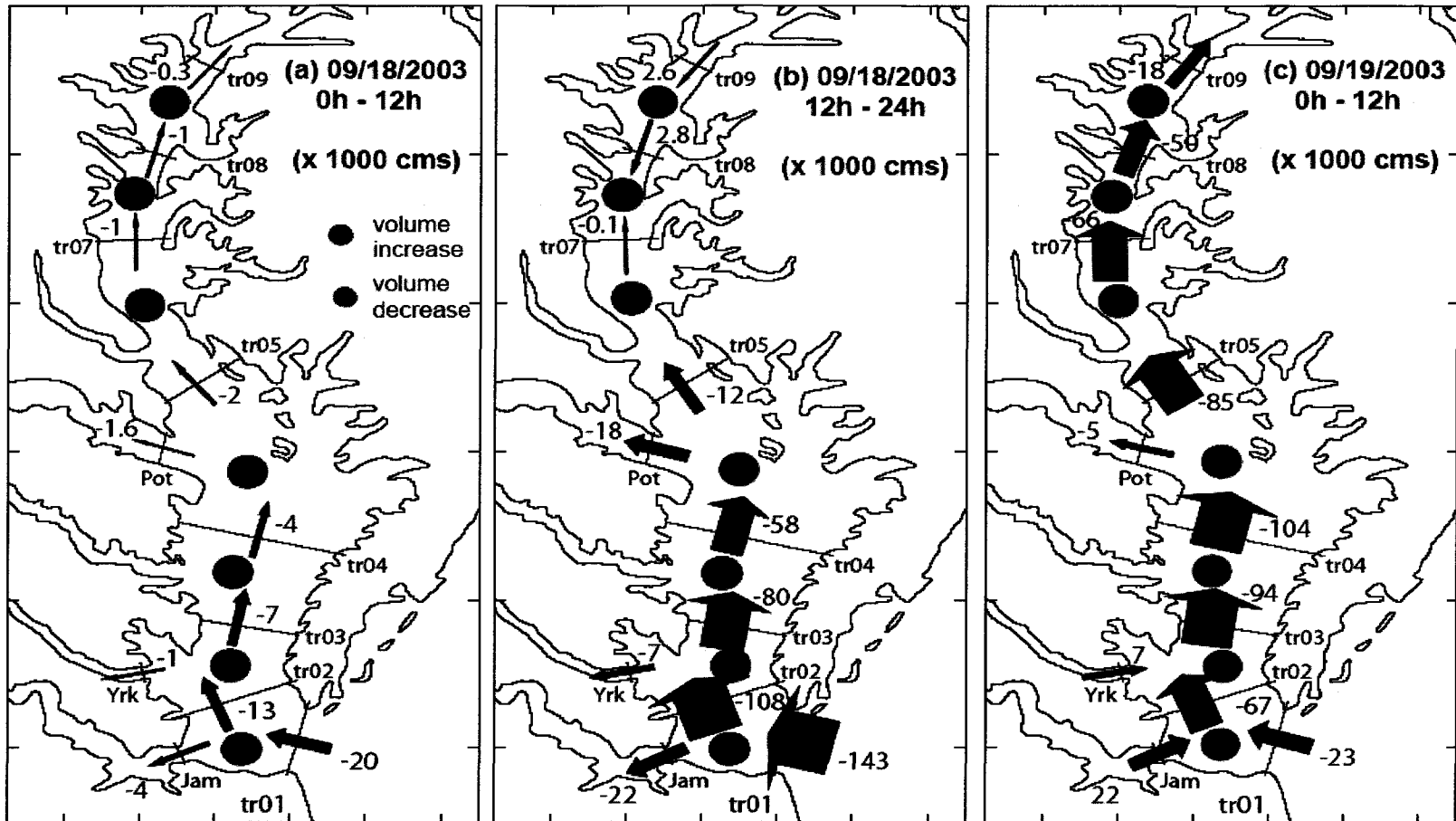


Fig. 5-17 Time sequence of volumetric net transport ( $\text{m}^3 \text{s}^{-1}$ ) averaged over a tidal cycle at transects in the lower Chesapeake Bay during Hurricane Isabel, 2003. The positive value denotes seaward flux and red and blue colors represent the increase and decrease of water volume, respectively.

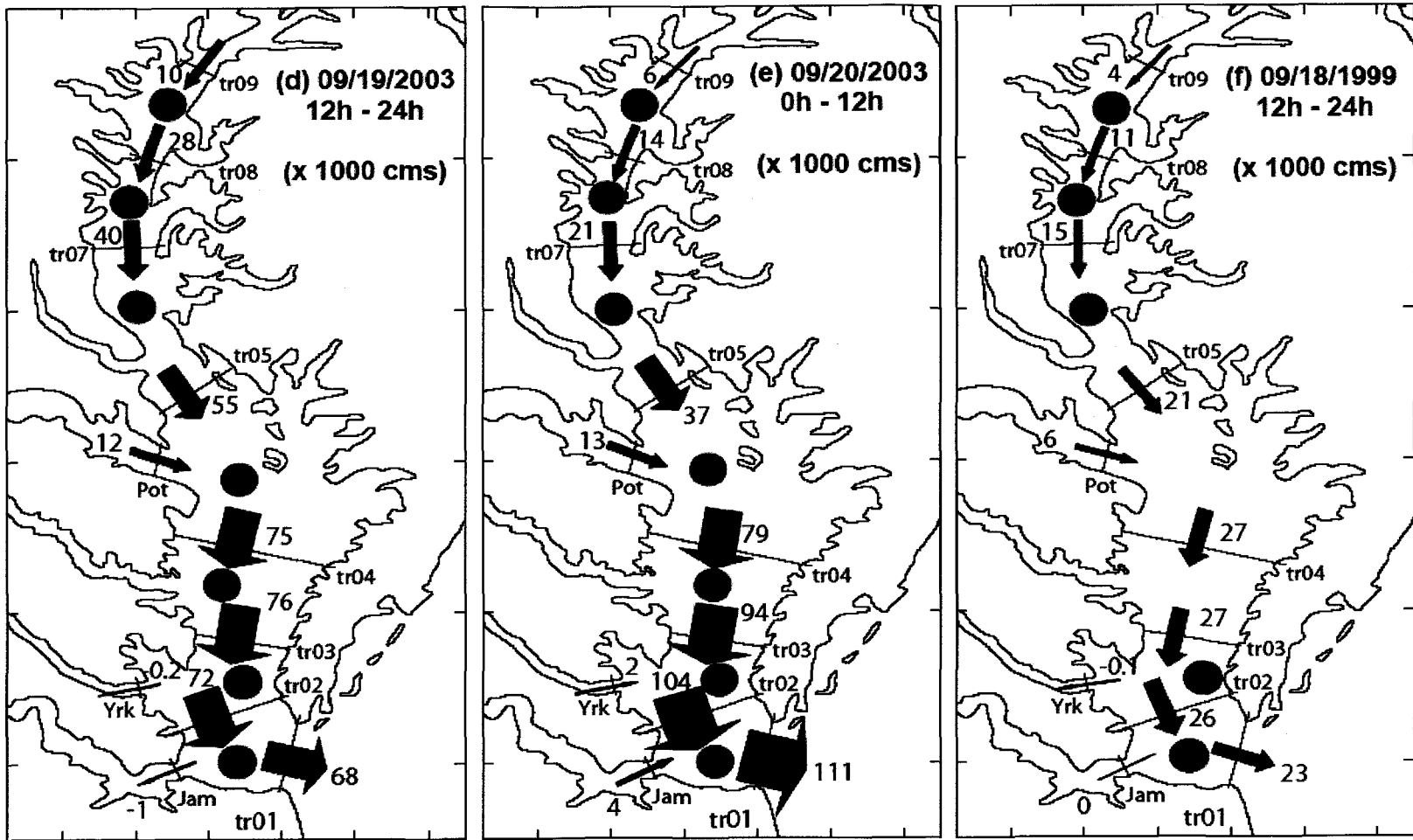


Fig. 5-17 Continued.

## **5.4 Effects of external forcing on sea surface elevation**

The effects of local and remote winds are examined in this section. Since it is difficult to define and separate the remote wind, first the local wind was defined as the wind blowing inside the Chesapeake Bay model area. In contrast, the wind in the remaining model domain was defined as the remote wind (Shen et al., 2006a; Shen et al., 2006b; Gong et al., 2009). Two additional numerical experiments were performed using local and remote winds for each hurricane. These experiments will verify how local/remote winds play significant roles on the water surface elevation in the Chesapeake Bay.

Next, the effect of river inflows on the water surface elevation has been investigated. Typically, a hurricane event brings a large quantity of rainfall that causes a huge river discharge. During Hurricane Isabel, not only high water surface elevation, but also a huge amount of river discharge, was recorded at Washington, DC in the upstream portion of the Potomac River. It is noteworthy to investigate the relationship between storm surge and river inflows because the combined effect will give us inundation damage in the upstream areas of the tributaries, which have a large urban population.

### **5.4.1 Effect of local and remote winds**

The time series of storm surge height for the experiments was compared at five selected stations (Figure 5-18). Three experiments during Hurricane Floyd were plotted on the left panels and those during Hurricane were plotted on the right panels. Some general features can be found: 1) the surge induced by remote winds propagated from the Bay mouth to upper Bay with the same magnitude of the surge, 2) the effect of local

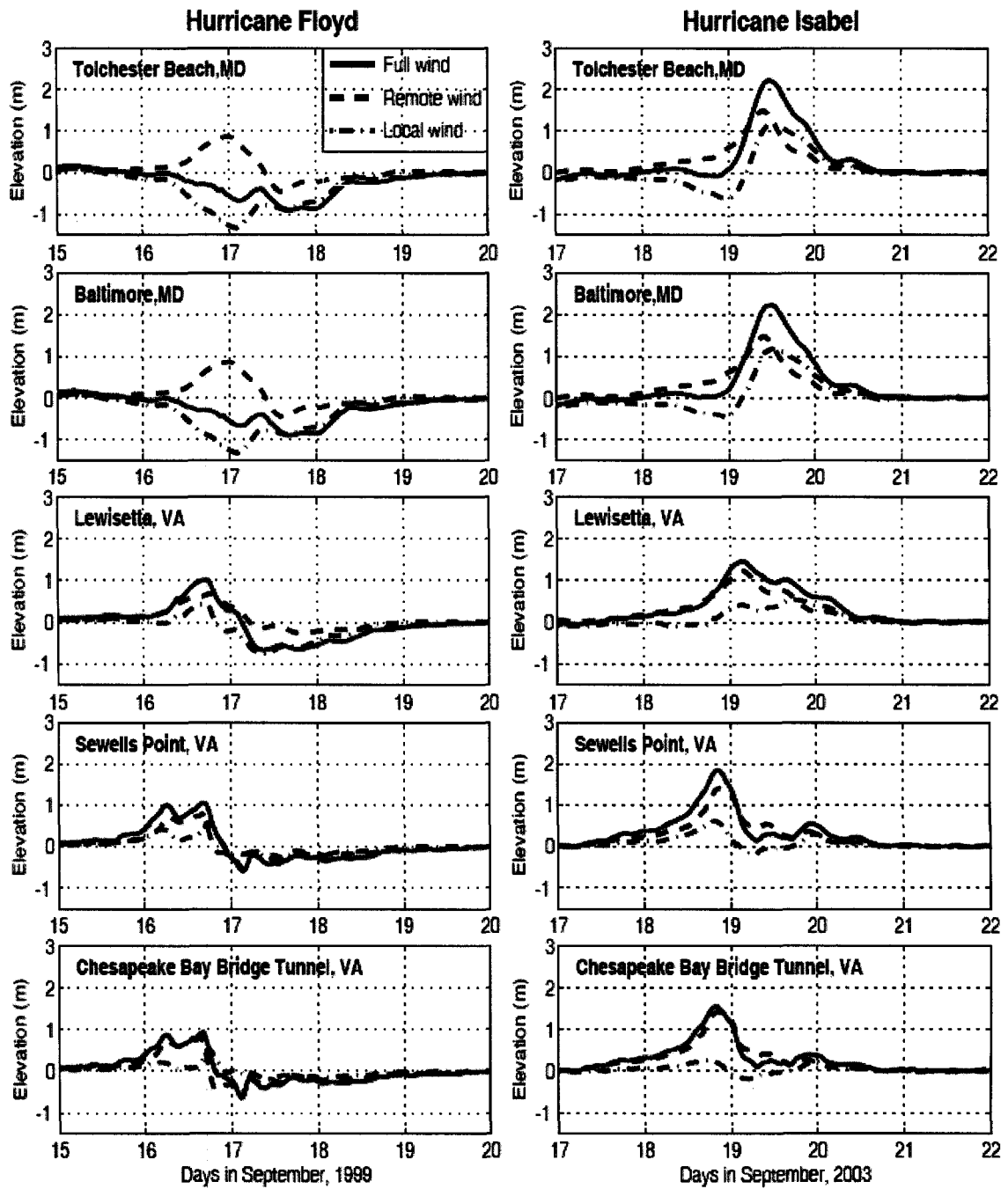


Fig. 5-18 Comparison of storm surge height among three cases, local (dash-dotted), remote (dashed), and combination (solid), at five selected stations during Hurricane Floyd, 1999 (left panels) and Hurricane Isabel, 2003 (right panels).

winds on water surface elevation dominated in the upper Bay, and 3) in the upper Bay, northerly local winds (Hurricane Floyd) dominantly made elevation set-down whereas southerly local winds (Hurricane Isabel) dominantly generated the elevation set-up. The results indicate that the effects of local and remote winds have nearly linear relationships with the sea surface elevation to lowest order.

#### 5.4.2 Effect of river inflows

The effect of river inflows during Hurricane Isabel was tested in the Potomac River, the second largest tributary of the Chesapeake Bay. The daily mean river streamflow obtained from USGS at the Little Falls Pump Station near Washington, DC, was applied as a river boundary condition. Two experiments were performed: 1) without river discharge and 2) with river discharge. The time series of storm tide in two cases are plotted in Figure 5-19. Without river inflow, the model result reproduced the observed water surface elevation until September 20 1800 UTC. After that time, the model prediction underestimated. However, with river inflow, the model result reproduced the two peaks of water elevation. The results indicate that the first peak of water elevation at Washington, DC was purely caused by storm surge propagating from downstream, and the second peak was induced by river inflows from the upstream portion of the Potomac River. The river discharge in Potomac River was increased from September 20 (Figure 2-11), effectively increasing water surface elevation independently.



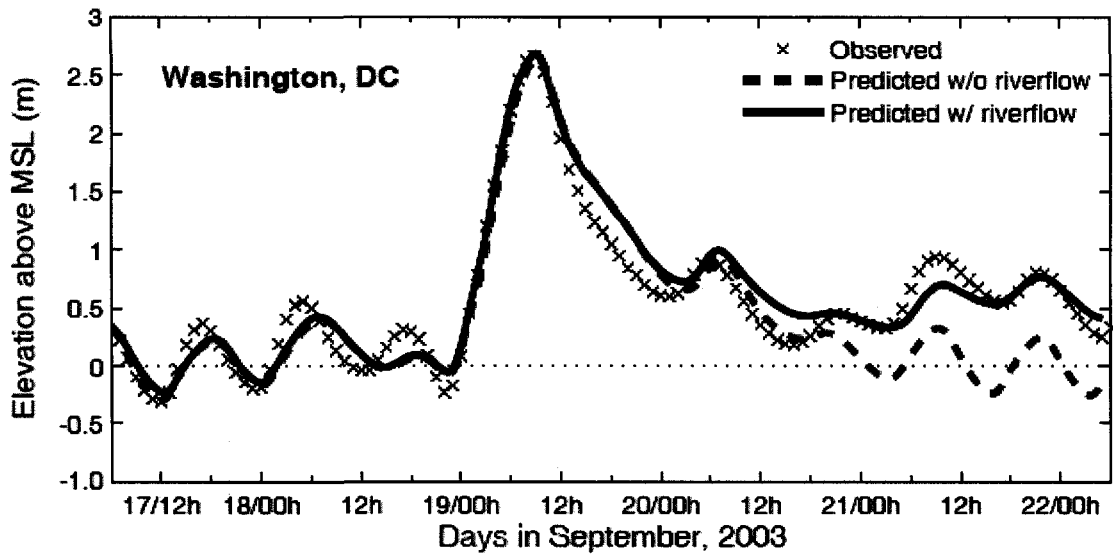


Fig. 5-19 Comparison of observed and predicted water surface elevations at Washington, DC, during Hurricane Isabel on September 2003.

## 5.5 Summary

The barotropic response of the Chesapeake Bay to the hurricanes has been investigated by terms of storm surge, depth-integrated barotropic transport, and external forcing. Based on the classification of two types of storms for the Chesapeake Bay, the model verified that the eastern-type storm, Hurricane Floyd, generated the maximum surge in the southern part of the Bay whereas the western-type storm, Hurricane Isabel, created the highest surge in the northern part of the Bay. In the upper Bay, the surge propagating from the Bay mouth was set down by northerly local winds during Hurricane Floyd whereas it was set up by southerly local winds during Hurricane Isabel. Independent of these two types, both hurricanes had three stages in terms of storm surge at the mouth of the Bay: 1) growing (pre-storm) stage, 2) transition (ongoing-storm) stage, and 3) decaying (post-storm) stage. However, there are two major differences between the two hurricanes: 1) On the growing stage, the surge during Hurricane Floyd increased due to the seaward flux induced by Bay (local) winds that was restricted by the landward flux induced by shelf (remote) winds. In contrast, the surge during Hurricane Isabel increased due to the landward flux induced by shelf winds that exceeded the seaward flux induced by Bay winds. 2) The seaward flux on the decaying stage during Hurricane Floyd dominated and this generated the divergence in the lower Bay to decrease the surge, whereas the landward flux dominated during Hurricane Isabel and this generated the divergence to decrease the surge in the lower Bay. Therefore, the temporal variation of local convergence/divergence in barotropic transport is the key to understanding better the propagation and evolution of storm surge. Additionally the barotropic exchange

between Bay (estuary) and its tributaries (sub-estuary) will be determined by the local convergence and divergence processes.

The numerical experiments for the effect of local and remote winds lead us to understand that both hurricanes has the same magnitude of remote wind effect but the opposite local wind effect on storm surge and barotropic transport. The model result suggests that river inflows should be the secondary forcing to increase the water surface elevation in the upstream of the Bay tributaries, which gives rise to the inundation damage.

The barotropic, the depth-integrated and laterally integrated volumetric transport (i.e., Eq. 5-2) across a transect denotes only the quantitative net flux during the hurricane events. The vertical structure and lateral variation of volumetric transport become important in the partially mixed estuary because it is characterized by the effects of stratification/destratification and Earth's rotation on the estuarine circulation. During a hurricane event, the circulation in the estuary should be controlled by the wind-driven circulation and the gravitational circulation. The sea surface elevation remaining after the storm passage is a combination of a quasi-stationary trough geostrophically adjusted with the depth-averaged currents and a sea surface elevation induced by the baroclinic effects (Ginis and Sutyrin, 1995). Therefore, the baroclinic effect during hurricane events on the circulation in the Chesapeake Bay will be discussed in Chapter VI.

## **Chapter VI**

# **A BAROCLINIC RESPONSE OF THE CHESAPEAKE BAY TO HURRICANES FLOYD AND ISABEL**

### **6.1 Introduction**

The baroclinic response of the Bay to a moving storm is characterized by volume and salt influx from the ocean, wind-induced vertical mixing, the effect of buoyancy induced by heavy rains and fresh water inflows, and accompanied by storm-induced barotropic/baroclinic flow motions. Vertical mixing has been shown to have a significant role in the gravitational circulation of estuaries (Pritchard, 1967). Increased exchange between surface and bottom water results in an increase in the potential energy of the system. In estuaries, vertical mixing is assumed to be primarily generated by the tide. However, wind-induced mixing often exceeds tide-induced mixing. In other words, the magnitude of wind-driven circulation frequently exceeds that of the gravitational circulation (Goodrich et al., 1987).

Typically, a tropical storm moving from the open ocean to coastal seas brings salt water with storm surge into estuaries. Associated rainfall also increases freshwater discharges from the upstream of estuaries. These two aspects increase horizontal density and pressure gradients in estuaries and affect the estuarine circulation. Hurricane-induced saltwater influx in a partially mixed estuary or river has significant effects on not

only physical properties but also biogeochemical dynamics (Valle-Levinson et al., 2002; Roman et al., 2005; Boicourt, 2005; Frazer et al., 2006; Miller et al., 2005; Reay and Moore, 2005; Tango et al., 2006; Trice et al., 2005; Gong et al., 2007; Li et al., 2007). In particular, hurricane-induced pulses of high salinity have important consequences for submersed aquatic vegetation (SAV) and shifts in distribution and abundance of ocean fish (Conner, 1993; Gresham, 1993; Williams, 1993). Saltwater flooding can also be caused by storm surges that significantly alter forest communities (Conner and Inabinette, 2005). Thus, the effects of the exchange of saltwater induced by a hurricane will be examined in this study.

Wind-induced destratification in the Chesapeake Bay was frequently observed to occur from early autumn through mid-spring (Goodrich et al., 1987). Blumberg and Goodrich (1990) numerically verified that the destratification resulted from storms in early autumn. Their numerical experiments indicate that internal shear is a more effective mechanism for destratification than direct propagation of turbulence from the surface. Recently, however, Li et al. (2007) explored the hurricane-induced destratification and post-storm restratification processes in the Chesapeake Bay during Hurricane Isabel, 2003. They suggested that the combined remote and local wind forcing can cause the different effects on turbulent mixing, and after the hurricane passed, turbulent mixing due to tides or subsequent winds works against the gravitational adjustment to produce quasi-steady salinity distribution in the Bay.

Alternatively, wind stress increases estuarine stratification by reducing the longitudinal density gradient (Geyer, 1997; North et al., 2004; Scully et al., 2005). Geyer (1997) showed that down-estuary winds enhanced surface outflow, significantly reducing

the along-estuary salinity gradient. North et al. (2004) demonstrated that increased stratification was associated with down-estuary wind events, but did not address the role that the increased stratification may play in reducing vertical mixing and enhancing the baroclinically driven estuarine circulation. In the York River Estuary, VA, Scully et al. (2005) found that down-estuary winds enhance the tidally averaged vertical shear, which interacts with the along-channel density gradient to increase vertical stratification, whereas up-estuary winds tend to reduce, or even reverse, the vertical shear, reducing vertical stratification, called *wind-induced straining*. Wind stress not only plays a predominant role in mixing away estuarine stratification, but also acts on straining the along-channel estuarine density gradient. In a partially mixed estuary system, down-estuary winds tend to enhance tidally averaged vertical shear increasing vertical stratification, whereas up-estuary winds tends to reduce or reverse vertical shear decreasing vertical stratification. In the Chesapeake Bay, two hurricanes that had different post-storm winds – northerly (down-estuary) winds after the passage of Hurricane Floyd (1999) but southerly (up-estuary) winds after the passage of Hurricane Isabel (2003) – may cause different de-stratification/re-stratification processes after the hurricanes passed. It is questionable how vertical destratification/restratification proceeds through the water column during the hurricane events.

The effect of the precipitation or freshwater input on the baroclinic circulation deserves to be verified because the buoyancy forcing from the river discharge tends to increase the horizontal density gradient on the surface of the water column and then increase the vertical density gradient. The freshwaters flowing out of the Bay generate a plume that could affect the interaction between the inner shelf and the Bay estuary.

The purpose of this study, therefore, is to examine the baroclinic response of the Chesapeake Bay to hurricane events, comparing Hurricanes Floyd and Isabel. Thus, the first goal is to investigate the saltwater transport in the Chesapeake Bay during the hurricanes, the second goal is to obtain further insights into the physics of storm-induced mixing in the Bay, and the last goal is to explore the influences of local and remote winds, and precipitation. The outline of this chapter is as follows. In Section 6.2 the saltwater transport induced by meteorological forcing in the Chesapeake Bay estuary is described. Hurricane-induced mixing process is examined in Section 6.3. The effects of local and remote winds and the influences of precipitation are discussed in Section 6.4 and Section 6.5, respectively. Concluding remarks are summarized in Section 6.6.

## **6.2 Meteorologically induced oceanic influx**

### **6.2.1 Profiles of velocity and salinity during Hurricanes Floyd and Isabel**

Based on three-dimensional, baroclinic SELFE model simulation as described in Chapter IV, the velocity and salinity model results responding to the two hurricanes were analyzed.

#### Longitudinal distribution of velocity and salinity

Longitudinal distributions of 25-hour averaged velocity and salinity were plotted in Figure 6.1 for Hurricane Floyd and in Figure 6.2 for Hurricane Isabel. As general remarks, both hurricanes generated vertical mixing and de-stratified the entire water column. However, stratification with a  $\Delta S$  around 2 ppt still remained in the mid-Bay

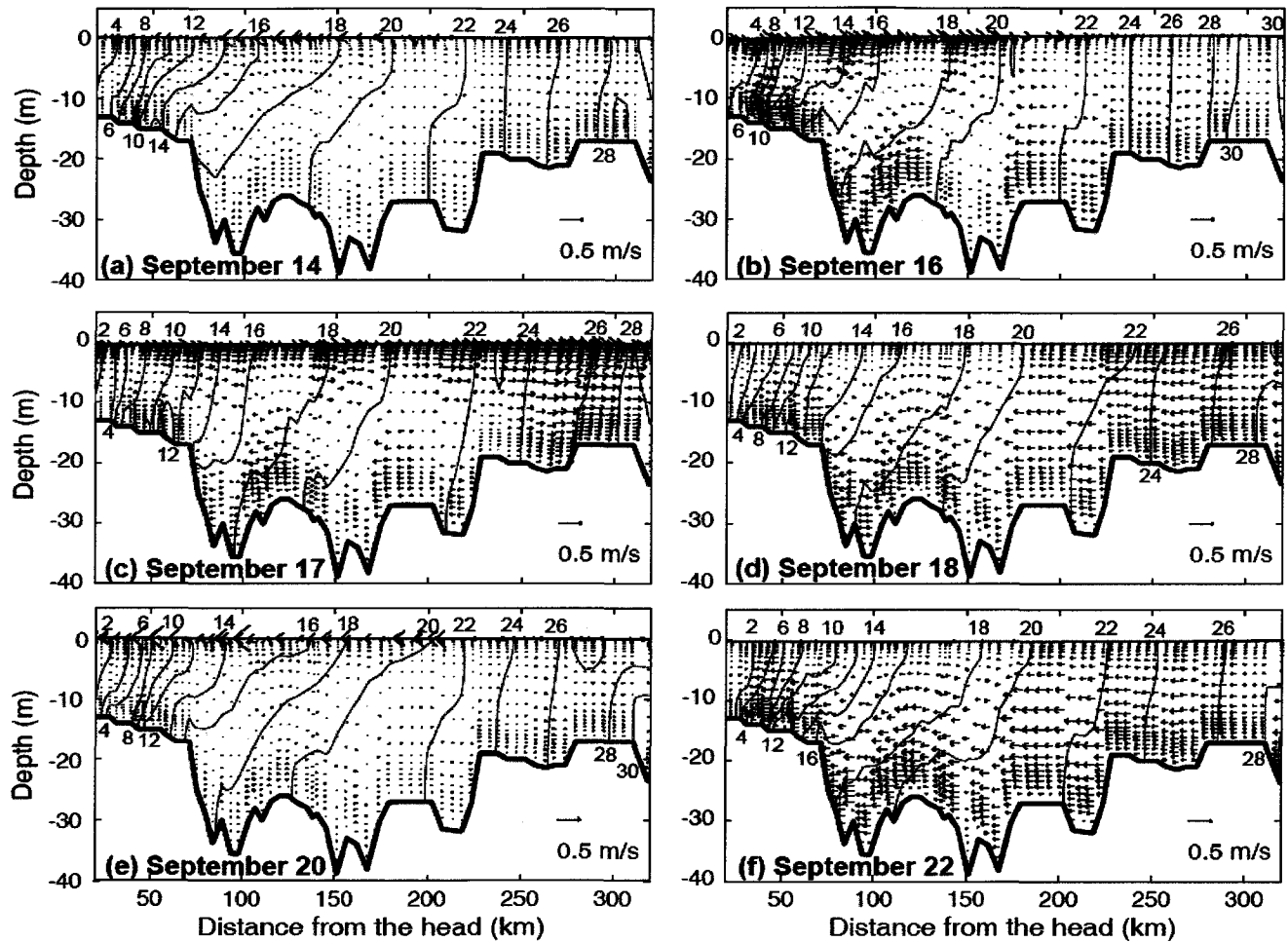


Fig. 6-1 Longitudinal distributions of tidally averaged (25 hours) velocity and salinity in the along-channel section of the Chesapeake Bay at six selected days during Hurricane Floyd, 1999.



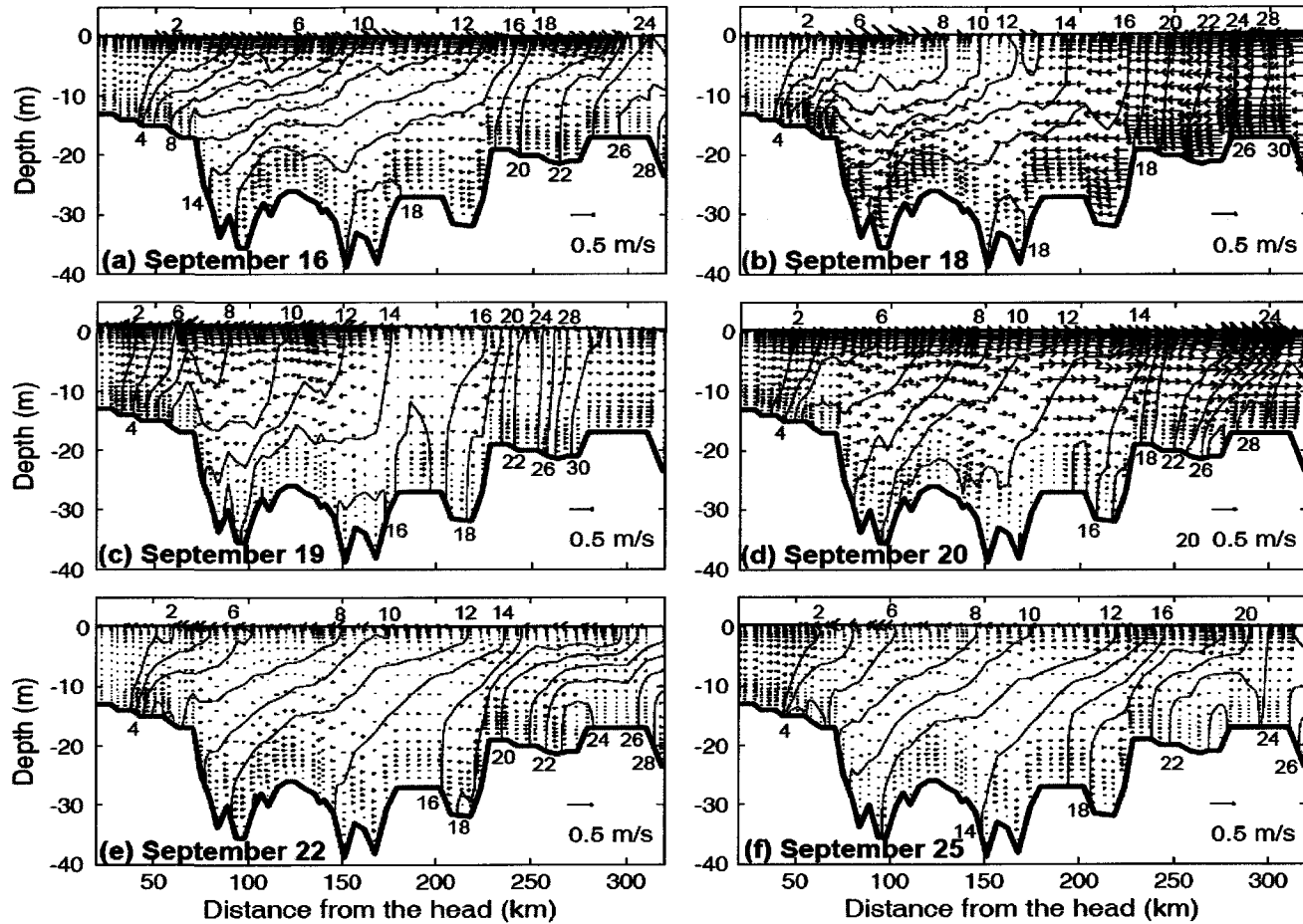


Fig. 6-2 Longitudinal distributions of tidally averaged (25 hours) velocity and salinity in the along-channel section of the Chesapeake Bay at six selected days during Hurricane Isabel, 2003.

during events although the surface mixed layer reached to 20 m in depth. Prior to the storm, the observed stratification ( $\Delta S$ ) in the Bay shows a significant difference between September 1999 and September 2003 (Table 6-1). At CB4.4, pre-Floyd stratification was nearly 4 ppt whereas pre-Isabel stratification was nearly 11.5 ppt. The model results showed that stratification in the mid Bay decreased by 2 ppt during Hurricane Floyd but decreased by 7 ppt during Hurricane Isabel. In the lower Bay, it is clear that the saltwater intrusion occurred during both hurricanes (see Figures 6-1b, 6-2b and c). In a semi-enclosed water body such as Chesapeake Bay, hurricane-induced saltwater influx from the ocean mainly occurs by the current that is driven by direct wind stress and a bayward barotropic pressure gradient. However, it is questionable how much saltwater flux exists and how far saltwater intrudes during these two hurricanes.

#### Lateral variation of velocity and salinity

During Hurricane Floyd, the lateral gradients of velocity and salinity were changed. Figure 6-3 shows the tidally averaged (25-h averaged) axial velocity and salinity transversely across the Bay mouth (tr01 in Figure 5-2), which represents a typical lateral distribution pattern of axial velocity and salinity during the storm. Prior to the passage of the hurricane's eye (Figure 6-3a), the region south of the Bay mouth had a two-layer circulation pattern, which shows that fresher water flows out of the Bay on the surface, whereas completely mixed saltier water flows into the Bay through the bottom. The area north of the Bay mouth (Cape Charles) was dominated by the landward saltwater flow. On September 16, an entirely seaward flow was dominant in the area south of the mouth (Cape Henry) and the water column became de-stratified showing

approximately 1 ppt salinity difference between surface and bottom. Completely well-mixed, laterally homogeneous net landward flow was characterized across the northern section, which is 10 to 25 km north of Cape Henry. After the passage of the eye over the mouth (September 17), the flow direction changed to seaward along the entire cross-section. The net surface flow in the deep channel was slightly stronger than that in the shallow region, which shows that salinity decreased by approximately 3-4 ppt. On the next day, the landward return flow occurred through the entire transect (Figure 6-3d). Stratification in the deep channel was slightly enhanced by 3-4 ppt due to relatively strong saltier water inflow through the bottom layer. Within a week, the net flow across the transect appeared to return to a two-layer circulation pattern and the vertical salinity structure appeared to be adjusted by the re-stratification process (Figure 6-3e and 6-3f).

During Hurricane Isabel, prior to the storm, the net flow across the transect showed a similar two-layer circulation pattern as that observed during Hurricane Floyd (Figure 6-4a). The salinity difference between surface and bottom waters in the deep channel was approximately 6-7 ppt, which is 4-5 ppt larger than the pre-Floyd condition. On September 18, the storm elicited the landward flows with vertically homogeneous saltwater from the ocean (Figure 6-4b). The surface flow was stronger than the bottom flow due to wind-generated vertical shear stress. Lateral salinity gradient was shrunk into the side of Cape Henry. The net flow started to change into the seaward flow through the entire transect on the next day and stratification in the deep channel started to be enhanced as well (Figure 6-4c). The seaward net flow became intensified on September 20, and a lateral salinity gradient began to extend to the side of Cape Charles (Figure 6-4d). Within a week, the net flow appears to return to a two-layer circulation pattern

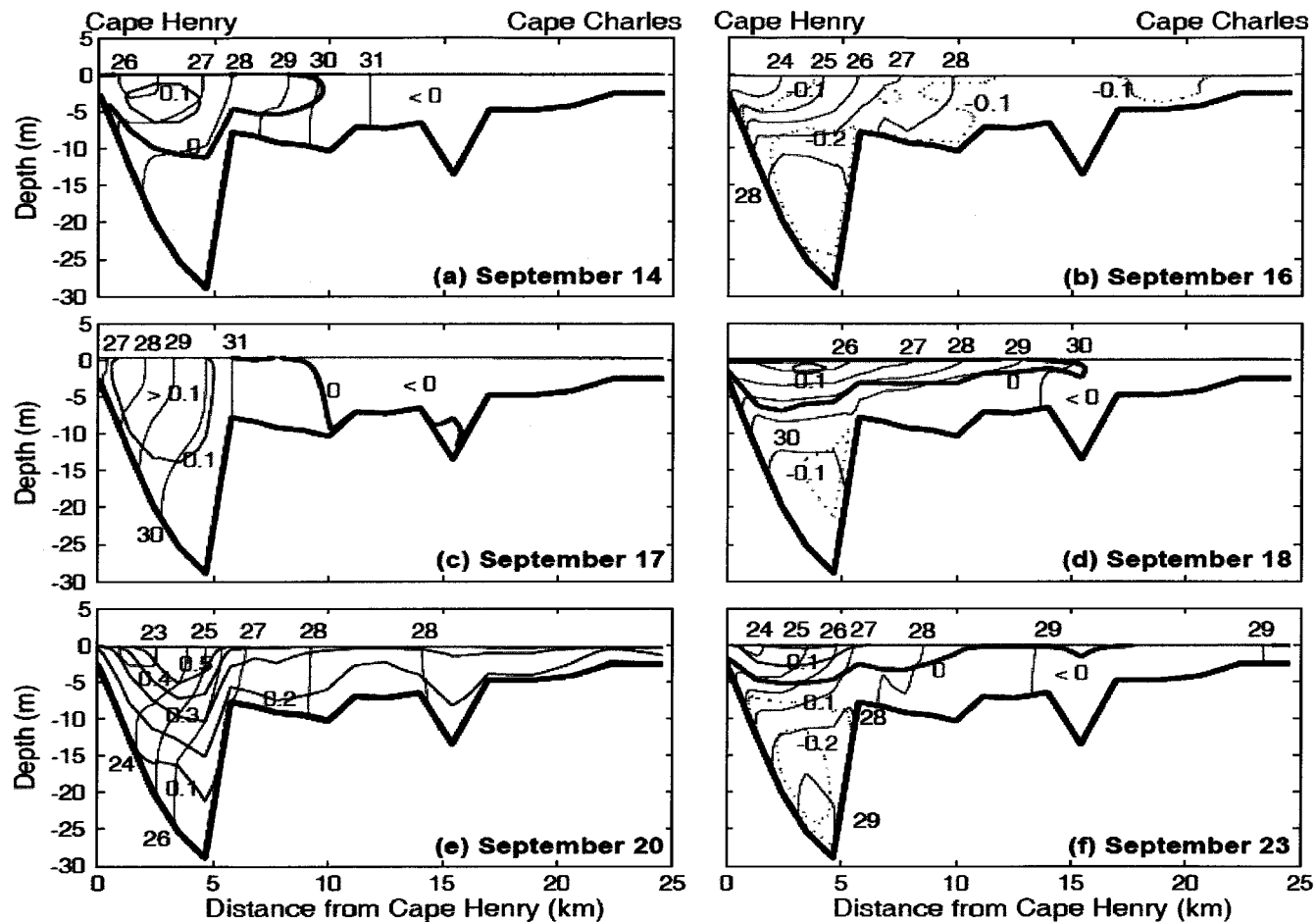


Fig. 6-3 Distributions of tidally averaged (25 hours) axial velocity (blue lines) and salinity (red lines) at the transect tr01 at six selected days during Hurricane Floyd, 1999. Velocity is represented by solid lines (seaward), dotted lines (landward), and thick lines (zero) in  $\text{m s}^{-1}$ .

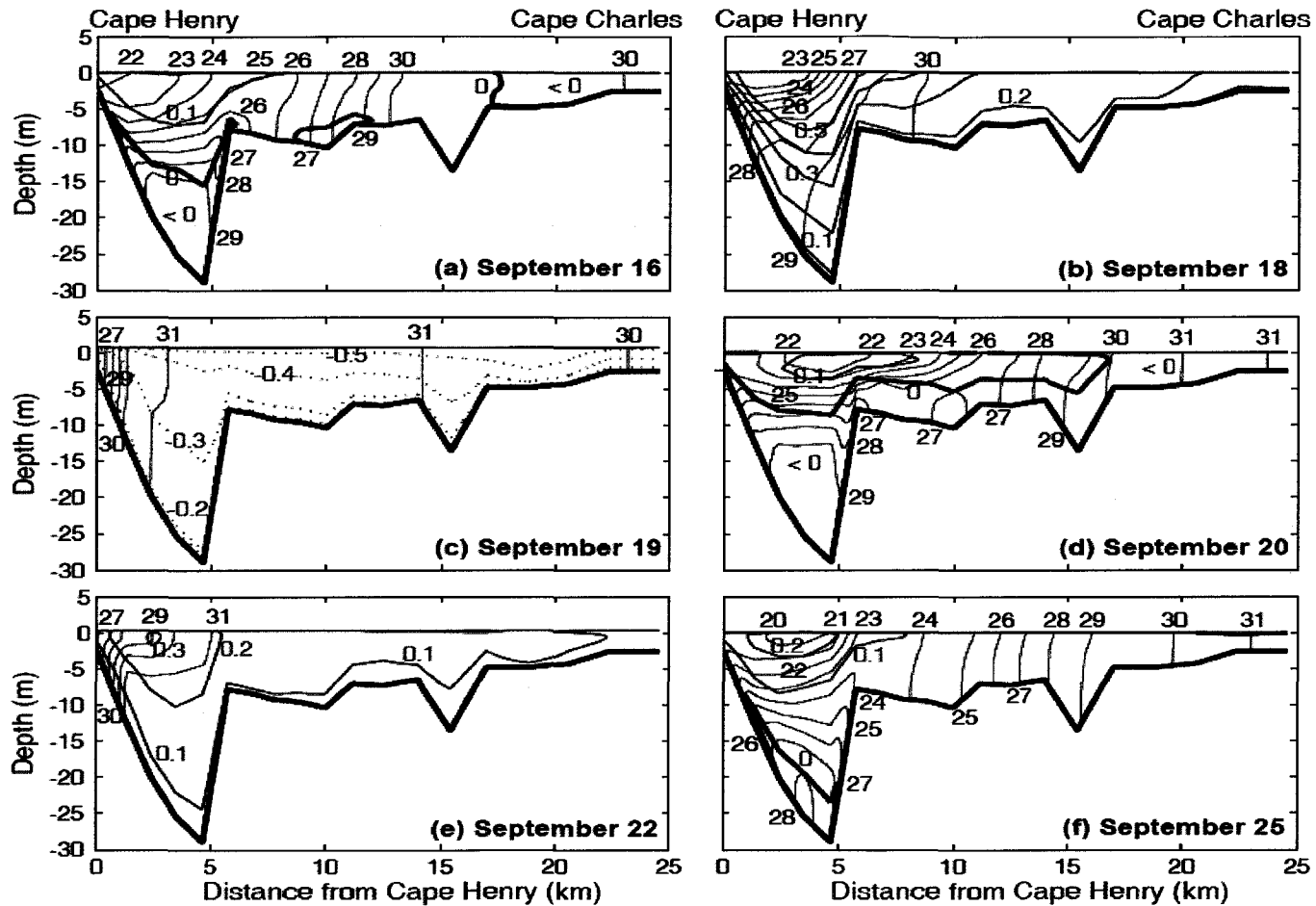


Fig. 6-4 Distributions of tidally averaged (25 hours) axial velocity (blue lines) and salinity (red lines) at the transect tr01 at six selected days during Hurricane Isabel, 2003. Velocity is represented by solid lines (seaward), dotted lines (landward), and thick lines (zero) in  $\text{m s}^{-1}$ .

showing a 7-8 ppt salinity difference between surface and bottom waters in the channel (Figures 6-4e and 6-4f). Using these cross-sectional distributions of axial velocity and salinity, net volume flux and net salt flux can be calculated across selected transects.

### 6.2.2 Calculation of volume fluxes along the cross-sections

The volume flux has been calculated by using Eq. (5-2) across each transect. The volume flux at the tr01 transect, which is a significant intersection between the Bay and the continental shelf, is analyzed to estimate how much oceanic influx occurred during both hurricanes.

#### Hurricane Floyd

Figure 6-5(a) shows the time series of total volume flux across tr01. As described in Section 5.3.2, the influx across tr01 slightly occurred on September 16. Consequently, on next day volume flux was dominated by huge outflux due to northerly winds. Across the transect tr01, spatial distribution of net volume flux averaged over one tidal-cycle (~12.5 hours) on September 16 are shown in Figure 6-5b. Net volume influx occurred dominantly through two portions, main channel and northern portion. The magnitude of influxes at mid depths was in ranges of  $4$  to  $6 \times 10^3 \text{ m}^3 \text{ s}^{-1}$ . Flows into the Bay tend to be influenced by Coriolis force and to veer to the right portion of Bay entrance. Across the transect tr06 in the mid-Bay, net volume influx occurred due to tidal fluctuations (Figure 6-5c). Cross-sectional distribution of net volume flux shows two-layered pattern due to northerly winds, which represents that seaward flux occurred in the surface layer whereas

landward flux occurred in the bottom layer (Figure 6-5d). This indicates that baroclinic component is dominant in this portion.

### Hurricane Isabel

During Hurricane Isabel, the time series of net volume flux across tr01 is shown in Figure 6-6a. Volume influx across both transects occurred on September 18 to 19, 2003, followed by outflux afterwards. Spatial distribution of net volume flux averaged over two tidal cycles on September 18 to 19 is shown in Figure 6-6b. Similar to the influx pattern during Hurricane Floyd, net volume influx occurred dominantly through two portions. However, its magnitude during Hurricane Isabel was twice larger than that during Hurricane Floyd, showing approximately  $8$  to  $12 \times 10^3 \text{ m}^3 \text{ s}^{-1}$  at mid depths. Across tr05, net volume influx occurred on September 18 to 19 (Figure 6-5c). Cross-sectional distribution of net volume flux shows uni-direction pattern, which represents that landward flux occurred in the whole water column (Figure 6-5d).

#### 6.2.3 Calculation of salt fluxes along the cross-sections

The amount of salt transport should be obtained by spatial integration of the product of velocity and salinity over the portion of the cross-section A (Kuo and Park, 1992):

$$M = \int_A u S \, dA \quad (6.1)$$

where  $u$  is the component of the current velocity normal to the sectional area and  $S$  is the salinity of the water. Quantitatively, salt fluxes have been analyzed by the same method as that described in Section 5.3.2.

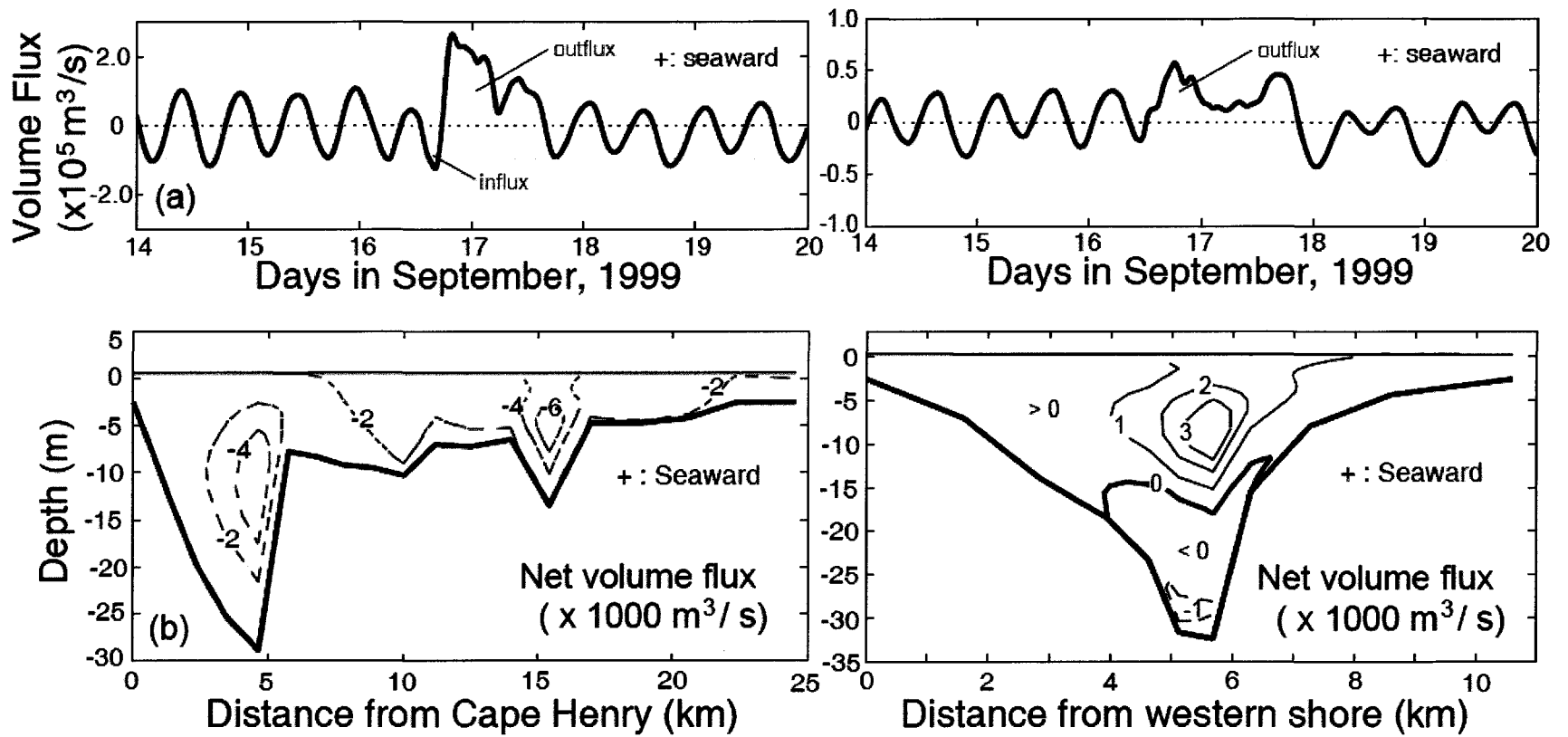


Fig. 6-5 Estimated net volume flux during Hurricane Floyd; (a) temporal variation and (b) spatial distribution across tr01; (c) temporal variation and (d) spatial distribution across tr06. Spatial distributions of net volume flux were averaged over one tidal-cycle on September 16, 1999.



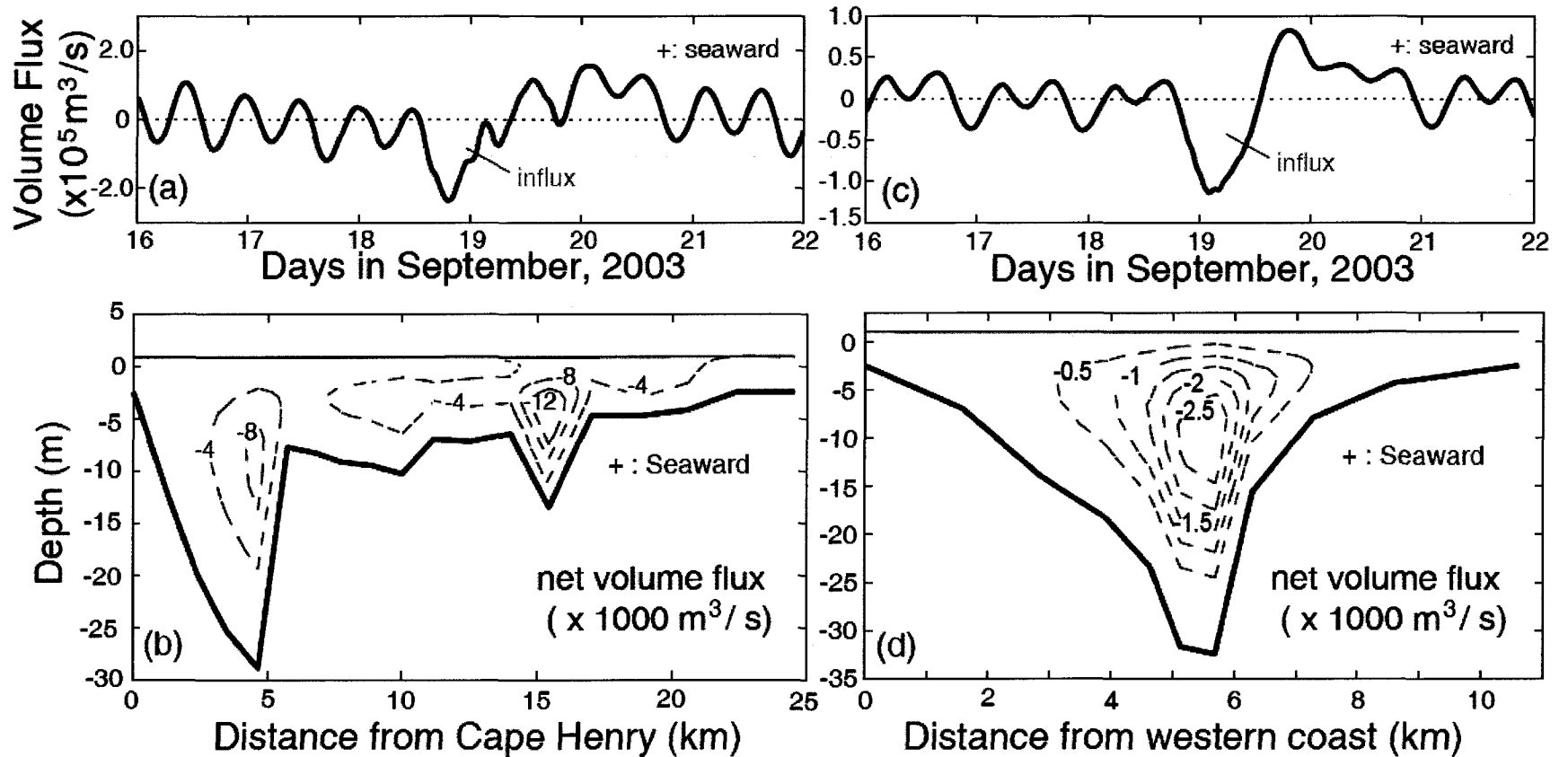


Fig. 6-6 Estimated net volume flux during Hurricane Isabel; (a) temporal variation and (b) spatial distribution across tr01; (c) temporal variation and (d) spatial distribution across tr06. Spatial distributions of net volume flux were averaged over two tidal cycles on September 18-19, 2003.

## Hurricane Floyd

The time series and spatial distributions of net salt flux across tr01 and tr06 are presented in Figure 6-7. It is evident that oceanic influx occurs a certain period when Hurricane Floyd approached. It shows similar patterns to net volume fluxes across two transects. Oceanic salt influx across tr01 does not seem to reach the mid-Bay portion since seaward flux overcame the influx due to northerly winds. Half-daily net salt flux across each transect is shown in Figure 6-8. During Hurricane Floyd, the net salt flux in the main Bay is characterized by the following three general patterns: 1) landward salt fluxes at all transects were dominant through September 14, 2) seaward salt flux became dominant from September 15 to 17, and 3) landward salt flux again occurred after September 18 (Figure 6-8a). These patterns follow the patterns of volume flux described in Section 5.3.2. In other words, the net salt flux shows the maximum value at the Bay mouth transect (tr01) and decreases at transects to the north (tr02 to tr09). Interestingly, during the second half of September 15, the net salt flux across tr01 was smaller than that across tr02. This indicates that salt increased in the region surrounded by tr01, tr02, and Jam. This caused a convergence and increased the water volume in the region, and consequently landward net salt flux occurred across the James River transect (Figure 6-9a). Seaward salt fluxes were dominant in mid-Bay and the upper Bay (Figure 6-10a). During the first half of September 16 (Figures 6-9b and 6-10b), the salt flux in the lower Bay began to change landward, but still seaward salt fluxes remained in the mid Bay. The signal of salt increase propagated up to the mid-Bay portion near Potomac River in spite of seaward salt flux. This indicates that the mid portion of the Bay proper was converged upon by landward salt flux from the ocean and seaward salt flux from the

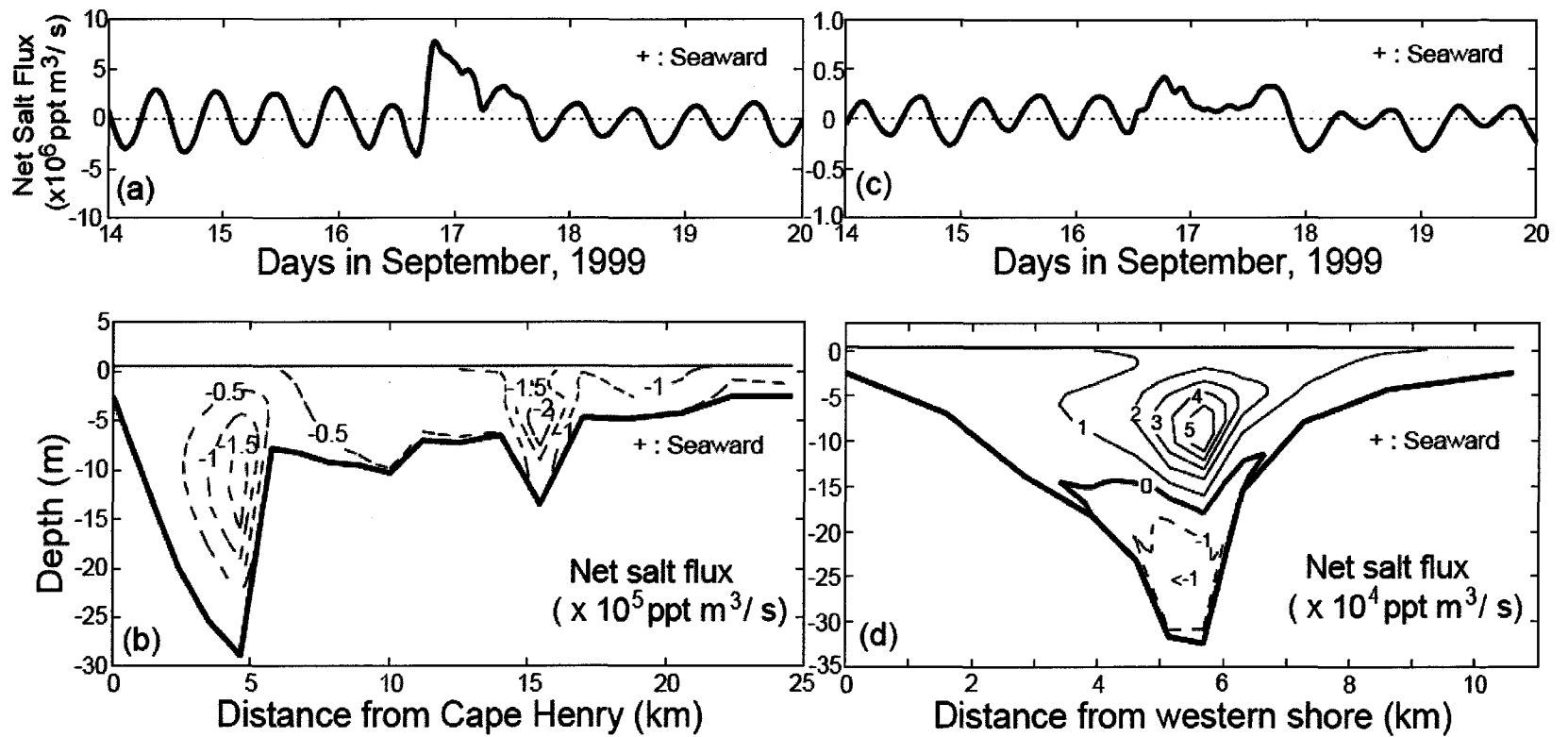


Fig. 6-7 Estimated net salt flux during Hurricane Floyd; (a) temporal variation and (b) spatial distribution across tr01; (c) temporal variation and (d) spatial distribution across tr06. Spatial distributions of net salt flux were averaged over one tidal cycle on September 16, 1999.

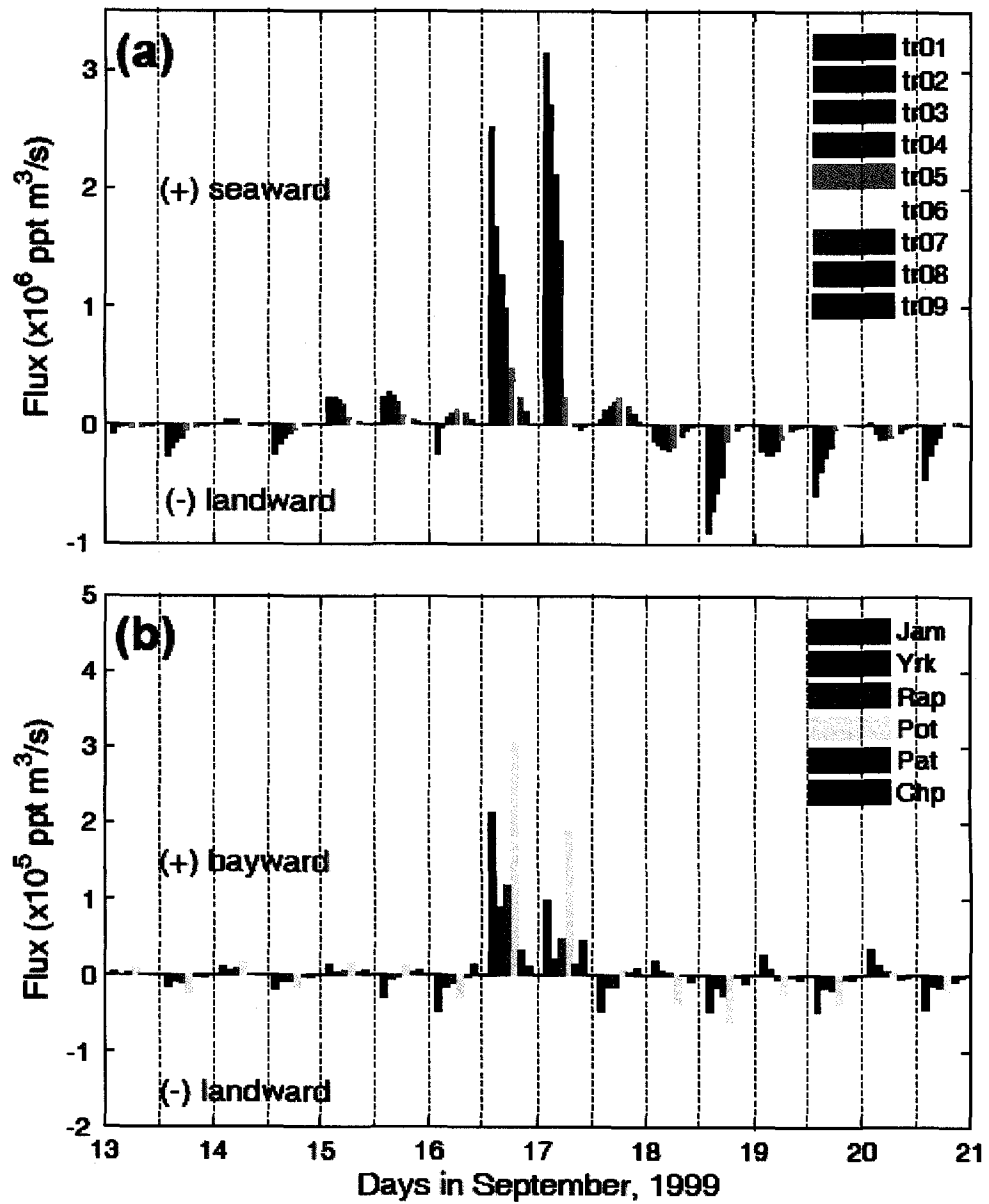


Fig. 6-8 One tidal-cycle averaged net salt flux at each transect (a) in the Chesapeake Bay mainstem and (b) its tributaries during Hurricane Floyd, 1999.

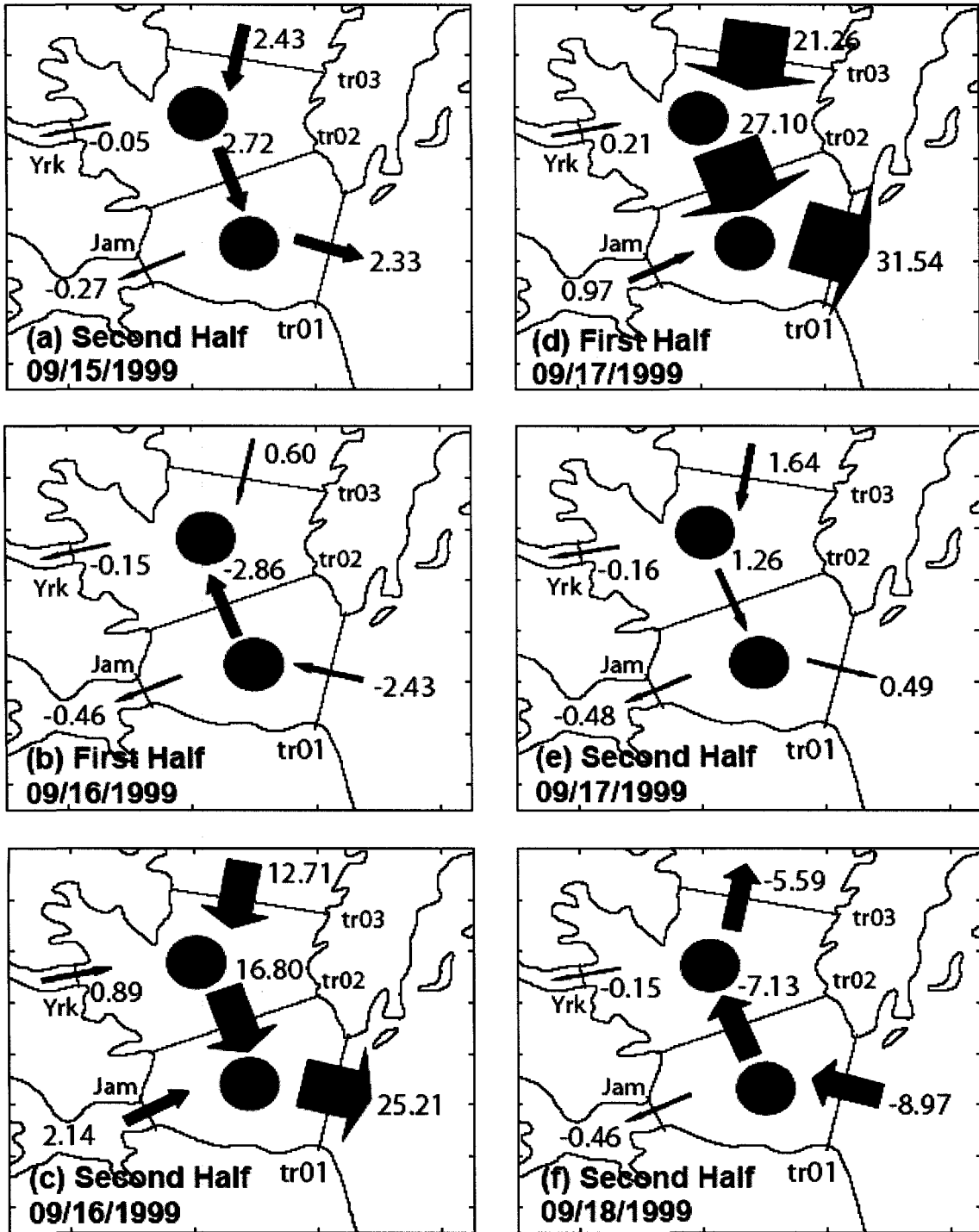


Fig. 6-9 Time sequence of net salt flux ( $\times 10^5$  ppt  $m^3 s^{-1}$ ) averaged over a tidal cycle at transects in the lower Chesapeake Bay during Hurricane Floyd, 1999. The positive value denotes seaward flux and red and blue colors represent the increase and decrease of salt, respectively.

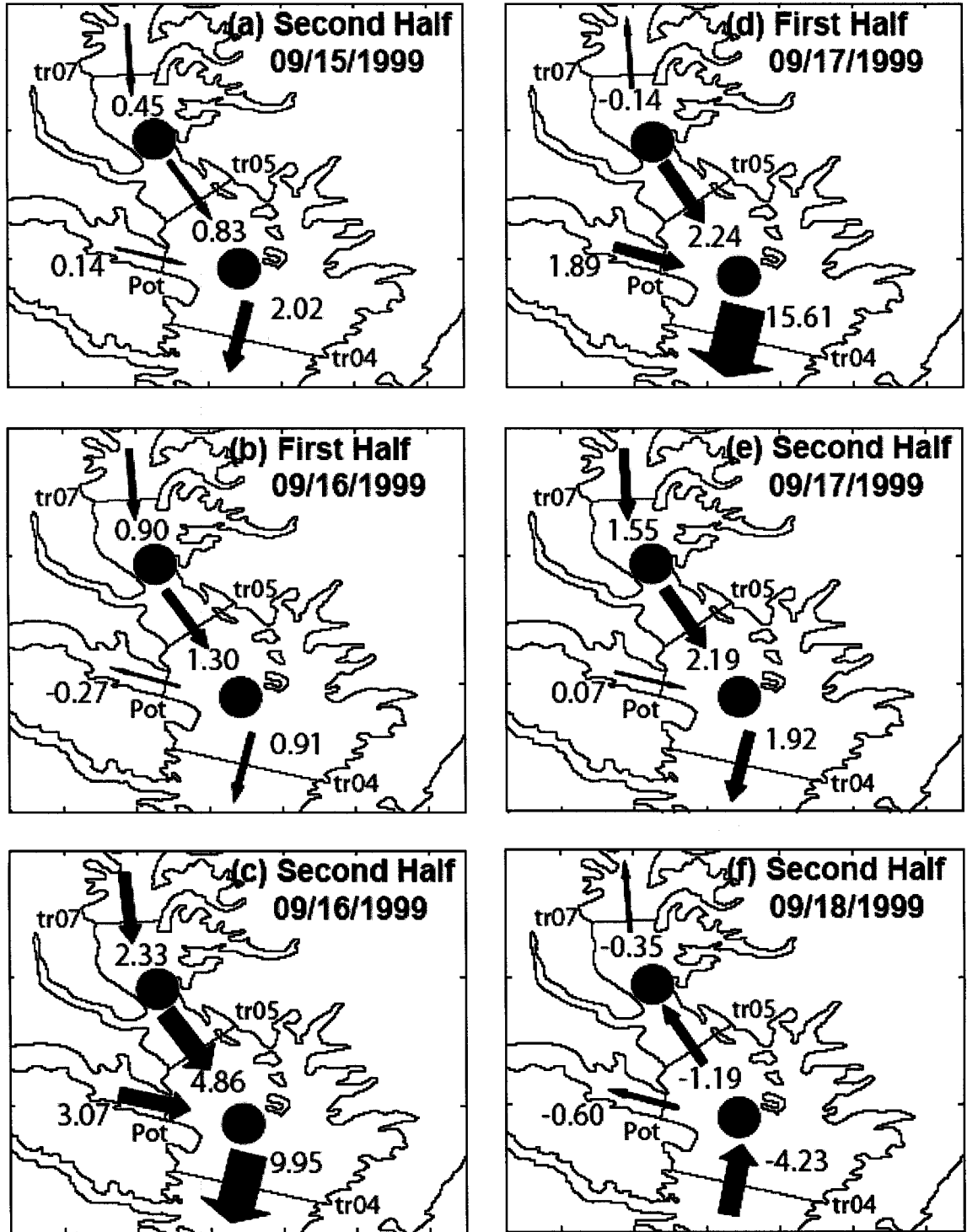


Fig. 6-10 Time sequence of net salt flux ( $\times 10^5 \text{ ppt m}^3 \text{ s}^{-1}$ ) averaged over a tidal cycle at transects in the mid Chesapeake Bay during Hurricane Floyd, 1999. The positive value denotes seaward flux and red and blue colors represent the increase and decrease of salt, respectively.

upper Bay. The signal of salt decrease occurred at the Bay mouth. During the second half of September 16 (Figures 6-9c and 6-10c), the change to seaward salt flux occurred at two transects in the lower Bay and decreased the amount of salt. The signal of salt decrease appears to propagate to the upstream. The maximum value of seaward salt fluxes across transects in the southern portion of the Bay was represented during the first half of September 17. However, across transects in the northern portion of the Bay, the salt fluxes preferably decreased and rather the negative flux occurred across tr07 (Figures 6-9d and 6-10d). This means that the down-Bay winds enhanced the divergence in both the upper Bay and the mid Bay. During the second half of September 17 (Figures 6-9e and 6-10e), seaward salt flux decreased remarkably across each transect and it generated the convergence of salt flux up to the portion of Potomac River. One day later (Figures 6-9f and 6-10f), the change to landward salt flux across each transect with a return flow prolonged the convergence of net salt flux throughout the entire Bay.

### Hurricane Isabel

The time series and spatial distributions of net salt flux across tr01 and tr06 are presented in Figure 6-11. The pattern of net salt flux is similar to that of net volume flux. The salt influx across tr03 had the same magnitude of the salt flux across tr01. The salt influx across tr06 is supposed to be smaller than the salt influx across tr01, because mean salinity and volume flux across tr06 were smaller than mean salinity and volume flux across tr01. This indicates that southerly winds tend to enhance salt influx to the upstream of the Bay. Net salt flux across each transect during Hurricane Isabel was calculated (Figure 6-12). During Hurricane Isabel, the net salt flux in the Bay proper is

characterized by three general patterns as follows: 1) landward salt fluxes across all transects were dominant through September 17, 2) a huge landward salt flux occurred from the second half on September 18 through the first half on September 19, and 3) a huge return salt flux headed seaward from the second half on September 19 to the first half on September 20 and then decreased. Similar to the volume flux as described in Chapter V, from the second half of September 17 to the second half of September 18, landward salt flux induced by northeasterly and easterly winds across downstream transects was larger than that across upstream transects. This caused the generation of a convergence to increase salt in the Bay (Figures 6-13a,b and 6-14a,b). During the first half of September 19, when the winds changed to southeasterly and southerly winds, landward salt flux across transects weakened in the lower Bay but strengthened in the mid Bay and upper Bay. As a result, divergence occurred in the lower Bay but convergence was prolonged in two upper portions of the Bay (Figures 6-13c and 6-14c). The rapid change to seaward salt flux generated the divergence of salt flux throughout the entire Bay during the second half of September 19 and seaward salt flux was enhanced during the next half day (Figures 6-13d,e and 6-14d,e). The seaward salt flux across the lower Bay transects and the change to landward salt flux across the upper Bay transects coincide with the loss of salt flux in the entire portions of the Bay (Figures 6-13f and 6-14f).

The oceanic salt influx obviously occurred from the Bay mouth during both hurricanes and the signal propagated upstream through the convergence process. However, during Hurricane Floyd, strong seaward flow induced by down-Bay winds restricted landward salt flux to the upper Bay whereas landward flow enhanced by up-



Bay winds during Hurricane Isabel strengthened landward salt flux to the upper Bay. Supposedly, during both hurricanes, landward salt flux should be balanced by seaward salt flux if assuming an equilibrium state. During Hurricane Floyd, across the Bay mouth transect (tr01) the sum of net salt flux was nearly  $(+) 48.2 \times 10^5 \text{ ppt m}^3 \text{ s}^{-1}$ . However, during Hurricane Isabel, the sum of net salt flux was nearly  $(-) 4.3 \times 10^5 \text{ ppt m}^3 \text{ s}^{-1}$ . This indicates that landward salt flux is expected to occur after Hurricane Floyd, whereas slightly seaward salt flux will occur after Hurricane Isabel. This will affect the time scale of estuarine recovery in the Bay.

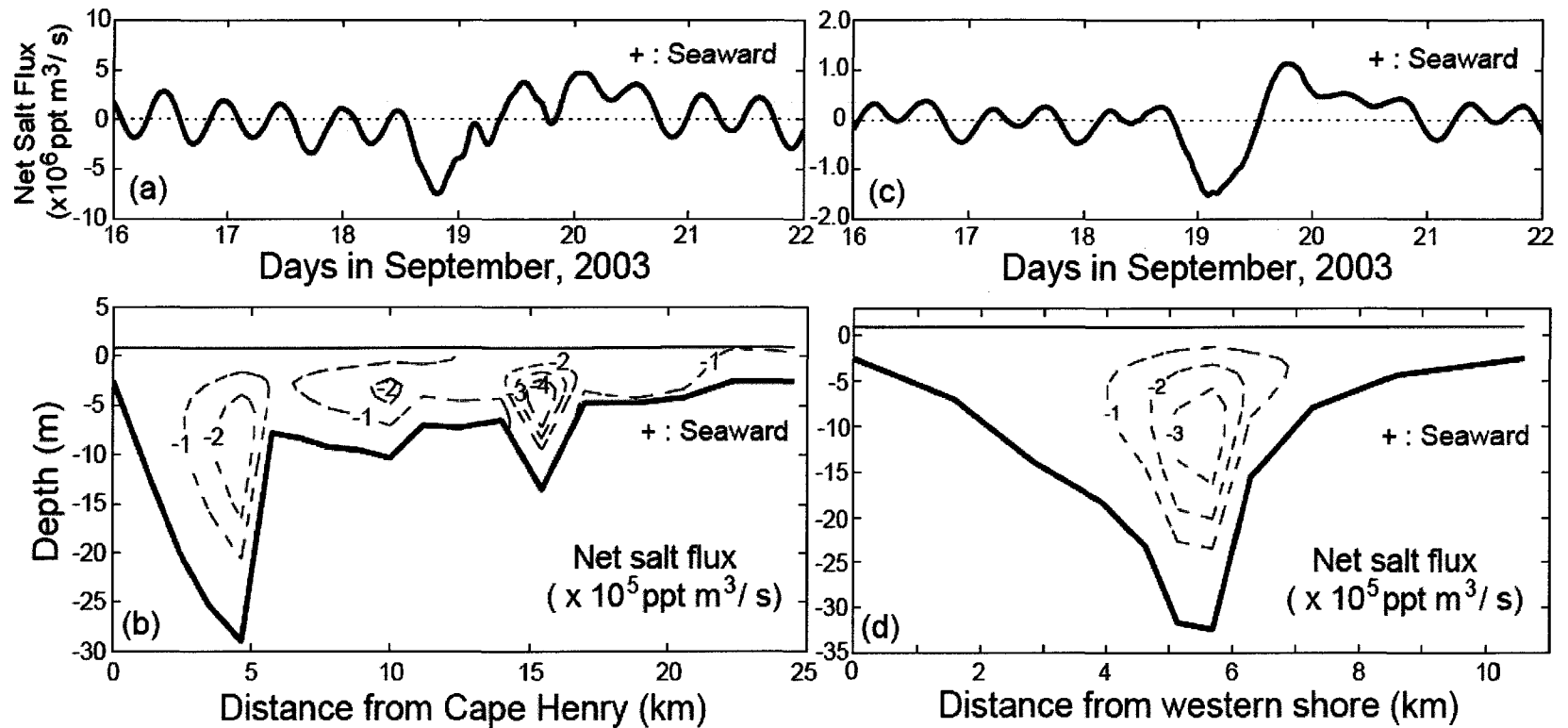


Fig. 6-11 Estimated net salt flux during Hurricane Isabel; (a) temporal variation and (b) spatial distribution across tr01; (c) temporal variation and (d) spatial distribution across tr06. Spatial distributions of net salt flux were averaged over two tidal cycles on September 18-19, 2003.

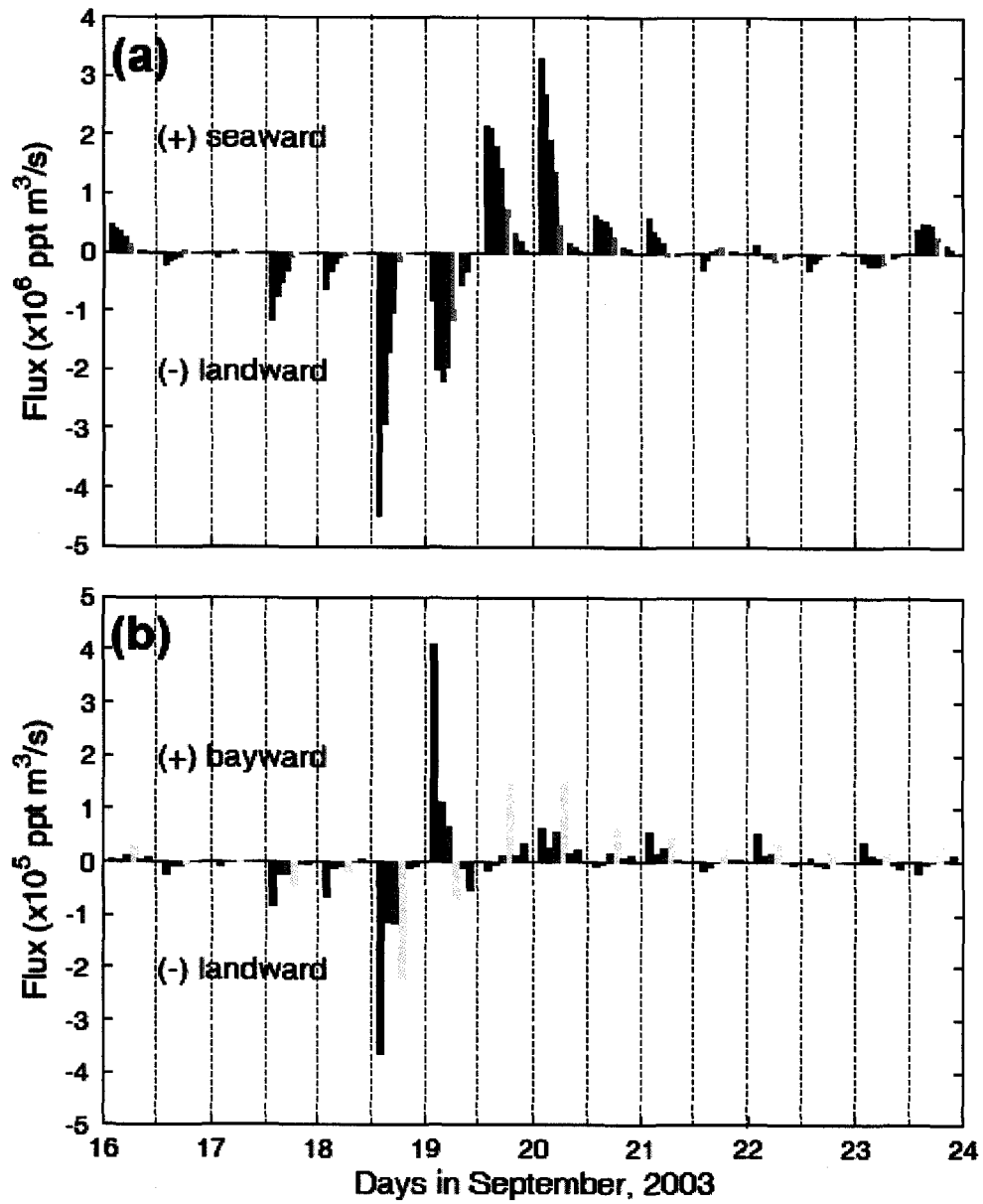


Fig. 6-12 One tidal-cycle averaged salt flux at each transect (a) in the Chesapeake Bay mainstem and (b) its tributaries during Hurricane Isabel, 2003 (same legend as Figure 6-8).

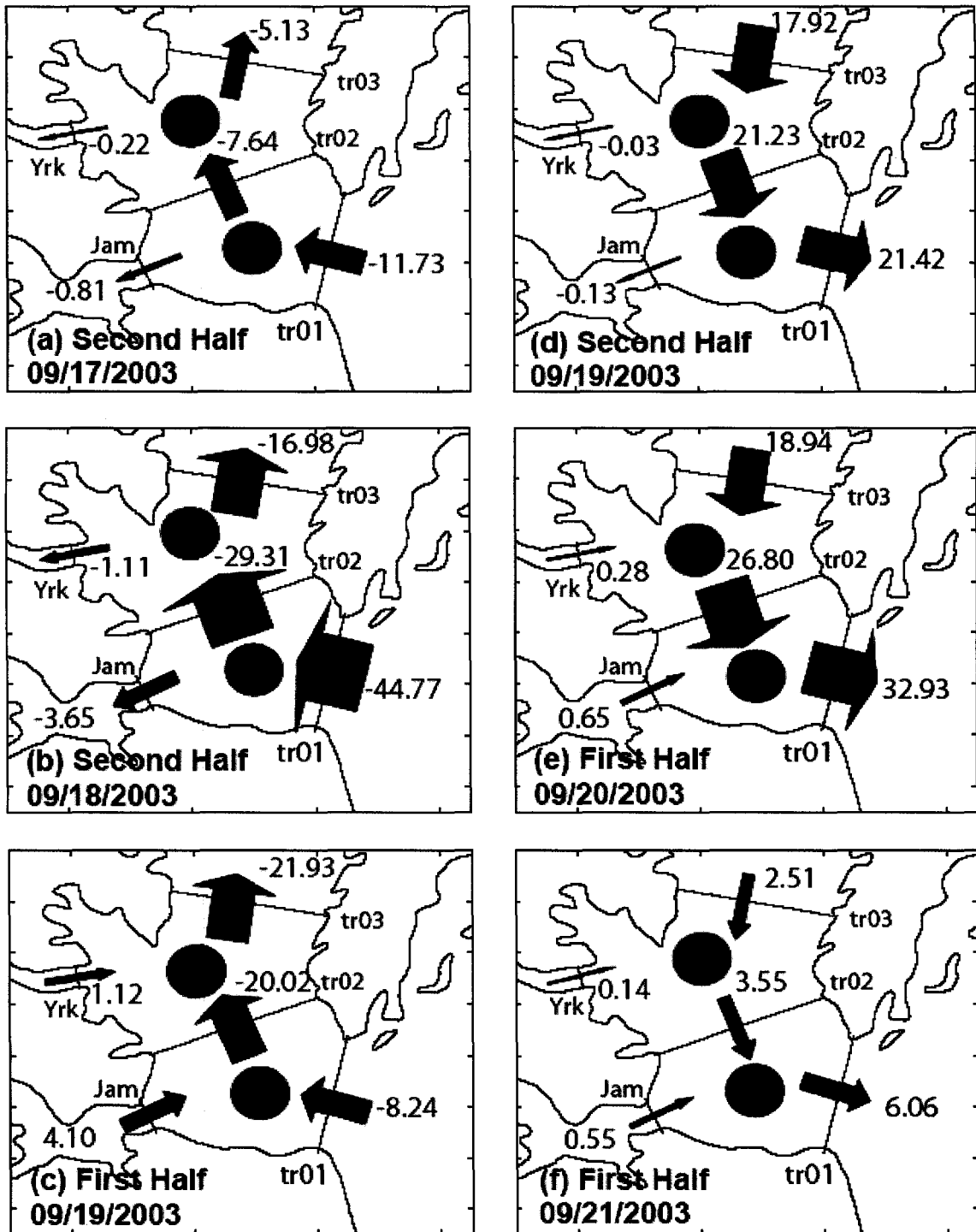


Fig. 6-13 Time sequence of net salt flux ( $\times 10^5 \text{ ppt m}^3 \text{ s}^{-1}$ ) averaged over a tidal cycle at transects in the lower Chesapeake Bay during Hurricane Isabel, 2003. The positive value denotes seaward flux and red and blue colors represent the increase and decrease of salt, respectively.

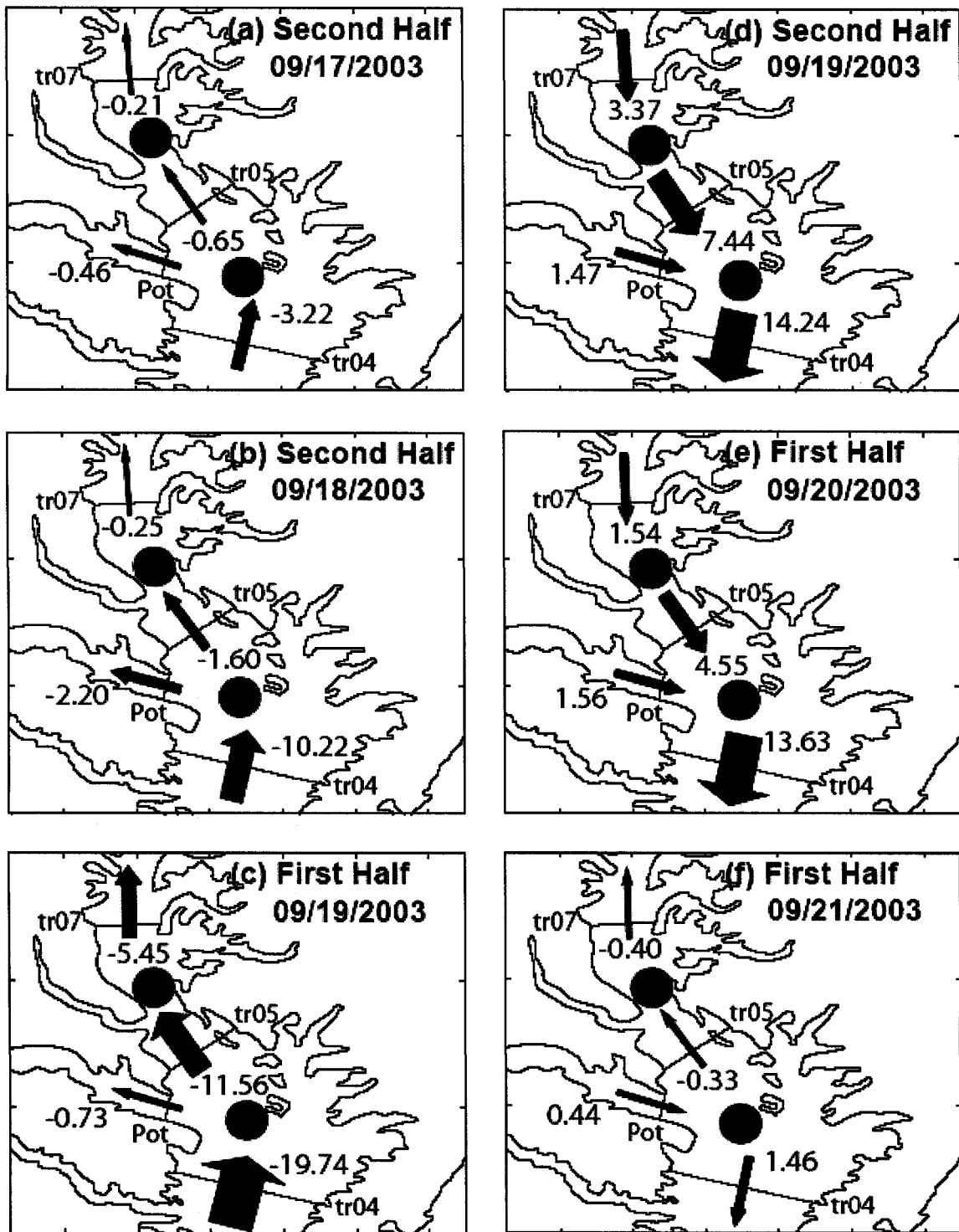


Fig. 6-14 Time sequence of net salt flux ( $\times 10^5$  ppt  $m^3 s^{-1}$ ) averaged over a tidal cycle at transects in the mid Chesapeake Bay during Hurricane Isabel, 2003. The positive value denotes seaward flux and red and blue colors represent the increase and decrease of salt, respectively.

### 6.3 Hurricane-induced mixing process

#### 6.3.1 Storm event experiments

In a semi-enclosed water body such as Chesapeake Bay, winds generate turbulent mixing either through wind stress to mix the surface water directly or through internal velocity shear produced by the wind-generated slope, which drives the bottom water in the opposite direction (Wang, 1979a; Vieira, 1986; Li et al., 2007). Li et al. (2007) showed that strong hurricane-forced winds caused intense turbulent mixing and complete de-stratification in the water column and suggested the effect of the combined local and remote wind forcing. A surge wave generated in the Bay mouth propagates to the upper Bay (see Chapter V). Simultaneously, saltwater influx from the ocean occurs due to the current driven by direct wind stress and the landward horizontal pressure gradient as described in Section 6.2. Thus, in this section, two main mechanisms of destratification during two hurricanes will be focused: 1) surge-induced mixing and 2) local wind-induced mixing. However, to compare the mixing and stratification between two types of hurricanes, the initial condition for stratification needs to be considered. For example, the Chesapeake Bay had a different pre-storm condition of stratification for two hurricanes (Table 6-1). In order to make a fair comparison of the effects of two different types of hurricanes, a series of numerical experiments needs to be conducted. Six experiments have been performed to examine the mixing process induced by meteorological external forcing (Table 6-2). The base run was specified with only the  $M_2$  tidal constituent, constant ambient current of  $10 \text{ cm s}^{-1}$ , and constant river discharge of  $550 \text{ m}^3 \text{ s}^{-1}$  as an average summer flow in 1985, which was considered as one of the driest summers (Krome and Corlett, 1990). The use of a single semi-diurnal tidal constituent precludes the effect of spring-neap tides on salinity. A constant value of ambient current

Table 6-1 Comparison of observed stratification between pre-storm and post-storm at four selected CBP stations during Hurricanes Floyd (1999) and Isabel (2003).

Station ID	Salinity Stratification (ppt)			
	Floyd (1999)		Isabel (2003)	
	pre-storm (Aug/17-18)	post-storm (Sep/21-22)	pre-storm (Sep/15-16)	post-storm (Sep/22-23)
CB3.1	2.43	7.80	9.03	2.39
CB3.2	1.77	6.72	8.37	1.75
CB4.4	4.10	4.85	11.52	4.97
CB5.3	3.04	5.45	10.90	8.61

Table 6-2 Summary of numerical experiments performed.

Experiments	Winds	Total River Discharge ( $m^3 s^{-1}$ )	Ambient Current ( $cm s^{-1}$ )	Subtidal Alongshore PG*
NW	no wind	550	10	
FL-C	combined winds (Floyd)	550	10	O
IS-C	combined winds (Isabel)	550	10	O
FL-L	local winds (Floyd)	550	10	
IS-L	local winds (Isabel)	550	10	
FL-R	remote winds (Floyd)	550	10	O
IS-R	remote winds (Isabel)	550	10	O

\* PG represents the pressure gradient.

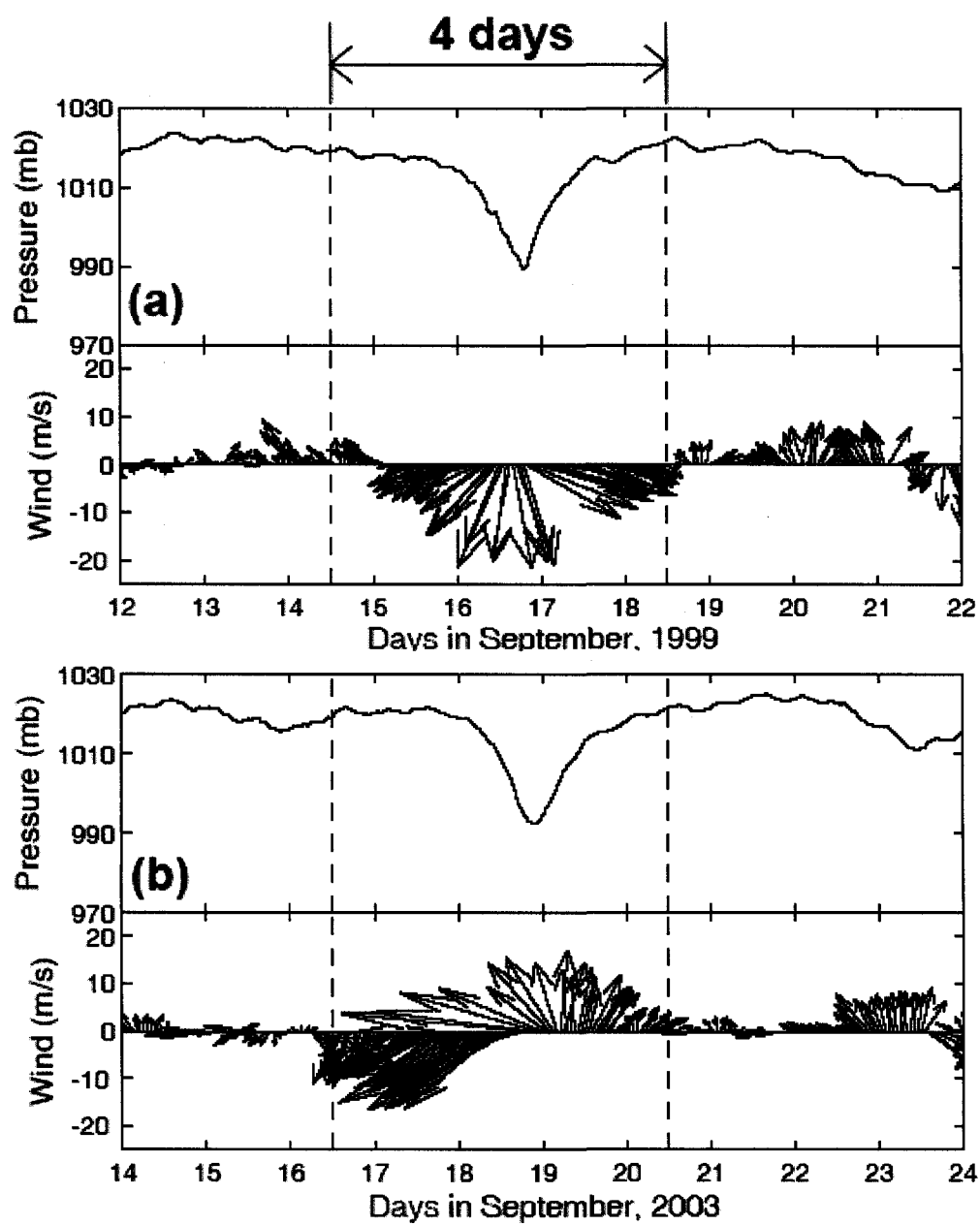


Fig. 6-15 Selected period of four days for atmospheric forcing during Hurricane Floyd (a) and Hurricane Isabel (b).



was used as a non-tidal flux boundary condition on two cross-shore open boundaries. The numerical tests to determine the value of  $10 \text{ cm s}^{-1}$  for the ambient current are described in Chapter VIII. To get the initial condition for salinity in the equilibrium state, without meteorological forcing, the model was spun up for 180 days from the cold start that salinity has a linear variation horizontally from Bay head (0 ppt) to open ocean (34~35 ppt) and no stratification in vertical. When the relative gradient of tidally averaged salinity difference with respect to time reduces to an insignificantly small value (0.1 %), it is assumed that the salinity reached the equilibrium state. The modeled salinity reached the equilibrium state at nearly 150 days from the cold start.

As depicted in Figures 2-2 and 2-7, relatively strong winds were recorded before and after the hurricane events. In order to exclude these wind effects, significant periods of four days have been chosen from each hurricane, and winds and atmospheric pressure have been extracted from these periods as surface boundary conditions which vary with time and space (Figure 6-15). These forcings are turned on at Day 186 and turned off at Day 190. In the next sections, the results are presented, followed by four scenarios depicting the effects of local and remote winds.

### 6.3.2 Temporal variations of vertical structures

#### Instantaneous velocity and salinity

Time series of instantaneous axial velocities at five selected stations are plotted in Figure 6-16 for Experiment FL-C (combined remote and local wind forcing of Hurricane Floyd) and Experiment IS-C (combined remote and local wind forcing of Hurricane Isabel). The top to bottom panels show results for the upper Bay station (CB3.3c) to the

lower Bay station (CB7.4). For the FL-C case (Figures 6-16a to 6-16e), in the upper Bay the seaward surface velocity dominated whereas the landward bottom velocity dominated. From the lower Bay to mid-Bay, the velocities had a similar pattern whereby landward flow at both depths initially dominated but then suddenly changed to seaward flow. The magnitude of velocity decreased from the lower Bay to mid-Bay. The surface velocity was intensified by surface wind stress and the bottom friction influenced on diminishing the bottom velocity. The velocities were nearly recovered within a week after wind forcing was turned off. In the IS-C case (Figure 6-16f to 6-16j), the velocities at five stations had a similar pattern that initially the landward flow increased until it reached a peak and changed to seaward flow. The bottom and surface velocities at the stations had the identical direction most of time during the event. The velocities were nearly recovered within a week after wind forcing was switched off.

Time series of instantaneous bottom and surface salinities for both experiments are shown in Figure 6-17. Results common to both experiments, FL-C and IS-C, are:

- 1) the surface salinity at all stations increased during the storm,
- 2) the bottom salinity from the Bay mouth up to the mid-Bay station (CB5.3) increased,
- 3) stratification decreased during the storm, and
- 4) a completely well-mixed condition in the lower Bay persisted longer.

On the contrary, results differing between the experiments are:

- 1) the bottom salinity from the mid-Bay (CB4.4) to the upper Bay decreased during Hurricane Floyd, but increased during Hurricane Isabel,
- 2) surface and bottom salinities in the lower Bay remained with high values during Hurricane Isabel but quickly dropped at Day 188.5 during Hurricane Floyd,

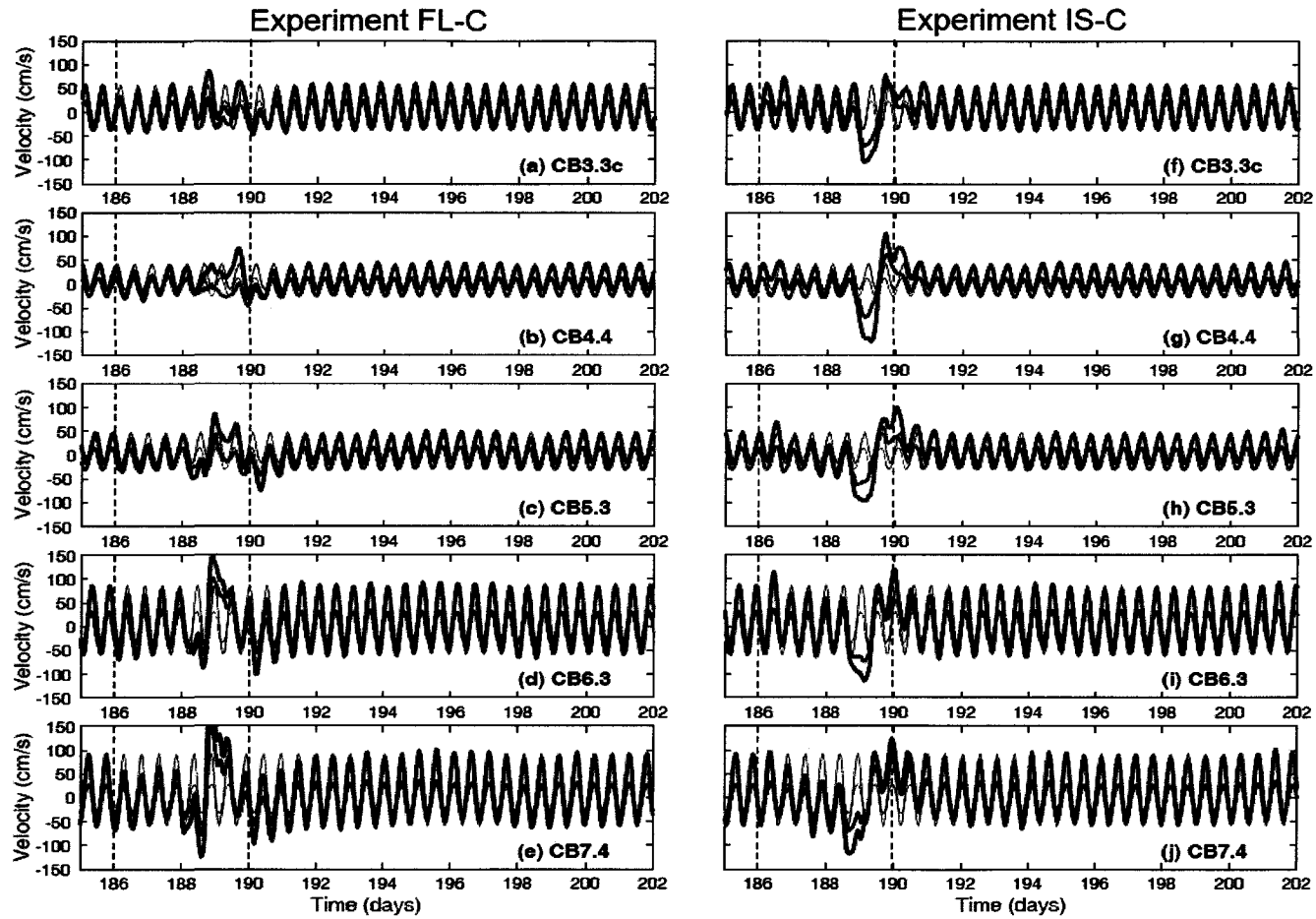


Fig. 6-16 Time series plots of surface (blue) and bottom (red) along-channel velocities at five selected stations for the FL-C case (a to e) and for the IS-C case (f to j). Thin lines denote no wind case, vertical dashed lines denote the period of wind forcing, and positive value represents a seaward flow.

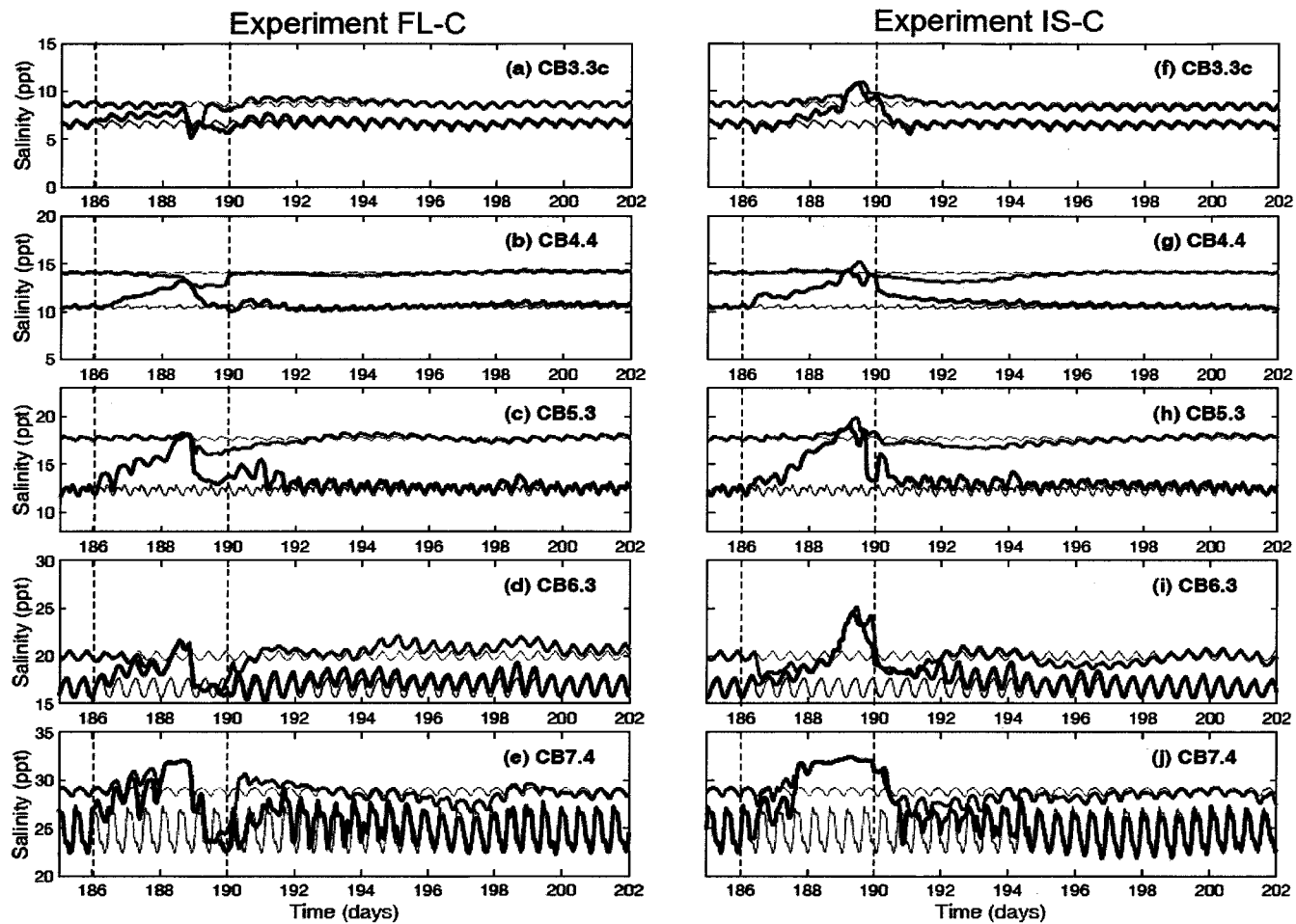


Fig. 6-17 Time series plots of surface (blue) and bottom (red) salinities at five selected stations for the FL-C case (a to e) and for the IS-C case (f to j). Thin lines denote the no wind case and vertical dashed lines denote the period of wind forcing.

3) during Hurricane Floyd, a well-mixed water column in the upper Bay was rapidly re-stratified even though the wind forcing was not switched off, and

4) in the lower Bay, the stratification quickly increased when Hurricane Floyd wind stopped but the de-stratified water column was still maintained over one day or more.

Similar to the observation as depicted in Table 6-1, the model results showed that the stratification after Hurricane Floyd tends to be larger than the pre-storm condition, whereas the stratification after Hurricane Isabel tends to be smaller than the pre-storm condition. During these two hurricanes, the salinity stratification appears to be influenced by the combination of local and remote winds (Li et al., 2007). This combined effect will be discussed in Section 6.4.

#### Vertical profiles of tidally averaged velocity

To examine the temporally varying vertical structure of velocity, tidally averaged (over  $M_2$  period) along-channel velocities at three stations were plotted in Figure 6-18. A station was selected from each of three regimes: CB3.3c in the upper Bay, CB5.3 in the mid-Bay, and CB7.4 in the lower Bay. The time sequence was selected as  $t_0=186.0$ ,  $t_1=187.0$ ,  $t_2=188.0$ ,  $t_3=188.5$ ,  $t_4=189.0$ ,  $t_5=189.5$ ,  $t_6=190.0$ , and  $t_7=192.0$  (in days). In Figure 6-18, the depths were normalized with total depth at each station and positive values of velocity represent seaward flow. For the FL-C case (left panels in Figure 6-18), the three regimes show different profiles. At CB3.3c (Figure 6-18a), the initial two-layered gravitational circulation is shown ( $t=t_0$ ). When the down-Bay (northerly) winds began to blow, seaward flow in the surface layer started to strengthen ( $t=t_1$  to  $t_2$ ). At  $t=t_3$ , the zero-velocity depth became depressed to the bottom and the maximum seaward flow

occurred in the surface layer. After the next tidal cycle ( $t=t_4$ ), when the winds began to weaken, the velocity profile was bounded landward, and then seaward flow became strengthened again at  $t=t_5$ . The change to landward flow in the surface layer resulted in uni-directional landward flow at  $t=t_6$ . After  $t=t_6$ , the vertical profile of along-channel velocity was restored to the pre-storm condition. The velocity profile fully reversed back-and-forth twice. At CB5.2 (Figure 6-18b), an initial two-layer circulation pattern is shown ( $t=t_0$ ). Then, landward bottom flow slightly weakened until  $t=t_1$ . The change to landward flow in the surface layer resulted in landward flows throughout the water column at  $t=t_3$ . Next, the surface flow changed to seaward until  $t=t_5$  and then it was again rebounded to landward at  $t=t_6$ . Landward bottom flow increased until  $t=t_3$  and then decreased. After  $t=t_6$ , the flow pattern began to be restored to the two-layer flow. Interestingly, during the storm, the flow in the surface layer changed its direction four times whereas that in the bottom layer had no changes in direction. This indicates that, in the mid Bay, the surface flow is more sensitive to the balance between wind stress and horizontal pressure gradient force than the bottom flow. At CB7.4 (Figure 6-18c), a two-layer pattern in circulation was shown as the pre-storm condition ( $t=t_0$ ): relatively strong seaward flow in the surface layer but weak landward flow in the bottom layer. The change to landward flow occurred in the surface layer at  $t=t_2$  and resulted in vertically homogeneous landward flow. However, it was followed by strong seaward flow at  $t=t_3$  and this vertically uni-directional seaward flow strengthened at  $t=t_4$  showing much enhanced surface flow. The strong return flows to landward occurred the next day from  $t=t_5$  to  $t=t_6$ . After  $t=t_6$ , landward bottom flow weakened and the surface flow changed to

seaward, and subsequently the vertical profiles of along-channel velocity began to return to the pre-storm condition.

For the IS-C case (right panels in Figure 6-18), the vertical profiles of the velocity represented different patterns at three locations. The initial profiles of the velocity at three locations are identical to those in the FL-C case. At CB3.3c (Figure 6-18d), in contrast to the FL-C case, landward bottom flow first began to increase until  $t=t_3$ . At  $t=t_4$ , strong landward flow throughout the water column occurred to destroy two-layer circulation. This landward flow was driven by the combination of local up-Bay (southerly) winds and the propagated storm surge. When the seaward horizontal pressure gradient overwhelmed the landward wind stress, the entire water column flow rapidly changed to seaward ( $t=t_6$ ). As the flow weakened after  $t=t_6$ , the vertical profile of the velocity was restored to the pre-storm condition. At CB5.2 (Figure 6-18e), similar to the flow at CB3.3c, two-layer circulation began to be destroyed by landward flow. This landward flow over the entire water column remained until  $t=t_4$  and then rapidly changed to seaward at  $t=t_5$  as a return flow. At  $t=t_6$ , bottom flow changed to landward and seaward surface flow decreased, showing the two-layer circulation pattern. The vertical pattern began to be restored to the initial two-layer circulation afterwards. At CB7.4 (Figure 6-18f), similar to the FL-C case, a uni-directional landward flow occurred at  $t=t_2$  but it was followed by strengthened landward flow at  $t=t_3$ . At  $t=t_4$ , the flow was mostly zero and the change to seaward flow over the entire water column occurred at  $t=t_5$ . This seaward flow remained for the next one day ( $t=t_6$ ). Two days later ( $t=t_7$ ), the vertical profiles of along-channel velocity nearly returned to the pre-storm condition.

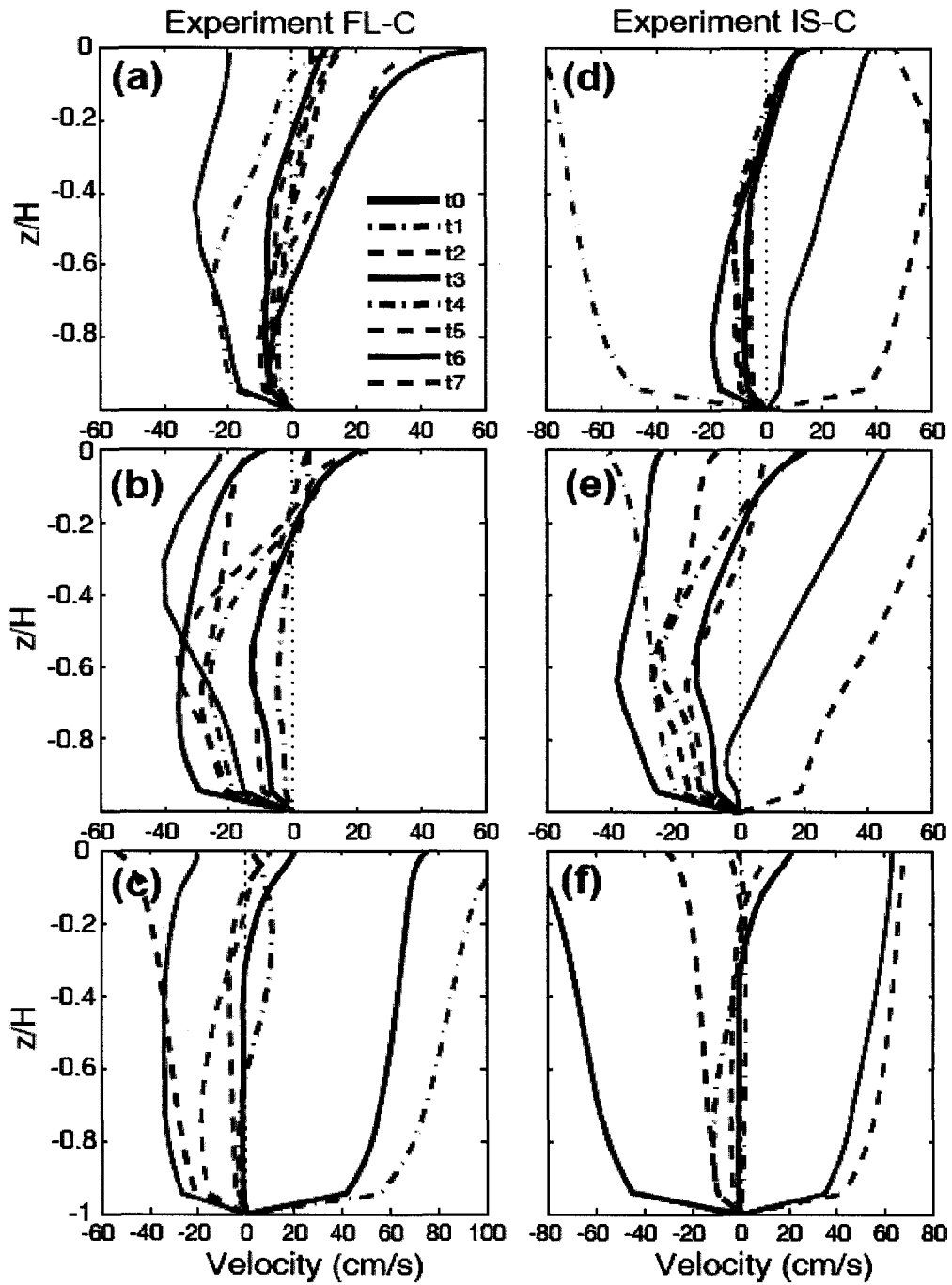


Fig. 6-18 Vertical profiles of tidally averaged along-channel velocity at three stations with time sequence: (a) upper Bay; (b) mid Bay; (c) lower Bay for the FL-C case and (d) upper Bay; (e) mid Bay; (f) lower Bay for the IS-C case. The positive value represents a seaward flow.



### Vertical profiles of tidally averaged salinity

As shown in Figure 6-19, the vertical salinity was analyzed by the same method as described above. For the FL-C case (left panels in Figure 6-19), at CB3.3c, the initial salinity difference between bottom and surface ( $\Delta S$ ) was approximately 2 ppt. The local winds deepened surface mixed-layer depth to  $z/H=-0.4$ , increasing surface salinity at  $t=t_2$ . At  $t=t_3$ , the water column became more de-stratified to decrease surface salinity by 1 ppt and decrease bottom salinity by approximately 1.5 ppt. This destratification corresponds to the strong seaward flow as depicted in Figure 6-19a. When the winds weakened, the water column began to be re-stratified. The  $\Delta S$  began to increase at  $t=t_4$  representing two distinct mixed layers in the surface and the bottom, and it is shown that surface salinity decreased by 1 ppt and bottom salinity increased by 1 ppt at  $t=t_5$ . Both bottom and surface salinities began to increase ( $t=t_6$ ), and the stratification slightly increased two days later. At CB5.2 (Figure 6-19b), when the wind was forced on the surface layer, the stratification began to decrease, showing that surface salinity increased and bottom salinity decreased ( $t=t_1$  and  $t_2$ ). At  $t=t_3$ , the water column was completely mixed. Interestingly, the increase of surface salinity (approximately 2.5 ppt) exceeded the decrease of bottom salinity (approximately 0.5 ppt). This corresponds to the strong landward flow through the water column. This indicates that landward flow affects to increase surface salinity but to decrease bottom salinity slightly. At  $t=t_4$ , only surface salinity decreased and  $\Delta S$  increased. Subsequently, bottom salinity decreased at  $t=t_6$ . Two days later ( $t=t_7$ ), the salinities throughout the water column increased by 0.5 ppt showing a smaller  $\Delta S$  than the initial value. At CB7.4 (Figure 6-19c), in contrast to the other 2 locations, initially both surface and bottom salinities rapidly started to increase

and deepened the surface mixed-layer depth ( $t=t_1$ ). A vertically homogeneous condition occurred at  $t=t_2$  with high salinity approximately 31.5 ppt. This high salinity condition remained with destratification until  $t=t_3$ . Although similar salinity profiles occurred for two tidal cycles, the velocity profiles during these two tidal cycles showed opposite directions as depicted in Figure 6-18c, which were landward flow at  $t=t_2$  and seaward flow at  $t=t_3$ . Due to this seaward flow, the salinity remarkably decreased by 5 ppt at  $t=t_4$  but remained well-mixed. When the flow changed to landward, the lowest salinity occurred at  $t=t_5$ . After the next tidal cycle ( $t=t_6$ ), bottom salinity first increased due to landward bottom flow. Two days later, both salinities increased, overshooting the initial condition. The salinity profile is expected to return to normal afterwards. The detailed recovery process will be discussed in Chapter VII.

For the IS-C case (right panels in Figure 6-19), at CB3.3c, the local wind started to deepen surface mixed-layer depth, increasing the salinity over the entire water column ( $t=t_2$ ). At  $t=t_3$ , both bottom and surface salinities increased whereas the salinity in mid-depth slightly decreased. The bottom salinity was supposed to decrease due to vertical mixing but the enhanced landward bottom flow increased the bottom salinity. After the next tidal cycle ( $t=t_4$ ), the water column was completely de-stratified and the salinity increased to approximately 10.4 ppt. This corresponds to the strong landward flow as shown in Figure 6-14d. The surface salinity first retreated at  $t=t_5$ , and the salinity over the entire water column decreased at  $t=t_6$ . Afterwards, the salinity again decreased to the initial level. At CB5.2 (Figure 6-19e), the surface salinity began to increase deepening surface mixed-layer depth whereas the bottom salinity slightly increased. At  $t=t_4$ ,  $\Delta S$  was nearly zero, showing that the increase of surface salinity from the initial value was

approximately 4 ppt whereas that of bottom salinity was only 1 ppt. Similar to the pattern at CB3.3c, the surface salinity retreated first ( $t=t_5$ ) and then the both salinities decreased next ( $t=t_6$ ). The water column began to re-stratify afterwards ( $t=t_7$ ). At CB7.4 (Figure 6-19f), similar to the patterns at the two other locations, the surface salinity increased first due to local wind-induced mixing and then bottom salinity increased at  $t=t_1$ . The landward flow at  $t=t_2$  began to increase the salinity throughout the water column, and a completely mixed water column was represented at  $t=t_3$  when the strongest landward flow occurred. When the flow was nearly zero ( $t=t_4$ ), the highest salinity (32.4 ppt) was shown in a de-stratified condition. Although strong seaward flow occurred at  $t=t_5$ , high salinity with a well-mixed condition still remained for four tidal cycles. The salinity began to decrease due to strong seaward flow at  $t=t_6$ , and continuously decreased to approximately 27 ppt. The stratification subsequently appears to begin to increase.

The vertical structures of velocity and salinity play an important role in determining the destratification and restratification processes during storm events. Therefore, some mixing parameters used by those two physical parameters will be discussed in the next section.

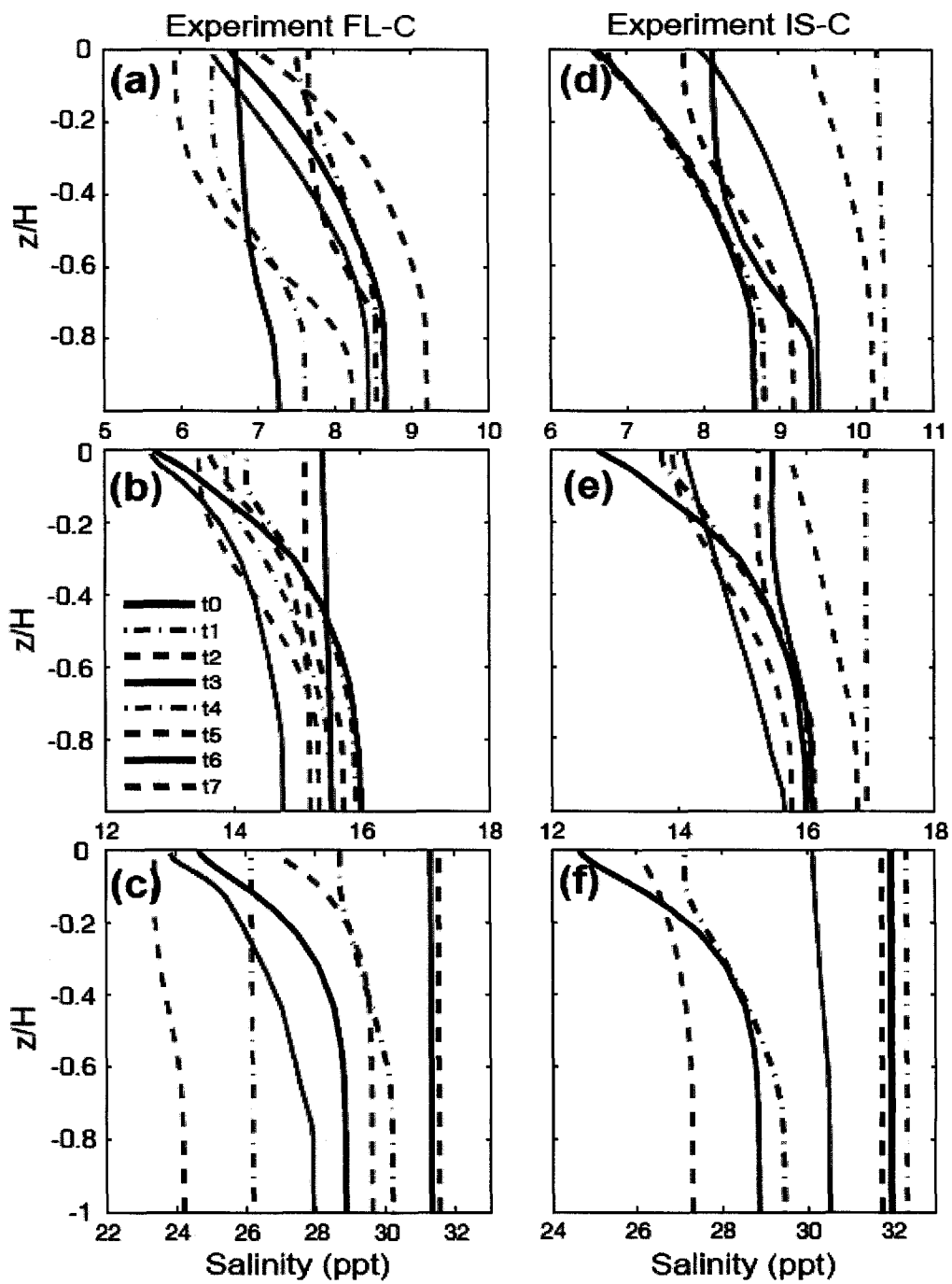


Fig. 6-19 Vertical profiles of tidally averaged salinity at three stations with time sequence: (a) upper Bay; (b) mid Bay; (c) lower Bay for the FL-C case and (d) upper Bay; (e) mid Bay; (f) lower Bay for the IS-C case.

### 6.3.3 Dimensionless mixing parameters

Mixed-layer dynamics was initially classified in lakes by Spigel and Imberger (1980). They suggested the dimensionless parameter to examine the strength of the interaction between mixing and motions. The interaction is determined by the relative importance of the two sources of turbulent kinetic energy (TKE), which are the stirring mechanism at or near the water surface by winds and the mechanism arising from the interaction of Reynolds stresses with shear, both within and at the base of the mixed layer. The gradient Richardson number (Ri) is a dimensionless ratio related to the buoyant production or consumption of turbulence divided by the shear production of turbulence, indicating dynamic stability and the formation of turbulence given by:

$$Ri = \frac{-\frac{g}{\rho_0} \frac{\partial \rho}{\partial z}}{\left(\frac{\partial u}{\partial z}\right)^2} \quad (6.2)$$

where  $g$  is gravitational acceleration,  $\rho$  is density,  $u$  is velocity, and  $z$  is depth. If internal shear causes the turbulent mixing, Ri is expected to fall below 0.25.

Thompson and Imberger (1980) and Monismith (1986) introduced a dimensionless parameter called the Wedderburn number (W) to quantify the interaction between mixing and motions induced by wind stress in lakes. Geyer (1997) suggested that the Wedderburn number (W) can characterize the influence of wind stress in the dynamics on stratified estuaries, which is defined as:

$$W = \frac{\tau_w L}{\Delta \rho g h_1^2} \quad (6.3)$$

where  $\tau_w$  is the surface wind stress,  $L$  is the length of the estuary,  $\Delta \rho$  is the density

variation along the estuary,  $g$  is the gravitational acceleration, and  $h_1$  is the thickness of the surface mixed layer.  $W \approx 1$  indicates the important role of wind stress in the estuarine circulation. In Chesapeake Bay, the longitudinal density gradient commonly has a spatial variation during hurricane events due to the salt water influx to the lower Bay. Therefore, Eq. 6.3 was modified as:

$$W = \frac{\tau_w}{\frac{\partial \bar{\rho}}{\partial x} g h_1^2} \quad (6.4)$$

where  $\partial \bar{\rho} / \partial x$  is the longitudinal gradient of vertically averaged density.

Another non-dimensional parameter to examine the interaction of shear, stratification and mixing is the horizontal Richardson number ( $Ri_x$ ) defined as (Stacey et al., 2001):

$$Ri_x = \frac{g \beta \Gamma H^2}{u_*^2} \quad (6.5)$$

where  $\beta$  is the saline expansivity ( $\cong 7.7 \times 10^{-4} \text{ psu}^{-1}$  (MacCready, 2004)),  $\Gamma$  is the horizontal salinity gradient,  $u_*$  is the friction velocity at the bottom layer, and  $H$  is the water depth. However, this parameter does not include the effect of wind stress on the surface layer. Recently, Chen and Sanford (2009) have defined the modified horizontal Richardson number, which is combined with the Wedderburn number ( $W$ ), as:

$$(Ri_{x,cs})^2 = \frac{(H^4 N_x^4 / 48 K_M)(1 - W)}{R_f (u_{*s}^3 / kh_s + u_{*B}^3 / kh_B)} \quad (6.6)$$

where  $N_x (\approx g \beta \Gamma)$  is the horizontal buoyancy frequency,  $K_M$  is the effective vertical eddy viscosity (Dyer, 1997), and  $u_{*s}$  and  $u_{*B}$  are the root-mean-square values of friction velocities on the surface and bottom layers, respectively. The surface and bottom

boundary layer thickness ( $h_s$  and  $h_B$ ) are estimated by an entrainment model

(Trowbridge, 1992; Chant et al., 2007)

$$h_s = \sqrt{2\gamma Ri_C^{1/2} \frac{u_{*s}^2}{N_\infty} \Delta t}, \quad h_B = \sqrt{2\gamma Ri_C^{1/2} \frac{u_{*B}^2}{N_\infty} \Delta t}$$

where  $\gamma$  is a constant (=1.22),  $Ri_C$  is a critical gradient Richardson number (=0.25),  $\Delta t$  is a characteristic time scale chosen as 3 hrs, and  $N_\infty$  represents background stratification.

Following Ralston et al.(2008),  $K_M$  is assumed to scale as  $a_0 C_d U_t \ell$  where  $a_0$  is 0.028 and  $\ell$  is a vertical mixing length scale. When the surface and bottom boundary layers merge ( $h_s + h_B \geq H$ ),  $\ell$  scales with  $H$ . Otherwise, the average of  $h_s$  and  $h_B$  is used for  $\ell$  (Chen and Sanford, 2009). For values of  $Ri_{x,CS}$  greater than a threshold value (of order 1), the water column should stratify, and for sub-critical values the water column should remain unstratified (Stacey et al., 2001).

These three parameters in Eqs. (6.2), (6.4), and (6.6) were calculated at the selected stations along the channel of the Bay proper during both hurricanes. The time series of the gradient  $Ri$  for three experiments were plotted in Figure 6-20. Without wind forcing, the minimum values of  $Ri$  at three locations are approximately 12, 7, and 2, respectively (Figures 6-20a to 6-20c). These minimum values are caused by flood tides.  $Ri$  in the upper Bay shows a larger value than that in the mid Bay. Generally, when a hurricane approaches,  $Ri$  begins to decrease due to the vertical mixing induced by winds. For the FL-C case,  $Ri$  started to decrease in the upper Bay and lower Bay whereas it initially increased in the mid Bay (Figures 6-20d to 6-20f). The northeasterly winds in the mid Bay tend to increase the vertical density gradient although they tend to increase vertical velocity shear as well. The strongest wind reduced  $Ri$  below 0.25, generating the

turbulent condition in three regimes. When the wind weakened,  $Ri$  began to increase. In the IS-C case (Figures 6-20g to 6-20i),  $Ri$  started to decrease in all three regimes. Similar to the FL-C case, the highest wind decreased  $Ri$  below 0.25, generating the turbulent condition in three regimes.  $Ri$  rapidly increased during the second half of Day 189 even though southerly winds were still strong. This occurred because vertical velocity shear became significantly small when landward current changed to seaward due to a seaward horizontal barotropic pressure gradient. In the mid Bay, after winds were turned off, the value of  $Ri$  still remained low. Since the gradient Richardson number only expresses the relation between vertical density gradient and vertical velocity shear, it is difficult to distinguish wind-induced straining from vertical mixing.

Figure 6-21 shows the time series of the Wedderburn number ( $W$ ) at three different locations comparing three cases, the base case run (a to c), Experiment FL-C (d to f), and Experiment IS-C (g to i). During Hurricane Floyd,  $W$  represented the negative values due to dominant down-Bay (northerly) winds. The magnitude of  $W$  attained a value on the order of 1 in the lower Bay whereas those in the mid Bay and the upper Bay reached values of -0.1 and -0.02, respectively. The temporal variations of  $Ri_x$  for three experiments are plotted in Figure 6-18. Without wind forcing, although  $Ri_x$  showed the tidal variability, the minimum values of  $Ri_x$  at all three locations are approximately 0.2, 1.0, and 0.3, respectively (Figures 6-22a to 6-22c). This indicates that tidally induced mixing dominates in the upper Bay and the lower Bay whereas stratification is relatively significant in the mid Bay. In FL-C case (Figures 6-22d to 6-22f),  $Ri_x$  decreased at all three locations. The value of  $Ri_x$  dropped below 0.1 in the upper Bay and the lower Bay whereas, in the mid Bay, its value reached 0.25. Interestingly, the value of  $Ri_x$  increased



to greater than 1 rapidly in the upper Bay and the mid Bay. In the lower Bay, the value of  $Ri_x$  persisted below 0.1 for one day and then increased until the end of the Floyd-wind period. The period of increase in the value of  $Ri_x$  appears to be consistent with the period of  $N_x$  increase due to down-Bay winds. This indicates that straining becomes important when down-Bay winds blow. In the IS-C case (Figures 6-22g to 6-22i),  $Ri_x$  gradually began to decrease and rapidly dropped below 0.1 at all three locations. The low value of  $Ri_x$  persisted until the Isabel-wind period ended. This indicates that the  $N_x$  expansion was restricted by up-Bay winds towards the end of the Isabel-wind period. The peaks of  $Ri_x$  between Day 189 and Day 190 appear to occur by the small value of friction velocity when the landward flow changed to seaward flow. Therefore, the modified horizontal Richardson number appears to be more reasonable to analyze the vertical mixing and restratification for both types of hurricanes.

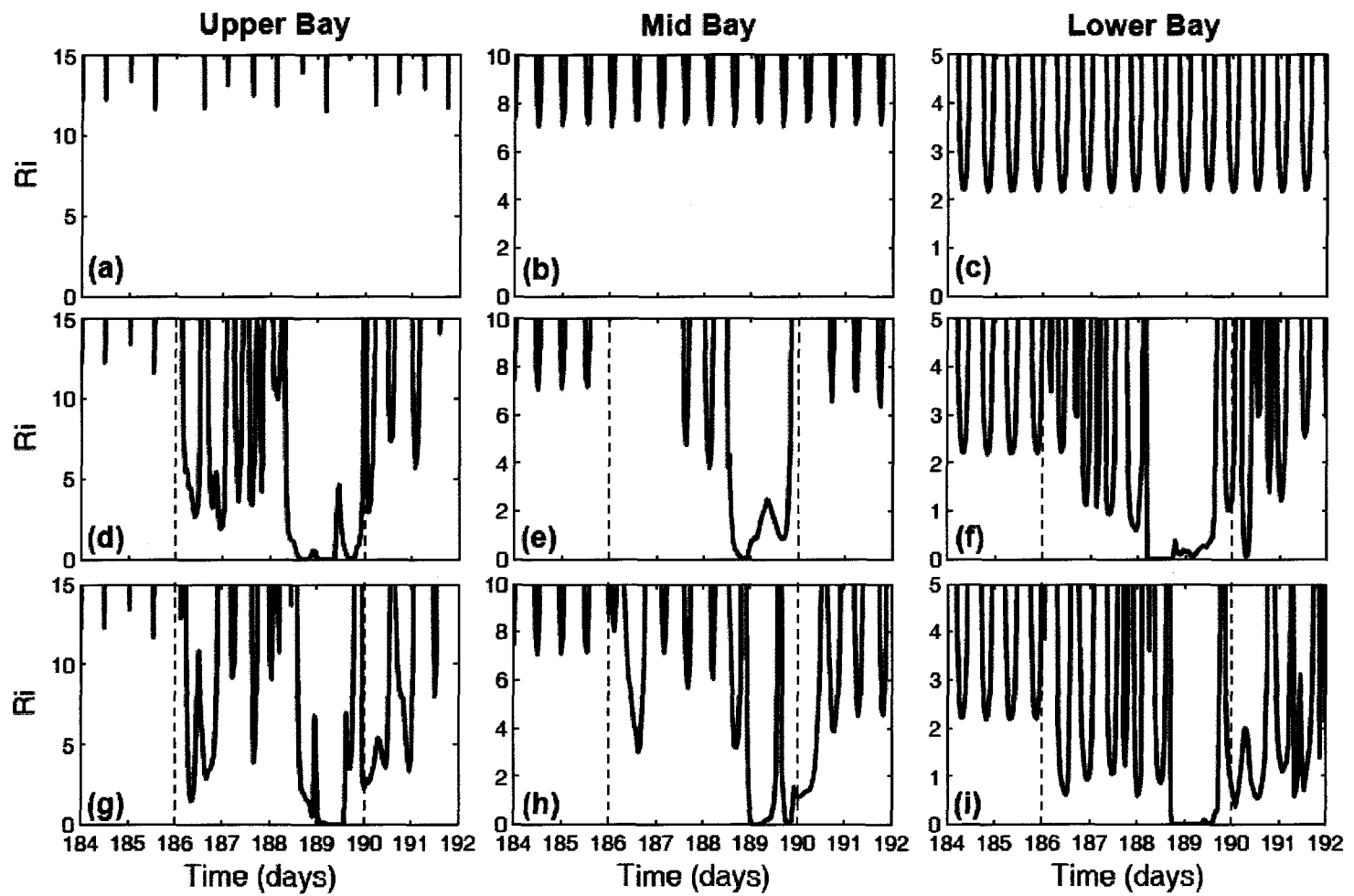


Fig. 6-20 Temporal variations of the gradient Richardson number (Ri) at three regimes for no wind case (a to c), the FL-C case (d to f), and the IS-C case (g to i).

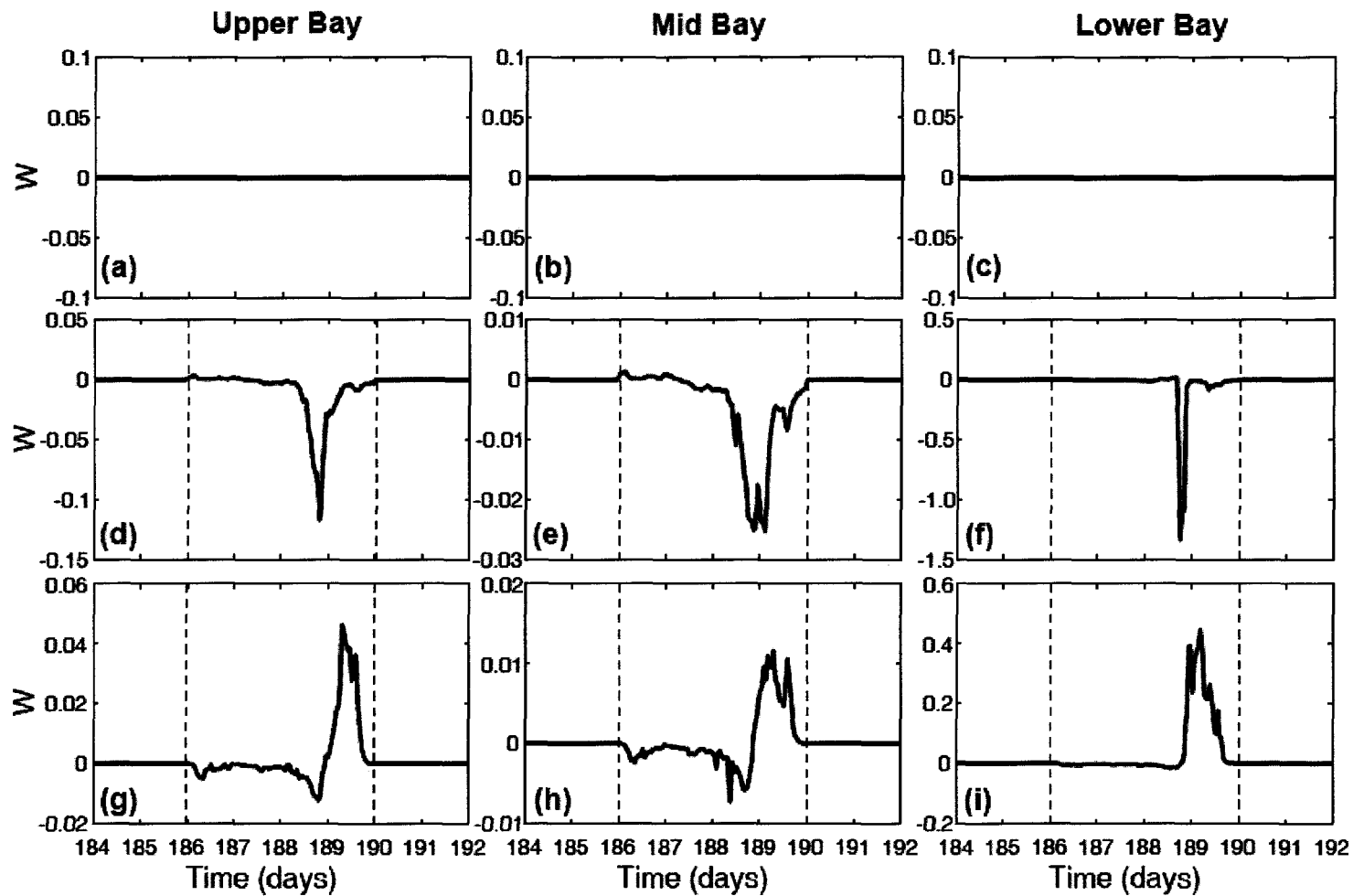


Fig. 6-21 Temporal variations of the Wedderburn number ( $W$ ) at three regimes for no wind case (a to c), the FL-C case (d to f), and the IS-C case (g to i).

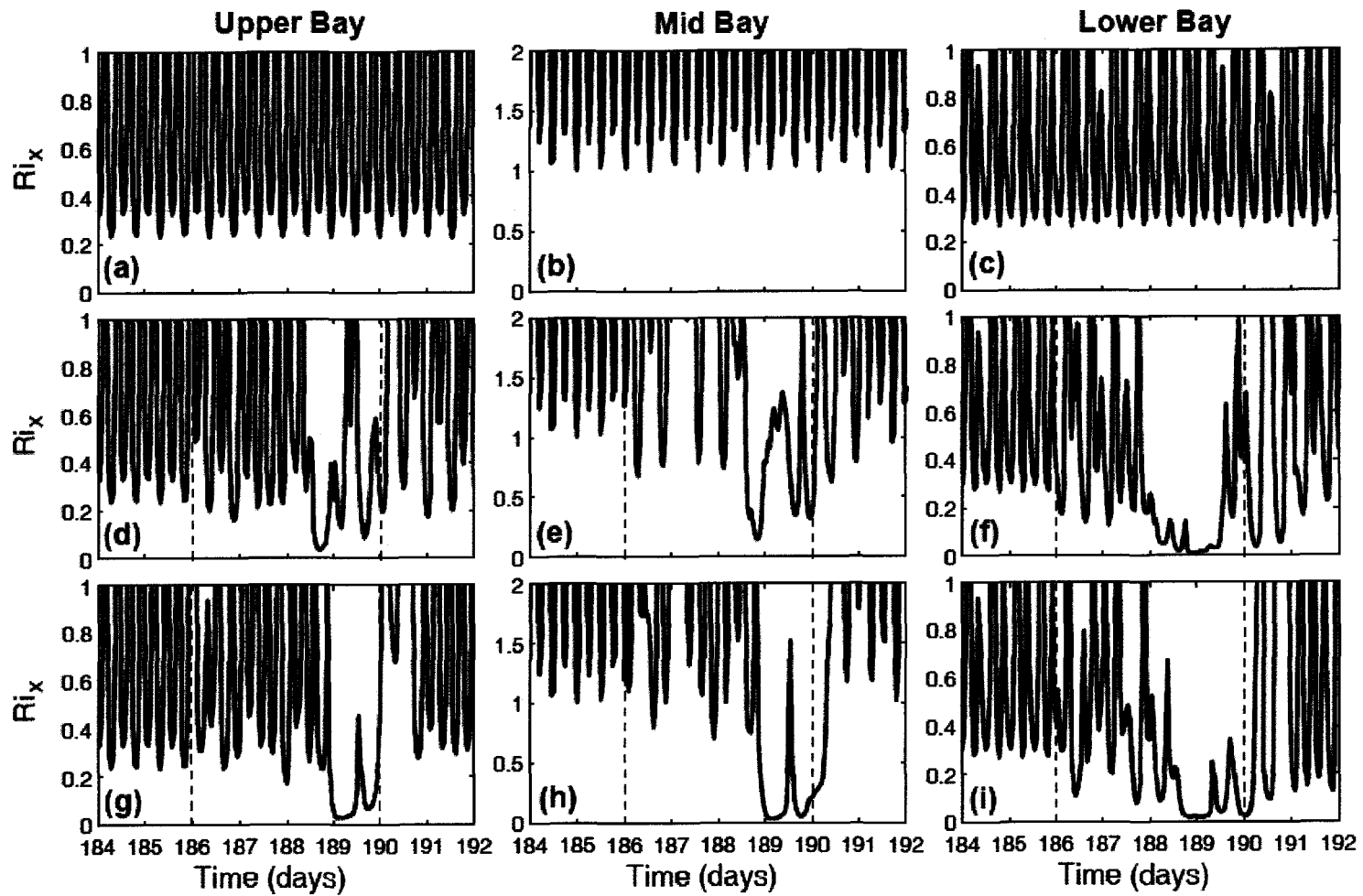


Fig. 6-22 Temporal variations of the horizontal Richardson number ( $Ri_x$ ) at three regimes for no wind case (a to c), the FL-C case (d to f), and the IS-C case (g to i).

## 6.4 Effects of local and remote winds on circulation and stratification

### 6.4.1 Vertical profiles of axial velocity

#### Hurricane Floyd

In the same fashion as the procedure described in Section 6.3, vertical structures of tidally averaged (one tidal cycle) along-channel velocity at three stations are analyzed in this section. For the FL-L case (left panels in Figure 6-23), the model results represent different salinity profiles at three locations. At CB3.3c (Figure 6-23a), an initial two-layered flow was destroyed by strong seaward flow. When local down-Bay wind began to blow, seaward flow in the surface layer started to strengthen ( $t=t_1$  to  $t_2$ ). At  $t=t_3$ , the flow throughout the entire water column became seaward, showing a vertically linear distribution. When the local wind began to weaken, the change to landward flow throughout the water column rapidly occurred representing the maximum in mid-depth at  $t=t_4$ . This landward flow began to decrease to its initial value at  $t=t_5$ , and uni-directional landward flow occurred at  $t=t_6$ . After  $t=t_6$ , the vertical profile of along-channel velocity was restored to the pre-storm condition. At CB5.2 (Figure 6-23b), both landward bottom flow and seaward surface flow slightly weakened initially until  $t=t_1$ . Only landward bottom flow became strengthened until  $t=t_3$ . During the next three tidal cycles, the surface flow changed to seaward and vertically uni-directional flow remained until  $t=t_6$  showing the maximum value in mid-depth. After  $t=t_6$ , the flow pattern began to be restored to a two-layer flow. At CB7.4 (Figure 6-23c), when the up-Bay wind blew, an initial two-layer pattern in circulation was destroyed by seaward bottom flow at  $t=t_1$ . The surface flow began to change to landward at  $t=t_2$ , showing the reversed two-layer pattern that represents landward flow in the surface layer and seaward flow in the bottom layer. When the wind changed to down-Bay wind, the rapid change to seaward flow occurred in

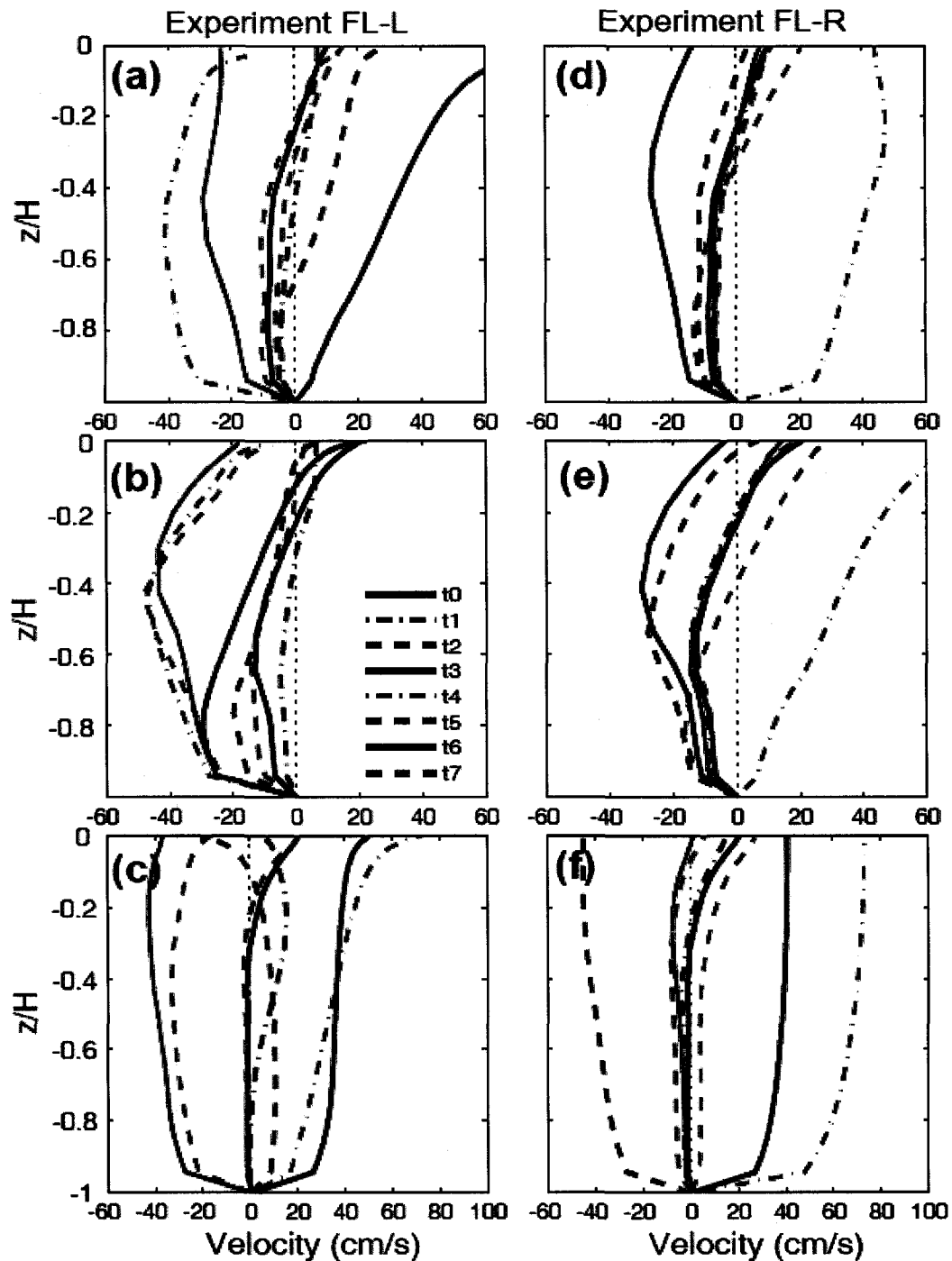


Fig. 6-23 Vertical profiles of tidally averaged along-channel velocity with time sequence for the FL-L case (left) and for the FL-R case (right) at three regimes (a,d: upper Bay; b,e: mid Bay; c,f: lower Bay). The positive value represents a seaward flow.

the surface layer and landward bottom flow strengthened at  $t=t_3$ . This vertically uniform seaward flow was strained by seaward surface stress at  $t=t_4$ . However, it was followed by strong landward return flow at  $t=t_5$  and this vertically uni-directional landward flow strengthened until  $t=t_6$ . After  $t=t_6$ , landward bottom flow weakened and the surface flow changed to seaward, and subsequently the vertical profiles of along-channel velocity began to return to the pre-storm condition.

For the FL-R case, the vertical profiles of the velocity represented different patterns from the FL-L case at all three locations. At CB3.3c (Figure 6-23d), the velocity profile began to change from  $t=t_2$ . Landward bottom flow strengthened and the changed to landward flow occurred in the surface layer until  $t=t_3$ . At  $t=t_4$ , the flow throughout the water column rapidly changed to seaward. This rapid change to seaward appears to be induced by a seaward horizontal pressure gradient between the Bay and the continental shelf. As the flow weakened after  $t=t_6$ , the vertical profile of the velocity was restored to the pre-storm condition. The remote wind initially drove the entire water column landward, whereas the local wind initially drove water seaward. During the period of  $t=t_3$  to  $t_4$ , two wind cases showed opposite directions in velocity profiles. These opposite flows were offset to incur two-layered flow during the same period as shown in Figure 6-18a. At CB5.2 (Figure 6-23e), similar to the flow at CB3.3c, two-layer circulation began to be destroyed by landward flow ( $t=t_3$ ). Different from the pattern in the local wind case, this landward flow throughout the entire water column changed to seaward at  $t=t_4$  and then the vertical profile rapidly returned to the pre-storm condition afterwards. The seaward flow at  $t=t_4$  was cancelled out by landward flow induced by local wind and subsequently two-layered flow occurred in the combined wind case (Figure 6-18b). At

CB7.4 (Figure 6-18f), a uni-directional landward flow occurred at  $t=t_2$  but it was followed by seaward flow at  $t=t_3$ . At  $t=t_4$ , landward flow was enhanced by a seaward horizontal pressure gradient. The vertical profile of the velocity returned to the initial profile with several fluctuations afterwards. In this case landward flow occurred initially and then retreated seaward whereas seaward flow occurred at first and then retreated to landward in the FL-L case. Consequently, the combined effects of the two winds generated landward flow initially followed by a strong seaward flow, and then the rebounded landward flow, as shown in Figure 6-18c.

### Hurricane Isabel

For the IS-L case (left panels in Figure 6-24), at CB3.3c (Figure 6-24a), an initial two-layered flow was enhanced by a local northeasterly wind until  $t=t_3$ . When local up-Bay wind began to blow, a two-layered flow changed to landward flow that reached  $80 \text{ cm s}^{-1}$  in the surface layer ( $t=t_4$ ). This landward flow rapidly changed to seaward after the next tidal cycle ( $t=t_5$ ) and then started to return to the pre-storm condition ( $t=t_7$ ). At CB5.2 (Figure 6-24b), initially landward bottom flow strengthened and a seaward surface flow began to change to landward until  $t=t_3$ . At  $t=t_4$ , landward surface flow was enhanced whereas bottom flow started to weaken. Similar to the pattern at CB3.3c, the flow throughout the water column became seaward at  $t=t_5$ , and then bottom flow was restored to regenerate a two-layered flow ( $t=t_6$  and  $t_7$ ). At CB7.4 (Figure 6-24c), when the easterly wind blew, a landward surface flow occurred and bottom flow headed seaward until  $t=t_3$ , and then bottom flow rapidly changed to landward at  $t=t_4$ . When the wind weakened, the return flow to seaward occurred until  $t=t_6$ . After  $t=t_6$ , the bottom



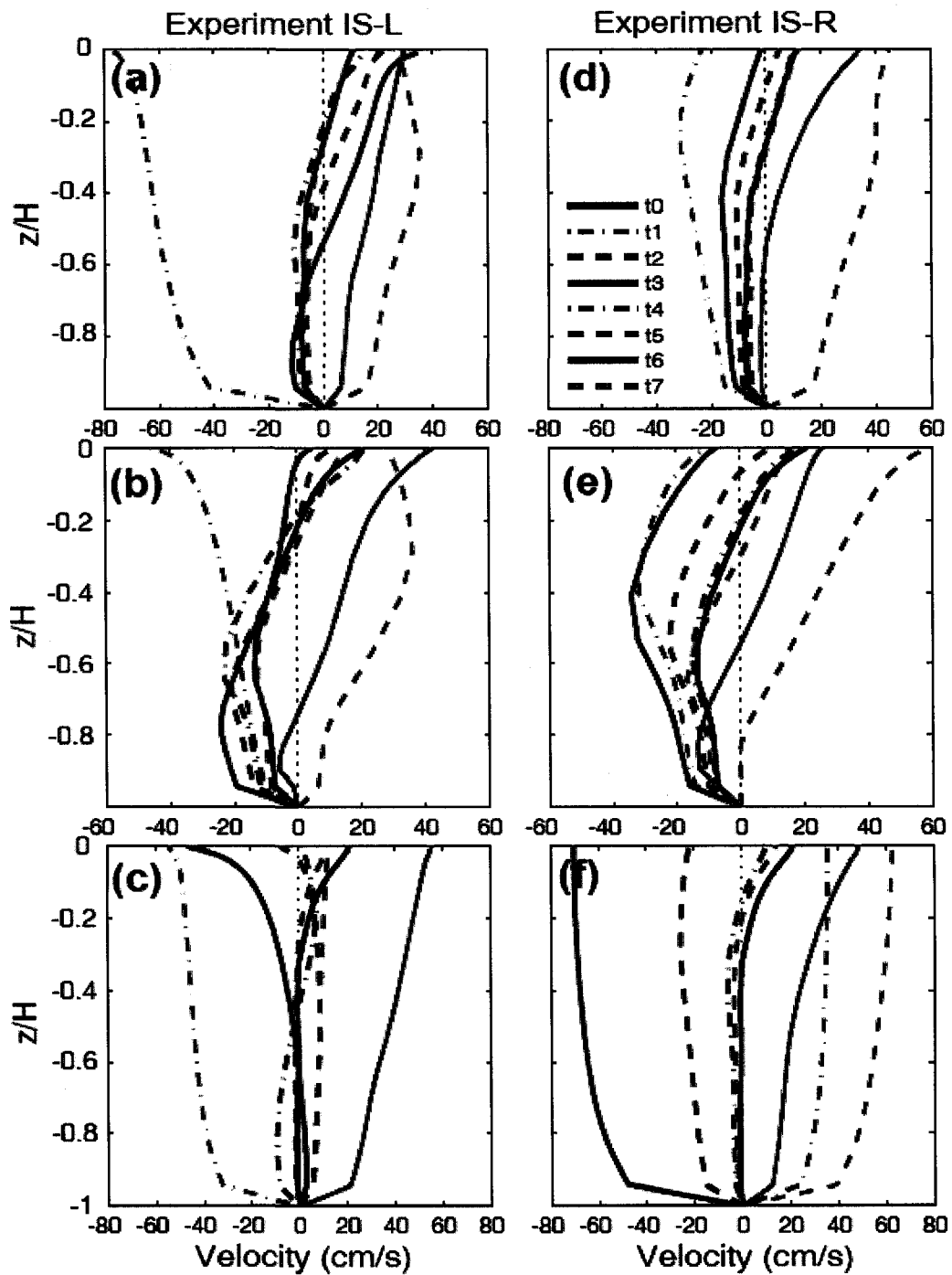


Fig. 6-24 Vertical profiles of tidally averaged along-channel velocity with time sequence for the IS-L case (left) and for the IS-R case (right) at three regimes (a,d: upper Bay; b,e: mid Bay; c,f: lower Bay). The positive value represents a seaward flow.

flow changed to landward and seaward surface flow was reduced to return to the normal condition.

For the IS-R case, the velocity profiles at three locations are characterized by the pattern as follows: 1) an initial two-layered flow changed to a uni-directional landward flow, 2) the return flow to seaward occurred throughout the water column, and 3) the bottom flow initially returned to landward flow and the surface flow weakened to be restored to the initial value. Consequently, the combined effects of local and remote winds generated the flow pattern at each location, as shown in Figure 6-18d to 6-18f. At CB3.3c, strong landward flow at  $t=t_4$  was dominantly induced by local wind but strong seaward flow at  $t=t_5$  was influenced by both local and remote winds. At CB5.2, the bottom flow and surface flow were dominated by local wind, whereas the landward flow at mid-depth was influenced by remote wind. At CB7.4, a strong landward flow at  $t=t_3$  was influenced by remote wind, the seaward flow of the IS-R case at  $t=t_4$  was cancelled out by landward flow of the IS-L case, and the seaward flow at  $t=t_6$  was influenced by seaward flows of local and remote cases.

#### 6.4.2 Time series of surface and bottom salinities

##### Hurricane Floyd

The time series of instantaneous surface and bottom salinities are plotted in Figure 6-25. The five stations were selected for both the FL-L and FL-R cases. In the FL-L case (Figure 6-25a to 6-25e), three baroclinic phenomena for salinities are represented: 1) initially, wind-induced mixing gradually increased the surface salinity, whereas it decreased the bottom salinity and consequently the stratification decreased,

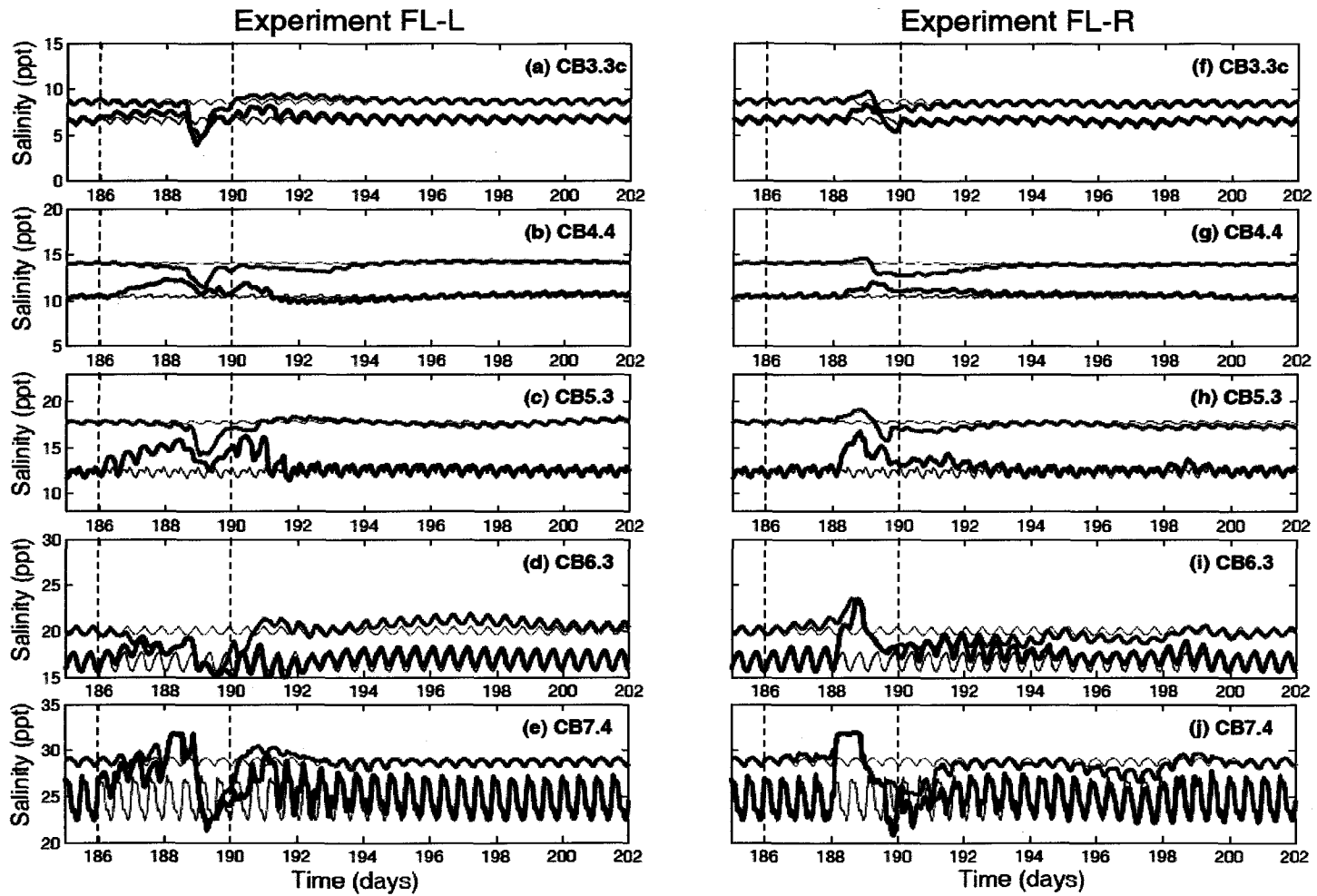


Fig. 6-25 Time series plots of surface (blue) and bottom (red) salinities at five selected stations for the FL-L case (a to e) and for the FL-R case (f to j). Thin lines denote the no wind case and vertical dashed lines denote the period of wind forcing.

2) both surface and bottom salinities rapidly decreased when the strong northerly/northwesterly winds began to blow, and 3) the stratification began to be restored when the wind intensity weakened. The destratification of the water column in this case was mostly influenced by the local wind-induced mixing, except the increase of surface and bottom salinities in the lower Bay. The local easterly/southeasterly winds drove the water upstream and generated the set-down in the lower Bay. Consequently, the landward horizontal barotropic pressure gradient drove the salt water into the Bay from the continental shelf (Figure 6-25e). The saltwater intrusion affected the CB6.3 station increasing the bottom salinity at the station by approximately 1.5 ppt (Figure 6-25d), even though the influence of saltwater intrusion was diminished by the down-Bay (northerly) wind-induced salinity drop upstream of the CB5.3 station. The occurrence of rapidly decreasing salinity in the upper Bay was earlier than that in the lower Bay. The signal of salinity drop in the lower Bay appears to be retarded by the influence of saltwater intrusion. The magnitude of salinity drop was approximately 10 ppt in the lower Bay. The combination of the seaward wind stress force and the seaward horizontal pressure gradient force results in such a big drop in salinity. After the local wind was turned off, the increased surface salinity persisted throughout the entire Bay for one day or more.

The FL-R case, as shown in Figure 6-25f to 6-25j, represented three remarkable baroclinic patterns for salinity as follows: 1) initially both of the surface and bottom salinities increased as stratification decreased, 2) the time lag in occurrence of destratification existed from the lower Bay to the upper Bay, and 3) the de-stratification persisted in the lower Bay for a while after the wind was switched off. Initially, the

surface and bottom salinities in the lower Bay slightly increased due to northeasterly winds on the continental shelf. When southeasterly/easterly winds strengthened, they drove well-mixed salt water into the Bay and both salinities in the lower Bay rapidly increased showing completely mixed status. However, the magnitude of de-stratification decreased to the upper Bay. This indicates that the stratified water inside Bay and the destratified water from the ocean compete each other maintaining certain stratification as the surge propagated to the upper Bay. As depicted in Figure 5-18, the surge induced by remote winds propagated from the Bay mouth to the upper Bay with the same order of its magnitude. The increase of surface salinity exceeded that of bottom salinity by approximately 2-6 ppt. The surface salinity increase played a significant role in destratifying the water column until the bottom salinity began to decrease. Similar to the FL-L case, the stratification remained in the mid Bay and the upper Bay until the winds on the shelf changed to northwesterly winds. The salinity drop occurred from the lower Bay because the seaward horizontal pressure gradient due to offshore (northwesterly) winds drove the water from the lower Bay to the shelf. The degree of salinity drop was approximately 5 ppt, which is smaller than the 10-ppt drop represented in the FL-L case. Its signal appears to propagate to the upper Bay as the set-down of water elevation in the lower Bay propagates to the upper Bay. One of the biggest differences from the FL-L case is that the destratification remained in the lower Bay after winds stopped. This indicates that the influence of the continental shelf could play an important role in restoring the stratification in the lower Bay.

In the mid Bay (CB4.4 and CB5.3), interestingly, the surface and bottom salinities were not completely mixed in both wind cases. However, the FL-C case represented

completely mixed condition (see Figure 6-17c). This indicates that the vertical mixing induced by local winds was enhanced by the surge which was propagated from the Bay mouth. During the period of salinity drop, the water column in the mid Bay for the combined wind case was more stratified than that for the other cases. The salt intrusion through the bottom layer appears to prevent the bottom salinity from decreasing. When the destratification proceeded, the patterns of surface and bottom salinities in the combined wind case were mostly similar to those in the local wind case. However, the influence of the remote winds on restratification process was accentuated when it propagated to the upper Bay. Therefore, during Hurricane Floyd, the destratification was primarily controlled by local winds, and both destratification and restratification were enhanced by the influence of the remote winds.

### Hurricane Isabel

The time series of instantaneous surface and bottom salinities were plotted at five stations for both wind cases as shown in Figure 6-26. In the IS-L case (Figure 6-26a to 6-26e), three remarkable features for salinities are shown: 1) the surface salinity at all stations increased, the bottom salinity increased at CB3.3c and CB7.4 but decreased at CB4.4, CB5.3, and CB6.3, and consequently the stratification decreased, 2) the rapid changes in salinity occurred when the southeasterly/southerly winds began to blow, and 3) the completely destratified water columns at all stations began to be re-stratified when the wind intensity was weakened, but the destratified status remained in the lower Bay for a while after the winds ceased. As described in the previous section, the destratification in this case was mostly influenced by the local wind-induced mixing.

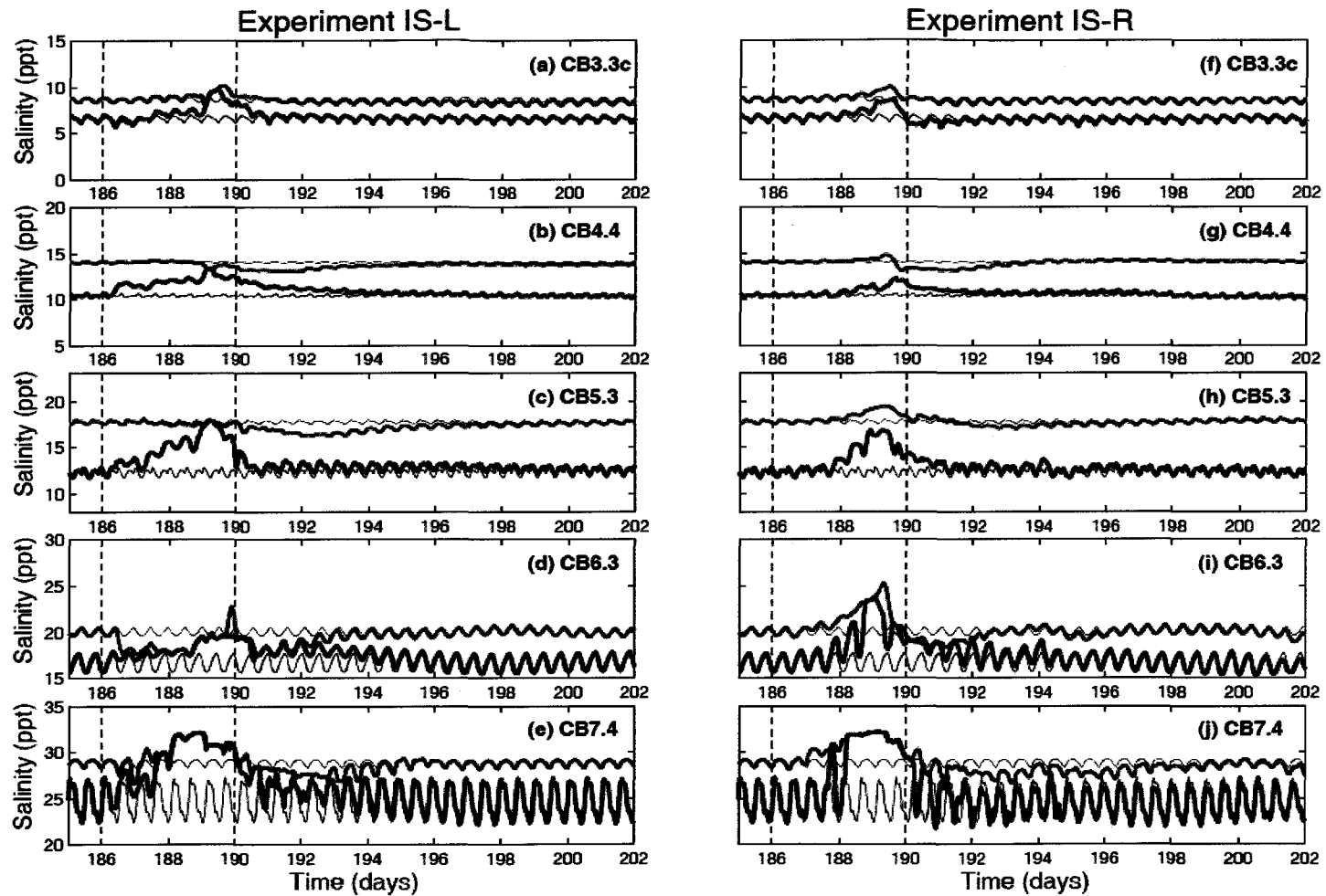


Fig. 6-26 Time series plots of surface (blue) and bottom (red) salinities at five selected stations for the IS-L case (a to e) and for the IS-R case (f to j). Thin lines denote the no wind case and vertical dashed lines denote the period of wind forcing.

The increase of both salinities in the lower Bay resulted from the salt water inflow driven by the local easterly/southeasterly winds near the Bay mouth. Subsequently, the landward horizontal barotropic pressure gradient drives the salt water into the Bay from the continental shelf (Figure 6-26e). The saltwater effectively intruded to the CB6.3 station, increasing the bottom salinity by approximately 2 ppt (Figure 6-26d). The peak of bottom salinity at CB6.3 near Day 190 appears to have resulted from the lateral salt intrusion from the east side of the Bay. In spite of strong local winds, the bottom salinity did not significantly decrease at CB4.4 and CB5.3. This indicates that the decrease of the bottom salinity was prohibited by the up-Bay (southerly) wind-induced salt intrusion. The occurrence of rapidly-increased surface salinity in the lower Bay was earlier than that in the upper Bay. As in the pattern of local southerly winds moving to the upper Bay, the signal of the surface salinity increase appears to move to the upper Bay. When the wind intensity weakened, the surface and bottom salinities decreased throughout the entire Bay. Interestingly, the bottom salinity in the lower Bay decreased in this case whereas that in the FL-L case increased. The de-stratified status in the lower Bay remained for 2-3 days after the local wind was turned off and the bottom salinity increased to be restored afterwards.

The IS-R case, as shown in Figure 6-26f to 6-26j, presented the similar patterns to the FL-R case: 1) the surface and bottom salinities increased but the stratification decreased, 2) the time lag in occurrence of de-stratification existed throughout the Bay, and 3) the de-stratification remained in the lower Bay for a while after the wind was turned off. Initially, the surface and bottom salinities in the lower Bay slightly increased due to northeasterly winds on the continental shelf. When easterly/southeasterly winds



became strong, those drove salt water into the Bay and both salinities in the lower Bay rapidly increased, showing a completely mixed condition. However, the magnitude of destratification decreased in the upper Bay. The increase of surface salinity was larger than that of bottom salinity. This means that the surface salinity increase played a significant role in destratifying the water column until the bottom salinity began to decrease. After the peak, both salinities decreased due to the seaward return flow. In contrast to the FL-R case, the seaward horizontal pressure gradient between the upper Bay and the lower Bay dominantly controlled the decrease of salinity. This caused the high salinity to remain longer than when the additional seaward flow was generated by offshore winds on the continental shelf. Similar to the IS-L case, the de-stratification in the lower Bay remained for 2-4 days after winds ceased. In the lower Bay, however, the surface salinity was out of phase with the bottom salinity. This indicates that the surface salinity could interact with tides.

Above the mid Bay (CB3.3c, CB4.4, and CB5.3), the surface and bottom salinities were completely mixed in the IS-L case, whereas they were not in the IS-R case. Interestingly, the IS-C case represented a completely mixed condition twice (see Figure 6-17g and 6-17h). The vertical mixing induced by local winds generated the first complete mixing and the surge propagated from downstream caused the second complete mixing in the mid Bay. This indicates that the moving speed of the storm was slightly faster than the propagating speed of the storm surge. At CB6.3 (Figure 6-17i), the first peak of the bottom salinity was caused by the remote wind-induced salt intrusion and the second peak was occurred by the lateral salt intrusion, as shown in the IS-L case (Figure 6-26d). For the first two days of the storm event, the patterns of surface and bottom

salinities in the IS-C case were mostly similar to those in the IS-L case. For the latter two days, the influence of remote winds on de-stratification was combined with the local wind influence. Therefore, during Hurricane Isabel, the de-stratification for the first two days of the event was dominantly determined by local winds, and this process was enhanced by the influence of remote winds afterwards.

#### 6.4.3 Vertical profiles of tidally averaged salinity

As described in Section 6.3.2, three locations were selected to examine the effects of local and remote winds on temporal variations of tidally averaged vertical salinity structures during both hurricanes.

##### Hurricane Floyd

In the FL-L case, at CB3.3c (Figure 6-27a), the surface mixed-layer depth began to deepen by increasing surface salinity and decreasing bottom salinity at  $t=t_1$ , and then the mid-depth salinity decreased at  $t=t_2$ . Strong down-Bay winds decreased vertical salinity by approximately 2 ppt at  $t=t_3$ . On the next tidal cycle, surface salinity first began to increase and then bottom salinity increased. During the period of  $t_6$  to  $t_7$ , the salinity throughout the water column exceeded that of the initial salinity profile. At CB5.2 (Figure 6-27b), the vertical structure became linear at  $t=t_3$  with a value for  $\Delta S=0.4$  ppt. The salinity throughout the water column decreased until it started to be restored at  $t=t_6$ . The lowest salinity was delayed two tidal cycles after it occurred at CB3.3c. At 7.4 (Figure 6-27b), the surface salinity increased first and then the bottom salinity increased to generate a vertically well-mixed structure at  $t=t_2$ . This homogeneous structure rapidly retreated to the lowest value within the next two tidal cycles ( $t=t_4$ ). The stratification

returned to the initial level but slightly overshoot at  $t=t_7$ , similar to the pattern shown at CB3.3c and CB5.2.

For the FL-R case, the increase of salinity throughout the water column was characterized by persistent stratification during the first three tidal cycles at CB3.3c (Figure 6-23d). The bottom salinity decreased prior to the drop of surface salinity. The lowest salinity value with increasing stratification at  $t=t_5$  was followed by an increase of salinity to the initial value at  $t=t_7$ . The salinity structures at CB5.2 were similar to its patterns at CB3.3c. At CB7.4 (Figure 6-27f), initially the bottom salinity increased and then the surface salinity increased to make a vertically well-mixed condition until  $t=t_3$ . The salinity over the entire water column began to decrease in the de-stratified condition at  $t=t_4$ . Subsequently, the stratification was generated by a decrease of surface salinity and the decrease of stratification was caused by a decrease of bottom salinity. The salinity structure began to return to the pre-storm condition afterwards.

Compared to the FL-C case (Figure 6-19a,b,c), in the mid Bay and upper Bay, vertical mixing was dominantly induced by local wind, whereas that in the lower Bay was influenced by both local and remote winds. Additionally, in the mid Bay and upper Bay, restratification at  $t=t_5$  was influenced by two factors: the increase of bottom salinity induced in FL-L and the decrease of surface salinity induced in FL-R case. For the entire Bay, it is clear that vertical mixing induced by local wind was enhanced by the effect of remote wind.

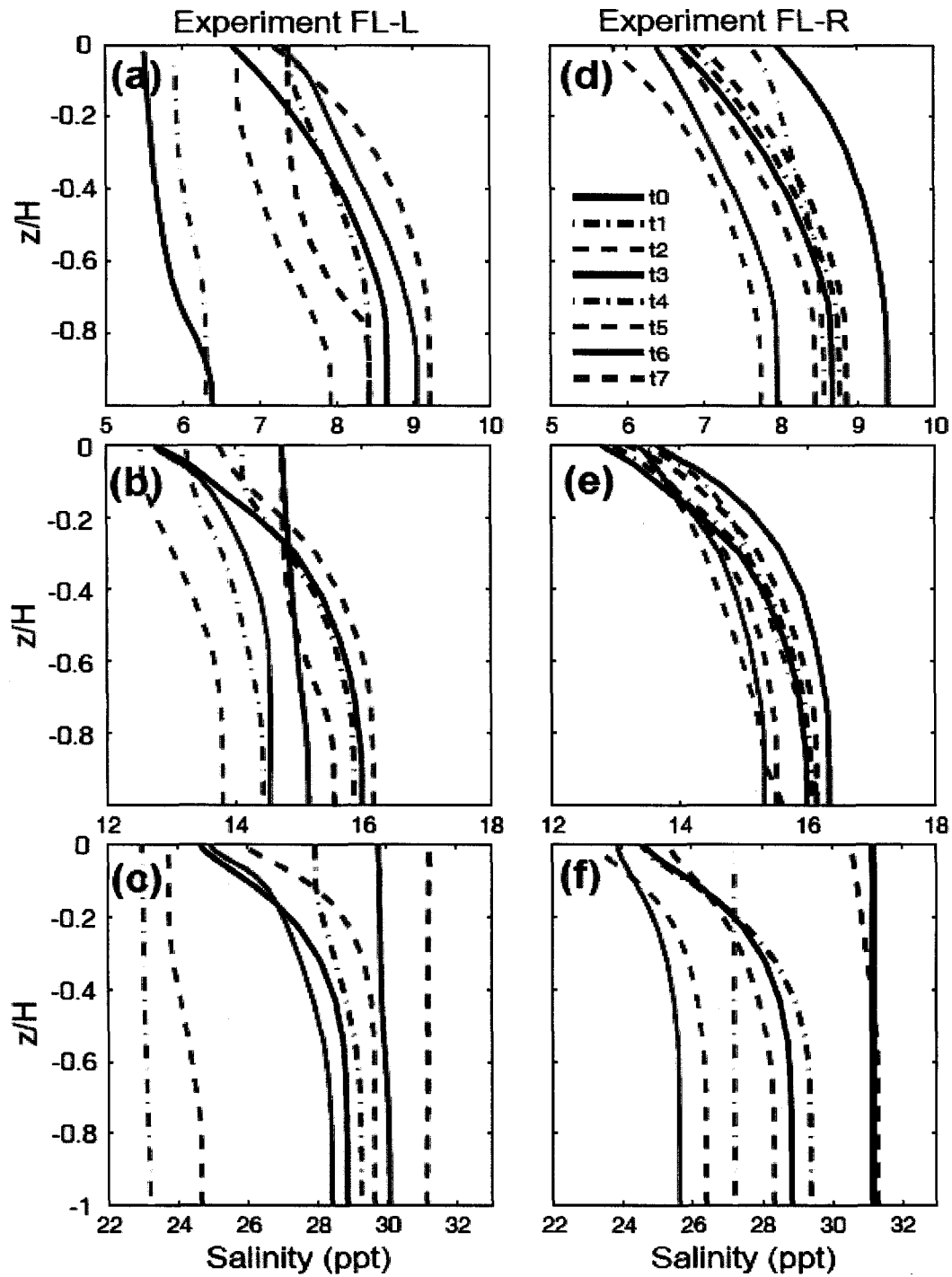


Fig. 6-27 Vertical profiles of tidally averaged salinity with time sequence for the FL-L case (left) and for the FL-R case (right) at three regimes (a,d: upper Bay; b,e: mid Bay; c,f: lower Bay).

## Hurricane Isabel

For the test case using only the local wind (IS-L), at CB3.3c (Figure 6-28a), initially the bottom salinity increased slightly and at  $t=t_3$  the surface mixed-layer depth rapidly deepened to  $z/H = -0.4$  corresponding to an increase of surface salinity. The salinity in the surface layer and mid-depth increased more than that in the bottom layer, and subsequently the entire water column was mixed at  $t=t_4$ . As the bottom salinity increased and the surface salinity decreased, the water column re-stratified at  $t=t_5$ . The salinity structure began to return to the pre-storm condition. At CB5.2 (Figure 6-28b), initially the surface salinity decreased and then bottom salinity decreased until  $t=t_3$ . After the salinity increased slightly throughout the water column, the decrease of surface salinity occurred prior to the decrease of bottom salinity at  $t=t_6$ . At  $t=t_7$ , the water column remained de-stratified relative to the pre-storm condition. At CB7.4 (Figure 6-28c), the entire water column was well-mixed at  $t=t_2$  and its salinity increased to 32 ppt at  $t=t_3$ . In contrast to the pattern in the FL-L case, high salinity remained throughout the entire water column until  $t=t_5$ . During the next two tidal cycles ( $t=t_7$ ), the salinity throughout the water column decreased by approximately 4 ppt, which restored the stratification ( $\Delta S=2$ ppt), but still a de-stratified condition remained relative to the initial structure.

Only with the remote wind (IS-R), the increase of salinity throughout the water column persisted until  $t=t_4$ , represented as a thick bottom mixed-layer at CB3.3c (Figure 6-28d). At  $t=t_6$ , the decrease of surface salinity enhanced the stratification relative to the initial status. The surface salinity increased again to return to the initial value at  $t=t_7$ . At CB5.2 (Figure 6-28e), the evolution of the vertical salinity structure was similar to the

patterns described at CB3.3c, except that the surface and bottom salinities did not drop below the initial values when they decreased from the maximum value. At CB7.4 (Figure 6-28e), similar to the patterns in the FL-R case, initially the bottom salinity increased and then the surface salinity increased to generate a well-mixed condition. After a vertically homogenous condition occurred for three tidal cycles, the water column was re-stratified by the decrease of surface salinity. The salinity continuously decreased until  $t=t_7$  but the stratification slightly recovered.

In contrast to the IS-C case, as in the Floyd-wind cases, vertical mixing was primarily caused by local wind in the upper Bay and mid Bay. However, the effect of remote wind increased the salinity in the mid Bay whereas the combined effect of both winds increased the salinity in the upper Bay. The effects of both winds were present in the lower Bay, so that the salinity structure was influenced by the combined effects of local and remote winds.

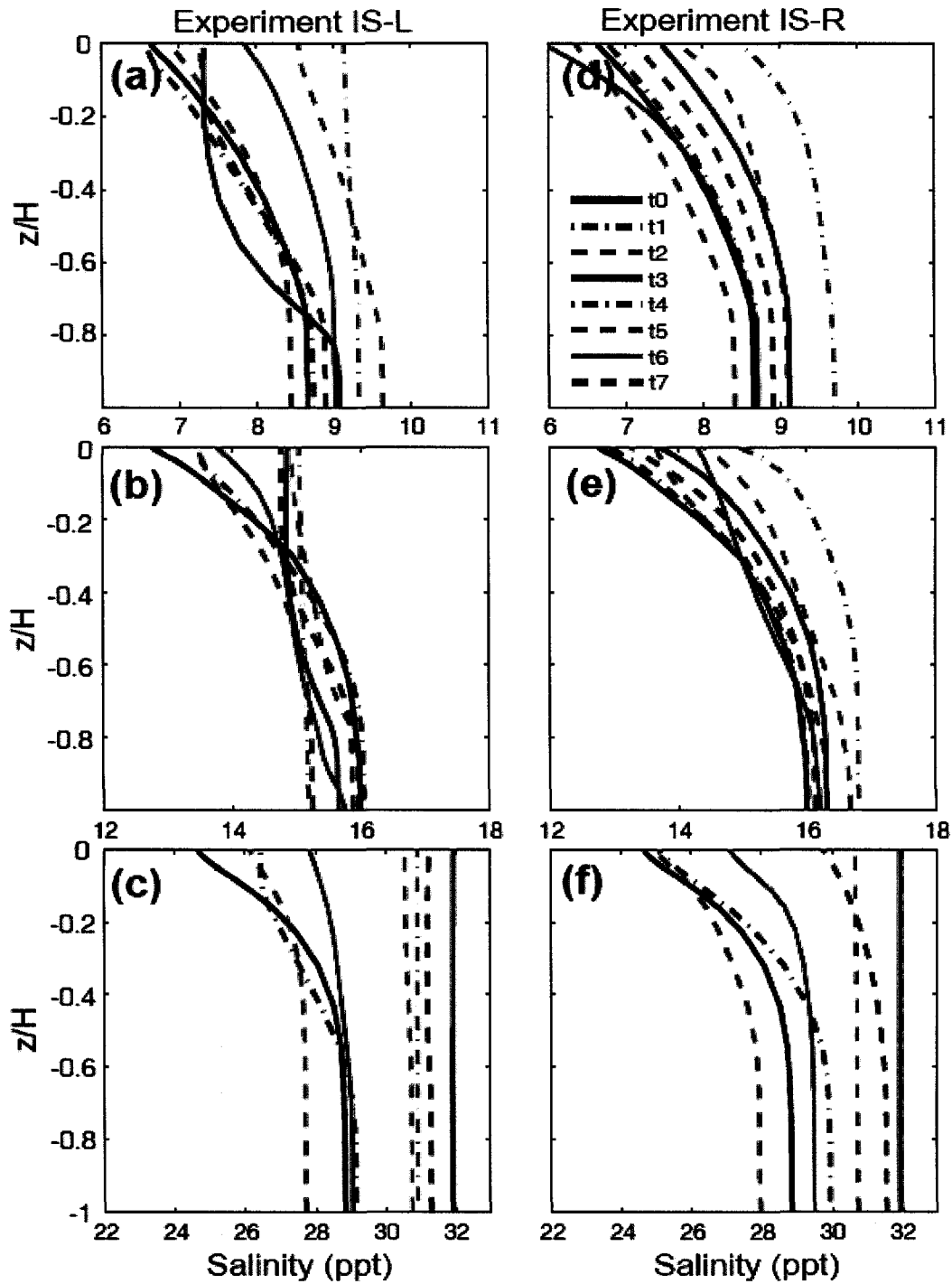


Fig. 6-28 Vertical profiles of tidally averaged salinity with time sequence for the IS-L case (left) and for the IS-R case (right) at three regimes (a,d: upper Bay; b,e: mid Bay; c,f: lower Bay).

## 6.5 Effects of precipitation during hurricane event

We have so far investigated in detail about the effect of wind and pressure fields on the response of the Bay to the hurricane forcing. All hurricanes carried precipitation. For certain storms, the precipitation directly onto Bay's water surface is so large that it could have a potential influence on the immediate response of the Bay. During Hurricane Floyd, a band of rainfall totals of 4 to 12 inches aligned closely with the Bay were recorded from eastern North Carolina through eastern Virginia and eastern Maryland. At Wilmington, North Carolina, the storm total of 19.06 inches included a 24-hour record of 15.06 inches. In Yorktown, Virginia, the storm total was 18.13 inches (Zervas et al., 2000). The questions of what are the effects of such an extreme rainfall on the response of the Bay drove us to make additional study about the influence of precipitation on the salinity field.

### 6.5.1 Numerical scheme for representation of precipitation input

The SELFE model code released as the community model version 1.5k7 has a precipitation scheme. The way it was formulated and implemented is described as follows. First, let the rainfall rate be  $R$  and denote the surface area of the unit element by  $A$ . The volume of water added by the rain per unit time is then  $Q_R = R \cdot A$ . If there is no flux (except for the rainfall), conservation of volume in the top layer requires that the amount of water per unit time after rainfall ( $Q_{\text{new}}$ ) has to balance by that before rainfall ( $Q_{\text{old}}$ ) plus  $Q_R$ :

$$Q_{\text{new}} = Q_{\text{old}} + Q_R \quad (6.7)$$

Conservation of salt requires that the amount of salt per unit time after rainfall ( $S_{\text{new}}$ ) has



to be balanced by the amount of salt before rainfall ( $S_{old}$ ). Since rain does not add salt to the water, the salt balance contains only two terms:

$$S_{new} Q_{new} = S_{old} Q_{old} \quad (6.8)$$

The volume balance (1) and salt balance (2) in the top layer give us one equation for the unknown  $S_{new}$ . Solving for  $S_{new}$  is given by:

$$\begin{aligned} S_{new} &= S_{old} \frac{Q_{old}}{Q_{new}} = S_{old} \frac{Q_{old}}{Q_{old} + Q_R} \\ &= S_{old} \frac{Q_{old} + Q_R}{Q_{old} + Q_R} - S_{old} \frac{Q_R}{Q_{old} + Q_R} \\ &= S_{old} - S_{old} \frac{Q_R}{Q_{new}} \end{aligned} \quad (6.9)$$

This formulation can be applied to the transport equation for salt (Eq. 3.3.4) described in Chapter III. However, since this method assumes that  $Q_R$  is negligible relative to  $Q_{new}$  or  $Q_{old}$ , the continuity equation does not include  $Q_R$ . The horizontal barotropic pressure gradient between Bay and continental shelf will be not generated by precipitation.

Instead of assuming steady state balance for the conservation of volume and salt flux, we propose to treat precipitation as an additional external input in the time-varying continuity equation. In this vein,  $R$  ( $= Q_R / A$ ) is added into the continuity equation as a point source on the right hand side of the Eq. (3.3.2), which gives

$$\frac{\partial \eta}{\partial t} + \nabla \cdot \int_{-h}^{\eta} \bar{u} dz = R \quad (6.10)$$

As shown in Figure 6-29, the precipitation rate was recorded at Norfolk, VA. Based on this data,  $R$  ( $m s^{-1}$ ) was determined as a surface boundary condition in the model to allow the momentum from precipitation to transfer to water velocities. The velocities obtained

in the momentum equations are used in the salt balance equation. Spatially different rainfall input should generate the horizontal pressure gradient, which enables influences on velocity and salinity distributions.

#### 6.5.2 Effect of precipitation on salinity

Without precipitation, although the model reproduced salinity decreases at two stations near the Bay mouth promptly, the predicted salinity rapidly rebounded within two days, showing approximately 5 ppt of difference from the observed salinity, as shown in Figure 6-30. To improve the accuracy of the model for salinity, two methods described above were applied to the model by using the cap shape of precipitation (solid line in Figure 6-29) to the Bay proper. The first method failed to reduce the 5-ppt difference (not shown here) whereas the second method mostly reproduced the observed salinity, as shown in Figure 6-30 (thick solid line). An additional model test was performed by using the second method with precipitation over the entire domain including the continental shelf. This case was not much different from the case using the first method. These model results indicate that seaward horizontal barotropic pressure gradient induced by precipitation plays a significant role in retarding the salinity rebound after salinity rapidly dropped. To improve model accuracy, the spatial distribution of precipitation input based on observed records is suggested to use in the model simulation during Hurricane Floyd.

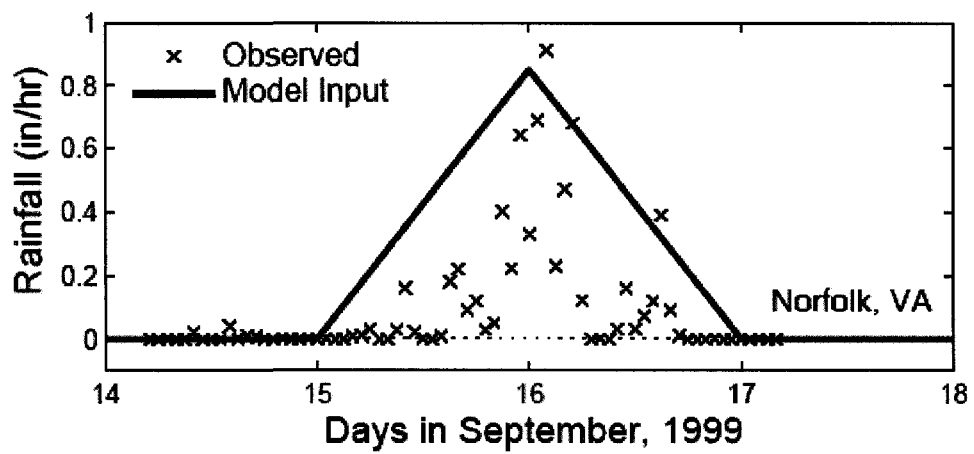


Fig. 6-29 Time series of observed precipitation (crosses) recorded at Norfolk International Airport, VA, during Hurricane Floyd and simplified precipitation as a model input (solid line).

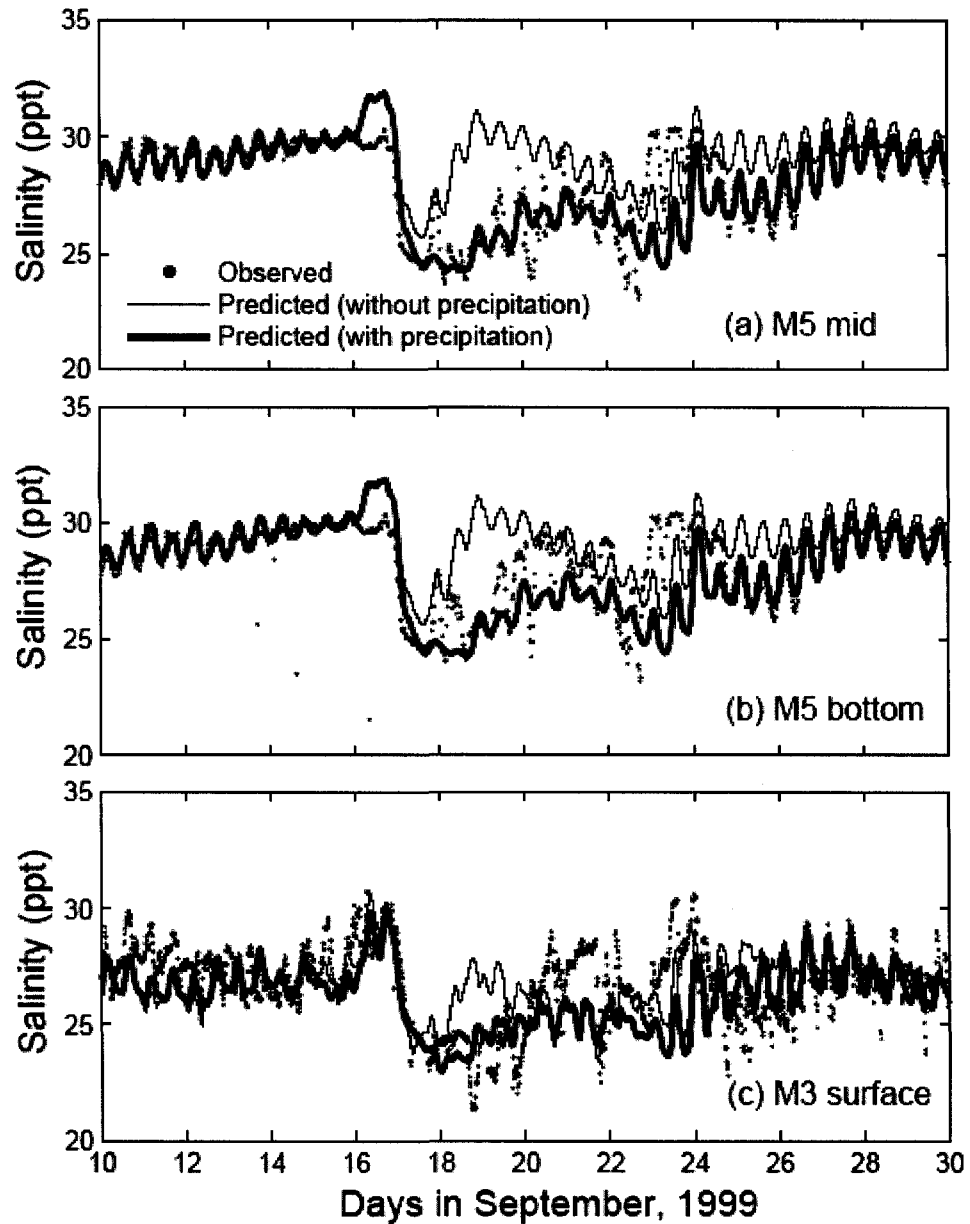


Fig. 6-30 Instantaneous salinity comparison between observation (red) and modeled results without precipitation (thin solid lines) and with precipitation (thick solid lines), at the observation stations near the Bay mouth: (a) mid-depth at M5, (b) near bottom at M5, and (c) near surface at M3, during Hurricane Floyd.

## 6.6 Summary

The baroclinic response of Chesapeake Bay to Hurricanes Floyd (1999) and Isabel (2003) has been investigated by using a semi-implicit Eulerian-Lagrangian finite-element SELFE model. The Chesapeake Bay has both similar and different baroclinic responses to two types of hurricanes. Oceanic saltwater influx obviously occurred from the continental shelf to the Bay through its entrance during both Hurricanes Floyd and Isabel, and the signal propagated upstream in the forms of storm surge and salt intrusion. Strong down-Bay (northerly) winds corresponding to the passage of eastern-type hurricanes restricts landward oceanic saltwater flux to the upper Bay, whereas up-Bay (southerly) winds corresponding to the passage of western-type hurricanes strengthens landward ocean saltwater flux to the upper Bay. During a hurricane event, surface wind stress is the primary agent to de-stratify water column by transferring generated turbulent kinetic energy to the lower layer. Advection of well-mixed salty water influx from the ocean is the second agent to change the stratification inside Bay. The rebound of bottom salinity is faster than that of surface salinity in the upper Bay due to the convergence effect, and thus this time lag of salinity rebound may generate the destratified condition. Down-Bay winds of eastern-type storms tend to enhance the stratification whereas up-Bay winds of western-type storms tend to reduce the stratification. Alternatively, down-Bay winds decrease the surface and bottom salinities to prohibit the salt intrusion whereas up-Bay winds increase the surface and bottom salinities to enhance the salt intrusion.

Precipitation as a point source of water mass on the surface not only dilutes saltwater but also generates a seaward barotropic horizontal pressure gradient. It plays a

significant role in dropping the salinity and retarding the salinity rebound after salinity rapidly dropped, so that model results show better agreement with observations. It is suggested that spatially distributed precipitation input based on observed records should be taken into account in a model simulation for a hurricane that has a huge rainfall.

## **Chapter VII**

# **ESTUARINE RECOVERY FROM HURRICANE FORCING AND INFLUENCE OF CONTINENTAL SHELF DYNAMICS**

### **7.1 Introduction**

When the hurricane approaches the Chesapeake Bay, it brings in an oceanic water influx associated with the storm surge from the mouth; at the same time, it brings in freshwater river discharge from the watershed and stronger wind fields, which mix the Bay water from the surface of the water. Chapter VI outlined the effects of these forcings on the Bay during the event of a hurricane. However, the effects of a hurricane can far exceed a 2-to-3-day window, and reach beyond the domain of the Bay into the continental shelf water. It is the purpose of this chapter to expand the scope of the response of the Bay to the hurricane to cover temporal scales on the order of weeks to months during the estuarine recovery process, and to address the spatial extent of the influence beyond the Chesapeake Bay to the continental margin.

Wind-induced mixing from a hurricane tends to destratify the water column, increasing the potential energy of the system. Oceanic salty water influx, on the other hand, increases the horizontal salinity gradient in an estuary. Once the wind forcing ceases, the circulation and density fields in the Bay begin to adjust to the changes incurred. During the adjustment stage, both river flow and normal tide-induced mixing

are important elements in setting up the estuarine gravitational circulation. The river flow creates the appropriate stratification, which is then mixed vertically either by growth of the tidal bottom boundary layer or by shear instability within the water column (Geyer and Farmer, 1989; Jay and Smith, 1990; MacCready, 1999). Occasionally, a significant amount of river flow occurs after the hurricane event brings in heavy rainfall. A large amount of river flow can have an influence on the recovery of the salinity structure to normal conditions since it sufficiently suppresses the salinity gradient in an estuary. A few studies of the estuarine recovery process from a hurricane forcing have been conducted. Kuo et al. (1976) observed that the transient response of the salinity structure to a sudden, large injection of river flow in the Chesapeake Bay during Hurricane Agnes, 1972. Recently, Gong et al. (2007) estimated the timescale of estuarine recovery from Hurricane Isabel of 2003 in the York River estuary in the range of 10 to 120 days, indicating that it depends on the storm surge energy and the amount of river discharge. Li et al. (2007) investigated the post-storm restratification process with respect to the gravitational adjustment of a fluid containing a horizontal density gradient and the geostrophic adjustment of a rotating fluid. However, the effects of hurricane types and the amount of river flow on the estuarine recovery still remain unclear. Therefore, the influences of the hurricane wind forcing and river flow on the estuarine recovery were explored in this chapter. It is well-known that, when a hurricane strikes the coast, the change of the wind field and interference of coasts will produce convergence (or divergence) to the horizontal transport of water along the coast (Neumann and Pierson, 1966). It thus will have impact on the exchange of water through the Bay mouth.



Specifically, the effects of Ekman dynamics and the along-shelf pressure gradient on the inflow/outflow at the entrance of the Bay were examined.

## **7.2 Estuarine recovery from hurricane forcing and influence of river discharge**

When considering estuarine recovery from a hurricane forcing, the premise has been made that, prior to the hurricane, the estuarine system is in a quasi-steady state, and at some time subsequent to the passage of the hurricane with the wind and buoyancy-induced perturbations, the system will return to the quasi-steady state again. As described in Chapter VI, the SELFE model has been successfully tested to ensure the estuarine system reaches the exact same quasi-steady state when the forcings and boundary conditions are kept constant. Not all the coastal ocean models achieve this, especially for salinity. In SELFE, it was achieved through using high-order advection schemes for transport and the second-order turbulence closure scheme in which the advection of salt flux and vertical mixing strike a delicate balance. If the system is displaced by external forcings from a quasi-steady state, there are net restoring forces on the system, tending to bring it back to equilibrium. In the coupled Chesapeake Bay and continental shelf system, when it is disturbed by a hurricane forcing, the restoring forces are the pressure gradient force, consisting of the surface elevation gradient force and the horizontal density gradient force, manifested in different modes and frequencies in response.

### 7.2.1 Method to estimate the estuarine recovery time scale

Based on the premise above, the definition of recovery time was defined as the time scale that is required for the estuarine system to return to the pre-storm condition, responding to the transient forcings of hurricanes. Given the error inherent in using numerical methods, the time scale, instead, will be estimated and tolerated within certain ranges based on prescribed criteria.

#### Criterion for elevation

To examine how long it takes when sea surface elevation recovers to pre-storm condition, the criterion for elevation recovery should be selected. The formula for the criterion is given by:

$$|\alpha| = |\eta_{\text{storm}} - \eta_{\text{nostorm}}| < C_{\eta} \quad (7.1)$$

where  $\eta_{\text{storm}}$  and  $\eta_{\text{nostorm}}$  are the sea surface elevations with and without the storm condition, respectively. If  $\alpha$  converges on the criterion  $C_{\eta}$  at a given time and all subsequent times, the time corresponding to the first occurrence of  $\alpha$  is specified as the recovery time (Gong et al., 2007). The value of 0.5 cm has been chosen as a  $C_{\eta}$  since the gradient of the salinity difference with respect to time reduces to an insignificantly small value when  $|\alpha|$  is smaller than 0.5 cm.

#### Criterion for salinity

As for salinity recovery, the formula for the criterion is used as follows:

$$|\gamma| = \left| \frac{S_{\text{storm}} - S_{\text{nostorm}}}{S_{\text{nostorm}}} \right| < C_s \quad (7.2)$$

where  $S_{\text{storm}}$  and  $S_{\text{nostorm}}$  are the values of salinity with and without the storm condition, respectively. The relative error formulation is reasonable rather than the absolute error formulation since the salinity spatially varies in the Bay. The value of 0.02 (2 %) has been selected as a  $C_S$  for salinity since the gradient of salinity difference with respect to time reduces to an insignificantly small value when  $|\gamma|$  is smaller than 0.02. This translates to difference of 0.1 ppt in the Upper Chesapeake Bay where the mean salinity normally is approximately 5 ppt.

### 7.2.2 Estimation of recovery time from wind forcing

A series of ideal experiments were designed to study the recovery time from the hurricane wind forcing. The steps are as follows: First, the initial condition was generated after 180 days of spin-up to ensure that the system was in quasi-steady state as described in Section 6.3.1. Second, realistic wind forcings for different hurricane winds were imposed on the coupled Chesapeake Bay and continental shelf model system for 4 days. The wind forcing is further divided into a local wind scenario (the wind field only applied in the Bay) versus a remote wind scenario (the wind field only applied in the continental shelf). Third, after 4 days, the wind forcing was turned off, and the model continued to run until it reached the criteria of quasi-steady state described above. In the case of evaluating effect of river discharge on the salinity recovery time (section 7.2.3), river discharge was begun immediately after the wind forcing stopped, and specified for another 4 days. Afterwards, the model continued to run until it attained the criteria of quasi-steady state.

Table 7-1 Estimated recovery time for sea surface elevation in the Chesapeake Bay from four-day wind forcing. Days are calculated from the wind termination day.

(unit: days)

station	Experiments for Floyd			Experiments for Isabel		
	FL-C	FL-L	FL-R	IS-C	IS-L	IS-R
CB3.3c	5.6	2.2	4.0	7.7	5.7	5.8
CB4.4	4.9	2.3	3.5	6.6	1.8	5.1
CB5.2	2.8	2.0	3.4	6.5	4.9	5.4
CB6.3	4.4	2.1	3.2	6.4	1.5	2.4
CB7.4	3.8	2.8	3.5	6.8	4.4	6.8
Avg.	4.4	2.3	3.5	6.8	3.7	5.1

Six different experiments listed in Table 6-2 have been designed to investigate the estuarine recovery time under the wind forcing. The experiments were continuously run an additional 150 days after the four-day wind forcing period stopped; the Chesapeake Bay system obviously reaches quasi-steady state from the cold start after 150 days. This may not be universally true when the above-normal-high river discharge is injected into the system, as is further described in Section 7.2.3.

### Sea surface elevation

The recovery times for sea surface elevation were estimated at the selected five stations as shown in Table 7-1. The combined wind effects versus those of local wind (L) and remote wind (R) were separately evaluated. It is evident that sea surface elevations were restored to pre-storm condition within one week for Hurricanes Isabel and Floyd. The recovery time for remote wind effects tends to be slightly longer than that from local wind effects, which causes the recovery time from combined wind effects to be slightly longer overall.

### Salinity

The time series of the salinity difference between the “no storm” case and the “storm” case were plotted in Figure 7.1. For Experiment FL-C, the salinity differences converged to within the 2 % criterion within two weeks at CB7.4 of the lower Bay. At CB4.4, as described in Chapter VI, both salinities initially showed a rapid rebound immediately after winds ceased. The second rebounds occurred ten days later. Due to these oscillations, the bottom salinity difference met the criterion at approximately 22 days. At CB3.3c of the upper Bay, the second overshooting of bottom and surface salinities occurred 15-20 days after the wind was turned off and persisted from 42-52 days. This overshooting played a role in retarding salinity recovery to the pre-storm condition. For Experiment IS-C, salinity differences at all three stations converged to the criterion within 20 days since any significant overshooting did not occur. Salinity recovery times for each wind experiment are tabulated (Table 7-2). The recovery time from the remote wind of each hurricane had the same order of magnitude. Especially in

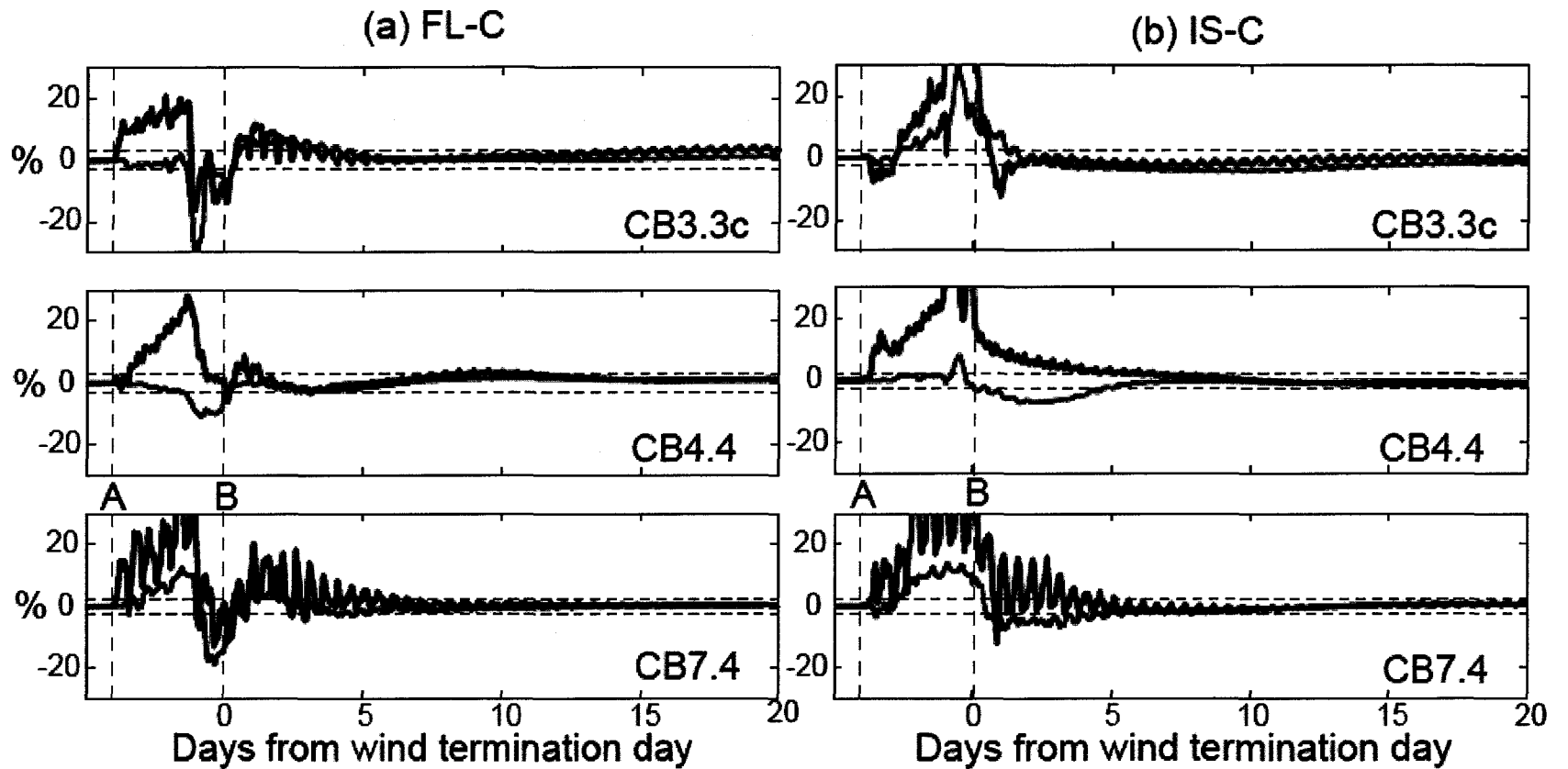


Fig. 7-1 Time series of salinity difference ( $\gamma$ ) at selected three stations for Experiment FL-C (a) and Experiment IS-C (b): Blue lines represent surface salinity and red lines represent bottom salinity. Black dashed lines denote 2% criterion of  $\gamma$  and green dashed lines denote wind turn-on day (A) and wind termination day (B).

the mid Bay and the upper Bay, salinity recovery time from Floyd wind forcing took longer than that from Isabel wind forcing. To better understand this discrepancy between both hurricanes, based on time sequence plots of salinity in the mid Bay (Figure 7-2), the schematic vertical salinity structures are mapped in Figure 7-3. Stage 1 is specified by surface salinity increase due to wind-induced mixing for both hurricanes. Stage 2 is represented by a well-mixed condition due to highest winds for both hurricanes. For Experiment FL-C, at Stage 3, surface salinity for Hurricane Floyd starts to decrease since down-Bay wind stress began to overcome the landward pressure gradient, and bottom salinity began to decrease through Stage 4 due to the seaward barotropic pressure gradient between the Bay and the shelf (see Figure 5-12). For Experiment IS-C, Stage 3 is characterized by the salinity increase under a well-mixed condition due to the combined effect of up-Bay winds and storm surge, which involves a landward barotropic pressure gradient and a landward wind stress. Through Stage 4, surface and bottom salinities decreased since the seaward barotropic pressure gradient overcame the landward wind stress. Bottom salinity did not decrease as much as surface salinity due to the landward baroclinic pressure gradient. After wind cessation, the vertical salinity structure in both cases began to rebound upstream. For Experiment FL-C, relatively strong return flow occurred due to landward barotropic pressure gradient. This drove surface and bottom salinities to increase on Stage 5 and even showed slight overshooting on Stage 6. Finally both salinities reached a quasi-steady state on Stage 7. For Experiment IS-C, the decreased bottom salinity started to increase again due to the landward baroclinic pressure gradient and surface salinity continuously decreased to a

quasi-steady state. As addressed above, the salinity recovery in Experiment FL-C took longer than that in Experiment IS-C in the mid Bay and upper Bay.

Table 7-2 Estimated recovery time for salinity in the Chesapeake Bay from four-day wind forcing. Days are calculated from the wind termination day.

(unit: days)

station	Experiments for Floyd						Experiments for Isabel					
	FL-C		FL-L		FL-R		IS-C		IS-L		IS-R	
	bott	surf	bott	surf	bott	surf	bott	surf	bott	surf	bott	surf
CB3.3c	42	52	42	52	14	10	18	13	18	10	14	14
CB4.4	22	13	22	13	13	10	8	9	7	7	8	13
CB5.2	18	12	15	10	15	12	8	12	8	12	7	13
CB6.3	18	12	16	11	11	11	16	14	7	7	16	14
CB7.4	11	11	7	7	11	11	14	15	7	7	14	15
Avg.	22	20	20	19	13	11	13	13	9	9	12	14



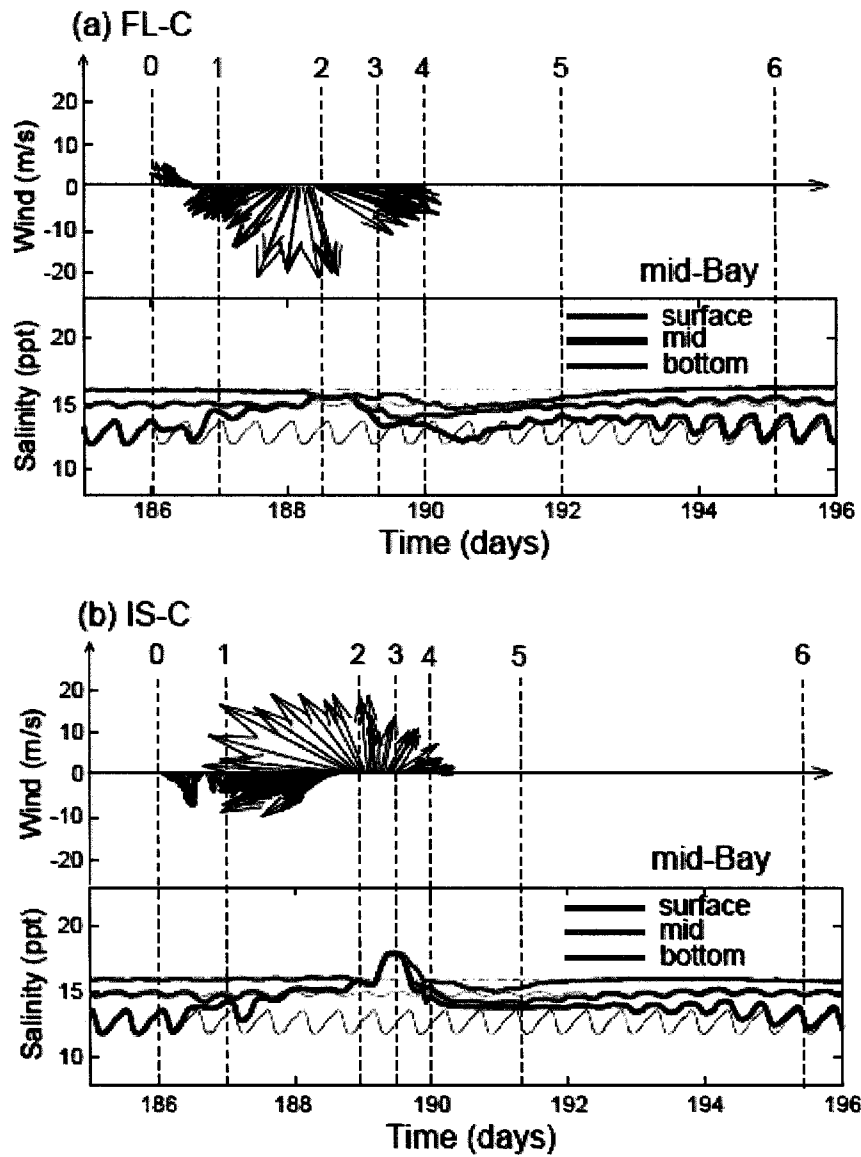


Fig. 7-2 Time series of wind and salinity in the mid Bay during (a) Hurricanes Floyd and (b) Hurricane Isabel. Vertical dashed lines represent each characterized stage.

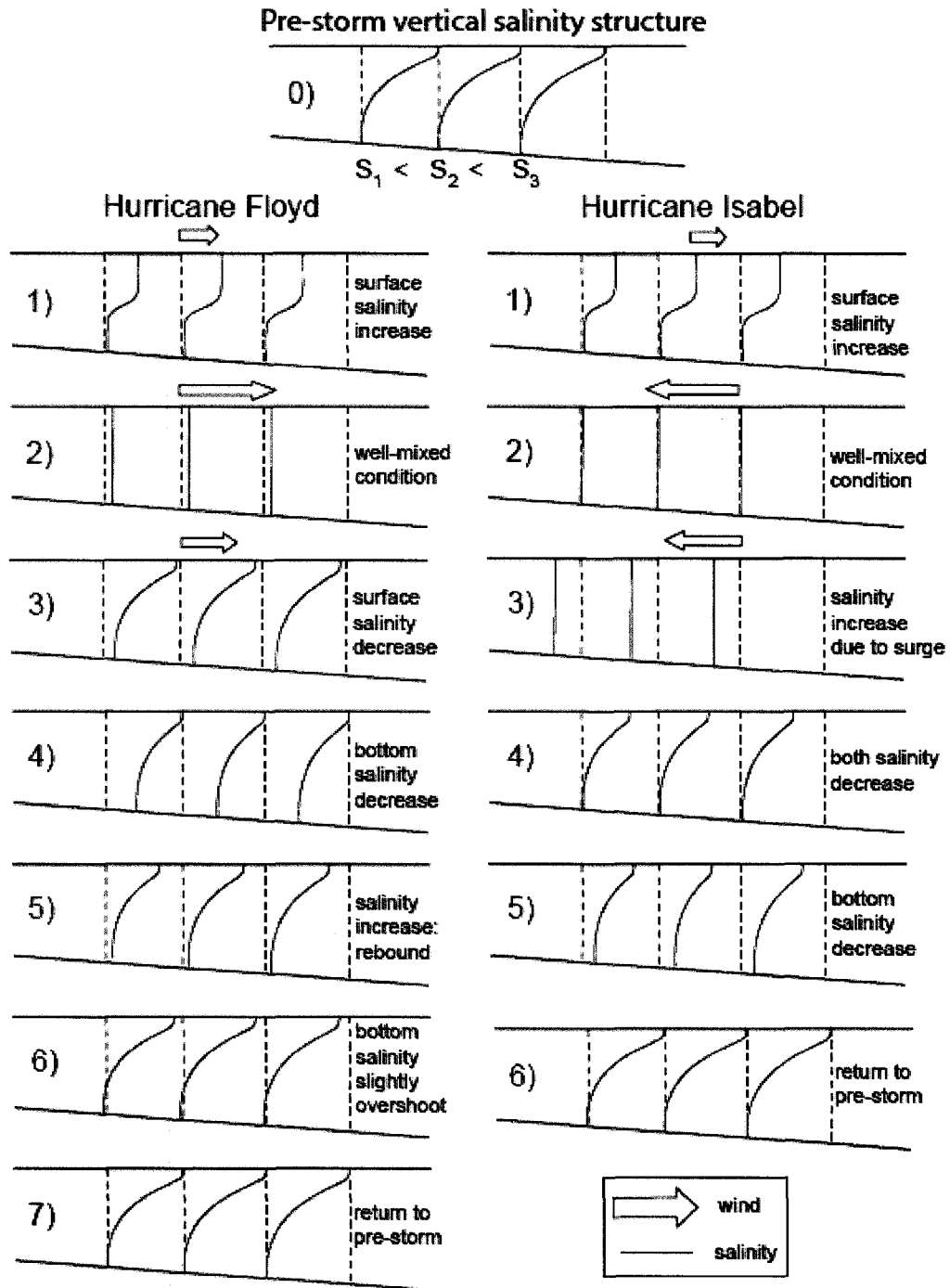


Fig. 7-3 Schematic maps of vertical salinity structure at each stage during Hurricanes Floyd (left) and Isabel (right).

### 7.2.3 Effect of river discharge on salinity recovery time

A hurricane event is usually followed by high river discharge. During Hurricane Isabel, the river discharge began to increase immediately after winds weakened, as shown in Figure 7-4. It was hypothesized that river discharge could affect the salinity rebound induced by wind forcing when river discharge increases immediately after wind cessation. Of course, if the amount of river discharge is extremely huge after Hurricane Agnes in 1972 (Kuo et al., 1976), or high river discharge event persists for a long time, salinity suppression by river discharge forcing will be dominant more than salinity rebound by wind forcing. This means that estuarine recovery time scale is mainly determined by river discharges. Thus, two idealized river discharges were tested and are shown in Figure 7-5. One is fivefold the base river discharge of  $Q=550 \text{ m}^3 \text{ s}^{-1}$  (i.e.,  $5Q=2750 \text{ m}^3 \text{ s}^{-1}$ ), and the other is tenfold this discharge (i.e.,  $10Q=5500 \text{ m}^3 \text{ s}^{-1}$ ). The river discharge event was specified for 4 days, the same duration as the wind forcing period, immediately after the wind forcing stopped. Based on this design, additional six experiments were conducted, as listed in Table 7-3.

Figure 7-6 shows the time series of salinity differences between base run and Experiment NW-MR (a), between base run and Experiment FL-CMR (b) and between base run and Experiment IS-CMR (c). The biggest difference from Figure 7-1 is that the second overshooting of bottom and surface salinities at CB3.3c disappeared in Experiment FL-CMR. The river discharge of  $5Q$  caused  $\gamma$  to converge to within the 2% criterion rapidly, so that salinity recovery time became shorter than that in Experiment FL-C in the upper Bay. In contrast, in Experiment IS-CMR, the river discharge suppressed the surface and bottom salinities more due to seaward barotropic pressure

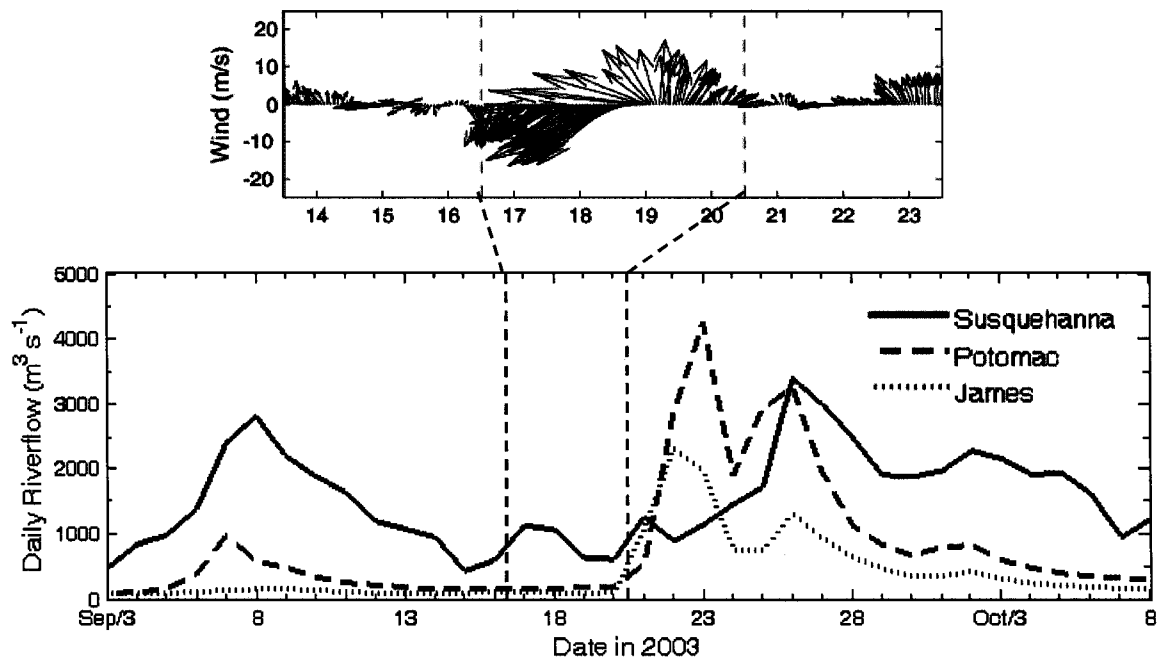


Fig. 7-4 The records of winds at CBBT (upper panel) and river discharges in three rivers of the Chesapeake Bay (lower panel) on September, 2003.

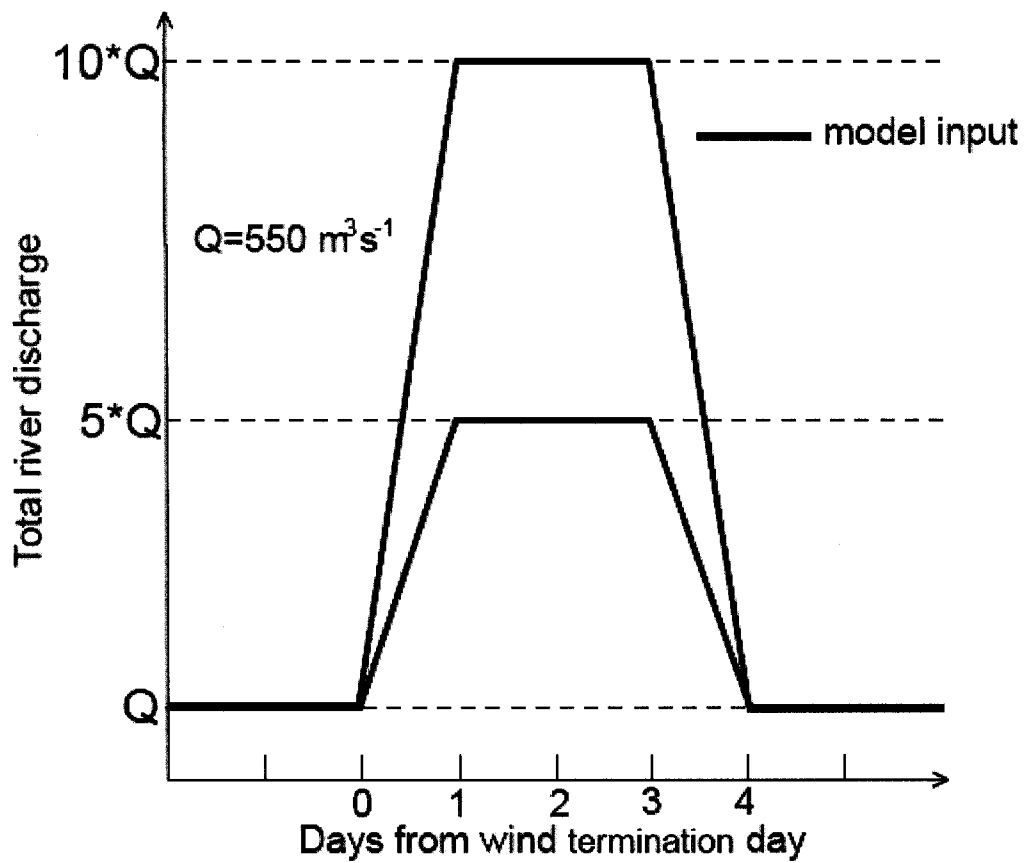


Fig. 7-5 Idealized river discharge inputs for the experiments.

Table 7-3 Summary of additional experiments performed for river discharge event.

Experiments	Winds	Total Maximum River Discharge ( $\text{m}^3 \text{s}^{-1}$ )	Ambient Current ( $\text{cm s}^{-1}$ )	Subtidal Alongshore PG*
FL-CMR	combined winds (Floyd)	2,750	10	yes
IS-CMR	combined winds (Isabel)	2,750	10	Yes
NW-MR	no wind	2,750	10	no
FL-CHR	combined winds (Floyd)	5,500	10	yes
IS-CHR	combined winds (Isabel)	5,500	10	yes
NW-HR	no wind	5,500	10	no

\* PG represents the pressure gradient and was imposed in the wind forcing period.

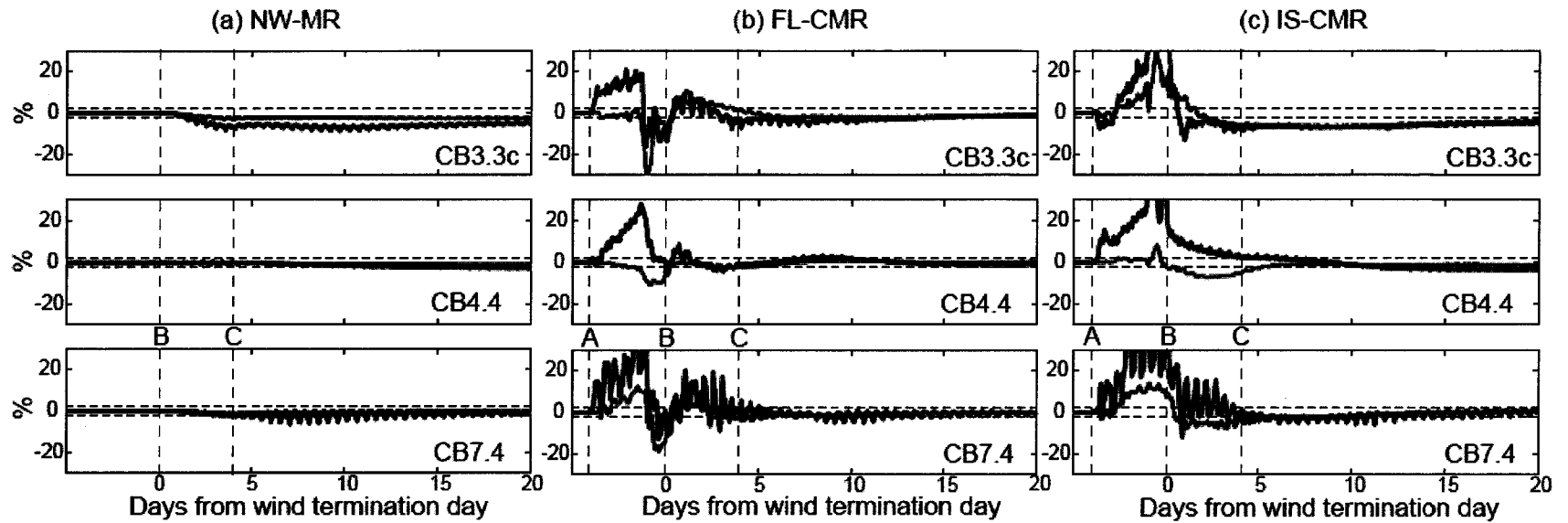


Fig. 7-6 Time series of salinity difference ( $\gamma$ ) at selected three stations for Experiments NW-MR (a), FL-CMR (b), and IS-CMR(c). Blue lines represent surface salinity and red lines represent bottom salinity. Dashed lines denote 2% criterion of  $\gamma$  and green dashed lines denote wind turn-on day (A), wind termination and 5Q river discharge turn-on day (B), and 5Q river discharge termination day (C).

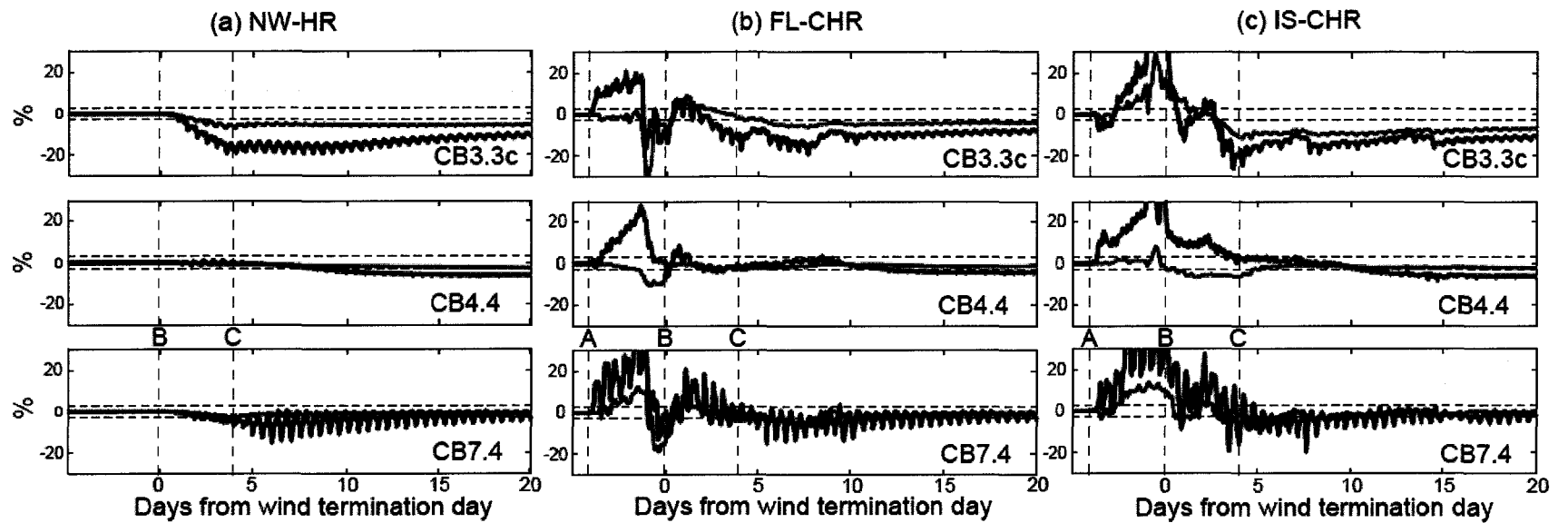


Fig. 7-7 Time series of salinity difference ( $\gamma$ ) at selected three stations for Experiments NW-HR (a), FL-CHR (b), and IS-CHR(c). Blue lines represent surface salinity and red lines represent bottom salinity. Dashed lines denote 2% criterion of  $\gamma$  and green dashed lines denote wind turn-on day (A), wind termination and 10Q river discharge turn-on day (B), and 10Q river discharge termination day (C).



Table 7-4 Estimated recovery time for salinity in the Chesapeake Bay for high river discharge experiments. Days are calculated from the wind termination day.

(unit: days)

station	FL-CMR		FL-CHR		IS-CMR		IS-CHR	
	bottom	surface	bottom	surface	bottom	surface	bottom	surface
CB3.3c	18	18	100	137	58	88	>150	>150
CB4.4	18	12	18	82	10	54	90	130
CB5.2	17	16	12	54	10	12	22	100
CB6.3	16	10	18	32	15	14	20	40
CB7.4	10	18	12	28	14	19	18	30
Avg.	16	15	32	67	21	37	60	90

gradient, so that it caused the salinity recovery time to increase. Figure 7-7 shows the time series of salinity differences for high river discharge ( $5500 \text{ m}^3 \text{ s}^{-1}$ ). Overall, strong barotropic pressure gradient induced by high river discharge suppressed bottom and surface salinity and the recovery time was longer than those for the experiments using 5Q river discharge. A summary of the salinity recovery time for each experiment using 5Q and 10Q is provided in Table 7-4.

### **7.3 Influence of continental shelf dynamics**

#### **7.3.1 Effect of Ekman transport**

The wind stress imposing on the rotational earth generates a surface Ekman layer. The wind-driven horizontal transport depends on the magnitude of the wind stress and the thickness of the surface Ekman layer. Due to the Earth's rotation, the transport is oriented at an angle clockwise to the direction of the wind stress in the Northern Hemisphere (Ekman, 1905; Cushman-Roisin, 1994). During Hurricane Isabel, northeasterly winds of  $20$  to  $25 \text{ m s}^{-1}$  were recorded at the Chesapeake Bay Light and Virginia Beach stations for the two days ( $> 2\pi/f \sim 17.4 \text{ h}$ ) (Figure 2-7). These wind stress-induced drift currents are balanced by the Coriolis force and the bottom frictional force and thus generate Ekman transport into the Chesapeake Bay, as a remote-wind-induced forcing. The transport is expected to influence the subtidal sea surface elevation and salinity. Figure 7-8 (a) and (b) shows the surge elevation and salinity comparisons, respectively, during Hurricane Isabel at the CBBT (Chesapeake Bay Bridge Tunnel). The modeled subtidal surge elevation, represented by the heavy blue curve, caught the entire hurricane event reasonably well. In the same simulation, if all conditions stayed the same

except that the Coriolis force was not included, the results were different, as shown by the thin blue line. As one can see, the surge level before the surge peak of the hurricane was under-predicted whereas, after the peak, it was over-predicted. It is argued that without proper representation of the Coriolis force, no Ekman transport into the Bay can be generated during the first phase of the wind from the north, resulting in under-prediction. After the hurricane made the landing, the hurricane wind turned from northerly to southerly in the second phase of the wind forcing. In this case, the Ekman transport is offshore, in the opposite direction as compared with the first phase, which resulted in over-prediction.

The Ekman transport in the first phase not only generated higher surface elevation by 0.2 to 0.3 m than that without the Coriolis force, but also created higher surface and bottom salinity by 2 to 3 ppt in the lower Bay, as shown in Figure 7-8b. Furthermore, the surface and bottom velocities also increased by 0.15 to 0.2 m s<sup>-1</sup> as well (not shown). This value is a reasonable agreement with the estimation from an analytical solution given by

$$\mathbf{u} = \frac{\mathbf{U}}{H} = \frac{\boldsymbol{\tau}^y}{\rho_0 f H} \sim (-) 0.2 \text{ m s}^{-1} \quad (7-3)$$

where negative values are landward.

During the northerly wind event, the local Bay wind can push the water from northern Bay into the southern Bay and offset the remote wind effect. A similar phenomenon can also be described for the effect of a southerly wind event. Nevertheless, Garvine's (1985) investigation indicated that the remote wind has dominant effect over the local wind on the subtidal sea level change.

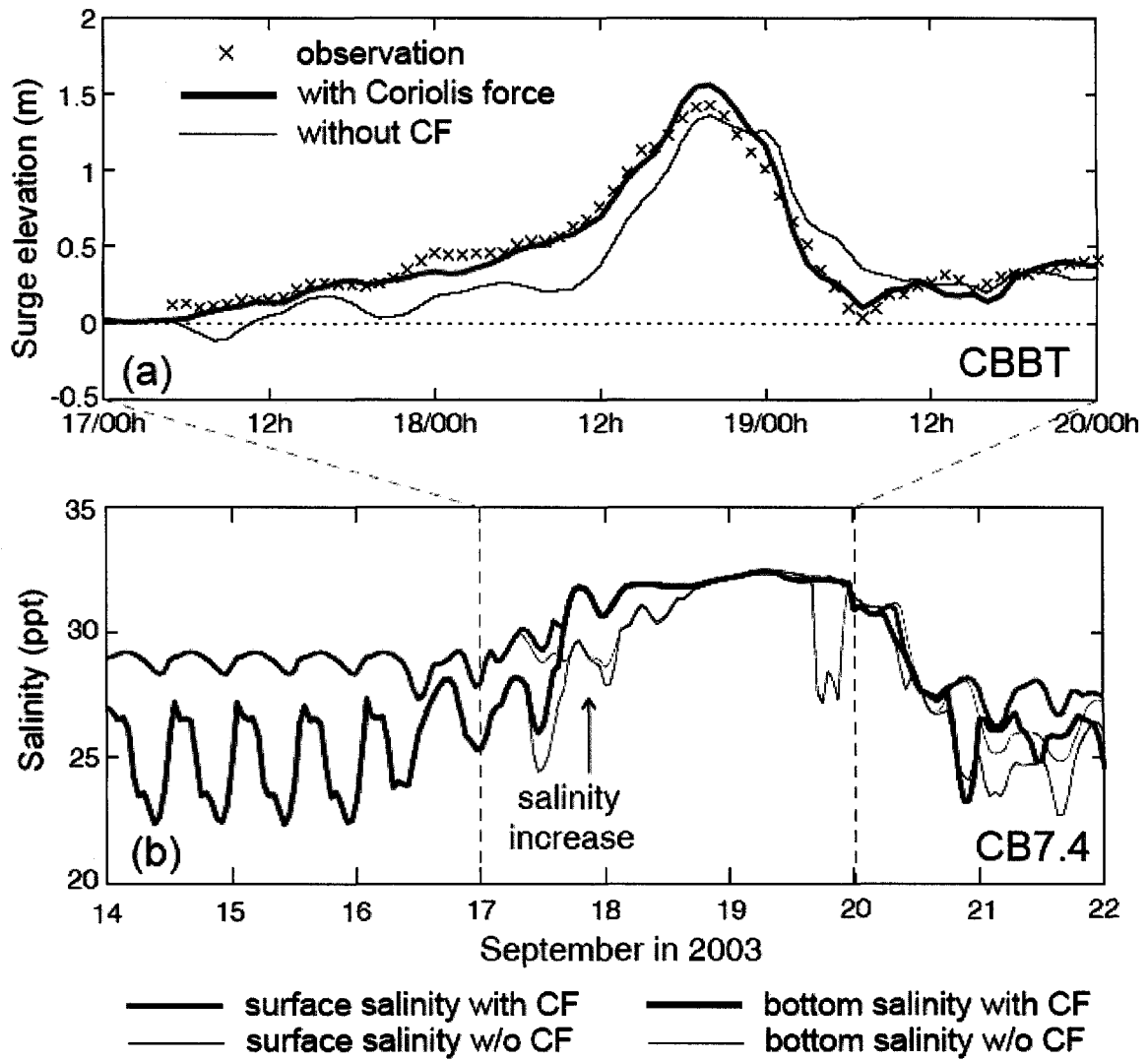


Fig. 7-8 Time series of simulated storm surge elevation (a) and salinity (b) at the entrance of the Chesapeake Bay during Hurricane Isabel with/without Coriolis force.

The above results are significant and have the following implications:

- (1) When properly calibrated, the SELFE model does have the proper modeling capability in modeling Ekman dynamics and simulating effects of the Coriolis force in the coupled estuarine and coastal ocean system.
- (2) Based on the model results, it clearly demonstrated that the continental shelf dynamics do affect the estuarine system and thus the approach to couple the Bay and continental shelf was a proper strategy and can shed light on future research.

### 7.3.2 Effect of alongshore pressure gradient on the geostrophic balance

It has been proven that wind-induced variations dominate the sub-tidal frequency fluctuations of coastal sea level along the East Coast of the United States (Wang, 1979a; Chao and Pietrafesa, 1980). During Hurricanes Floyd and Isabel, sea surface elevations were measured at Duck, NC near the southern boundary and at Ocean City Inlet, MD near the northern boundary, as shown in Figure 3-2. It clearly showed that a subtidal alongshore pressure gradient existed during hurricane events. The origin of it, as indicated above, is due to the non-uniform wind field (both in terms of its direction and magnitude) and the interference of the coastline. In the northern hemisphere, hurricanes circulate cyclonically. As a hurricane approaches the East Coast, the northern half of the hurricane using hurricane track as a dividing line generates onshore wind, and thus set-up; conversely, the southern half of the hurricane generates offshore wind, and thus set-down. In combination, the hurricane wind direction alone can set-up an alongshore pressure gradient from the north to the south. This make the continental shelf dynamics very different from the classic Ekman theory, in which wind is assumed to be uniform

and the ocean is unbounded.

According to geostrophic approximation (Pedlosky, 1987), the equations of the quasi-geostrophic motion are developed in an asymptotic series in the small parameter:

$$R_o = \frac{U}{Lf} \quad (7.4)$$

where  $R_o$  is the Rossby number and  $U$ ,  $f$ , and  $L$  are characteristic values for the horizontal velocity, the Coriolis parameter, and the horizontal length scale of the motion, respectively. If  $D$  is the vertical scale of the motion, the smallness of the Rossby number ( $R_o \ll 1$ ) and the smallness of the aspect ratio of the motion,  $\delta$ , given by

$$\delta = \frac{D}{L} \ll 1 \quad (7.5)$$

develop the quasi-geostrophic motions (Pedlosky, 1996). For the quasi-geostrophic current that have been estimated on the continental shelf of the mid-Atlantic Ocean,  $U = O(0.1 \text{ m s}^{-1})$ ,  $L = O(200 \text{ km})$ , and  $D = O(100 \text{ m})$  so that, for these scales,  $R_o = O(5 \times 10^{-3})$  and  $\delta = O(5 \times 10^{-4})$ . Assuming quasi-geostrophic motions with small scales of  $R_o$  and  $\delta$ , the northward pressure gradient force develops the seaward geostrophic current whereas the southward pressure gradient force generates the landward geostrophic current. During Hurricane Isabel, a large northward pressure gradient occurred briefly and then a large southward pressure gradient occurred for one day ( $> 2\pi/f \sim 17.4 \text{ h}$ ) from September 18, 18:30 (UTC). Those large pressure gradients are expected to have an influence on subtidal sea surface elevation during the hurricane event. An additional experiment was performed without subtidal sea surface elevation specification on open boundaries. Figure 7-9 shows the surge elevation and salinity comparisons between the experiments with and without the subtidal sea surface elevation

effect. The subtidal effect plays a significant role in increasing surge by 15 cm on average in the lower Bay. A southward alongshore pressure gradient balanced by Coriolis force generates onshore quasi-geostrophic currents that prohibit the surge elevation from rapidly dropping (Figure 7-9a). Due to subtidal sea surface elevation effect, the salinity slightly increased until it rapidly dropped (Figure 7-9b,c). Interestingly, after dropping, the bottom salinity decreased 1-2 ppt more than the case without the subtidal effect. It can be noted that the downwelling-favorable quasi-geostrophic current induced by southward alongshore pressure gradient tends to decrease the bottom salinity at the Bay mouth (Figure 7-10). For downwelling conditions, quasi-geostrophic current causes the sea surface to rise and the pycnocline to deepen, driving an outward transport in the lower layer of the estuary (Klinck et al., 1981b). Therefore, the results of the experiments indicate that a numerical model for hurricane events need to include the influence of alongshore pressure gradient from subtidal sea surface elevation, in order to preserve its accuracy.

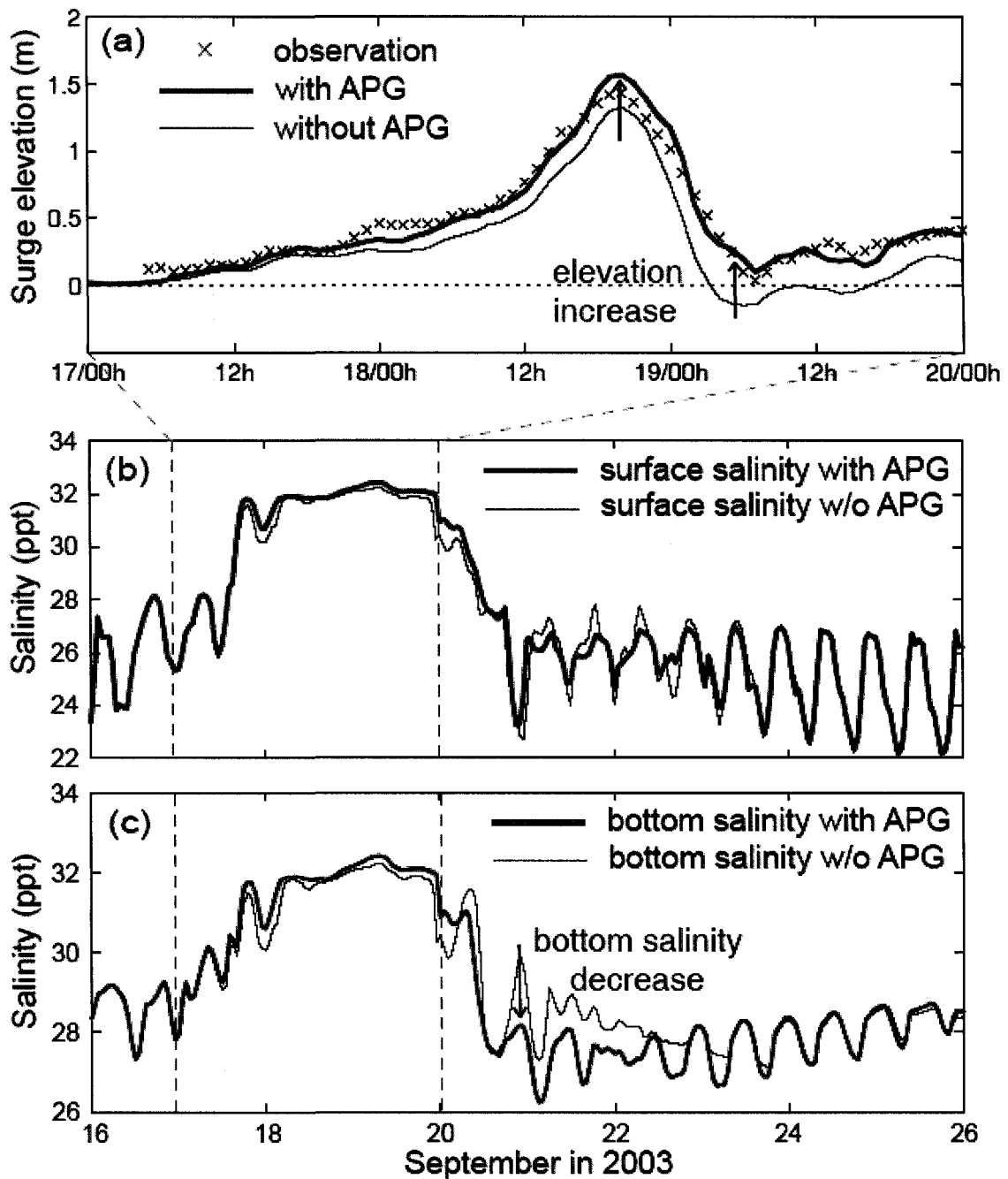


Fig. 7-9 The influence of subtidal alongshore pressure gradient (APG) during Hurricane Isabel on (a) surge elevation with observation (red cross) at CBBT, (b) surface salinity and (c) bottom salinity at CB7.4. Thin and thick lines denote the cases without and with APG, respectively.



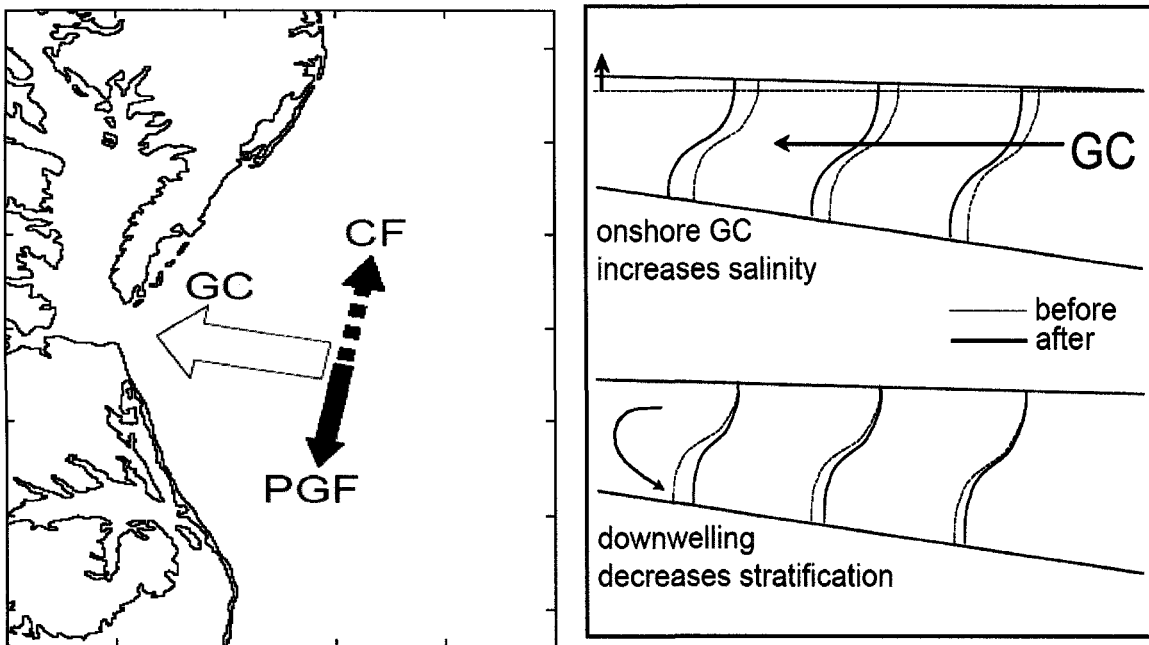


Fig. 7-10 Schematic maps of onshore current (GC) induced by geostrophic balance between barotropic pressure gradient force (PGF) and Coriolis force (CF) (left panel) and vertical salinity profile at cross-shore transect (right panel) on the continental shelf.

## 7.4 Summary

The SELFE model is a robust tool to examine the estuarine recovery, because it uses the high-order advection scheme for transport and the second-order scheme for turbulence closure and allows the estuarine system to reach quasi-steady state. The recovery time of sea surface elevation from hurricane forcing is shorter than that of salinity. Basically, at the sea surface, the density difference between air and water is the order of  $1000 \text{ kg m}^{-3}$ . The buoyancy frequency in the interface is sufficiently large and it rapidly adjusts the fluctuation at the sea surface. The adjustment time of sea surface disturbance from both hurricanes is nearly seven days in the Chesapeake Bay.

For the salinity, the recovery time mainly depends on the direction of local winds under certain amount of river discharge following the hurricane event. Strong down-Bay winds suppress the salinity structure to increase the horizontal density gradient as a restoring force. Those cause a strong oscillation of salinity and thus take longer time for salinity to reach a quasi-steady state than up-Bay winds do. The suppression of subsequent river discharge to the salinity structure plays a role not only in competing against the salinity rebound caused by wind forcing but also in pushing the salinity structure further downstream. As a result, it makes the salinity recovery time shorter in the Hurricane Floyd case and longer in the Hurricane Isabel case.

Lastly, the influence of continental shelf dynamics involving Ekman transport and quasi-geostrophic current induced by alongshore pressure gradient, plays a significant role in the inflow and outflow through the entrance of the Chesapeake Bay. By including the continental shelf grid and using a proper open boundary condition, the model was able to verify the influence of continental shelf dynamics successfully.

## Chapter VIII

### DISCUSSION AND CONCLUSIONS

#### Discussion

In Chapter V, as a barotropic response, it is verified that storm surges are primarily produced by remote winds at the entrance of the Chesapeake Bay and combined with set-up/set-down effects induced by local winds during hurricane events. Figure 8-1 shows spatial distributions of surge ranges for six experiments described in Chapter V, which are remote-wind case and local-wind case during each hurricane event. A surge range can be obtained by subtracting the minimum surge from the maximum surge during the event. The distributions for remote-wind cases show nearly same pattern as that of mean tidal range in the Chesapeake Bay. As the characteristics of long waves (or shallow water waves), a larger range is presented at the entrance of the Bay, decreases to minimum around 100 km (nodal point) from the mouth, and then increases in the upper Bay (Figure 8-1a and 8-1d). In contrast, the range for the Isabel local-wind case increases linearly with distance from the mouth (Figure 8-1e) even though it shows somewhat complicated pattern for the Floyd local-wind case. According to Garvine (1985), sea level variation is produced dominantly by the remote wind effect but the surface slope is dominantly produced by the local wind. He addressed that sea level variations within the estuary on the wavelength scale ( $2\pi c/\omega$ ) depend on the scale of the estuary. For the shorter estuary, the primary contributor to surface slope is local wind set-

up, and its contribution to sea level increases linearly with distance from the mouth to lowest order. However, the experiments represent that the maximum surge decreases linearly with distance from the mouth during Floyd but increases linearly during Isabel (not shown), which is consistent with the results obtained by Shen et al. (2006a). Shen et al. (2006a) assumed that the sea level variation is caused by combination of offshore storm tide propagating into the Bay and the set-up (or set-down) generated by local wind. They found that, to lowest order, the storm tide propagating from the offshore can reach the Bay head without attenuation and the local wind causes set-up/set-down with a constant slope in the Bay. It is suggested that the location of nodal point inside Bay would be mostly influenced by the competition between local wind and remote wind effects. Consistently, in this study, the nodal points for combined wind effects during Floyd and Isabel occurred at 250 km and 75 km from the Bay mouth, respectively (Figure 8-1c and 8-1f). The primary surge induced by remote winds acts as a free wave and set-up/set-down effect induced by local winds acts as a forced wave in the Chesapeake Bay. Therefore, it is suggested that the surge range induced by the combined winds decrease (increase) to the upper Bay when two waves are in phase (out of phase) during Isabel (Floyd).

In Chapter VI, as a baroclinic response, vertical profiles of along-channel velocity and salinity were presented for both Hurricanes Floyd and Isabel. Floyd remained down-Bay wind whereas Isabel remained up-Bay wind. Hansen and Rattray (1965) developed the first theory for the central regime of an estuary, which incorporated wind-driven circulation into the gravitational circulation. MacCready (2004) developed a unified theory of tidally-averaged, width-averaged estuarine salinity and circulation in a

rectangular estuary. Even though the solution for longitudinal velocity with wind forcing was not provided, it can be easily found. First  $u$  and salinity,  $s$ , are split into depth-averaged (overbar) and depth-varying (prime) parts:

$$u = \bar{u}(x) + u'(x, t), \quad s = \bar{s}(x) + s'(x, t) \quad (8-1)$$

With some assumptions, MacCready developed the partial equation for  $u$  as follows:

$$\frac{\partial^3 u}{(\partial z)^3} = -\frac{g\beta\bar{s}_x}{K_M} \quad (8-2)$$

where  $g$  is gravity,  $\beta \cong 7.7 \times 10^{-4} \text{ psu}^{-1}$ ,  $\bar{s}_x$  is horizontal gradient of depth-averaged salinity, and  $K_M$  is the effective vertical eddy viscosity (Dyer, 1997). Assuming that  $K_M$  and water depth ( $H$ ) are constants, and wind forcing ( $T$ ) as a boundary condition is constant, Eq. (8-2) can be integrated directly to find the classic cubic profile (see Appendix):

$$u' = \bar{u}P_1 + u_E P_2 + u_W P_3, \quad \text{where}$$

$$P_1 = \frac{1}{2} - \frac{3}{2}\zeta^2, \quad P_2 = 1 - 9\zeta^2 - 8\zeta^3, \quad P_3 = 1 + 4\zeta + 3\zeta^2,$$

$$\eta = \frac{z}{H}, \quad u_E = \frac{g\beta\bar{s}_x H^3}{48K_M}, \quad u_W = \frac{TH}{4} = \frac{\tau_w H}{4K_M} \quad (8-3)$$

The analytical solutions of tidally-averaged velocity with wind forcings were plotted in Figure 8-2a. Without wind stress (black line), tidally-averaged  $u$  has two layered circulation pattern which is seaward in the upper layer and landward in the lower layer. When  $T=0.1 \text{ s}^{-1}$  (blue), down-Bay wind enhanced two-layered circulation. In contrast, up-Bay wind ( $T=-0.1 \text{ s}^{-1}$ ) generated three-layered circulation which shows landward in the top layer. As shown in Figure 8-2b, however, numerical experiments demonstrated two differences from analytical solutions: 1) Bottom current was enhanced but surface

current was reduced during Floyd (down-Bay wind). 2) Landward current on the entire water column occurred during Isabel (up-Bay wind). There could be two main reasons for these differences. Firstly, analytical solutions were obtained regardless of wind-induced set-up/set-down ( $\partial\eta/\partial x$ ). During Floyd, down-Bay winds produced surge set-up in the lower Bay and surge set-down in the upper Bay, which generate landward barotropic pressure gradient. It tends to enhance landward bottom current but reduce seaward surface current. Secondly, analytical solutions were obtained by assuming that the eddy viscosity is constant with depth. This means that vertical mixing induced by wind stress is limited by constant vertical eddy viscosity and wind stress tends to enhance vertical shear. Therefore, constant eddy viscosity could produce three-layered circulation pattern instead of uni-direction flow.

In the mid-Atlantic region of the continental shelf, it has been observed that there exists a low-frequency along-shelf component of 5-20 cm/sec (Bumpus, 1973; Boicourt, 1973; Butman, 1979; Beardsley et al., 1981). Based on the geostrophic balance between the cross-shore pressure gradient and Coriolis force, Yankovsky and Chapman (1997) suggested that typical ambient flows of 5 to 10 cm s<sup>-1</sup> are fairly reasonable values for the mid-Atlantic Bight shelf. Among various functions, this low frequency ambient flow plays a critical role in shaping the plume that comes out of the Chesapeake Bay to reach steady-state. According to Fong and Geyer (2002), the plume is an unsteady phenomenon; it will keep expanding or shrinking if without an ambient flow. A set of plume experiments performed over an idealized rectangular domain verified that an ambient flow of 10 cm s<sup>-1</sup> is the best value for the system to reach steady-state. Additional model experiments were performed to examine the influence of an ambient

flow on the salinity field in the Chesapeake Bay domain in 2003 and during hurricane events. As shown in Figure 8-1, using an ambient flow of  $10 \text{ cm s}^{-1}$  improved the accuracy of the salinity field at Duck, NC. Without an ambient flow, the freshwater from the Bay does not sufficiently flow out of the domain, so that the stratification on the continental shelf becomes increased until the system reaches steady state. On the other hand, an ambient flow effectively washes out the freshwater to the southern boundary, so that the stratification remains fairly intact. An ambient flow of  $10 \text{ cm s}^{-1}$  shows the best match between modeled and observed salinities, and therefore this value was applied to the simulations for Hurricanes Floyd and Isabel as base runs. The model results indicate that the effect of altering ambient flow does not appear during wind events when surges come into the Bay because the effect of ambient flow is relatively weak compared to the wind effect. However, after hurricane events, the ambient flows will have influence on the adjustment of surface and bottom salinities. Generally, as a weak ambient flow allows the plume width to extend offshore, the volume and salt transports at transect of the Bay mouth salt intrusion to the Bay tends to decrease (Valle-Levinson et al., 1996).

One interesting feature that emerged from the SELFE model results after hurricane forcing was the appearance of seiche motion in the coupled Bay and adjacent continental shelf model simulation. Seiche motion is one of the responses of an estuary to wind forcing. Elliott (1976) indicated that the local surface slopes induced by a winter storm provided evidence for the presence in the Patuxent River of a surface oscillation with a period of approximately 88 hours that may have arisen in response to internal seiching of the halocline. Chuang and Boicourt (1989) reported that seiche motions in the Chesapeake Bay are generally driven by the longitudinal (N-S) wind at 2- to 3-day

time scales and are characterized by a node at the mouth and an antinode at the head of the Bay. What we have found was that a 4-to-5-day oscillation of the elevation field manifested in an x-t plot, as shown in Figure 8-2, where the horizontal axis is the distance  $x$  in km from the head of the Bay to the continental shelf edge and the vertical axis is time,  $t$ , in units of days. The wind forcing was confined within a 4-day period between day 6 and Day 10 shown by the dashed red line. The oscillations began at day 9 when it was first generated, and then repeated itself twice, once at the day 14 and the other at Days 19-20. For the oscillations at day 9 and Day 14, the oscillation occupied entire Bay and continental shelf domain whereas, for the oscillation at days 19-20, it was confined to the lower Bay and the continental shelf. The 4-to-5-day oscillation was indeed one of Wang's (1979a) signature, subtidal sea level variations observed in the Chesapeake Bay in response to atmospheric forcing. The answer to the crucial question as to whether the phenomenon observed by Wang (1979a) was actually simulated by the model will have to wait until further research.

The SELFE model used for this dissertation represents the state-of-the-art unstructured grid model development. The present SELFE version was run on a single processor which takes 16 hours computational time for a 10-day simulation. Recently, the parallel versions of ELCIRC and SELFE models have been released and these allow us to simulate the models with multi-processors. The test on the parallel code was performed and the run time on an 8-processor cluster now becomes 2 hours for a 10-day simulation, a speed up by a factor of 8. With the parallel version capability, further improvement can be made in refining the model grid to reduce numerical dispersion errors generated from a coarse grid. The high resolution results will help to better understand the small scale



physical phenomena, not only on turbulent eddies but also on lateral circulation driven by wind forcing in the tributaries of the Chesapeake Bay.

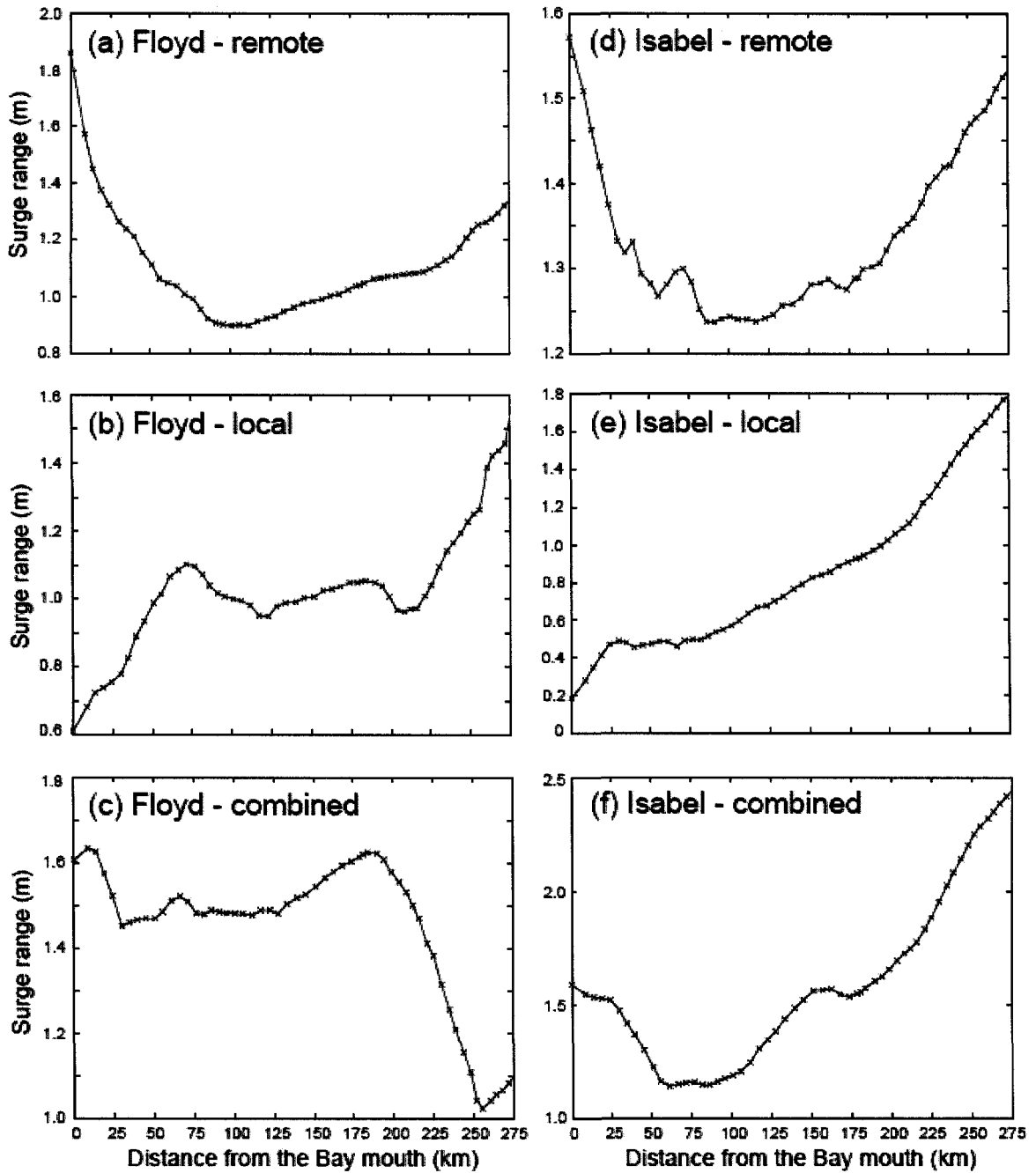


Fig. 8-1 Spatial distributions of surge ranges for six experiments during hurricane events, Floyd (a, b, and c) and Isabel (d, e, and f).

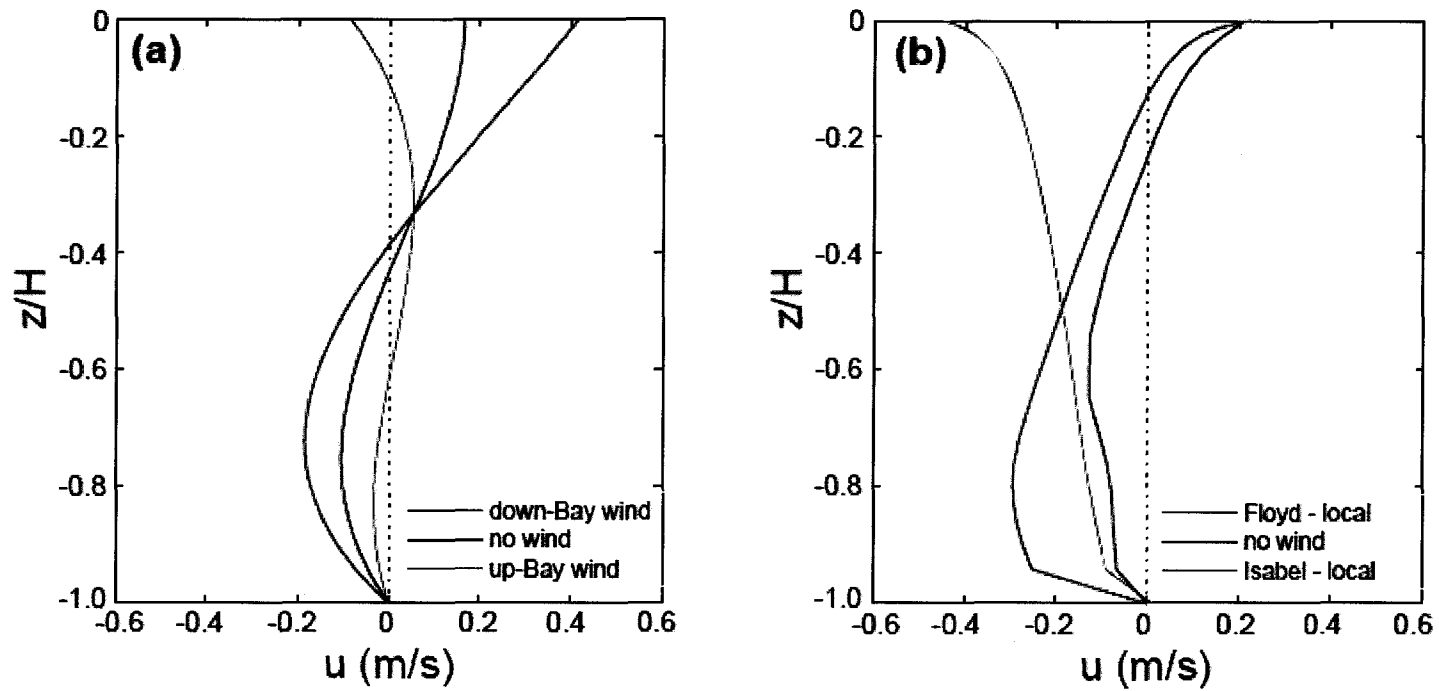


Fig. 8-2 Vertical profiles of alongshore velocity for wind forcings: (a) analytical solutions for central regime (Hansen and Rattray, 1965) and (b) numerical simulations in the mid-Bay. Positive is seaward.

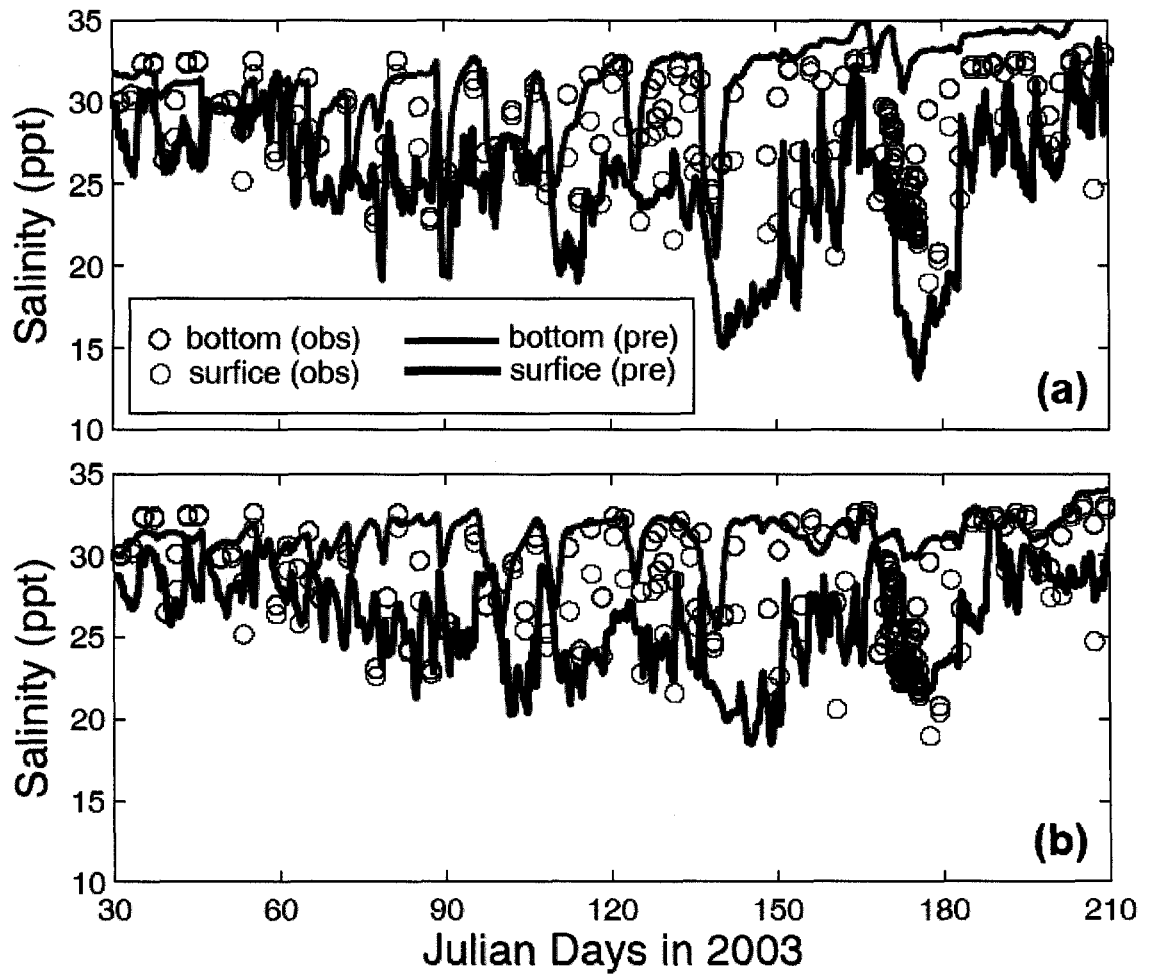


Fig. 8-3 Instantaneous salinity comparisons between observations, bottom (black circles) and surface (green circles), and predictions, bottom (red lines) and surface (blue lines), at Duck, NC, for two cases: (a) without an ambient flow and (b) with an ambient flow of 10 cm s<sup>-1</sup>.

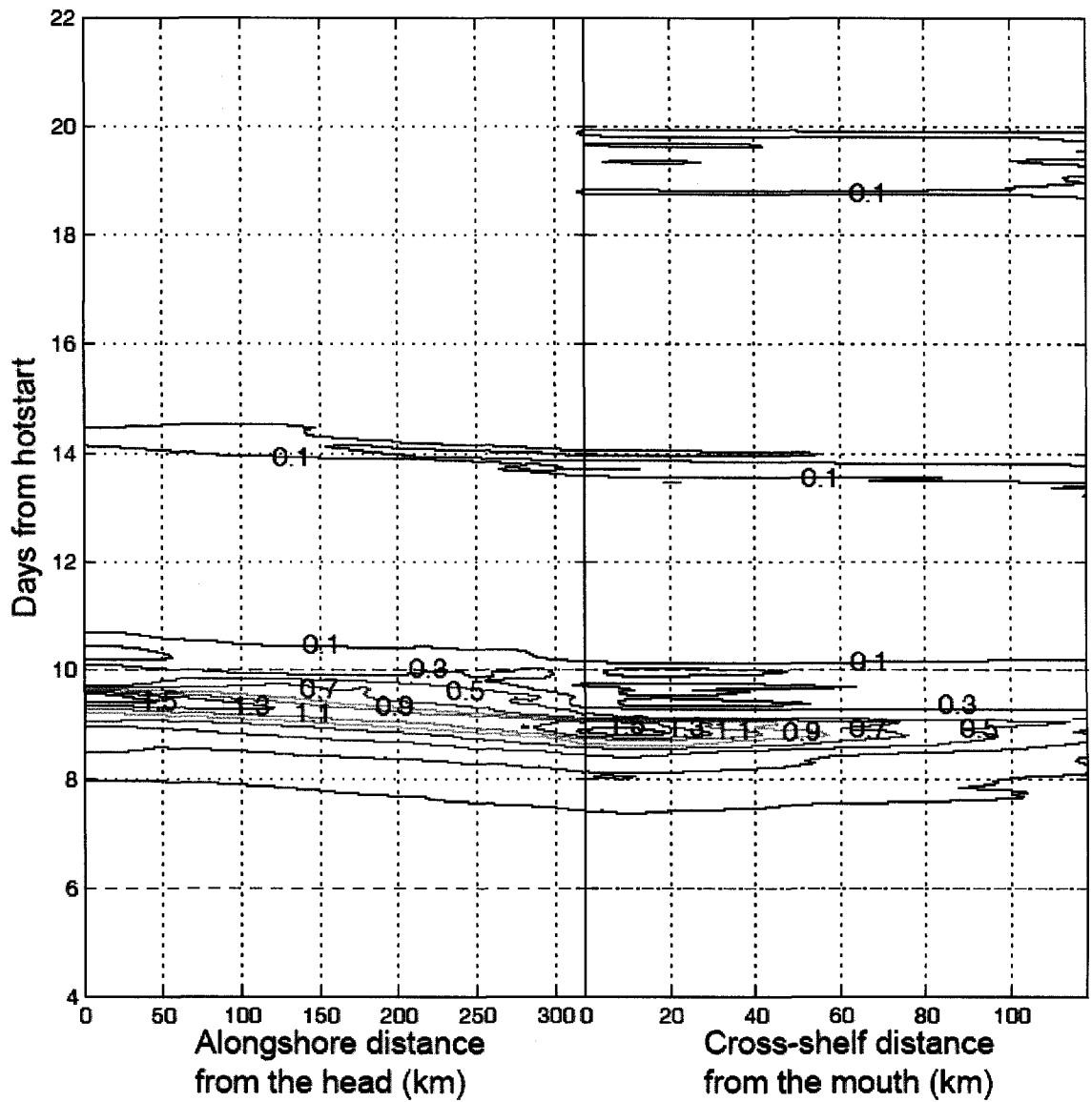


Fig. 8-4 Subtidal sea surface distribution in time-distance frame: along-channel in the Chesapeake Bay (left panel) and cross-shore on the continental shelf (right panel). The interval of contour lines is 0.2 m. Red dashed lines denote the period of Hurricane Isabel.

## Conclusions

The research presented in this dissertation represents progress made towards a better understanding of the responses of the Chesapeake Bay to two different types of hurricanes, Hurricane Floyd (an eastern-type storm) and Hurricane Isabel (a western-type storm) using the unstructured grid three-dimensional model.

### **Barotropic responses of the Chesapeake Bay to two hurricanes**

Independent of two types of hurricanes, both hurricanes had three stages in terms of storm surge at the mouth of the Bay: growing (pre-storm) stage, transition (ongoing-storm) stage, and decaying (post-storm) stage. The storm surge evolution is represented by two main behaviors: 1) Non-local (remote) winds generate the first set of storm surge at the entrance of the Bay due to the seaward and the surge wave propagates to the upper Bay with same magnitude of surge height. 2) Local winds play a role in creating the second thrust of the surge wave, which influences on the first surge wave. The effect of local winds depends on two types of hurricanes: down-Bay (northerly) winds during Hurricane Floyd decrease the surge height (wind-induced set-down) in the upper Bay, whereas up-Bay (southerly) winds during Hurricane Isabel increase the surge height (wind-induced set-up) in the upper Bay.

The inverted barometric pressure increased the sea surface elevation by 20-25 cm during both hurricanes corresponding to a 20-25 mb atmospheric pressure drop. This influence on the sea surface elevation rising is nearly 20 % of total meteorological forcing. That is, 80 % comes from direct wind forcing.

Temporal and spatial variations of net volume flux across each transect reveal that

its convergence/divergence is the key to dominate the exchange of barotropic volume transport not only between the shelf and the Bay, but also between the Bay and its tributaries. The huge amount of river flow following a hurricane event generates the second rise of sea surface elevation in the upstream of the Bay's tributaries, which gives rise to the inundation damage.

### **Baroclinic responses of the Chesapeake Bay to two hurricanes**

The Chesapeake Bay has both similar and different baroclinic responses to two types of hurricanes. Oceanic volume and salt influxes obviously occurs from the continental shelf to the Bay through its entrance during both Hurricanes Floyd and Isabel. At the onset and end of the hurricane events, barotropic adjustment drives strong transient salt fluxes. The influxes signal propagates upstream in the forms of storm surge and salt intrusion. Strong down-Bay (northerly) winds corresponding to the passage of eastern-type hurricanes restricts landward net salt flux to the upper Bay, whereas up-Bay (southerly) winds corresponding to the passage of western-type hurricanes strengthens landward net salt flux to the upper Bay.

During a hurricane event, surface wind stress is the primary agent to destratify water column by transferring generated turbulent kinetic energy to the lower layer (local wind effect). Advection of well-mixed salty water influx from the ocean is the second agent to change the stratification inside Bay (remote wind effect). Down-Bay winds of eastern-type storms tend to enhance the stratification whereas up-Bay winds of western-type storms tend to reduce the stratification. A modified horizontal Richardson number incorporated with the Wedderburn number ( $W$ ) represents reasonably wind-induced

straining/mixing during hurricane events.

In addition, precipitation as a point source of water mass on the surface in the Chesapeake Bay not only dilutes surface water but also generates a seaward barotropic horizontal pressure gradient, which competes barotropic adjustment at the end of the wind events. It plays a significant role in dropping the salinity and retarding the salinity rebound after salinity has rapidly dropped.

### **Estuarine recovery and influence of continental shelf dynamics**

The adjustment time of sea surface disturbance from both hurricanes is nearly seven days in the Chesapeake Bay. For the salinity, the recovery time mainly depends on the direction of local winds under a certain amount of river discharge following the hurricane event. Strong down-Bay winds suppress the salinity structure to increase the horizontal density gradient as a restoring force, and quick barotropic adjustment induced by the landward horizontal pressure gradient drives salt flux when winds stop. These barotropic and baroclinic pressure gradients have the same upstream direction and generate salinity overshooting. These gradients cause an oscillation of salinity in the upper Bay and thus a longer time is required for salinity to reach an equilibrium state than is the case with up-Bay winds. Salinity in the upper Bay attained a relatively high value due to overshooting after Hurricane Floyd, whereas salinity in the upper Bay quickly dropped after Hurricane Isabel. When subsequent river discharge begins, it suppresses salinity structure downstream and retards salinity recovery time.

The influence of continental shelf dynamics plays a significant role in exchanging transport at the entrance of the Chesapeake Bay. Onshore Ekman transport raised the sea

surface elevation and increased the salinity at the Bay entrance during Hurricane Isabel. The wind change to southerly winds leads offshore Ekman transport to decrease the sea surface elevation and surface salinity. This leads to an upwelling condition to increase the bottom and surface salinities a couple of days later. Onshore quasi-geostrophic current plays a role in increasing sea surface elevation. This leads to a downwelling condition that enhances seaward flow in the bottom layer and decreases the bottom salinity.



## APPENDIX

As reviewed in MacCready (2004), assuming that the estuary is rectangular in cross-section estuary, the tidally-averaged along-channel momentum balance is dominated by the along-channel pressure gradient and vertical Reynolds stress divergence:

$$0 = -\frac{1}{\rho_0} \frac{\partial p}{\partial x} + \frac{\partial}{\partial z} \left( K_M \frac{\partial u}{\partial z} \right) \quad (\text{A-1})$$

The pressure gradient term on the right hand side of Eq. (A-1) is separated into barotropic and baroclinic parts:

$$-\frac{1}{\rho_0} \frac{\partial p}{\partial x} = -g \frac{\partial \eta}{\partial x} + g \int \frac{1}{\rho_0} \frac{\partial \rho}{\partial x} dz \quad (\text{A-2})$$

Since the equation of state is approximated as  $\rho = \rho_0(1 + \beta s)$ , the pressure term can be expressed by salinity instead of density:

$$\begin{aligned} -\frac{1}{\rho_0} \frac{\partial p}{\partial x} &= -g \frac{\partial \eta}{\partial x} + g \int \frac{\partial(1 + \beta s)}{\partial x} dz \\ &= -g \frac{\partial \eta}{\partial x} + g\beta \int \frac{\partial(\bar{s} + s')}{\partial x} dz \quad \because \frac{\partial \bar{s}}{\partial x} \gg \frac{\partial s'}{\partial x} \\ &= -g \frac{\partial \eta}{\partial x} + g\beta \int \frac{\partial \bar{s}}{\partial x} dz \end{aligned} \quad (\text{A-3})$$

Substituting Eq. (A-3) into Eq. (A-1) and taking  $\frac{\partial}{\partial z}$ , we find

$$\begin{aligned} 0 &= -g\eta_x + g\beta \overline{s_x z} + (K_M u_z)_z & 0 &= +g\beta \overline{s_x} + (K_M u_z)_{zz} \\ \therefore u_{zzz} &= -\frac{g\beta \overline{s_x}}{K_M} = -B \end{aligned} \quad (\text{A-4})$$

Three boundary conditions are provided as follows:

$$\frac{\partial u}{\partial z} = T = \frac{\tau_w}{K_M} \quad \text{at } z=0 \quad (\text{A-5a})$$

$$u = 0 \quad \text{at } z = -H \quad (\text{A-5b})$$

$$\frac{1}{H} \int_{-H}^0 u \, dz \equiv \bar{u} \quad (\text{A-5c})$$

Integrating Eq. (A-4) twice in  $z$  yields

$$\frac{\partial^2 u}{\partial z^2} = -Bz + C_1,$$

$$\frac{\partial u}{\partial z} = -\frac{1}{2}Bz^2 + C_1z + C_2 \quad (\text{A-6})$$

Then Eq. (A-5a) is applied to Eq. (A-6), thus

$$\left. \frac{\partial u}{\partial z} \right|_{z=0} = -\frac{1}{2}B(0)^2 + C_1(0) + C_2 = T, \quad \therefore C_2 = T$$

Next, integrating Eq. (A-6) in  $z$  yields,

$$u = -\frac{B}{6}z^3 + \frac{C_1}{2}z^2 + Tz + C_3 \quad (\text{A-7})$$

Applying Eq. (A-5b) to Eq. (A-7)

$$u|_{z=-H} = +\frac{B}{6}H^3 + \frac{C_1}{2}H^2 - TH + C_3$$

$$0 = +\frac{B}{6}H^3 + \frac{C_1}{2}H^2 - TH + C_3 \quad (\text{A-8})$$

By integrating Eq. (A-7) in  $z$ , depth-averaged part can be found:

$$\int u \, dz = -\frac{B}{24}z^4 + \frac{C_1}{6}z^3 + \frac{T}{2}z^2 + C_3z + C_4$$

$$\frac{1}{H} \int_{-H}^0 u \, dz = \frac{1}{H} \left[ -\frac{B}{24}0^4 + \frac{C_1}{6}0^3 + \frac{T}{2}0^2 + C_3(0) + C_4 \right] - \frac{1}{H} \left[ -\frac{B}{24}H^4 - \frac{C_1}{6}H^3 + \frac{T}{2}H^2 - C_3H + C_4 \right]$$

$$\bar{u} = \frac{B}{24}H^3 + \frac{C_1}{6}H^2 - \frac{T}{2}H + C_3 \quad (\text{A-9})$$

Subtracting Eq. (A-9) from Eq. (A-8),  $C_1$  can be found:

$$-\bar{u} = \frac{B}{8}H^3 + \frac{C_1}{3}H^2 - \frac{T}{2}H$$

$$\therefore C_1 = -\frac{3B}{8}H + \frac{3T}{2}\frac{1}{H} - \frac{3}{H^2}\bar{u} \quad (\text{A-10})$$

By inserting Eq. (A-10) to Eq. (A-8),  $C_3$  can be determined:

$$0 = \frac{B}{6}H^3 + \frac{1}{2}\left(-\frac{3B}{8}H + \frac{3T}{2}\frac{1}{H} - \frac{3}{H^2}\bar{u}\right)H^2 - TH + C_3$$

$$\therefore C_3 = \frac{3}{2}\bar{u} + \frac{B}{48}H^3 + \frac{T}{4}H \quad (\text{A-11})$$

Inserting Eq. (A-10) and Eq. (A-11) into Eq. (A-7), we find

$$u = -\frac{B}{6}z^3 - \left(\frac{3B}{16}H - \frac{3T}{4}\frac{1}{H} + \frac{3}{2H^2}\bar{u}\right)z^2 + Tz + \frac{3}{2}\bar{u} + \frac{B}{48}H^3 + \frac{T}{4}H$$

By definition of  $u = \bar{u} + u'$ , depth-varying velocity can be found:

$$u' = \bar{u}\left(\frac{1}{2} - \frac{3}{2}\frac{z^2}{H^2}\right) + \frac{B}{48}H^3\left(1 - 9\frac{z^2}{H^2} - 8\frac{z^3}{H^3}\right) + \frac{T}{4}H\left(1 + 4\frac{z}{H} + 3\frac{z^2}{H^2}\right) \quad (\text{A-12})$$

Putting  $\zeta \equiv \frac{z}{H}$ , Eq. (A-12) can be written as

$$u' = \bar{u}\left(\frac{1}{2} - \frac{3}{2}\zeta^2\right) + \frac{B}{48}H^3(1 - 9\zeta^2 - 8\zeta^3) + \frac{T}{4}H(1 + 4\zeta + 3\zeta^2)$$

$$u' = \bar{u}P_1 + u_E P_2 + u_W P_3, \quad \text{where}$$

$$P_1 = \frac{1}{2} - \frac{3}{2}\zeta^2, \quad P_2 = 1 - 9\zeta^2 - 8\zeta^3, \quad P_3 = 1 + 4\zeta + 3\zeta^2$$

$$u_E = \frac{g\beta \overline{s_x} H^3}{48K_M}, \quad u_W = \frac{TH}{4} = \frac{\tau_w H}{4K_M} \quad (\text{A-13})$$

## LITERATURE CITED

- Austin, J.A., 2002. Estimating the mean ocean-bay exchange rate of the Chesapeake Bay. *Journal of Geophysical Research*, 110, 3192.
- Baptista, A.M., 1987. Solution of advection-dominated transport by Eulerian-Lagrangian methods using the backwards methods of characteristics. PhD thesis, Massachusetts Institute of Technology, Cambridge, Massachusetts, USA, Civil Engineering. 260pp.
- Baptista, A.M., Y.-L.Zhang, A. Chawla, M.A. Zulauf, C. Seaton, E. P. Myers, J. Kindle, M. Wilkin, M. Burla, and P.J. Turner, 2005. A cross-scale model for 3D baroclinic circulation in estuary-plume-shelf systems: II. Application to the Columbia River. *Continental Shelf Research*, 25, 935-972.
- Beardsley, R. C. and W. C. Boicourt, 1981. On estuarine and continental-shelf circulation in the Middle Atlantic Bight. In Warren B.A. and C. Wunsch (eds.): *Evolution of Physical Oceanography*. The MIT Press, Cambridge, Massachusetts, 198 - 233.
- Bills, P.J., 1991. Barotropic depth-averaged and three-dimensional tidal programs for shallow seas. PhD thesis, The University of Adelaide. South Australia. Department of Applied Mathematics.
- Bishop, W.F., 1980. Petroleum geology of northern Central America. *Journal of Petroleum Geology*, 3, 3-59.
- Blayo, E. and L. Debreu, 2005. Revisiting open boundary conditions from the point of view of characteristic variables. *Ocean Modelling*, 9, 231-252.
- Blumberg, A.F. and D.M. Goodrich, 1990. Modeling of wind-induced destratification in

- Chesapeake Bay. *Estuaries*, 13(3), 231–249.
- Blumberg, A.F. and L.H. Kantha, 1985. Open boundary condition for circulation models. *Journal of Hydraulic Engineering*, 111, 255-273.
- Blumberg, A.F. and G.L. Mellor, 1987. A description of a three-dimensional coastal ocean circulation model. In: Heaps, N.S. (Ed.), *Three-Dimensional Coastal Ocean Models*. In: Coastal and Estuarine Science, vol. 4. American Geophysical Union, Washington, DC, pp. 1-16.
- Boicourt, W.C., 1973. The circulation of water on the continental shelf from Chesapeake Bay to Cape Hatteras. Ph.D. Dissertation. The Johns Hopkins University, Baltimore, MD, 183 p.
- Boicourt, W.C., 1992. Influences of circulation processes on dissolved oxygen in the Chesapeake Bay. In Smith D.E., M. Leffler, and G. Mackiernan (eds.): *Oxygen Dynamics in the Chesapeake Bay*. Maryland Sea Grant Publication, College Park, MD, USA, pp 7-59.
- Boicourt, W.C., 2005. Physical response of Chesapeake Bay to hurricanes moving to the wrong side: Refining the forecasts. In Sellner, K.G. (ed.): *Hurricane Isabel in Perspective*. Chesapeake Research Consortium, CRC Publication 05-160, Edgewater, MD, 39-48.
- Brasseur, L.H., A.C. Trembanis, J.M. Brubaker, C.T. Friedrichs, T. Nelson, L.D. Wright, and L.W. Haas, 2005. Physical response of the York River estuary to Hurricane Isabel. In: Sellner, K.G. (ed.), *Hurricane Isabel in Perspective*. Chesapeake Research Consortium, CRC Publication 05-160, Edgewater, MD, 57-63.
- Bretherton, F.P., R.E. Davis, and C.B. Fandry, 1976. A technique for objective analysis

- and design of oceanographic experiments applied to MODE-73. *Deep-Sea Research*, 23, 559-582.
- Bretschneider, C.L., 1959. Hurricane surge predictors for Chesapeake Bay. Technical Report, AD 699408. Corps of Engineers, Washington, DC, 51 p.
- Bretschneider, C.L., 1966. Storm surge. In: Fairbridge W. R. (ed.), *The encyclopedia of oceanography I*. Reinhold Publishing Corporation, New York, 856-860.
- Bumpus, D. F. 1973. A description of the circulation on the continental shelf of the east coast of the United States, *Progress Oceanography*, 6, 111-156.
- Butman, B, M. Noble, and D. Folger, 1979. Long-term observations of bottom current and bottom sediment movement on the Mid-Atlantic continental shelf. *Journal of Geophysical Research*, 84(C3), 1187-1225.
- Canuto, V.M., A. Howard, Y. Cheng, M.S. Dubovikov, 2001. Ocean turbulence I: one-point closure model. Momentum and heat vertical diffusivities. *Journal of Physical Oceanography*, 31, 1413-1426.
- Carter, G.S. and M.A. Merrifield, 2007. Open boundary conditions for regional tidal simulations. *Ocean Modelling*, 18, 194-209.
- Carter, H.H. and D.W. Pritchard, 1988. Oceanography of Chesapeake Bay. In: Kjerfve, B. (Ed.), *Hydrodynamics of Estuaries: Dynamics of Partially Mixed Estuaries*, vol. 1. CRC Press, Boca Raton, FL, 1-16.
- Casulli, V. and E. Cattani, 1994. Stability, accuracy and efficiency of a semi-implicit method for 3D shallow water flow. *Computers and Mathematics with Applications*, 27, 99-112.
- Casulli, V. and R. Cheng, 1992. Semi-implicit finite difference methods for three-

- dimensional shallow water flow. *International Journal for Numerical Methods in Fluids*, 15, 629-648.
- Casulli, V. and R.V. Walters, 2000. An unstructured grid, three-dimensional model based on the shallow water equations. *International Journal for Numerical Methods in Fluids*, 32, 331-348.
- Casulli, V. and P. Zanolli, 1998. A three-dimensional semi-implicit algorithm for environmental flows on unstructured grids. Institute for Computational Fluid Dynamics Conference on *Numerical Methods for Fluid Dynamics*, VI.
- Cerco, C.F. and T.M. Cole, 1994. Three-dimensional eutrophication model of Chesapeake Bay. Technical Report EL-94-4. U.S. Army Corps of Engineers. Vicksburg, Mississippi.
- Chant R.J., W.R. Geyer, R. Houghton, E. Hunter, and J.A. Lerczak, 2007. Estuarine boundary layer mixing processes: Insights from dye experiments. *Journal of Physical Oceanography*, 37, 1859-1877.
- Chao, S.-Y. and L.J. Pietrafesa, 1980. The subtidal response of sea level to atmospheric forcing in the Carolina Capes. *Journal of Physical Oceanography*, 10, 1246-1255.
- Chatwin, P.C., 1976. Some remarks on the maintenance of the salinity distribution in estuaries. *Estuarine and Coastal Marine Science*, 4, 555-566.
- Chen, S.N. and L.P. Sanford, 2009. Axial wind effects on salinity structure and longitudinal salt transport in idealized, partially-mixed estuaries. *Journal of Physical Oceanography*, accepted.
- Chesapeake Bay Program (CBP), 1993. Guide to using Chesapeake Bay Program water quality monitoring data. CBP/TRS 78/92, Chesapeake Bay Program, Annapolis,

- Maryland, 127 pp.
- Chuang, W. and W.C. Boicourt, 1989. Resonant seiche motion in the Chesapeake Bay. *Journal of Geophysical Research*, 94, 2105-2110.
- Conner, W.H., 1993. Artificial regeneration of baldcypress in three South Carolina forested wetland areas after Hurricane Hugo. In Brissette J.C. (ed.): *Proceedings of the Seventh Biennial Southern Silvicultural Research Conference*. U.S. Department of Agriculture, Forest Service, Southern Forest Experiment Station: New Orleans, LA. Gen. Tech. Rep. SO-93, 185–188.
- Conner, W.H. and L.W. Inabinette, 2005. Identification of salt tolerant baldcypress (*Taxodium distichum* (L.) Rich) for planting in coastal areas. *New Forests*, 29, 305-312.
- Csanady, G.T., 1967. Large-scale motion in the great lakes. *Journal of Geophysical Research*, 72, 4151-4162.
- Csanady, G.T., 1968. Motions in a model Great Lake due to a suddenly imposed wind. *Journal of Geophysical Research*, 73, 6435-6448.
- Csanady, G.T., 1972. Response of Large Stratified Lakes to Wind. *Journal of Physical Oceanography*, 2, 3-13.
- Csanady, G.T., 1976. Mean circulation in shallow seas. *Journal of Geophysical Research*, 81, 5389-5399.
- Csanady, G.T., 1982. *Circulation in the Coastal Ocean*. D. Reidel Publishing Company, Dordrecht, Holland. 279 p.
- Csanady, G.T., 1984. Circulation induced by river inflow in well mixed water over a sloping continental shelf. *Journal of Physical Oceanography*, 14, 1703-1711.



- Cushman-Roisin, B., 1994. *Introduction to Geophysical Fluid Dynamics*. Prentice-Hall, Inc., New Jersey, 320 p.
- Dyer, K.E., 1997. *Estuaries: A Physical Introduction, 2nd edition*. John Wiley and Sons Ltd, New York, 195 p.
- Ekman, V.W., 1905. On the influence of the Earth's rotation on ocean-currents. *Arkiv for Matematik, Astronomi och Fysik*, 2, 1-52.
- Elliott, A.J., 1976. Response of the Patuxent estuary to a winter storm. *Chesapeake Science*, 17, 212-216.
- Elliott, A.J., 1978. Observations of the meteorologically induced circulation in the Potomac Estuary. *Estuarine and Coastal Marine Science*, 6, 285-299.
- Elliott, A.J., D.-P. Wang, and D.W. Pritchard, 1978. The circulation near the head of Chesapeake Bay. *Journal of Marine Research*, 36, 643-655.
- Fischer, H.B., 1972. Mass transport mechanisms in partially stratified estuaries. *Journal of Fluid Mechanics*, 53, 671-687.
- Flather, R.A., 1976. A tidal model of the north-west European continental shelf. *Memories de la Societe Royale des Sciences de Liege*, 6, 141-164.
- Flather, R.A., 1994. A storm surge prediction model for the Northern Bay of Bengal with application to the Cyclone Disaster in April 1991. *Journal of Physical Oceanography*, 24, 172-190.
- Fong, D.A. and W.R. Geyer, 2002. The alongshore transport of freshwater in a surface-trapped river plume. *Journal of Physical Oceanography*, 32, 957-972.
- Forristall, G.Z., 1974. Three-dimensional structure of storm-generated currents. *Journal of Geophysical Research*, 79, 2721-2729.

- Franke, R. and G. Nielsen, 1980. Smooth interpolation for large sets of scattered data. *International Journal for Numerical Methods in Engineering*, 15, 1691-1704.
- Frazer, T.K., S.K. Notestein, C.A. Jacoby, C.J. Littles, S.R. Keller, and R.A. Swett, 2006. Effects of storm-induced salinity changes on submersed aquatic vegetation in Kings Bay, Florida. *Estuaries and Coasts*, 29, 943-953.
- Galperin, B., L.H. Kantha, S. Hassid, and A. Rosati, 1988. A quasi-equilibrium turbulent energy model for geophysical flows. *Journal of Atmospheric Science*, 45, 55-62.
- Garvine R., 1985. A simple model of estuarine subtidal fluctuations forced by local and remote wind stress. *Journal of Geophysical Research*, 90(C6), 11945-11948.
- Geisler, J.E., 1970. Linear theory of the response of a two layer ocean to moving hurricane. *Geophysical Fluid Dynamics*, 1, 249-272.
- Geyer, W.R., 1997. Influence of wind on dynamics and flushing of shallow estuaries. *Estuarine, Coastal and Shelf Science*, 44, 713-722.
- Geyer, W.R. and D.M. Farmer, 1989. Tide-induced variation of the dynamics of a salt wedge estuary. *Journal of Physical Oceanography*, 19, 1060-1072.
- Geyer, W.R., J.H. Trowbridge, and M.M. Bowen, 2000. The dynamics of a partially mixed estuary. *Journal of Physical Oceanography*, 30, 2035-2048.
- Ginis, I. and G. Sutyrin, 1995. Hurricane-generated depth-averaged currents and sea surface elevation. *Journal of Physical Oceanography*, 25, 1218-1242.
- Gong, W., J. Shen, and W.G. Reay, 2007. The hydrodynamic response of the York River estuary to Tropical Cyclone Isabel, 2003. *Estuarine, Coastal and Shelf Science*, 73, 695-710.
- Gong, W., J. Shen, K. Cho, and H. Wang, 2009. A numerical model study of the

- barotropic subtidal water exchange between estuary and subestuaries in the Chesapeake Bay during northeaster events. *Ocean Modelling*, 26, 170-189.
- Goodrich, D.M., 1988. On meteorologically induced flushing in three US east coast estuaries. *Estuarine, Coastal and Shelf Science*, 26, 111–121.
- Goodrich, D.M., W.C. Boicourt, P. Hamilton, and D.W. Pritchard, 1987. Wind-induced destratification in Chesapeake Bay. *Journal of Physical Oceanography*, 17, 2232-2240.
- Grano, V., 1982. On the non-tidal circulation of the Upper Chesapeake Bay. Ph.D. Dissertation, Johns Hopkins University, Baltimore, MD.
- Gresham, C.A., 1993. Changes in baldcypress-swamp tupelo wetland soil chemistry caused by Hurricane Hugo induced saltwater inundation. In Brissette J.C. (ed.): *Proceedings of the Seventh Biennial Southern Silvicultural Research Conference*. U.S. Department of Agriculture, Forest Service, Southern Research Station, New Orleans, LA. Gen. Tech. Rep. SO-93, 171–175.
- Grzechnik, M.P., 2000. Three-dimensional tide and surge modeling and layered particle tracking techniques applied to Southern Australian coastal seas. PhD thesis, The University of Adelaide. South Australia.
- Hamilton, P. and W.C. Boicourt, 1983. Long-term salinity, temperature and current measurements in Upper Chesapeake Bay. Technical report No. 81-04, Power Plant Siting Program, MD, 98 p.
- Hansen, D.V. and M. Rattray, 1965. Gravitational circulation in straits and estuaries. *Journal of Marine Research*, 23, 104-122.
- Harris, D.L., 1956. Some problems involved in the study of storm surges. National

- Hurricane Research Project Report, No. 4, U.S. Weather Bureau, Washington, DC, 16 p.
- Harris, D. L., 1963. Characteristics of the hurricane storm surge, Weather Bureau, Technical Paper No. 48, U.S. Dept. of Commerce.
- Hearn, C.J. and P.E. Holloway, 1990. A three-dimensional barotropic model of the response of the Australian North West Shelf to tropical cyclones. *Journal of Physical Oceanography*, 20, 60-80.
- Hicks, S.D., 1964. Tidal wave characteristics of Chesapeake Bay. *Chesapeake Science*, 5, 103-113.
- Holland, G.J., 1980. An analytic model of the wind and pressure profiles in hurricanes. *Monthly Weather Review*, 108, 1212-1218.
- Hovis, J. W. Popovich, C. Zervas, J. Hubbard, H.H. Shih, and P. Stone, 2004. Effects of Hurricane Isabel on water levels. NOAA Technical Report NOS CO-OPS 040, 120 p.
- Janowitz, G.S. and L.J. Pietrafesa, 1996. Subtidal frequency fluctuations in coastal sea level in the Mid and South Atlantic Bights: A prognostic for coastal flooding. *Journal of Coastal Research*, 12, 79-89.
- Jay, D.A., 1991. Estuarine salt conservation: A Lagrangian approach. *Estuarine, Coastal and Shelf Science*, 32, 547-565.
- Jay, D.A. and J.D. Smith, 1990. Residual circulation in shallow estuaries. 1. Highly stratified, narrow estuaries. *Journal of Geophysical Research*, 95, 711-731.
- Jelesnianski, C.P., 1965. A numerical calculation of storm tides induced by a tropical storm on a continental shelf. *Monthly Weather Review*, 93, 343-358.

- Jelesnianski, C.P., J. Chen, and W.A. Shaffer, 1992. SLOSH: Sea, Lake, and Overland Surges from Hurricane. National Weather Service, Silver Springs, MD.
- Johnson, B.H., K.W. Kim, R.E. Heath, B.B. Hsieh, and H.L. Butler, 1993. Validation of Three-Dimensional Hydrodynamic Model of Chesapeake Bay. *Journal of Hydraulic Engineering*, 119, 2-20.
- Kantha, L.H. and C.A. Clayson, 1994. An improved mixed layer model for geophysical applications. *Journal of Geophysical Research*, 99(25), 235-266.
- Klinck, J.M., L.J. Pietrafesa, and G.S. Janowitz, 1981a. Continental shelf circulation induced by a moving, localized wind stress. *Journal of Physical Oceanography*, 11, 836-848.
- Klinck, J.M., J.J. O'Brien, and H. Svendsen, 1981b. A simple model of Fjord and coastal circulation interaction. *Journal of Physical Oceanography*, 11, 1612-1626.
- Kourafalou, V.H., L.-Y. Oey, J.D. Wang, and T.N. Lee, 1996a. The fate of river discharge on the continental shelf: 1. Modeling the river plume and the inner shelf coastal current. *Journal of Geophysical Research*, 101, 3415-3434.
- Kourafalou, V.H., T.N. Lee, L.-Y. Oey, and J.D. Wang, 1996b. The fate of river discharge on the continental shelf: 2. Transport of coastal low-salinity waters under realistic wind and tidal forcing. *Journal of Geophysical Research*, 101, 3435-3455.
- Krome, E.C. and C.A. Corlett, 1990. Modeling of the Chesapeake Bay. CRC Publication No. 131.
- Kundu, P.K., 1990. *Fluid Mechanics*. Academic Press, Inc., San Diego, California, 683 p.
- Kuo, A.Y. and K. Park, 1992. Transport of hypoxic waters: an estuary-subestuary exchange. In D. Prandle (ed.): *Dynamics and Exchanges in Estuaries and the*

- Coastal Zone*. American Geophysical Union, Washington, DC, 599-615.
- Kuo, A.Y., E.P. Ruzicki, and C.S. Fang, 1976. The Effects of the Agnes flood on the salinity structure of the lower Chesapeake Bay and contiguous waters. In: *The Effects of Tropical Storm Agnes on the Chesapeake Bay Estuarine System*. The Chesapeake Research Consortium, Inc., vol. 54, 81-103.
- Le Provost, C., M.L. Genco, F. Lyard, P. Vincent, and P. Canceil, 1994. Spectroscopy of the world ocean tides from a finite element hydrodynamics model. *Journal of Geophysical Research*, 99, 24777-24797.
- Li, M., L. Zhong, W.C. Boicourt, S. Zhang, and D.-L. Zhang, 2007. Hurricane-induced destratification and restratification in a partially-mixed estuary. *Journal of Marine Research*, 65, 169-192.
- Liu, W., W. Chen, J. Kuo, and C. Wu, 2008a. Numerical determination of residence time and age in a partially mixed estuary using three-dimensional hydrodynamic model. *Continental Shelf Research*, 28, 1068-1088.
- Liu, W., W. Chen, and J. Kuo, 2008b. Modeling residence time response to freshwater discharge in a mesotidal estuary, Taiwan. *Journal of Marine Systems*, in press.
- Luettich, R.A., J.C. Muccino, and M.G.G. Foreman, 2002. Considerations in the calculation of vertical velocity in three-dimensional circulation models. *Journal of Atmospheric and Oceanic Technology*, 19, 2063-2076.
- MacCready, P., 1999. Estuarine adjustment to changes in river flow and tidal mixing. *Journal of Physical Oceanography*, 29, 708-726.
- MacCready, P., 2004. Toward a unified theory of tidally-averaged estuarine salinity structure. *Estuaries*, 27, 561-570.

- Mellor, G.L. and T. Yamada, 1982. Development of a turbulence closure model for geophysical fluid problems. *Reviews in Geophysics*, 20, 851-875.
- Miller, W.D., L.W. Harding Jr., and J.E. Adolf, 2005. The influence of Hurricane Isabel on Chesapeake Bay phytoplankton dynamics. In Sellner, K.G. (ed.): *Hurricane Isabel in Perspective*. Chesapeake Research Consortium, CRC Publication 05-160, Edgewater, MD, 155-160.
- Monismith, S., 1986. An experimental study of the upwelling response of stratified reservoirs to surface shear stress. *Journal of Fluid Mechanics*, 171, 407-439.
- Murty, T.S., 1984. Storm surges - meteorological ocean tides. Department of Fisheries and Oceans, Scientific Information and Publications Branch, Ottawa, Canada, 897 p.
- Myers, V.A. and W. Malkin, 1961. Some properties of hurricane wind fields as deduced from trajectories. National Hurricane Research Project Report, No. 49, NOAA, U.S. Department of Commerce, 43 pp.
- Neumann, G. and W.J. Pierson, 1966. *Principles of Physical Oceanography*. Prentice-Hall, Englewood Cliffs, New Jersey, 545 p.
- Niiler, P.P. and E.B. Kraus, 1977. One-dimensional models of the upper ocean: In Kraus E.B. (ed.): *Modelling and Prediction of the Upper Layers of the Ocean*. Pergamon, 143-172.
- North, E.W., S.-Y. Chao, L.P. Sanford, and R.R. Hood, 2004. The influence of wind and river pulses on an estuarine turbidity maximum: Numerical studies and field observations in Chesapeake Bay. *Estuaries*, 27, 132-146.
- Nycander, J. and K. Döös, 2003. Open boundary conditions for barotropic waves. *Journal of Geophysical Research*, 108(C5), 3168, doi:10.1029/2003JC001529.

- Ochi, M.K., 2003. *Hurricane-generated seas*. Elsevier Ltd., Kidlington, Oxford, UK, 140 p.
- Oey, L.-Y., G.L. Mellor, and R.I. Hires, 1985. A three-dimensional simulation of the Hudson-Raritan Estuary. Part I: Description of the model and model simulations. *Journal of Physical Oceanography*, 15, 1676-1692.
- Officer, C.B., 1976. *Physical Oceanography of Estuaries (and Associated Coastal Waters)*. Wiley, New York.
- Oliveira, A., and A.M. Baptista, 1998. On the role of tracking on Eulerian-Lagrangian solutions of the transport equation. *Advanced Water Research*, 21, 539-554.
- Olson, P., 1984. A Spectral Model for subtidal variability in the Chesapeake Bay. Tech. Report No. 82-04, Power Plant Siting Program, MD, 56 p.
- Osher, S., 1984. Riemann solvers, the entropy condition, and difference approximations. *SIAM Journal on Numerical Analysis*, 21, 217-235.
- Palma, E.D. and R.P. Matano, 1998. On the implementation of passive open boundary conditions for a general circulation model: the barotropic mode. *Journal of Geophysical Research*, 103, 1319-1341.
- Palma, E.D. and R.P. Matano, 2000. On the implementation of open boundary conditions for a general circulation model: the three-dimensional case. *Journal of Geophysical Research*, 105, 8605-8627.
- Park, K., H.-S. Jung, H.-S. Kim, and S.-M. Ahn, 2005. Three-dimensional hydrodynamic-eutrophication model (HEM-3D): application to Kwang-Yang Bay, Korea. *Marine Environmental Research*, 60, 171-193.
- Pedlosky, J., 1987. *Geophysical Fluid Dynamics*, 2nd edition. Springer-Verlag, New York,



710 pp.

Pedlosky, Joseph, 1996. *Ocean Circulation Theory*. Springer-Verlag, Heidelberg, 453 pp.

Pond, S., and G.L. Pickard, 1998. *Introductory Dynamical Oceanography*. Butterworth-Heinemann, 349 pp.

Pore, N. A., 1960. Chesapeake Bay hurricane surges. *Chesapeake Science*, 1, 178-186.

Pore, N. A., 1965. Chesapeake Bay extratropical storm surges. *Chesapeake Science*, 6, 172-182.

Price, J.F., E.A. Terray, and R.A. Weller, 1987. Upper ocean dynamics. *Reviews of Geophysics*, 25, 193-203.

Pritchard, D.W., 1952. Salinity distribution and circulation in the Chesapeake Bay estuaries system. *Journal of Marine Research*, 11, 106-123.

Pritchard, D.W., 1956. The dynamic structure of a coastal plain estuary. *Journal of Marine Research*, 15, 33-42.

Pritchard, D.W., 1967. Observations of circulation in coastal plain estuaries. In: Estuaries, G. Lauff (ed.). American Association for the Advancement of Science, 37-44.

Pritchard, D.W. and M.E.C. Vieira, 1984. Vertical variations in residual current response to meteorological forcing in the mid-Chesapeake Bay. In Kennedy, V.S. (ed.): *The Estuary as a Filter*. Academic Press, Orlando, 27-65.

Ralston, D.K., W.R. Geyer, and J.A. Lerczak, 2008. Subtidal salinity and velocity in the Hudson River estuary: Observations and modeling. *Journal of Physical Oceanography*, 38, 753-770.

Reay, W.G. and K.A. Moore, 2005. Impacts of Tropical Cyclone Isabel on shallow water quality of the York River estuary. In Sellner, K.G. (ed.): *Hurricane Isabel in*

- Perspective*. Chesapeake Research Consortium, CRC Publication 05-160, Edgewater, MD, 135-144.
- Reid, R.O., 1990. Waterlevel changes. Handbook of Coastal and Ocean Engineering. Gulf Publishing, Houston, Texas.
- Reynolds-Fleming, J.V. and R.A. Luettich, 2004. Wind-driven lateral variability in a partially mixed estuary. *Estuarine, Coastal and Shelf Science*, 60, 395-407.
- Rodi, W., 1984. Turbulence models and their applications in hydraulics: a state of the art review. Delft, The Netherlands, International Association for Hydraulics Research.
- Roman, M.R., J.E. Adolf, J. Bichy, W.C. Boicourt, L.W. Harding, Jr., E.D. Houde, S. Jung, D.G. Kimmel, W.D. Miller, and X. Zhang, 2005. Chesapeake Bay plankton and fish abundance enhanced by Hurricane Isabel. *EOS*, 86, 261-265.
- Sanford, L.P., 1988. Bathymetric control of tributary-mainstem interaction: the case of the Choptank River. *EOS*, 69, 1256.
- Sanford, L.P. and W.C. Boicourt, 1990. Wind-forced salt intrusion into a tributary estuary. *Journal of Geophysical Research*, 95 (C8), 13,357-13,371.
- Schubel, J.R. and D.W. Pritchard, 1986. Responses of upper Chesapeake Bay to variations in discharge of the Susquehanna River. *Estuaries*, 9(4A), 236-249.
- Schwiderski, E.W., 1980. On charting global ocean tides. *Reviews of Geophysics and Space Physics*, 18, 243-268.
- Scully, M.E., C. Friedrichs, and J. Brubaker, 2005. Control of Estuarine Stratification and Mixing by Wind-induced Straining of the Estuarine Density Field. *Estuaries*, 28, 321-326.
- Shapiro, R., 1970. Smoothing, filtering and boundary effects. *Reviews of Geophysics and*

- Space Physics*, 8, 359-387.
- Shay, L.K., S.W. Chang, and R.L. Elsberry, 1990. Free surface effects on the near-inertial ocean current response to a hurricane. *Journal of Physical Oceanography*, 20, 1405-1424.
- Shen, J., J.D. Boon, and A.Y. Kuo, 1999. A modeling study of a tidal intrusion front and its impact on larval dispersion in the James River estuary, Virginia. *Estuaries*, 22, 681-692.
- Shen, J., W. Gong, and H. Wang, 2005. Simulation of Hurricane Isabel using the advanced circulation model (ADCIRC). In: Sellner, K.G. (ed.), Hurricane Isabel in Perspective. Chesapeake Research Consortium, CRC Publication 05-160, Edgewater, MD, 107-116.
- Shen, J., W.P. Gong, and H.V. Wang, 2006a. Water level response to 1999 Hurricane Floyd in the Chesapeake Bay. *Continental Shelf Research*, 26, 2484-2502.
- Shen, J., H. Wang, M. Sisson, and W. Gong, 2006b. Storm tide simulation in the Chesapeake Bay using an unstructured grid model. *Estuarine, Coastal and Shelf Science*, 68, 1-16.
- Shepard, D., 1968. A two-dimensional interpolation function for irregularly spaced data. In: *Proceedings of the 1968 23rd ACM National Conference*, pp. 517-524.
- Simpson, J.E. and P.F. Linden, 1989. Frontogenesis in a fluid with horizontal density gradients. *Journal of Fluid Mechanics*, 202, 1-16.
- Smith, S.D., 1980. Wind stress and heat flux over the ocean in gale force winds. *Journal of Physical Oceanography*, 10, 709-726.

- Spigel, R.H. and J. Imberger, 1980. The classification of mixed layer dynamics in lakes of small to medium size. *Journal of Physical Oceanography*, 10, 1104-1121.
- Spitz, Y.H. and J.M. Klink, 1998. Estimate of bottom and surface stress during a spring-neap tide cycle by dynamic assimilation of tide gauge observations in the Chesapeake Bay. *Journal of Geophysical Research*, 103(C6), 12761-12782.
- Stacey, M.T., J.R. Burau, and S.G. Monismith, 2001. Creation of residual flows in a partially stratified estuary. *Journal of Geophysical Research*, 106, 17,013-17,037.
- Stommel, H. and H.G. Farmer, 1952. On the nature of estuarine circulation, Part I. Technical Report No. 52-88. Woods Hole Oceanographic Institute. Woods Hole, Massachusetts.
- Stommel, H. and A. Leetmaa, 1972. Circulation on the continental shelf. *Proceedings of the National Academy of Science USA*, 69, 3380-3384.
- Sweby, P.K., 1984. High resolution schemes using flux limiters for hyperbolic conservation laws. *SIAM Journal on Numerical Analysis*, 21, 995-1011.
- Tandon, A. and C. Garrett, 1994. Mixed layer restratification due to a horizontal density gradient. *Journal of Physical Oceanography*, 24, 1419-1424.
- Tandon, A. and C. Garrett, 1995. Geostrophic adjustment and restratification of a mixed layer with horizontal gradients above a stratified layer. *Journal of Physical Oceanography*, 25, 2229-2241.
- Tango, P., W. Butler, M. Trice, and C. Heyer, 2005. Phytoplankton community dynamics in Maryland's tidewaters in response to Hurricane Isabel. In Sellner, K.G. (ed.): *Hurricane Isabel in Perspective*. Chesapeake Research Consortium, CRC Publication 05-160, Edgewater, MD, 161-166.

- The Open University (TOU), 2001. *Ocean Circulation*. 2nd Ed., Butterworth-Heinemann, Oxford, England. 286 p.
- Thompson, R.O.R.Y. and J. Imberger, 1980. Response of a numerical model of a stratified lake to wind stress. *Proc. of 2nd Intl Symp. Stratified Flows*. Trondheim, June 1980, 1, 562-570.
- Trice, T.M., C. Heyer, B. Michael, B. Romano, P. Tango, and B. Cole, 2005. Impacts of Hurricane Isabel on Maryland water quality and living resources. In Sellner, K.G. (ed.): *Hurricane Isabel in Perspective*. Chesapeake Research Consortium, CRC Publication 05-160, Edgewater, MD, 145-154.
- Trowbridge, J.H., 1992. A simple description of the deepening and structure of a stably stratified flow driven by a surface stress. *Journal of Geophysical Research*, 97, 15529-15543.
- Umlauf, L. and H. Burchard, 2003. A generic length-scale equation for geophysical turbulence models. *Journal of Marine Research*, 61, 235-265.
- Umlauf, L. and H. Burchard, 2005. Second-order turbulence closure models for geophysical boundary layers. A review of recent work. *Continental Shelf Research*, 25, 795-827.
- Umlauf, L., H. Burchard, and K. Bolding, 2007. GOTM manual: Source code and test case documentation, version 4.0, 360 pp.
- Valle-Levinson, A., 1995. Observations of barotropic and baroclinic exchanges in the lower Chesapeake Bay. *Continental Shelf Research*, 15, 1631-1647.
- Valle-Levinson, A. and K.M.M. Lwiza, 1997. Bathymetric influences on the lower Chesapeake Bay hydrography. *Journal of Marine System*, 12, 221-236.

- Valle-Levinson, A. and R.E. Wilson, 1994. Effects of sill bathymetry, oscillating barotropic forcing and vertical mixing on estuary/ocean exchange. *Journal of Geophysical Research*, 99, 5149-5169.
- Valle-Levinson, A., J.M. Klinck, and G.H. Wheless, 1996. Inflows/outflows at the transition between a coastal plain estuary and the coastal ocean. *Continental Shelf Research*, 16, 1819-1847.
- Valle-Levinson, A., K.-C. Wong, and K.T. Bosley, 2001. Observations of the wind-induced exchange at the entrance to a coastal plain estuary. *Journal of Marine Research*, 59, 391-416.
- Valle-Levinson, A., K.-C. Wong, and K.T. Bosley, 2002. Response of the lower Chesapeake Bay to forcing from Hurricane Floyd. *Continental Shelf Research*, 22, 1715-1729.
- Valle-Levinson, A., C. Reyes, and R. Sanay, 2003. Effects of bathymetry, friction, and rotation on estuary-ocean exchange. *Journal of Physical Oceanography*, 33, 2375-2393.
- Vieira, M.E.C., 1983. A study of the non-tidal circulation in a segment in the middle reaches of the Chesapeake Bay. Ph.D. Dissertation, Johns Hopkins University, Baltimore, MD, 154 p.
- Vieira, M.E.C., 1985. Estimates of subtidal volume flux in mid-Chesapeake Bay. *Journal of Marine Research*, 21, 411-417.
- Vieira, M.E.C., 1986. The meteorologically driven circulation in mid-Chesapeake Bay. *Journal of Marine Research*, 44, 473-493.
- Wang, D.-P., 1979a. Subtidal sea level variations in the Chesapeake Bay and relations to

- atmospheric forcing. *Journal of Physical Oceanography*, 9, 413-421.
- Wang, D.-P., 1979b. Wind-driven circulation in the Chesapeake Bay, Winter 1975. *Journal of Physical Oceanography*, 9, 564-572.
- Wang, D.-P., 1980. Observation and modeling of the circulation in the Chesapeake Bay. In Hamilton, P. and K.B. Macdonald (eds.): *Estuarine and wetland processes with emphasis on modeling*. Plenum Press, New York, 35-48.
- Wang, D.-P., 1984. Mutual intrusion of a gravity current and density front formation. *Journal of Physical Oceanography*, 14, 1191-1199.
- Wang, D.-P. and A.J. Elliott, 1978. Non-tidal variability in the Chesapeake Bay and Potomac River: evidence for non-local forcing. *Journal of Physical Oceanography*, 8, 225-232.
- Wang, D.-P. and D.W. Kravitz, 1980. A semi-implicit two-dimensional model of estuarine circulation. *Journal of Physical Oceanography*, 10, 441-454.
- Wang, H.V. and B.H. Johnson, 2000. Validation and application of the second generation three dimensional hydrodynamic model of Chesapeake Bay. *Water Quality and Ecosystem Modeling*, 1, 51-90.
- Wang, H., J. Cho, J. Shen, and Y.P. Wang, 2005. What has been learned about storm surge dynamics from Hurricane Isabel model simulation? In: Sellner, K.G. (ed.), *Hurricane Isabel in Perspective*. Chesapeake Research Consortium, CRC Publication 05-160, Edgewater, MD, 117-125.
- Weatherill, N.P. 1988. A method for generating irregular computational grids in multiply connected planar domains. *International Journal for Numerical Methods in Fluids*, 8, 181-197.

- Weisberg, R.H., 1976. The non-tidal flow in the Providence River of Narragansett Bay: A stochastic approach to estuarine circulation. *Journal of Physical Oceanography*, 6, 721-734.
- Wilcox, D.C., 1998. Reassessment of scale determining equation for advance turbulence models. *AIAA Journal*, 26, 1299-1310.
- Williams, T.M., 1993. Salt water movement within the water table aquifer following Hurricane Hugo. In Brissette J.C. (ed.): *Proceedings of the Seventh Biennial Southern Silvicultural Research Conference*. U.S. Department of Agriculture, Forest Service, Southern Research Station, New Orleans, LA. Gen. Tech. Rep. SO-93, 177-184.
- Wiseman, W.J., 1986. Estuarine-shelf interactions. In Mooers, C.N.K. (ed.): *Baroclinic processes on continental shelves*. Coastal and Estuarine Sciences 3. American Geophysical Union, Washington, DC, 109-115.
- Wong, K.-C. And A. Valle-Levinson, 2002. On the relative importance of the remote and local wind effects on the subtidal exchange at the entrance to the Chesapeake Bay. *Journal of Marine Research*, 60, 477-498.
- Yankovsky, A.E. and D.C. Chapman, 1997. A simple theory for the fate of buoyant coastal discharges. *Journal of Physical Oceanography*, 27, 1386-1401.
- Zeng, X., M. Zhao, and R.E. Dickinson, 1998. Intercomparison of bulk aerodynamic algorithms for the computation of sea surface fluxes using TOGA COARE and TAO data. *Journal of Climatology*, 11, 2628-2644.
- Zervas, C., S. Duncan, D. Deitemyer, J. Hubbard, J. Culp, T. Landon, M. Connolly, D. Wright, and R. Bourgerie. 2000. Effects of Hurricane Floyd on water levels. NOAA



Technical Report NOS CO-OPS 027, 109 p.

Zhang, Y.-L., A.M. Baptista, and E.P. Myers, 2004. A cross-scale model for 3D baroclinic circulation in estuary-plume-shelf systems: I. Formulation and skill assessment.

*Continental Shelf Research*, 24, 2187-2214.

Zhang, Y. and A.M. Baptista, 2008. A semi-implicit Eulerian-Lagrangian finite-element model for cross-scale ocean circulation. *Ocean Modelling*, 21, 71-96.

Zhong, L. and M. Li, 2006. Tidal energy fluxes and dissipation in the Chesapeake Bay.

*Continental Shelf Research*, 26, 752-770.

## VITA

### KYOUNG-HO CHO

Born in Seoul, Republic of Korea, on December 23, 1972. Received B.S. in Oceanography from Inha University, Incheon, Republic of Korea, in 1998. Received M.A. in Physical Oceanography from Inha University in 2000. Was a research assistant of Korea Ocean Research and Development Institute (KORDI) for two years. Entered Ph.D. program at Virginia Institute of Marine Science/School of Marine Science, College of William and Mary in August, 2002.